Dissertation zur Erlangung des Doktorgrades
der Fakultät für Chemie und Pharmazie der
Ludwig-Maximilians-Universität München

Structural and biochemical characterization of the human SKI complex

Alexander Cäsar Robert Kögel

aus

Frankfurt am Main, Deutschland

2022

Erklärung

Diese Dissertation wurde im Sinne von § 7 der Promotionsordnung vom 28. November 2011 von Frau Prof. Dr. Elena Conti betreut.

Eidesstattliche Versicherung

Diese Dissertation wurde eigenständig und ohne unerlaubte Hilfe erarbeitet.

München, 12. April 2022

Alexander Kögel

Dissertation eingereicht am 12. April 2022

Erstgutachter: Prof. Dr. Elena Conti

Zweitgutachter: Prof. Dr. Karl-Peter Hopfner

Mündliche Prüfung am 27. Mai 2022

SUMMARY

The eukaryotic RNA-degrading exosome is universally present in nuclear and cytoplasmic cellular compartments and is involved in wide-spread RNA processing and degradation functions that rely on its 3'-5' RNA exonuclease activity. In the cytoplasm, it associates with the Ski complex via the Ski7 protein to function in mRNA turnover and surveillance pathways. As part of the Ski complex, together with the Ski3 and Ski8 proteins, the DExH helicase Ski2 binds and threads RNA to the exosome for degradation. The collaboration of the respective helicase and nuclease activities is conserved in eukaryotes and has been well studied in *S. cerevisiae*, but major questions regarding the molecular mechanisms of its regulation and unwinding activity remain open.

In this dissertation, we solved several cryo-EM structures of the human SKI (hSKI) complex in a resting state in absence of a substrate, in a substrate-binding but inactive state and in an active substrate-working state and uncovered the existence of two fundamentally different activity-related conformations. The open and closed conformations, are characterized by the detachment of the hSKI2 helicase core from the complex. In the closed state, the hSKI3 protein blocks the RNA exit site of the hSKI2 helicase like a gate to prevent threading of the substrate. In the open conformation, when the hSKI2 helicase is detached from the complex, the RNA exit site is free, allowing substrate translocation. When analyzed bound to the 80S ribosome, the inactive hSKI complex recognizes short RNA 3' overhangs at the mRNA entry site in the closed conformation. The activation of the complex the detaches the hSKI2 helicase and efficiently extracts RNA from the mRNA entry site of the ribosome.

The crystal structure of the *S. cerevisiae* Ski7-bound cytoplasmic exosome shows the interaction of Ski7 with a conserved binding interface with the nuclear exosome adaptor Rrp6. Knowing the precise mode of interaction between Ski7 and the exosome, we identified a human Ski7-like protein in a splicing variant of the HBS1L protein that bridges the interaction between the hSKI complex and the human cytoplasmic exosome. In subsequent biochemical experiments, we further verified its function and study the RNA channeling capabilities of the hSKI-exosome holocomplex. We conclude that RNA channeling to the cytoplasmic exosome requires the open conformation of hSKI and that RNA channeling between the two complexes follows a conserved principle similar to the nuclear Mtr4-exosome holocomplex. In addition, the

analysis and comparison to the homologous *S. cerevisiae* Ski complex allowed us to identify common principles of regulation with respect to the closed and open conformational states but also spots differences with respect to the auto-inhibition previously described in the *S. cerevisiae* complex.

The findings of this dissertation give unique insight into the molecular mechanisms of the human SKI complex and change the current understanding of how it functions together with the exosome to degrade mRNAs in the cytoplasm. These insights furthermore set the basis to begin to understand how hSKI-related mutations give rise to human disease.

LIST OF ABBREVIATIONS

A-site	Aminoacyl site
ADP	Adenosine diphosphate
ADP-BeF	ADP-beryllium fluoride
AMP-PNP	Adenosine 5′ -(β,γ-imido)triphosphate
ARE	AU-rich elements
ATP	Adenosine triphosphate
ATPase	ATP hydrolase
CrPV IRES	Cricket Paralysis Virus Internal Ribosome Entry Site
Cryo-EM	Cryo-electron microcopy
DNA	Deoxyribonucleic acid
EJC	Exon Junction Complex
eRNA	Enhancer RNA
Exo9/10	9-/10-subunit exosome
GTPases	GTP hydrolase
HB	Helical bundle
HLH	Helix-loop-helix
hSKI	Human SKI complex
$hSKI2_{arch}$	hSKI2 arch domain
$hSKI2_{cat}$	hSKI2 helicase core
$hSKI2_{N}$	N-terminus of hSKI2
$hSKI3_{C}$/$ySki3_{C}$	hSKI3/ySki3 C-terminal arm
$hSKI3_{N}$/$ySki3_{N}$	hSKI3/ySki3 N-terminal arm
mRNA	Messenger RNA
MW	Molecular weight
ncRNA	Non-coding RNA
NEXT	Nuclear exosome targeting
NGD	No-Go decay
NMD	Nonsense-mediated decay
NSD	Non-Stop decay

nt	Nucleotide
NTD	Amino-terminal domain
NTP	Nucleoside triphosphate
ORF	Open reading frame
P-site	Peptidyl site
PABP	Poly(A)-binding protein
PAXT	Poly(A) tail exosome targeting
poly(A)	Polyadenine
PROMTS	Promotor upstream transcripts
PTC	Premature stop codon
RNA	Ribonucleic acid
RNase	Ribonuclease
RNP	Ribonucleoprotein
rRNA	Ribosomal RNA
SF	Superfamily
Ski	Superkiller
snoRNA	Small nucleolar RNA
snRNA	Small nuclear RNA
THES	Tricho-hepato-enteric syndrome
TPR	Tetratricopeptide repeat
TRAMP	Trf4-Air2-MTR4 polyadenylation
tRNA	Transfer RNA
UTR	Untranslated region
WD-40	Trp-Asp 40
WH	Winged helix
ySki	Yeast Ski complex

LIST OF FIGURES AND TABLES

TABLE OF CONTENTS

1 INTRODUCTION

1.1 Degradation of mRNA in eukaryotes

The biological functions of RNAs in the eukaryotic cell are highly diverse. Besides coding and decoding of genetic information, RNAs take on a broad spectrum of regulatory tasks. A common principle for many classes of RNAs is their transcription as a precursor, which has to go through a sequence of processing or maturation steps in order to become fully functional. In the case of messenger RNAs (mRNAs), this constructive manner of RNA degradation often includes the splicing of introns and cleavage at polyadenylation signals. Other examples include the precise trimming of precursor ribosomal and transfer RNAs (rRNA, tRNA) to their required length. Besides the constructive functions, RNA degradation also has destructive effects, which aim at depleting certain RNA species from the cellular pool. These often terminal and potentially harmful processes are subject to tight regulation and for cytoplasmic mRNAs mainly follow two pathways, mRNA turnover and surveillance.

1.1.1 mRNA turnover

mRNA turnover refers to the complex cellular process by which functional mRNAs that become superfluous or detrimental for the cell are degraded in the cytoplasm. Different mRNAs are present for varying amounts of time in order to fulfil their function. Their half-lives can vary over several orders of magnitude from a few minutes to several hours and are based on a multiplicity of factors, but are ultimately determined by the present needs of the cell at a given time (Herrick et al. 1990; Munchel et al. 2011). Past their half-life, it is fundamental that mRNAs are degraded so as to regulate the number of transcripts in the cell and, by extension, the amount of protein expression. The process of mRNA turnover has been primarily studied in yeast (for a review, see Parker & Song 2004 or Parker 2012); however, the general principles are also valid for higher eukaryotes with some alterations.

Readily processed and exported mRNAs are equipped with a m^7Gppp-cap structure and a poly(A) tail at their respective 5' and 3' ends. Amongst other functions, the two structures protect mRNAs from the unspecific action of exonucleases in the cytoplasm (Pellegrini et al. 2008; Bernstein et al. 1989). Beyond that, the poly(A) tail has a regulative function for mRNA turnover. Its removal, in a process called deadenylation,

is a prerequisite for the decay of the mRNA body by downstream processes and considered to be the rate-limiting step in mRNA turnover (Decker & Parker 1993). Poly(A) tails vary at steady-state, but show lengths of up to 90 nt in *S. cerevisiae* and 250 nt in higher eukaryotes (C. E. Brown & Sachs 1998; Subtelny et al. 2014). Highly abundant poly(A)-binding proteins (PABPs; Pab1 in yeast, PABPC1 in humans) interact specifically and with high affinity to adenine bases to cover the entire length of the poly(A) tail and protect it from degradation (for a review, see Kühn & Wahle 2004).

Deadenylation is sequentially carried out by two poly(A) 3'-5' exonuclease complexes, Pan2-Pan3 and Ccr4-Not (for a review, see (Wahle & Winkler 2013). The Pan2-Pan3 complex possesses a poly(A)-specific 3'-5' exonuclease activity that resides within Pan2, a nuclease of the DEDD family of exonucleases (Schäfer et al. 2014). Its activity is stimulated by the presence of Pab1 bound to polyadenylated regions (Lowell et al. 1992). The initial shortening of the poly(A) tail by Pan2-Pan3 consecutively reduces the number of Pab1s bound to the poly(A) tail, and thereby the stimulatory effect on the nuclease complex. At a poly(A) length of approximately 30 nt, which allows for binding of not more than one Pab1 molecule, the activity of Pan2-Pan3 is significantly reduced (Lowell et al. 1992; Schäfer et al. 2019). In a current working model, the Ccr4-Not complex continues to erode the poly(A) tail once Pan2-Pan3 activity fades. The *S. cerevisiae* Ccr4-Not complex consists of up to seven subunits (up to eight subunits in humans), two of which Ccr4 and Caf1 are exonucleases of the EEP and RNase D families, respectively (Basquin et al. 2012). Caf1's activity is significantly inhibited in presence of Pab1. It is thought to degrade terminal poly(A) regions devoid of Pab1. In contrast, Ccr4 is stimulated by the presence of Pab1 (Yi et al. 2018; Webster et al. 2018; Raisch et al. 2019). Furthermore, while Pan2-Pan3, with some exceptions, is broadly recruited to poly(A) tails, Ccr4-Not activity is increased by the function of adaptor proteins which tether the complex to mRNA-specific sequence elements in the 3' UTR (Webster et al. 2019; Stowell et al. 2016). The functions of these two enzyme complexes, however, are partly redundant, and only the deletion of both activities together abolishes deadenylation in vivo (Tucker et al. 2001). The poly(A) tail also has interesting repercussions for mRNA translation, where Pab1s interact with eIF4F at the 5' m^7Gppp-cap to support the initiation of translation. Conversely, deadenylation and dissociation of Pab1 from the mRNA disfavors translation initiation (Wells et al. 1998).

Following deadenylation, the mRNA is subject to two different decay routes (Figure 1). In the 5'-3' direction, the body of the mRNA is degraded by the exonuclease Xrn1. This

pathway requires and is initiated by the removal of the protective 5' m^7Gppp-cap. Deadenylated mRNA 3' ends that contain no more than 5-10 As are recognized by the Pat1-Lsm1-7 complex. Bound to the 3' end, the complex recruits the decapping machinery to the m^7Gppp-cap structure at the mRNA 5' end (Tharun & Parker 2001; Chowdhury et al. 2007). The Dcp2 protein, a member of the Nudix family of pyrophosphatases, is central to the decapping machinery, as it cleaves the m^7Gppp-cap to produce m^7Gpp and a 5' monophosphorylated mRNA. It forms a complex with Dcp1 to promote Dcp2's catalytic activity (van Dijk et al. 2002; Steiger et al. 2003). Edc1/2 and Edc3 further associate with the decapping machinery to enhance its activity (Dunckley et al. 2001; Kshirsagar & Parker 2004). Recruitment of the decapping factors to the 5' cap by Pat1-Lsm1-7 competes with the binding of eIF4F to initiate translation. In this intermediate, translationally repressed state prior to decapping, the deadenylated mRNA can shuttle into processing bodies (P-bodies), cytoplasmic foci of translationally inactive mRNPs (for a review, see Decker & Parker 2012). Outside of P-bodies, successful decapping recruits the 5'-3' exonuclease Xrn1 to the monophosphorylated 5' end where it interacts with Pat1-Lsm1-7 at the same binding site as Dcp1-Dcp2 complex (Bouveret et al. 2000; Nissan et al. 2010). Xrn1 is a processive 5'-3' exonuclease similar to other enzymes of the Xrn family like the nuclear Rat1 nuclease. It has specificity for 5' monophosphorylated RNA, whereas 5'-triphosphorylation or m^7Gppp-capping of substrates decreases its activity by two orders of magnitude (Pellegrini et al. 2008). Xrn1 has an intrinsic ATP-independent unwinding activity which gives it high processivity (Jinek et al. 2011), and was recently shown to act co-translationally upstream of translating ribosomes (Tesina et al. 2019). The precise coordination of decapping and 5'-3' degradation activities is poorly understood.

In the 3'-5' direction, the deadenylated, unprotected mRNA 3' end is a substrate to a multiprotein 3'-5' exonuclease complex, called the RNA degrading exosome (for a review, see S. Lykke-Andersen et al. 2009). The exosome has several different exo- and endo-nuclease activities and features 30 nt long RNA channel to provide efficient RNA degradation. The complexity of the exosome requires it to associate with the Ski complex, an equally complicated helicase complex that specifies and regulates exosome function in the cytoplasm (J. S. J. Anderson & Parker 1998). Their combined function is coordinated by a protein of the family of translational GTPases, Ski7, which mediates their interaction (Araki et al. 2001). The exosome itself has no sequence

specificity, explaining its broad usage in mRNA degradation, but it is believed to be recruited to AU-rich elements (ARE) in the 3' UTR of certain mRNAs in higher eukaryotes (Chen et al. 2001; J. Lykke-Andersen & Wagner 2005).

The two decay routes are partly redundant in *S. cerevisiae*. Their disruption in either 5'-3' or 3'-5' direction significantly reduces mRNA degradation, but can be compensated for by the other direction. Yeast strains with deletions that render both decay routes inactive are not viable (A. W. Johnson & Kolodner 1995; J. S. J. Anderson & Parker 1998; He et al. 2003).

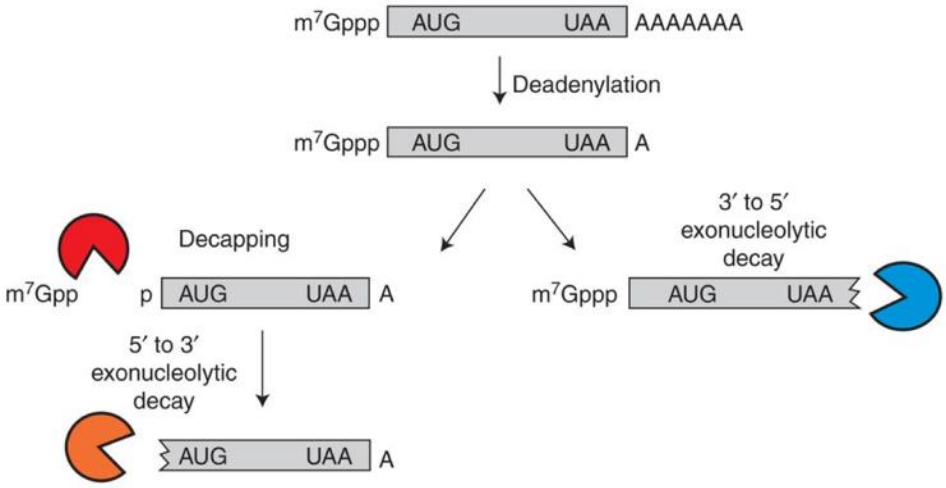

Figure 1. General mechanisms of eukaryotic mRNA turnover. The schematic shows a simplified model mRNA with a 5' m^7Gppp cap, AUG start and UAA stop codons and a poly(A) tail at the 3' end. The process of deadenylation as the rate-limiting step in mRNA turnover precedes the downstream decay routes in 5'-3' and 3'-5' direction. The decapping enzymes Dcp1-Dcp2 are illustrated by the red packman, the Xrn1 5'-3' exonuclease by the orange packman, and the exosome as the 3'-5' exonuclease by the blue packman. The schematic was taken and adapted from (Decker & Parker 2012).

1.1.2 mRNA surveillance

mRNA surveillance refers to the mechanism by which aberrant mRNAs are detected and degraded in eukaryotes. This specific mode of degradation generally differs from ‘conventional’ mRNA turnover in the cytoplasm by circumventing prior deadenylation (Parker 2012). Based on the nature of the aberrant transcript and the particularities of their decay, three general cytoplasmic pathways are suggested to exist in eukaryotes, No-Go (NGD), Non-Stop (NSD) and Nonsense-mediated (NMD) mRNA decay (Figure 2).

Substrates of NGD are recognized by translating ribosomes that undergo translational arrest when they encounter stem loops, rare codons, polyLys or polyArg codons in the open reading frame (ORF) (Doma & Parker 2006; Kuroha et al. 2010; Letzring et al. 2010; Tsuboi et al. 2012). The translational arrest leads to a failure of the ribosome to execute peptidyl transfer in the decoding center and leaves the ribosomal A-site unoccupied. The empty A-site is recognized by the Dom34 (Pelota in mammals) and Hbs1 ribosome recycling factors, paralogues of the eRF1-eRF3 translation termination factors (Shoemaker et al. 2010; Pisareva et al. 2011; Becker et al. 2011). In many cases, the binding of the Dom34-Hbs1 recycling complex results in an endonucleolytic cleavage of the mRNA in proximity of the stalled ribosome (Doma & Parker 2006). The resulting fragments upstream and downstream of the stalling site still contain a m^7Gppp-cap and a poly(A) tail and are rapidly degraded by the exosome in the 3'-5' and by Xrn1 in the 5'-3' direction without the need for prior decapping or deadenylation (Doma & Parker 2006). It appears that colliding ribosomes (Juszkiewicz et al. 2018; Ikeuchi et al. 2019) and their subsequent ubiquitination (by Hel2 or ZNF593 in higher eukaryotes) play a crucial role in initiating the endonucleolytic cleavage in NGD (Saito et al. 2015; Garzia et al. 2017; Simms et al. 2017; Matsuo et al. 2017; Juszkiewicz & Hegde 2017). The identity of the responsible endonuclease(s), however, is currently unknown, but there are promising candidates (D'Orazio et al. 2019; Glover et al. 2020).

NSD recognizes and rapidly degrades transcripts that do not contain a termination codon (for a review, see Klauer & van Hoof 2012). Such mRNAs can occur through mistakes during transcription, splicing or the false recognition of cryptic polyadenylation sites within the ORF during processing, which is estimated to happen in about 10% of transcribed mRNAs (van Hoof et al. 2002). Their translation is not conventionally terminated and is believed to continue until translating ribosomes encounter polyadenylated regions or the 3' end (Chandrasekaran et al. 2019). Degradation of NSD transcripts occurs rapidly by circumventing the deadenylation of the 3' end as shown in ΔCcr4 yeast strains (van Hoof et al. 2002; Frischmeyer et al. 2002). NSD is also largely independent of the 5'-3' decay route, as shown in ΔXrn1 and ΔDcp1-ΔDcp2 yeast stains (Frischmeyer et al. 2002), whereas deletions in the 3'-5' decay route (ΔSki2, ΔSki3, ΔSki8, ΔSKI7, ΔCsl4) stabilize the NSD mRNA (van Hoof et al. 2002). NSD is furthermore dependent on the translation of the defect transcript (Frischmeyer et al. 2002), and requires the C-terminal GTPase domain of the Ski7 protein (van Hoof et al. 2002).

NMD substrates are characterized by a premature termination codon (PTC) in the ORF that if recognized as a regular termination signal would result in a truncated protein product. Instead, the PTC is recognized as aberrant and the faulty mRNA rapidly degraded (for a review, see Kurosaki et al. 2019). NMD substrates can come from mutations and wrong intron splicing in the nucleus, but there are also physiological transcripts containing PTCs, for which NMD appears to be the mode of decay (Hillman et al. 2004). The mechanism of PTC recognition is still largely unclear, but several working models exist (for a review, see Karousis & Mühlemann 2019). In the Exon-junction complex (EJC) model, the proximity of a termination codon to an EJC marks it as premature. It is recognized by the canonical eRF1-eRF3 termination factors, which recruit Upf1, Upf2, Upf3 together with a set of yeast- or mammalian-specific NMD factors to sense the proximal EJC. In another prominent model, the NMD machinery senses an unusually long 3' UTR, in which the poly(A) tail with its PABPs is too far away from the PTC. The NMD transcript is thought to be cleaved by the SMG6 endonuclease in mammals (Eberle et al. 2009) and then degraded by Xrn1 in 5'-3' or in 3'-5 direction by the exosome.

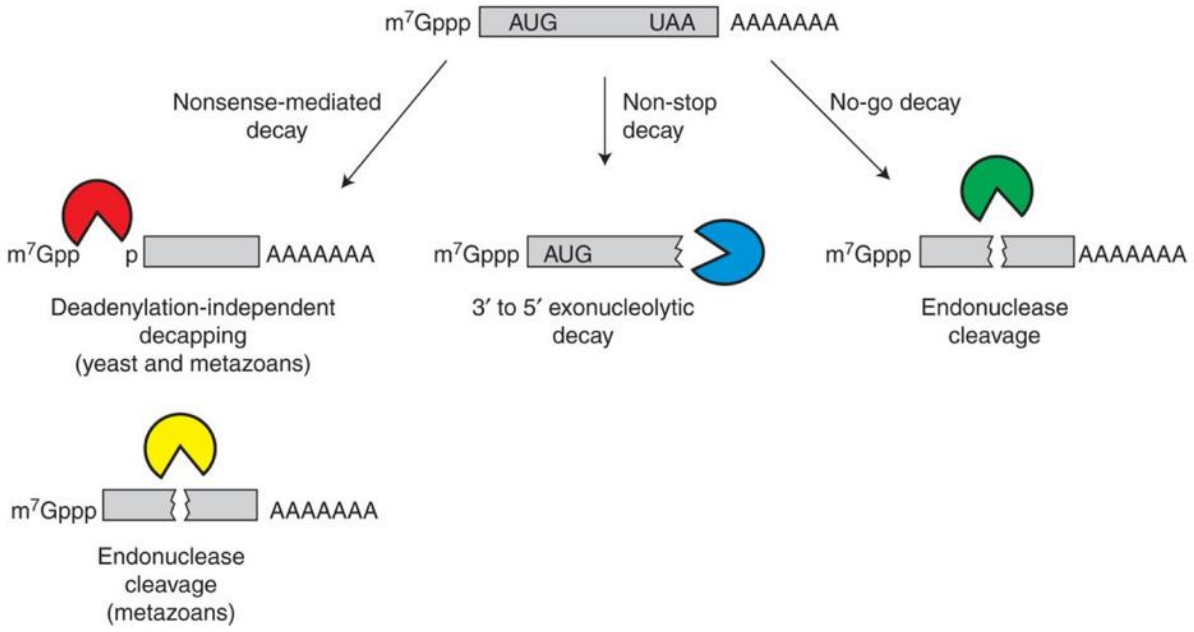

Figure 2. Cytoplasmic mRNA surveillance mechanisms in eukaryotes. The schematic describes the decay of a simplified aberrant mRNA in the NMD, NSD and NGD pathways. The decay pathway depends on the nature of the mRNA defect and is independent of prior deadenylation. The red packman in the NMD pathway **(Left)** illustrates the Dcp1-Dcp2 decapping enzyme in a deadenylation-independent decapping reaction, characteristic for this pathway. The yellow packman represents the presumed SMG6 endonuclease that acts in NMD in higher eukaryotes. The blue packman in the NSD pathway

(Middle) depicts the exosome in the 3'-5' directed mRNA decay. This pathway is independent of the 5'-3' decay route by Xrn1. The green packman in NGD **(Right)** represents the unknown endonuclease that produces up- and downstream cleavage fragments. The fragments are substrate to degradation in the 5'-3' and 3'-5' decay routes (not shown in the schematic). Note that the initiation of NSD and NGD is also independent of the decapping machinery. The schematic was taken and adapted from (Decker & Parker 2012).

1.2 The eukaryotic RNA degrading exosome

The eukaryotic exosome is universally present in the cell and is involved in processes that go beyond mRNA turnover and surveillance. It was first described in yeast, where mutations in the Rrp4p protein caused defects in the processing of the ribosomal 5.8S RNA (Mitchell et al. 1996; Mitchell et al. 1997). From its discovery, it took over a decade of biochemical and structural analysis to understand it at a molecular level. The core of the exosome consists of ten subunits (Exo10). Nine of the proteins are catalytically inactive and form a barrel-like structure (Exo9) with a central RNA channel that continues to the exonuclease active site of the tenth subunit, Rrp44 (Figure 3) (Bonneau et al. 2009; Makino et al. 2013).

The Exo9 barrel of the eukaryotic exosome consists of six proteins of the RNase PH family of exonucleases and three proteins that contain K-homology (KH) and ribosomal protein S1 (S1) domains, involved in RNA-binding (Grishin 2001; Suryanarayana & Subramanian 1984). The six RNase PH-like proteins (Rrp41p, Rrp42, Rrp43, Mtr3, Rrp45 and Rrp46) form a symmetric, heterohexameric ring structure with central RNA channel (Büttner et al. 2005; Lorentzen et al. 2005; Liu et al. 2006; Makino et al. 2013). Other than their homologues in archaea and bacteria, and several plant species (Büttner et al. 2005; Lorentzen et al. 2005; Ishii et al. 2003; Sikorska et al. 2017), the phosphorolytic exonuclease activity of the RNase PH-like proteins is lost in the eukaryotic exosome (Dziembowski et al. 2007). The three S1/KH domain proteins (Rrp4, Csl4 and Rrp40) bind the RNase PH-like ring like ‘cap’ to continue the RNA channel towards the ‘top’ (Büttner et al. 2005; Liu et al. 2006; Hernández et al. 2006; Makino et al. 2013).

Rrp44 is a multidomain protein similar to *Escherichia coli* RNase II (Frazão et al. 2006; Zuo et al. 2006). It consists of two cold shock domains (CSD), a 3'-5' exoribonuclease domain (RNB) with a Mg^{2+}-dependent hydrolytic activity and a S1 domain (Dziembowski et al. 2007; Lorentzen et al. 2008). In addition, Rrp44 has a N-terminal

PilT domain (PIN) with an endonuclease activity (Lebreton et al. 2008; Schaeffer et al. 2009; Schneider et al. 2009), which appears to be inactive in the cytoplasmic human homologue hDis3L (Tomecki et al. 2010; Staals et al. 2010). The protein binds the RNase PH-like ring at the 'bottom' and extends the RNA channel towards the active site in the RNB domain (Bonneau et al. 2009; Makino et al. 2013). In RNase protection experiments, which analyze radio-labelled RNA fragments bound by the protein(s) of interest and protected from RNase digestion, the 10-subunit exosome accommodates 31-33 nucleotide long single stranded RNA (Bonneau et al. 2009; Makino et al. 2013). At the same time, the exosome degrades RNA, provided that the substrate has a single stranded 3' overhang of minimum 35 nucleotides, long enough to traverse RNA channel and reach the Rrp44 exonuclease active site (Bonneau et al. 2009). In contrast to enzymes with a distributive exonuclease activity, where repeated cleavage is dependent on rebinding of the substrate, the RNA channel enables the exosome to 'hold on' to the substrate during an ongoing cleavage reaction, thereby providing processivity (Vuković et al. 2016).

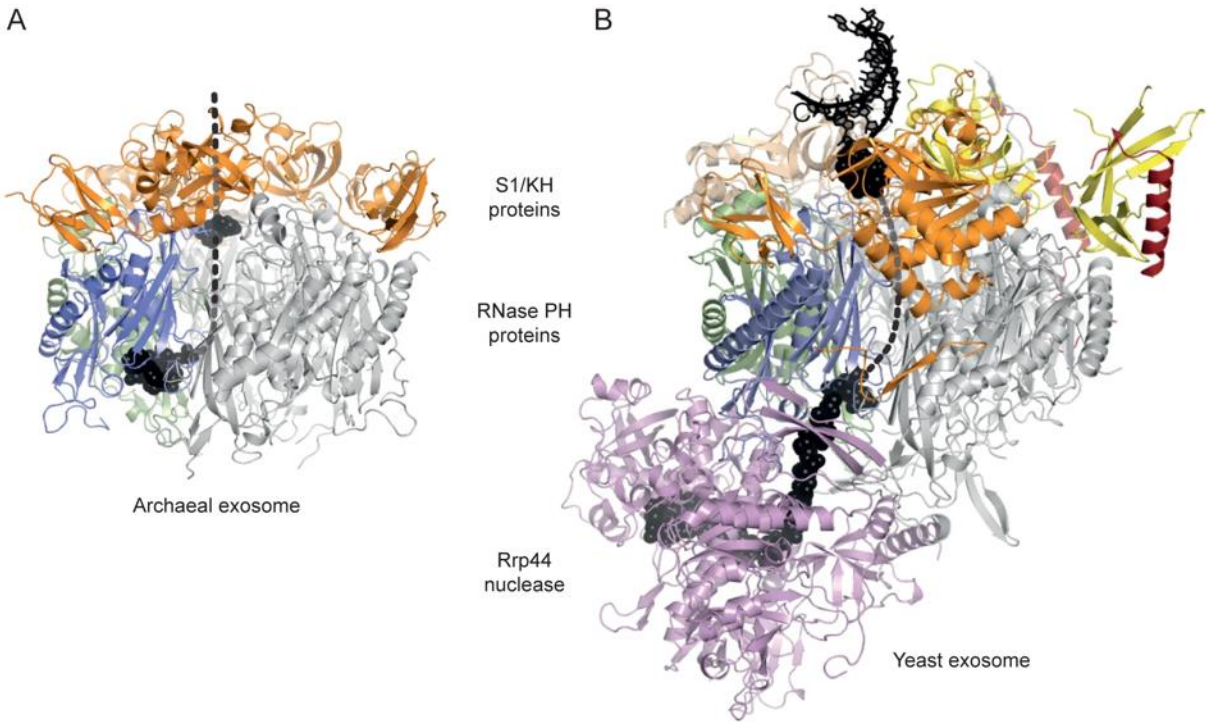

Figure 3. Composition and RNA channeling of the archaeal and eukaryotic exosomes. The archaeal exosome in **(A)** consists of three of Rrp41-Rrp42 dimers (blue and green) to form the RNase PH-like ring (grey), which is bound by three S1/KH cap proteins, Rrp4 or Csl1 or a potential combination of both (orange). The S1/KH cap and the RNase PH-like ring form a central RNA channel towards the phosphorolytic Rrp41 subunits. The eukaryotic exosome in **(B)** has a similar organization, but other than

the archaeal exosome, it forms a hetorhexameric ring of six different inactive RNase PH-like proteins (Rrp41 blue, Rrp42 green, rest grey), bound by three different S1/KH cap proteins, Rrp4 (orange), Csl4 (yellow) and Rrp40 (wheat). The RNA channel of the eukaryotic exosome traverses the cap and ring structures and continues towards the hydrolytic exonuclease, Rrp44 (pink). The RNA (black) is shown as surface and indicated with a dotted line. The Rrp6-CTD (red) is bound to Csl4 and a part of the RNase PH-like ring. This figure was taken and adapted from (Makino et al. 2013).

In the nucleus, the exosome is bound by another nuclease, Rrp6 (Briggs et al. 1998; Allmang et al. 1999). It stems from the family of DEDD type exonucleases. It contains a PMC2NT domain, a DEDD-Y domain and HRDC (helicase and RNase D C-terminal) (Januszyk et al. 2011; Makino et al. 2015). In active conformation, when the protein cleaves nucleotide monophosphates from the RNA 3' end in a distributive manner, Rrp6 binds the exosome on top of the cap like a lid to restrict access to the central exosome RNA channel (Makino et al. 2015). In the presence of substrates dedicated to the usage of the exosome channel and processive degradation by Rrp44, Rrp6 switches into a substrate channeling mode, in which the Rrp6 lid is detached from the entry pore, while its C-terminus remains bound at the side of the exosome barrel (Makino et al. 2013; Makino et al. 2015; Schuller et al. 2018).

1.3 The exosome is regulated by RNA helicases

The exosome is a highly efficient RNA degradation machinery, and as such is subject to strict regulation. Its inability to deal with RNA substrates that have strong secondary structures folds or are bound by proteins acts as a layer of regulation, which prevents uncontrolled RNA degradation in the cell. Except for the need of a single stranded 3' overhang long enough to traverse its RNA channel (Bonneau et al. 2009), it does not have any known specificity that would allow it to distinguish between substrates. The exosome is, therefore, dependent on additional factors to target the right substrate at the right time. These tasks are mainly executed by two Ski2-like RNA helicases from Superfamily 2 (SF2; for a review, see S. J. Johnson & Jackson 2013), which provide the exosome with an unwound single stranded RNA 3' end. In the nucleus, the exosome functions together with the Mtr4 helicase, in the cytoplasm, with Ski2.

The Superfamily 2 (SF2) of helicases is a functionally diverse group of enzymes with more than 100 recognized members in *H. sapiens* and *S. cerevisiae* (Fairman-Williams

et al. 2010). Their two consecutive Recombinase A (RecA) domains have a conserved set of at least 12 signature motifs, which are important for NTP-binding and hydrolysis, nucleic acid binding and the coordination of the respective binding sites. The presence of these signature motifs differentiates the helicases of SF2 from members of Superfamily 1 (SF1), which use an alternate set of these signature motifs. The enzymes of SF2 share a similar domain organization and structure (Ozgur et al. 2015; S. J. Johnson & Jackson 2013; Fairman-Williams et al. 2010), but their functions vary in terms of nucleotide usage, nucleic acid specificity, unwinding directionality and unwinding activity. With only a few known members (Fairman-Williams et al. 2010), the helicases of the SF2 family of Ski2-like helicases show considerable functional overlap as they exclusively hydrolyze ATP to unwind nucleic acids with a 3'-5' polarity. Some diversity with respect to their nucleic acid specificity, however, persists. An example of a Ski2-like helicase that has been analyzed in mechanistic detail is the DNA helicase Hel308 from *Archaeoglobus fulgidus* (Büttner et al. 2007). Its two consecutive RecA domains (RecA1 and RecA2) fold against a winged helix (WH) and helical bundle (HB) domain to create an overall globular helicase core with a central RNA-binding channel (Figure 4). In a current model for the translocation of nucleic acids, ATP hydrolysis at the DExH active site within RecA1 is thought to trigger small ratcheting motions between the two RecA domains which move the substrate through the helicase core, while the ‘ratchet’ helix in the HB domain holds on to it to prevent back-translocation. This model of nucleic acid translocation is often referred to as an inchworm model (Büttner et al. 2007; S. J. Johnson & Jackson 2013). At the entry pore for the substrate, the RecA2 domain has a conserved ß-hairpin which is thought to melt base pairs of nucleic acid duplexes prior to translocation (Büttner et al. 2007).

The mechanisms of unwinding by the nuclear Mtr4 and cytoplasmic Ski2 exosome helicases are thought to be similar to those of Hel308 (Weir et al. 2010; Halbach et al. 2012). Their helicase core shows a conserved domain organization with two RecA, WH and HB domains, but other than Hel308, the exosome helicases feature the insertion of an arch domain into the WH domain with additional RNA-binding properties (Weir et al. 2010; Halbach et al. 2012). The arch domain has been shown to aid in substrate recognition and regulation of the helicase (Lingaraju et al. 2019; Schuller et al. 2018; Weir et al. 2010; Schmidt et al. 2016; Halbach et al. 2013). Furthermore, unlike Hel308, the Mtr4 and Ski2 helicases specifically unwind RNA substrates and

present a single stranded RNA 3' end of sufficient length to the exosome for degradation.

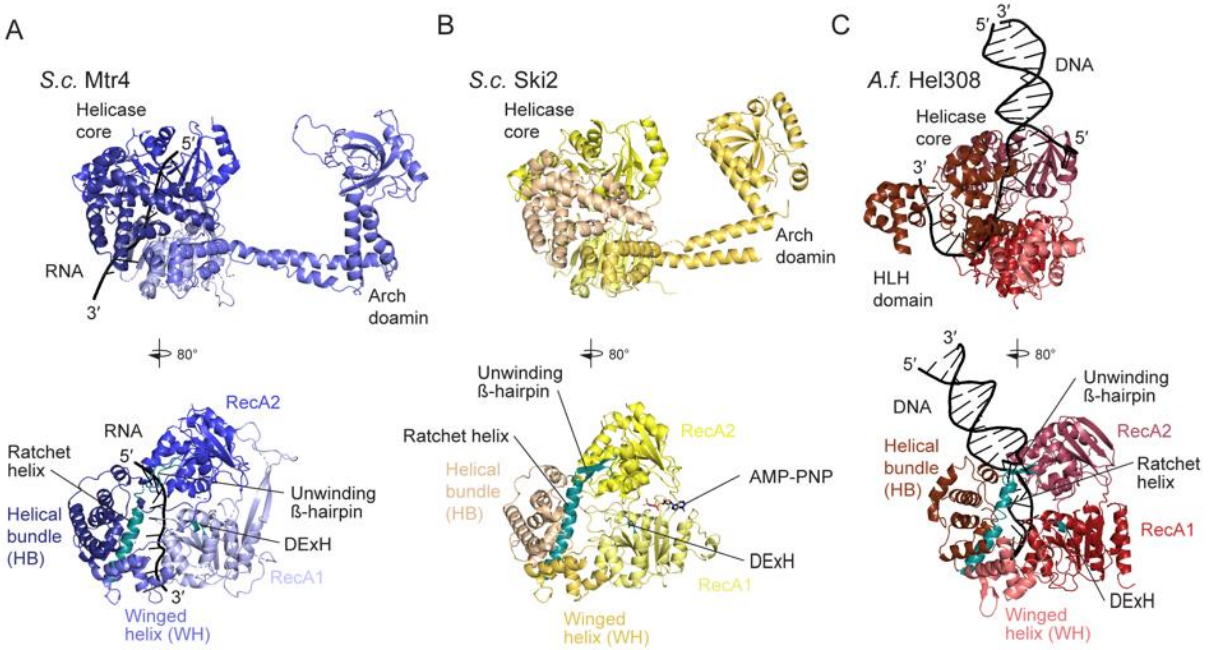

Figure 4. Comparison of the domain organization of three Ski2-like helicases from SF2. **(A)** shows the structure of the Mtr4 helicase from *S. cerevisiae* while channeling a substrate RNA with 3'-5' polarity. The interaction with the RNA are made with conserved residues of RecA2, RecA1 and HB domain (in this order from 5' to 3' end of the RNA). The depicted structure was taken out of the context of the pre60S ribosome substrate and the nuclear exosome for the purpose of this comparison. The interaction with the pre60S ribosome explains the wide open position of the arch domain. **(B)** shows the crystal structure of the Ski2 helicase from *S. cerevisiae* in complex with the nonhydrolyzable nucleotide analogue AMP-PNP close to the DExH active site. The arch domain is in a more closed conformation, tilted towards the helicase core, in comparison to (A). **(C)** shows the crystal structure of the DNA helicase Hel308 from *A. fulgidus* bound to a DNA duplex with a 10 nt single-stranded 3' overhang. The interactions with the DNA substrate are made with the domains described in (A). Hel308 is thought to function on the lagging strand in the replication fork, in which the helix-loop-helix (HLH) domain holds on to the leading strand with additional DNA interactions. Other than the nuclear and cytoplasmic exosome helicases (A, B), Hel308 does not have an arch domain inserted into the WH domain. The conserved RecA1, RecA2, WH, and HB domains are indicated in the structures, as well as the DExH active site, the unwinding ß-hairpin and the ratchet helix, which are colored in teal. The coordinates were taken from PDB 2XGJ (Mtr4; Weir et al. 2010), PDB 4A4Z (Ski2; Halbach et al. 2012) and PDB 2P6R (Hel308; Büttner et al. 2007). The arch and HLH domains are omitted from the lower panels for clarity.

In the nucleus, Mtr4 recruits the exosome to target a large variety of RNA substrates. In order to gain specificity for those substrates, the helicase associates with different sets of adaptor proteins in a variety of functionally different complexes (Kilchert et al. 2016). The Trf4-Air2-Mtr4 polyadenylation (TRAMP) complex, for example, targets the exosome for degradation of aberrant tRNAs, snRNAs, snoRNAs, and other non-coding, but also coding RNAs (for a review, see J. T. Anderson & Wang 2009). In this complex, the zinc finger protein (Trf4, Trf5) is thought to be involved in substrate recognition, while the Air1/2 polymerase adds short stretches of poly(A) to the 3' end that support loading of the Mtr4 helicase (LaCava et al. 2005; Jia et al. 2011; Falk et al. 2014; Das et al. 2021). In higher eukaryotes, TRAMP appears to be restricted to the nucleolus, but other nuclear Mtr4 complexes have evolved. As part of the nuclear exosome targeting (NEXT) complex (Lubas et al. 2011; Falk et al. 2016; Puno & Lima 2018), MTR4 associates with a different zinc finger protein (ZCCHC8) and the RRM domain protein RBM7 to recruit the exosome to target snRNAs, snoRNAs, enhancer RNAs (eRNAs) and promotor upstream transcripts (PROMTS) (Lubas et al. 2011; Lubas et al. 2015; Wu et al. 2020). As part of the poly(A) exosome targeting complex (PAXT), which involves another zinc finger (ZFC3H1) and the nuclear poly(A) binding protein PABPN1, Mtr4 recruits the exosome to target polyadenylated nuclear RNAs (Meola et al. 2016). The diversity of nuclear Mtr4 complexes and their substrates keeps increasing with new discoveries and is under constant investigation (Figure 5).

In contrast, in the cytoplasm, the Ski2 helicase associates with the exosome to target one major class of substrates – messenger RNAs. At the same time, it is part of a single, constitutive complex, the SKI complex. The Ski complex consists of the central Ski2 helicase and is surrounded by the large tetratricopeptide repeat (TRP) protein Ski3 and two ß-propeller Ski8 proteins. The Ski3 and Ski8 proteins are believed to regulate the unwinding activity of Ski2 (Halbach et al. 2013), but the detailed molecular mechanisms of this regulation are largely unclear.

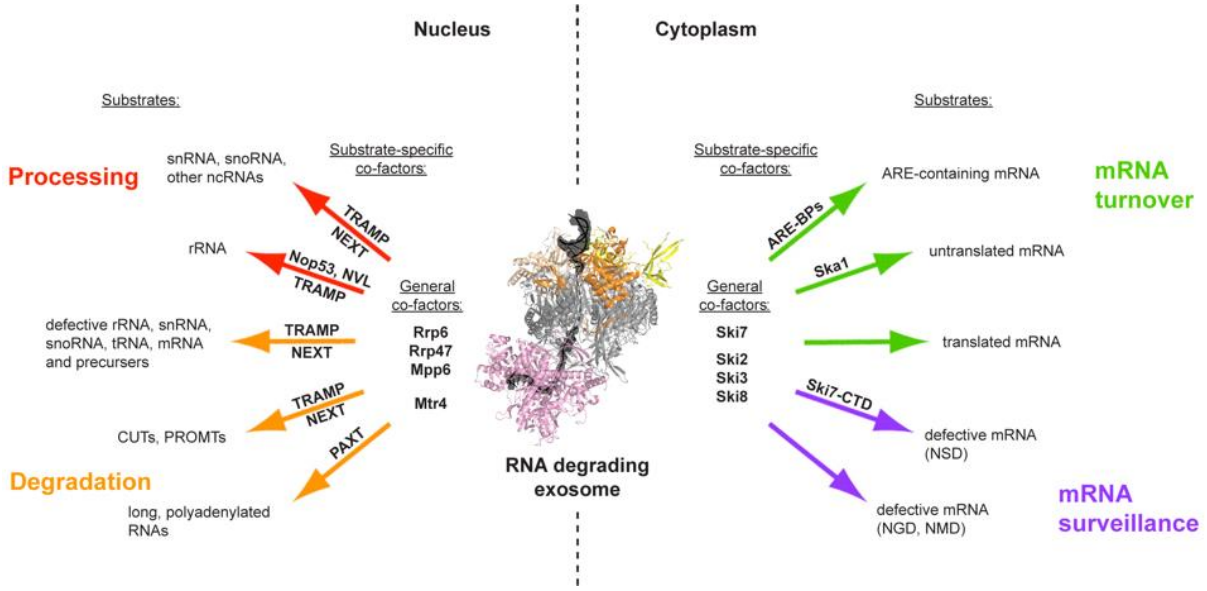

Figure 5. Functions of the nuclear and cytoplasmic exosome complexes. The schematic distinguishes Mtr4 and Ski2 as general exosome cofactors of the exosome from another layer of substrate-specific cofactors and gives and overview of the of functional diversity of the eukaryotic exosome. This figure was taken and adapted from (S. Lykke-Andersen et al. 2009).

Both Mtr4 and Ski2 helicases are recruited to the exosome by additional proteins to ensure a smooth ensemble of the respective helicase and nuclease activities. In the nucleus, the Mtr4 N-terminus interacts with the small protein Rrp47 (C1D in humans) and the Rrp6 N-terminus (with Rrp6 in substrate channeling mode) to keep the helicase close by (Schuch et al. 2014; Makino et al. 2015). Another small protein, Mpp6, interacts with the Mtr4 helicase core and the S1/KH cap proteins to position the helicase in proximity of the opening to the substrate channel of the exosome (Figure 6) (Falk et al. 2017; Weick et al. 2018; Gerlach et al. 2018; Schuller et al. 2018). In RNase protection experiments as described above for the 10-subunit exosome (31-33 nt, The eukaryotic RNA degrading exosome), the presence of Mtr4 (and Rrp6, Mpp6) shows the protection of RNA fragments of approximately 45 nt (Falk et al. 2017). The data is in agreement with several cryo-EM structures that show he formation of a continuous RNA channel between the Mtr4 helicase and the nuclear exosome (Schuller et al. 2018; Weick et al. 2018; Gerlach et al. 2018). While the interplay of the respective helicase and nuclease activities of the nuclear Mtr4-exosome complex has been intensively studied both biochemically and structurally, structural data for the cytoplasmic helicase-exosome interaction is particularly scarce. In vivo and in vitro biochemical data shows that the *S. cerevisiae* Ski7 protein contains a domain-lacking

N-terminus, which comprises Ski and exosome binding sites (Araki et al. 2001; Halbach et al. 2013). Mechanistic insight into the interactions of Ski7 between the Ski and exosome complexes remains elusive.

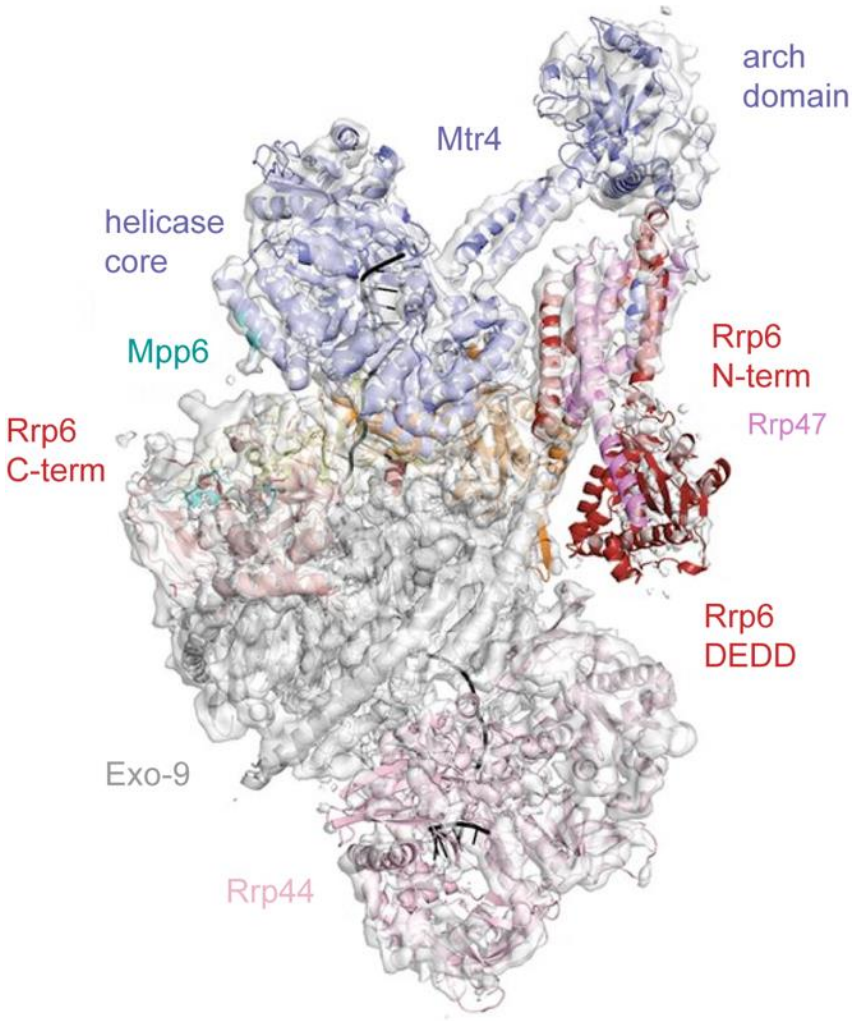

Figure 6. Structure of the *S. cerevisiae* Mtr4-exosome complex. The Mtr4 helicase interacts with Rrp4 at the S1/KH cap on top of the exosome to thread RNA (black) into the central substrate channel. It is tethered to the exosome via the Mpp6 protein on one side and the sandwich of Rrp47 and the N-termini of Mtr4 and Rrp6 on the other side. In substrate channeling mode, i.e. for RNA degradation by Rrp44, the Rrp6 DEDD nuclease domain is released from the cap and positioned on the side of the exosome. This figure was taken and adapted from (Schuller et al. 2018).

1.4 The cytoplasmic Ski-exosome complex requires the Ski7 bridging protein in yeast

The Ski7 protein mediates the interaction between the Ski complex and the cytoplasmic exosome in yeast. As such it is important for all 3'-5' mRNA degradation processes that involve the cytoplasmic exosome and its helicase, the Ski complex. The deletion of Ski7 in yeast leads to defects in mRNA turnover and the mRNA surveillance pathways NGD, NSD and NMD, similar to deletions of individual Ski and exosome components (Doma & Parker 2006; Frischmeyer et al. 2002; van Hoof et al. 2002; J. S. J. Anderson & Parker 1998). The Ski7 protein has a domain architecture similar to eRF3 and Hbs1 proteins of the family of translational GTPases. Its extended, domain-lacking N-terminus interacts with the Ski complex (residues 1-105) and the cytoplasmic exosome (residues 116-225) at mutually exclusive binding sites (Figure 7). The modular organization of the Ski- and exosome-binding sites explains how Ski7 can bind both complexes at the same time (Araki et al. 2001; Halbach et al. 2013). Furthermore, the protein comprises a GTPase-like domain at the C-terminus (residues 264-747), which is typical for proteins of the family of translational GTPases. Unlike the eRF3 and Hbs1 family members, which associate with their respective eRF1 and Dom34 binding partners and the ribosome to hydrolyze GTP in translation termination and ribosome recycling (A. Brown et al. 2015; Becker et al. 2011; Shao et al. 2016), a dedicated interaction partner for Ski7 has not been identified. It is therefore currently unclear whether Ski7 is an active GTPase, like eRF3 and Hbs1, and whether it has other functions in translation besides mediating the Ski-exosome interaction (Kowalinski et al. 2015). The Ski7 protein has been well characterized both biochemically and structurally. However, structural data in the context of the Ski complex or the exosome in particular were not available at the inception of the project, which will be important to understand the mechanistic interplay of the two complexes in mRNA decay.

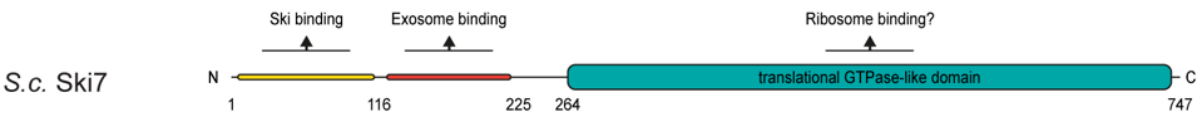

Figure 7. Domain organization of the *S. cerevisiae* Ski7 protein. The elongated N-terminus contains Ski- and exosome-binding sites, the C-terminus contains the GTPase-like domain. The numbers below the schematic indicate the register of the protein sequence.

Although both the Ski and exosome complexes are conserved in higher eukaryotes, proteins that facilitate their interaction, such as Ski7, could only be identified in *S. cerevisiae* and close relatives of the genus, where it originated from a whole genome duplication event of the *Hbs1* gene in a common ancestor. *Lachancea kluyveri*, another yeast but of a different genus, diverged from the common ancestor prior to the whole genome duplication. By alternative splicing of the *Hbs1* gene, it is capable of producing a Ski7-like protein that can complement Ski7 functions in ΔSki7 *S. cerevisiae* strains (Marshall et al. 2013; Marshall et al. 2018; van Hoof 2005). It is currently unknown whether alternative splicing creates a Ski7-like protein in higher eukaryotes. Such a Ski7-like protein will be crucial to study the molecular mechanism of the Ski-exosome complexes in humans and other eukaryotes.

1.5 The SKI complex

In total, seven *SKI* genes were originally identified in *S. cerevisiae* where their mutation cause an increased susceptibility for infections with a double-stranded RNA virus, the so-called Superkiller (Ski) phenotype (Toh-E & Wickner 1979; Ridley et al. 1984). All of the *SKI* genes were eventually shown to be part of the cytoplasmic mRNA degradation machinery. Among the ones not already described above, the *SKI1* gene was shown to encode the 5'-3' exonuclease Xrn1 (A. W. Johnson & Kolodner 1995) and two others, *SKI4* and *SKI6*, encode the exosome proteins Csl4 and Rrp41 (van Hoof et al. 2000; Benard et al. 1998; J. S. J. Anderson & Parker 1998).

The Ski2, Ski3 and Ski8 proteins assemble in a discrete, stable Ski complex in *S. cerevisiae* (J. T. Brown et al. 2000). The analysis of the intact Ski complex by mass spectrometry showed a molecular weight (MW) of approximately 400 kDa, which lead to the conclusion that the Ski complex is a hetero-tetramer with one copy of each Ski2 and Ski3, and two copies of Ski8 (1:1:2 stoichiometry) (Synowsky & Heck 2008). In yeast, the complex is well characterized, both biochemically and structurally (Halbach et al. 2012; Halbach et al. 2013; Schmidt et al. 2016). It hydrolyzes ATP in an RNA-dependent manner and in this way it is capable of unwinding RNA duplexes provided that they present a short 10 nt long, single-stranded RNA 3' overhang (Halbach et al. 2013). The catalytically active Ski2 protein is at the center of the complex and surrounded by the ySki3 and ySki8 proteins (Figure 8). ySki3 contains 34

tetratricopeptide repeats (TPRs), which arrange in a long solenoid structure with four superhelical turns. It functions as an interaction hub to scaffold the entire complex, which is a characteristic feature of TPR-containing proteins in general (Zeytuni & Zarivach 2012). At the C-terminal arm of ySki3 ($ySki3_C$, superhelical turns 3 and 4), the protein maintains multiple interactions with the unstructured ySki2 N-terminus ($ySki2_N$) at the convex and concave surfaces of the solenoid. $ySki3_C$ also binds the globular ySki2 helicase core and the two WD-40 ß-propeller proteins at inside ($ySki8_{IN}$) and outside ($ySki8_{OUT}$) locations within the complex. Together, $ySki3_C$ and its interacting partners form a compact assembly, while the N-terminal arm of ySki3 ($ySKI3_N$, superhelical turns 1 and 2) shows only minor interactions with the $ySki2_N$ and is naturally flexible (Halbach et al. 2013). In RNase protection experiments, the ySki complex alone protects 9-10 nt long single-stranded RNA fragments, which is in agreement with the substrate requirements in the unwinding assays described above (Halbach et al. 2013). In presence of Ski7, the ySki complex associates with the exosome to form a larger helicase-exosome assembly. RNase protection experiments of the Ski-exosome holocomplex show RNA fragments of 43-44 nt, approximately 10 nt longer than for the exosome alone (31-33 nt, The eukaryotic RNA degrading exosome) (Halbach et al. 2013). The emerging picture is that of a continuous RNA channel from the ySki2 helicase core through the inactive Exo9 barrel and into the Rrp44 exonuclease subunit of the exosome (Halbach et al. 2013).

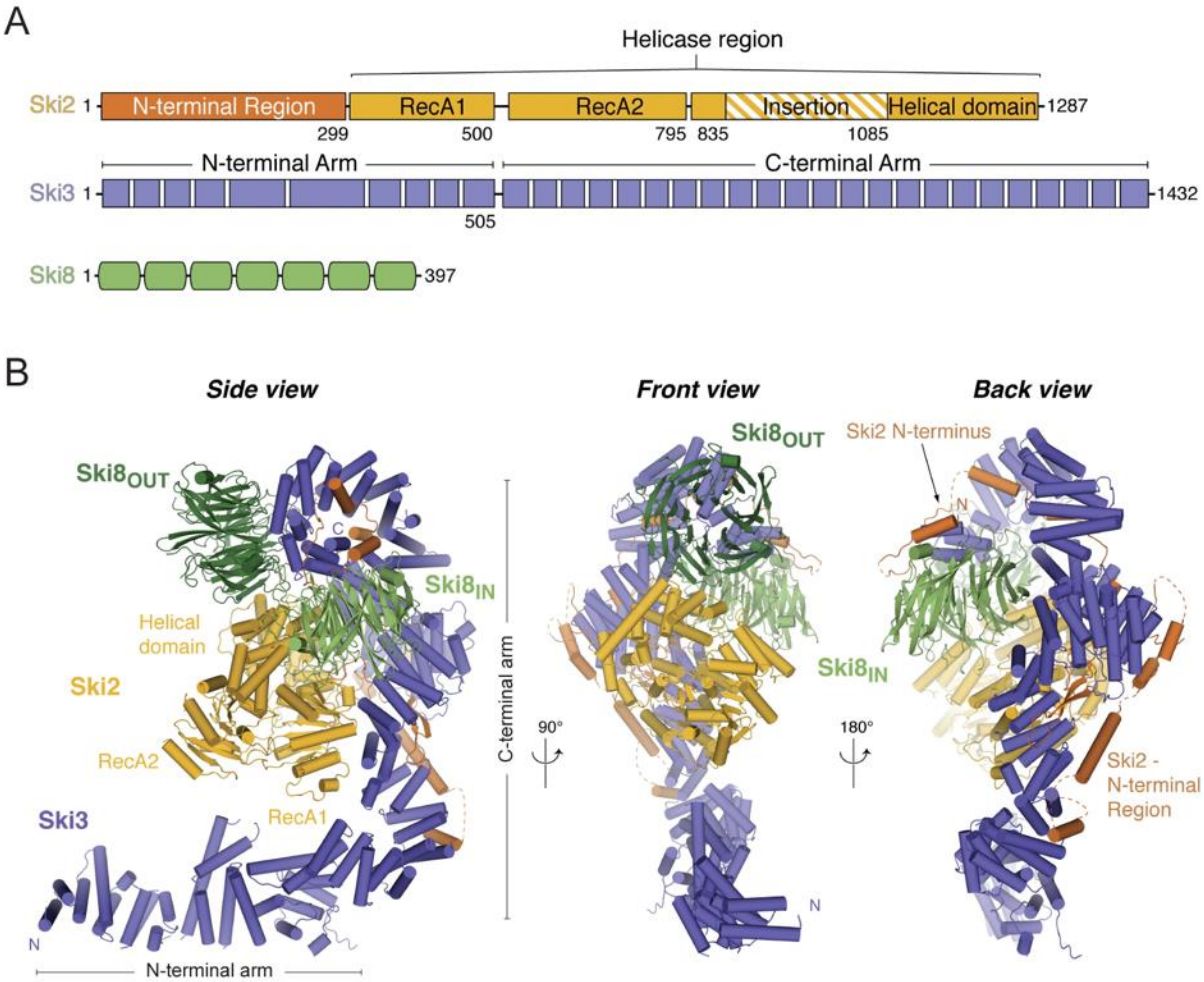

Figure 8. Domain organization and crystal structure of the *S. cerevisiae* Ski complex. The schematic in **(A)** shows the domain organization of the three proteins. The left-hand panel in **(B)** shows the crystal structure of the yeast Ski-Δarch complex in the side view, right-hand panels show the front and back view. The elongated N-terminal region of ySki2 is colored in orange to distinguish it from the globular ySki2 helicase core in yellow. N- and C-terminal arms of ySki3 are indicated. Note that a crystallization of the complex in presence of the ySki2 arch domain was not possible. This figure was taken and adapted from (Halbach et al. 2013).

The ySki complex recognizes short single stranded RNA 3' overhangs not only in solution, but also at the mRNA entry of the 40S ribosomal subunit of 80S ribosomes (Figure 9) (Schmidt et al. 2016). Coming out of the ribosome, the mRNA reaches into the ySki2 helicase core, where it interacts with residues of the RecA1, RecA2 and HB domains, as has been observed in a crystal structure of RNA-bound Mtr4 (Weir et al. 2010). The complex binds a large surface area between the head and shoulder of the 40S ribosomal subunit, contacting both protein and ribosomal RNA. The interaction requires many of the ySki subunits. The ySki2 RecA2 and arch domains engage in interactions with the ribosomal proteins eS10, uS10, uS3, as well as ribosomal RNA

(18S rRNA h16, h41), while ySki8$_{OUT}$ binds the ribosomal proteins uS2, uS5 and eS21. In the ySki-ribosome structure, the arch domain is a site of major interaction with the ribosome. When bound to the ribosome, and contrary to what was previously observed in the crystal structure of ySki2-ΔN (Halbach et al. 2012), the conformation required for this interaction adopts a more open angle, as the arch protrudes horizontally from the helicase core. It should be noted, however, that the conclusions drawn about the conformation of the arch domain in the crystal structure of ySki2-ΔN are limited by the fact that crystallization could not be done in the context of the complex.

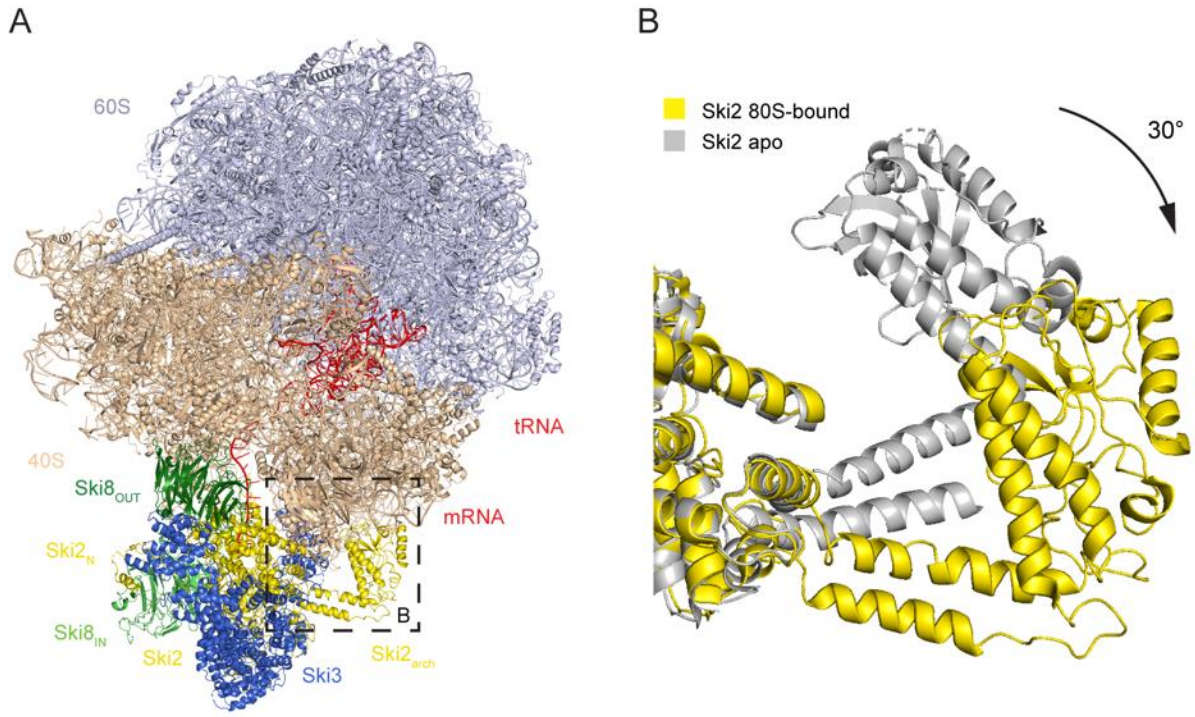

Figure 9. Structure of the *S. cerevisiae* Ski complex bound to the 80S ribosome. **(A)** Cryo-EM structure of the yeast Ski-ribosome complex (PDB: 5MC6). The overlay in **(B)** compares the ribosome-bound Ski2 (yellow) of the structure in (A) to the crystal structure of the apo Ski2-ΔN (PDB: 4A4Z) (grey). Bound to the ribosome the Ski2 arch domain assumes a wide open conformation, whereas in the apo Ski2-ΔN structure the arch domain is in a more closed conformation, moving towards the Ski2 helicase core.

It was proposed that the yeast Ski complex is regulated by an auto-inhibitory mechanism that involves the ySki2 arch domain and the ySki3 N-arm (Halbach et al. 2013). In ATPase activity assays, the ySki2 helicase alone shows RNA-dependent ATP hydrolysis, which is significantly reduced when ySki2 is in complex with ySki3 and ySki8. This auto-inhibitory effect could be reverted upon deletion of the arch domain in

a ySki-Δarch or the ySki3 N-arm in a ySki-ΔN-arm complex. Such a behavior is also observed in strand displacement and RNase protection experiments, where the ΔN-arm and Δarch complexes show increased unwinding activity and higher tendency to form a continuous ySki-exosome RNA channel, respectively. The precise mechanisms through which the Ski2 arch domain and the Ski3 N-arm regulate the functions of the complex remains to be elucidated.

The Ski complex is conserved in higher eukaryotes, where it is much less studied compared to yeast. The human complex also consists of three proteins, SKIV2L, TTC37 and WDR61, henceforth referred to as hSKI2, hSKI3 and hSKI8, respectively. Mutations in hSKI2 and hSKI3 (Fabre et al. 2012; Bourgeois et al. 2018) are cause to a rare autosomal recessive disease called tricho-hepato-enteric syndrome (THES) (Girault et al. 1994; Verloes et al. 1997; Fabre et al. 2014). The majority of the mutations reported (currently summarized in (Bourgeois et al. 2018) are frame shift, nonsense and splicing mutations likely to result in a severely damaged SKI complex, but there are also several point mutations and in-frame deletions, which potentially result in a locally distorted, but otherwise intact complex.

The human complex is thought to associate with the exosome to function in cytoplasmic mRNA degradation, similar to its yeast homologue, but data placing the human SKI complex in this context is limited. The hSKI2 protein was first described as an antigen in mammalian cells (Lee et al. 1995), where it was found to associate with ribosomes (Qu et al. 1998). In humans, cytoplasmic mRNA degradation is suggested to happen largely co-translationally in association with ribosomes. XRN1 is recruited to ribosome-occupied regions to mediate bulk mRNA turnover with only minor contributions to mRNA surveillance pathways. hSKI2 in contrast is thought to exclusively function on aberrant mRNAs (Tuck et al. 2020). These findings differ from recent yeast data, where the yeast Ski complex is also recruited to mRNA regions devoid of ribosomes by associating with the Ska1 protein (Zhang et al. 2019). Bound to stalled 80S ribosomes, the human SKI complex extracts the ribosome-bound mRNA provided that it shows a 3’ overhang not shorter than 19 nucleotides (from the P-site) (Zinoviev et al. 2020). This data complements the substrate spectrum of the Ski complex, which is not only able to unwind RNA secondary structures (Halbach et al. 2013), but also remove RNA-bound proteins. The molecular basis through which the Ski complex unwinds RNA and channels it to the exosome for degradation remain yet to be described.

2 AIM AND SCOPE OF THE THESIS

The nuclear Mtr4-exosome complex has been well characterized both in yeast and in humans. The function of the cytoplasmic Ski-exosome complex, in contrast, is less understood in yeast, and even less so in humans. In particular, our current limited understanding of the Ski helicase is hindering our progress towards a full characterization of the coordinated helicase and nuclease activities in the cytoplasmic Ski-exosome complex.

The first aim of this dissertation is to describe the molecular mechanisms of the human SKI complex. In a combined biochemical and structural approach, the hSKI helicase complex will be analyzed in various conformational, activity-related states and in presence of different kinds of substrates. The second aim is to gain insight into the function of hSKI in the context of the cytoplasmic exosome. A key objective to accomplish this aim will be to identify a human protein that mediates their interaction, as it is fundamental to analyze the ensemble of the two molecular machines in continuative biochemical experiments. The third aim is to identify the differences between the human and yeast Ski complexes that lead to alterations in their regulation. This will require the rigorous inspection and comparison of the structural and biochemical experiments performed.

3 RESULTS

3.1 Paper 1

Kögel A., Keidel A., Bonneau F., Schäfer I.B. and Conti E. (2022). The human SKI complex regulates channeling of ribosome-bound RNA to the exosome via an intrinsic gatekeeping mechanism. Molecular Cell, 82(4), 756-769.

Molecular Cell

The human SKI complex regulates channeling of ribosome-bound RNA to the exosome via an intrinsic gatekeeping mechanism

Graphical abstract

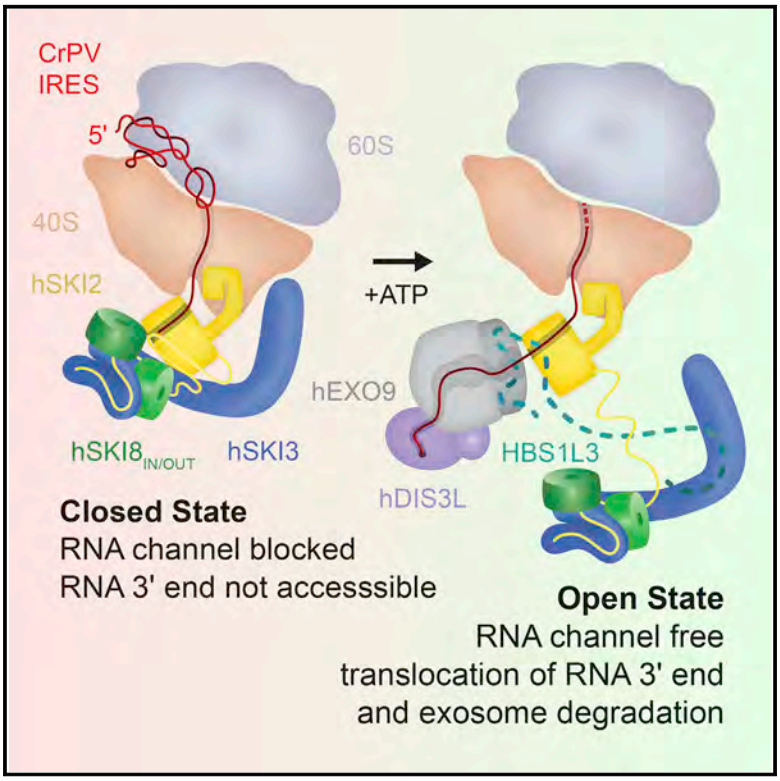

Highlights

- hSKI has closed and open states connected to different helicase conformations
- The intrinsic closed state traps the RNA 3′ end and blocks the RNA exit path
- ATP induces the open state of hSKI, allowing 80S ribosome-bound RNA extraction
- The hSKI open state primes hSKI2 for channeling RNA to the cytosolic exosome

Authors

Alexander Kögel, Achim Keidel, Fabien Bonneau, Ingmar B. Schäfer, Elena Conti

Correspondence

ischaefe@biochem.mpg.de (I.B.S.), conti@biochem.mpg.de (E.C.)

In brief

Kögel et al. show that the human SKI complex adopts distinct conformational states to recognize and extract ribosome-bound RNA in a nucleotide-dependent manner. These functional states regulate access of the RNA 3′ end to the cytoplasmic human exosome for co-translational degradation.

Kögel et al., 2022, Molecular Cell *82*, 756–769
February 17, 2022
https://doi.org/10.1016/j.molcel.2022.01.009

CellPress
OPEN ACCESS

Molecular Cell

Article

The human SKI complex regulates channeling of ribosome-bound RNA to the exosome via an intrinsic gatekeeping mechanism

Alexander Kögel,[1] Achim Keidel,[1] Fabien Bonneau,[1] Ingmar B. Schäfer,[1,*] and Elena Conti[1,2,*]
[1]Department of Structural Cell Biology, Max Planck Institute of Biochemistry, Am Klopferspitz 18, 82152 Martinsried, Munich, Germany
[2]Lead Contact
*Correspondence: ischaefe@biochem.mpg.de (I.B.S.), conti@biochem.mpg.de (E.C.)
https://doi.org/10.1016/j.molcel.2022.01.009

SUMMARY

The superkiller (SKI) complex is the cytoplasmic co-factor and regulator of the RNA-degrading exosome. In human cells, the SKI complex functions mainly in co-translational surveillance-decay pathways, and its malfunction is linked to a severe congenital disorder, the trichohepatoenteric syndrome. To obtain insights into the molecular mechanisms regulating the human SKI (hSKI) complex, we structurally characterized several of its functional states in the context of 80S ribosomes and substrate RNA. In a prehydrolytic ATP form, the hSKI complex exhibits a closed conformation with an inherent gating system that effectively traps the 80S-bound RNA into the hSKI2 helicase subunit. When active, hSKI switches to an open conformation in which the gating is released and the RNA 3′ end exits the helicase. The emerging picture is that the gatekeeping mechanism and architectural remodeling of hSKI underpin a regulated RNA channeling system that is mechanistically conserved among the cytoplasmic and nuclear helicase-exosome complexes.

INTRODUCTION

The exosome complex is a conserved RNA-degradation machinery present in both the nucleus and the cytoplasm of all eukaryotes studied to date (Chlebowski et al., 2013; Januszyk and Lima, 2014; Mitchell et al., 1997). In the nucleus, the RNA exosome functions in the processing and decay of a large variety of noncoding transcripts as well as pre-mRNAs (Lingaraju et al., 2019b; Schmid and Jensen, 2019). In the cytoplasm, it primarily targets mRNAs (Schaeffer and van Hoof, 2011; Tuck et al., 2020). The processive ribonuclease module of the RNA-exosome complex is similar in both cellular compartments. Nine subunits form a catalytically inert cage that is traversed by an internal channel (Bonneau et al., 2009; Liu et al., 2006). This channel binds RNA and threads it to the 3′–5′ processive exoribonuclease in the complex: Rrp44 in yeast and the cytoplasmic and nuclear orthologs DIS3 and DIS3L in human (Dziembowski et al., 2007; Gerlach et al., 2018; Liu et al., 2006; Tomecki et al., 2010; Weick et al., 2018). The processive 10-subunit ribonuclease module (Exo-10) has an irreversible degrading action on the RNAs it has accessed. Exo-10 itself, however, lacks substrate specificity and requires different co-factors to target to different RNAs. The exosome co-factors exist in complexes that are compartment-specific and are centered around two RNA helicases, nuclear Mtr4 and cytoplasmic Ski2 (Lingaraju et al., 2019b; Olsen and Johnson, 2021; Weick and Lima, 2021). Together with their adaptors, the helicase co-factors of the exosome appear to control substrate access to the ribonuclease.

Ski2 and Mtr4 harbor similar biochemical properties. Both helicases hydrolyze ATP to power RNA unwinding in a processive manner and with 3′–5′ polarity, melting RNA secondary structures to create a progressively longer single-stranded 3′ end (Khemici and Linder, 2018). Both helicases also share a similar domain organization, with an N-terminal low-complexity region followed by a DExH-unwinding core and an additional domain with RNA-binding and protein-binding properties known as the "arch" (Halbach et al., 2012; Jackson et al., 2010; Weir et al., 2010). However, the two helicases differ in aspects that go beyond the mere presence (in Mtr4) or absence (in Ski2) of a nuclear localization signal. In particular, Mtr4/hMTR4 interacts with a variety of adaptor proteins, forming mutually exclusive complexes that target the different types of RNA substrates in the nucleus (Dobrev et al., 2021; Falk et al., 2014, 2017; Lingaraju et al., 2019a; Schuller et al., 2018; Thoms et al., 2015; Wang et al., 2019). In the cytoplasm, the Ski2/hSKI2 helicase instead mainly targets mRNAs and is part of a single assembly, the Ski complex (Anderson and Parker, 1998; Brown et al., 2000; Tuck et al., 2020).

The Ski proteins were discovered in yeast and named after the superkiller (SKI) phenotype—defined as increased susceptibility to a viral "killer" toxin in strains containing mutations in the *SKI* genes (Toh et al., 1978). The Ski2, Ski3, and Ski8 proteins assemble with a 1:1:2 stoichiometry to form a stable tetrameric

assembly both *in vivo* and *in vitro* (Brown et al., 2000; Halbach et al., 2013; Synowsky and Heck, 2008). The crystal structure of a yeast Ski2-Ski3-Ski8 (Ski) complex has revealed a compact architecture, with the helicase core of Ski2 surrounded by the tetratricopeptide repeat (TPR) protein Ski3 and two WD40-repeat Ski8 subunits (Halbach et al., 2013). In biochemical assays, the RNA-dependent ATPase activity of the yeast Ski2 helicase is downregulated in the context of the Ski complex, but restored upon deletion of the Ski2 arch domain (Halbach et al., 2013). The Ski complex can also associate with translating 80S ribosomes, using the Ski2 arch domain as a major interaction site (Schmidt et al., 2016). The yeast 80S-Ski cryo-EM structure suggested that binding to ribosomes changes the conformation of the Ski2 arch domain, allowing 80S-bound mRNA to enter the helicase core of the Ski complex (Schmidt et al., 2016). The Ski complex also targets ribosome-free regions of mRNAs via the yeast-specific factor Ska1 (Zhang et al., 2019). Finally, the yeast Ski complex can bind Ski7, the adaptor that bridges the interaction to the Exo-10 exosome (Araki et al., 2001).

Orthologs of the yeast Ski2, Ski3, and Ski8 proteins can be identified in higher eukaryotes, such as the corresponding human proteins SKIV2L, TTC37, and WDR61, respectively. Deficiencies in SKIV2L and TTC37 cause trichohepatoenteric syndrome (THES), a congenital disease characterized by very early onset of chronic diarrhea and immune defects in children (Fabre et al., 2013). Several pathogenic mutations have been identified in THES patients, corresponding to either nonsense or missense mutations in SKIV2L or TTC37 (Fabre et al., 2011, 2012; Lee et al., 2016). Furthermore, human SKIV2L has also been linked to viral autoimmunity, as a mediator for the degradation of endogenous immuno-stimulatory RNAs that are produced by a cellular stress response (Eckard et al., 2014). SKIV2L activity has now been shown to act primarily in exosome-mediated degradation during co-translational mRNA surveillance pathways (Tuck et al., 2020) by extracting mRNA from stalled 80S ribosomes (Zinoviev et al., 2020). However, there is currently no structural information that would shed light on the physiological and pathological roles of the hSKI complex. In this work, we used biochemical and cryo-EM analysis to address the molecular mechanisms underlying the functions of the hSKI complex.

RESULTS AND DISCUSSION

The human SKI complex adopts closed and open states

For clarity, we will refer to the human orthologs of the yeast Ski complex subunits as hSKI2 (SKIV2L, ~137.8 kDa), hSKI3 (TTC37, ~175.5 kDa) and hSKI8 (WDR61, ~33.6 kDa) (Figure 1A). The hSKI2 subunit is a multidomain protein. In the text, we designate its individual domains as $hSKI2_N$ for the naturally unstructured N-terminal domain, $hSKI2_{cat}$ for the catalytic DExH core, and $hSKI2_{arch}$ for the arch domain (Figure 1A). In the case of hSKI3, analogous to the yeast ortholog, we refer to its N-terminal and C-terminal arch regions as $hSKI3_N$ and $hSKI3_C$ (Figure 1A; Halbach et al., 2013), respectively.

We co-expressed full-length hSKI2, hSKI3, and hSKI8 in insect cells and co-purified them as a homogeneous complex (Figure S1A). The purified hSKI complex was subjected to cryo-EM structural analysis (Figure S1B). Two-dimensional (2D) classifications of the cryo-EM images revealed the presence of two major subsets of particles (Figure S1C). Each subset was independently processed by three-dimensional (3D) classification followed by 3D refinement (Figure S1D). The subset with fewer particles (~40%) resulted in a reconstruction to a global resolution of ~3.7 Å and showed interpretable density for the majority of the complex (Figures 1B, 1C, and S2A–S2C). We will refer to this reconstruction as the "closed state" of hSKI. The second subset of particles (~60%) was refined to a similar resolution (~3.8 Å) and showed density for a smaller unit (Figures 1D, 1E, and S2D–S2F). We will refer to this reconstruction as the "open state" of hSKI.

The quality of the cryo-EM density map of the closed-state reconstruction enabled us to build most of the atomic model *de novo* (Figures 2A and S2G), with two exceptions. First, there was no ordered density for $hSKI3_N$ (predicted to contain TPRs 1–8); the N-terminal arm of hSKI3 was thus left unmodeled. Second, the density for the $hSKI2_{arch}$ domain displayed a local resolution of 4–12 Å in focused refinement (Figure S2H); therefore, this domain was built by docking a model generated via a structural prediction based on the yeast ortholog (Figure 2A; Halbach et al., 2012; Tunyasuvunakool et al., 2021). In the case of the open-state reconstruction there was no ordered density that would account for the $hSKI2_{cat}$ and $hSKI2_{arch}$ domains, suggesting that they detached from the rest of the complex (Figures 1D and 1E). Based on the structural analysis, we define $hSKI2_{cat}$ and $hSKI2_{arch}$ as the helicase module of hSKI, whereas $hSKI3_C$, $hSKI2_N$, and the two hSKI8 subunits are designated as the gatekeeping module (Figures 1C and 1E).

The gatekeeping module of hSKI forms the epicenter of the complex

We will start by describing the closed-state conformation of hSKI, which is generally similar to that observed in the structure of the *Saccharomyces cerevisiae* ortholog (Halbach et al., 2013; Figures 2A and S3). hSKI is scaffolded around its largest subunit, the TPR-containing protein hSKI3. TPRs are structural repeats consisting of two α-helices that arrange in tandem to form right-handed solenoids, with superhelical turns of approximately 8 TPRs each (Perez-Riba and Itzhaki, 2019). The TPRs 9–40 of the $hSKI3_C$ arm form a crescent-shaped solenoid with four superhelical turns (TPRs 9–16, 17–24, 25–32, 33–40) (Figures 1A and 2A). Most of the fourth superhelical turn is an extension of hSKI3 as compared with the yeast ortholog (Halbach et al., 2013; Figures S3A and S3B). This superhelical turn of hSKI3 is also a hotspot for disease-associated mutations in THES patients (L1485R, R1503C, and L1505S at TPR39—hereby defined as THES-1 hotspot, Figure 2B), suggesting that this region has physiological relevance. Since THES-associated mutations (Fabre et al., 2013) map to many different areas of the complex, we will point to them in the text when describing the corresponding structural features that are affected.

The $hSKI3_C$ arm wraps around the $hSKI2_N$ domain (Figure 2B, left panel). The $hSKI2_N$ domain is an extended region that can be subdivided into individual segments (Figure 2C). The first ("inner") segment (hSKI2 residues 1–121) binds inside the superhelical axis of $hSKI3_C$ with sparse secondary structure elements, spanning almost the entire length of the solenoid and forming

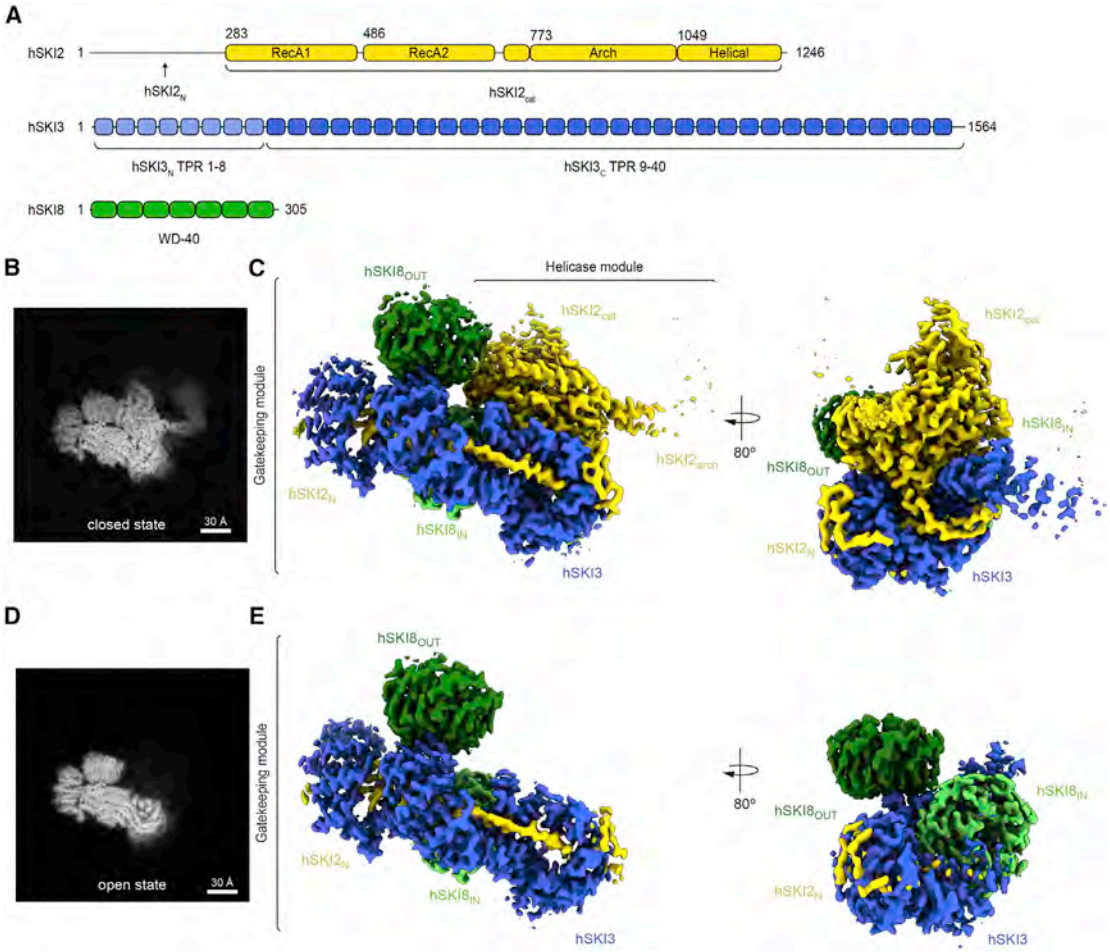

Figure 1. Structural organization and conformational states of hSKI

(A) Domain organization of the human SKI subunits hSKI2 (yellow), hSKI3 (blue), and hSKI8 (green). Predicted folds segments are indicated by rectangles and extended segments by lines. The N-terminal arm of hSKI3 ($hSKI3_N$; TPR 1–8) (light blue) is flexible in all current structural data.

(B and C) Single-particle cryo-EM reconstruction of the closed state of apo hSKI at a global resolution of 3.7 Å. 2D projection of the final reconstruction, showing the density for the $hSKI2_{arch}$ (B). Three-dimensional rendering of the reconstruction with the hSKI subunits in two orientations and colored as in (A). (C) The gatekeeping module ($hSKI2_N$-hSKI3-$hSKI8_{IN}$-$hSKI8_{OUT}$) and the helicase module ($hSKI2_{cat}$-$hSKI2_{arch}$) discussed in the text are indicated.

(D and E) Single-particle cryo-EM reconstruction of the open state of apo hSKI at a global resolution of 3.8 Å. The 2D projection (D) and the 3D reconstruction (E) are in a similar orientation as the closed state in (B) and (C). Only the gatekeeping module is visible in both 2D projection and 3D rendering.

See also Figures S1 and S2; Table S1.

an integral part of its hydrophobic core (Figure 2B, left panel, box 1). This segment ends with a highly conserved ''inner ß-hairpin'' that is embedded in the second superhelical turn of $hSKI3_C$ (at TPRs 17–19) (Figure 2B; box 2) and connects to an intricate loop structure that we will refer to as the ''wedge'' segment (hSKI2 residues 122–165) (Figure 2B; box 3). The $hSKI2_N$ wedge segment protrudes from the concave surface of $hSKI3_C$ at the second superhelical turn and, despite lacking secondary structure elements, is well structured by intra- and intermolecular interactions. $hSKI2_N$ continues by binding with an ''outer hairpin'' ($hSKI2_N$ residues 172–201) along the external convex surface of the solenoid, at the second superhelical turn of $hSKI3_C$ (Figure 2B; box 4). From here, the density of $hSKI2_N$ weakens as it reaches the first superhelical turn of $hSKI3_C$ with an ''outer α-helix'' (Figures 2C and S3C) and then fades at the linker segment that connects to the RecA1 domain of the well-ordered helicase module.

The $hSKI3_C$ arm also binds the hSKI8 subunits. hSKI8 is a seven-bladed ß-propeller with the wheel-like shape characteristic of WD40-repeat proteins (Stirnimann et al., 2010). The outer hSKI8 subunit ($hSKI8_{OUT}$) adopts an outward position at the third superhelical turn of $hSKI3_C$ (Figure 2A). The internal hSKI8 subunit ($hSKI8_{IN}$) is positioned at the inner concave surface of $hSKI3_C$, interacting with the third superhelical turn (Figure 2A, left panel). THES-associated mutations in hSKI3 map to the $hSKI8_{IN}$-binding site (P1270A and D1283N at TPR 33 and 34). These substitutions (THES-2 hotspot; Figure 2B) are expected to weaken the intermolecular interactions and/or stability of the gatekeeping module. Another cluster of THES-associated mutations in hSKI3 map to the region that wraps around the inner

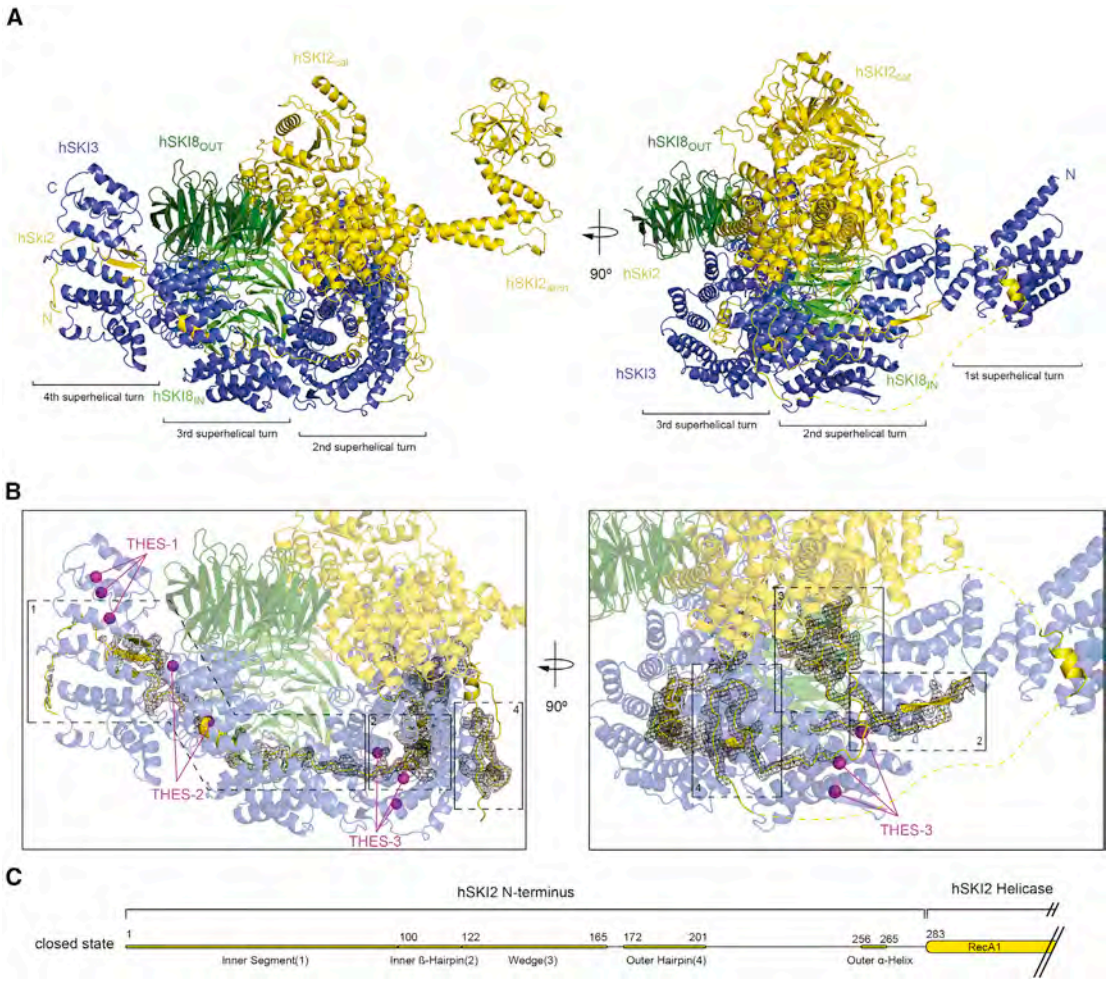

Figure 2. Closed-state conformation of hSKI

(A) Cartoon representations of hSKI in closed state, related by a 90° rotation around a vertical axis (left panel oriented as in Figure 1, same color scheme).

(B) Zoom-in of the gatekeeping module with the difference density for $SKI2_N$ displayed as black mesh. The two representations are oriented as those in (A). Numbering refers to the regions indicated in (B). Highlighted as purple spheres are the positions of THES disease mutants in the core of the gatekeeping module (clustered in the THES-1, THES-2 and THES-3 groups). The numerals 1–4 refer to the regions shown in (C).

(C) Schematic domain organization of $hSKI2_N$ highlighting distinct regions discussed in the text.

See also Figures S1, S2, and S3; Table S1.

segment and are expected to interfere with the proper folding of the superhelix (hSKI3 G673D, G721R, L761P at TPRs 19 and 20, THES-3 hotspot) (Figure 2B).

The helicase module can detach from the gatekeeping module

In the closed-state conformation of SKI, the basal surface of the $hSKI2_{cat}$ domain binds the hSKI3 solenoid at the first and second superhelical turns and hereby interacts with the adjacent $hSKI8_{OUT}$ and $hSKI8_{IN}$ subunits and with the wedge segment of $hSKI2_N$ (Figure 2). The $hSKI2_{arch}$ insertion instead protrudes from the top surface of the $hSKI2_{cat}$ domain, extending into solvent with a curved structure (Figure 2A). In the open-state conformation, not only is there no well-ordered density for the hSKI2 helicase module, but neither is there density for the wedge segment of $hSKI2_N$ or for the first superhelical turn of $hSKI3_C$ including the $hSKI2_N$ outer α-helix (Figures 3A and 3B). In contrast, the internal segment, both the inner ß-hairpin and the outer hairpin of $hSKI2_N$ are bound in the same manner to hSKI3. Thus, in this open-state conformation of hSKI, the hSKI2 helicase module appears to be flexible while it remains linked to the gatekeeping module via the $hSKI2_N$ domain.

The structural analysis suggests that the inner and outer hairpins of $hSKI2_N$ anchor the wedge segment as it undergoes conformational changes connected to the recruitment or detachment of the helicase core from the gatekeeping module. To test the impact of the wedge on the movement of the helicase module, we replaced this segment with a $(Gly\text{-}Ser)_5$ linker and purified the corresponding hSKI-Δwedge mutant complex for cryo-EM analysis (Figures S4A and S4B). The entire dataset of hSKI-Δwedge showed the presence of a complex in the open state (Figure S4B). Thus, the wedge segment of $hSKI2_N$ appears

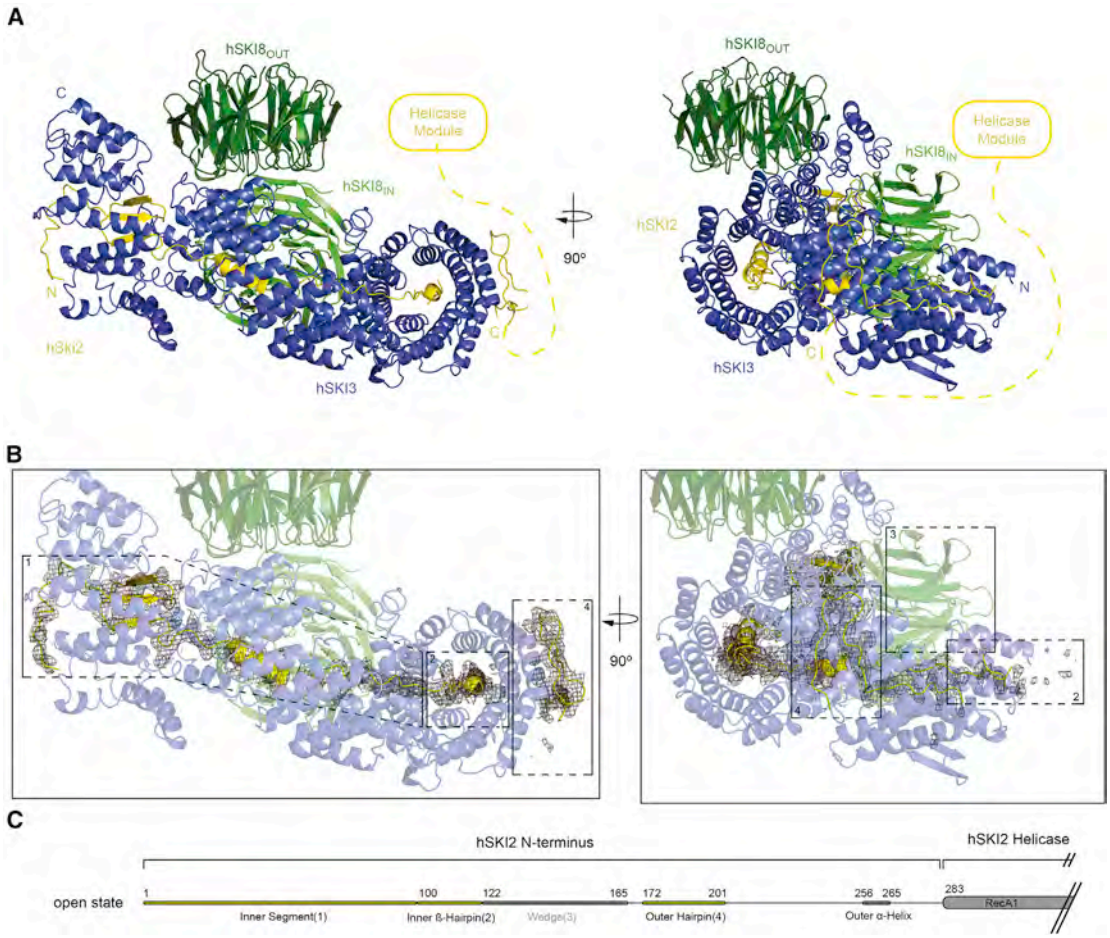

Figure 3. Open-state conformation of hSKI

(A) Cartoon representations of hSKI in open state, oriented as in Figure 2. The connection to the disengaged helicase module is indicated by a dotted yellow line. (B) Zoom-in of the gatekeeping module with the difference density for $SKI2_N$ displayed as black mesh. The two representations are oriented as in (A). Note that the density for the $hSKI2_N$ wedge (3) is absent and the $hSKI2_N$ inner ß-hairpin (2) is less well-ordered compared with the closed-state reconstruction in Figure 2B. (C) Schematic domain organization of $hSKI2_N$ highlighting the distinct regions discussed in the text.
See also Figures S1, S2, and S4; Table S1.

to stabilize the closed state. Notably, the structure of the apo *S. cerevisiae* Ski-Δarch complex also showed a similar closed-state architecture with an analogous wedge segment (RG motif, R149-G150) positioned at the bottom of the empty helicase channel (Halbach et al., 2013). However, it is likely that the crystallization procedure selected the most compact conformation for lattice formation, since cryo-EM analysis of the same complex indicates that it is present both in closed and open states (Figures S4C–S4E). Thus, we posit that the presence of the open and closed conformational states is an evolutionarily conserved feature of the Ski complex.

RNA is enclosed in the helicase core in closed-state hSKI

We proceeded to characterize how hSKI binds RNA. In biochemical spectrophotometric enzyme-coupled assays, recombinant hSKI showed RNA-dependent ATPase activity (hSKI-WT) (Figure 4A; Table S2). As control, the ATPase activity of hSKI was abolished in the case of a mutant complex with a glutamic acid to glutamine substitution in the helicase catalytic site (hSKI-DEAD containing the E424Q substitution in hSKI2) (Figure 4A; Table S2). We determined the kinetic parameters for the wild-type complex under steady-state conditions for varying ATP concentrations. Half-maximum velocity was reached at K_m = 149.4 μM ATP with a k_{cat} = 0.685 s^{-1}, which is well under physiological ATP concentrations, similar to *S. cerevisiae* Ski (Halbach et al., 2013).

For the structural analysis, we incubated wild-type recombinant hSKI with a 25-uracil (25U) RNA substrate and the nonhydrolyzable nucleotide analog ADP-BeF (which mimics a prehydrolytic ATP state). Cryo-EM data showed that essentially all particles were in the closed-state conformation, resulting in a 3D reconstruction of RNA-bound hSKI at a global resolution of 3.1 Å (Figures 4B and S5). The cryo-EM reconstruction revealed well-defined density for six ribonucleotides (N1–N6) bound in $hSKI2_{cat}$ in a single-stranded conformation (Figure 4B). $hSKI2_{cat}$

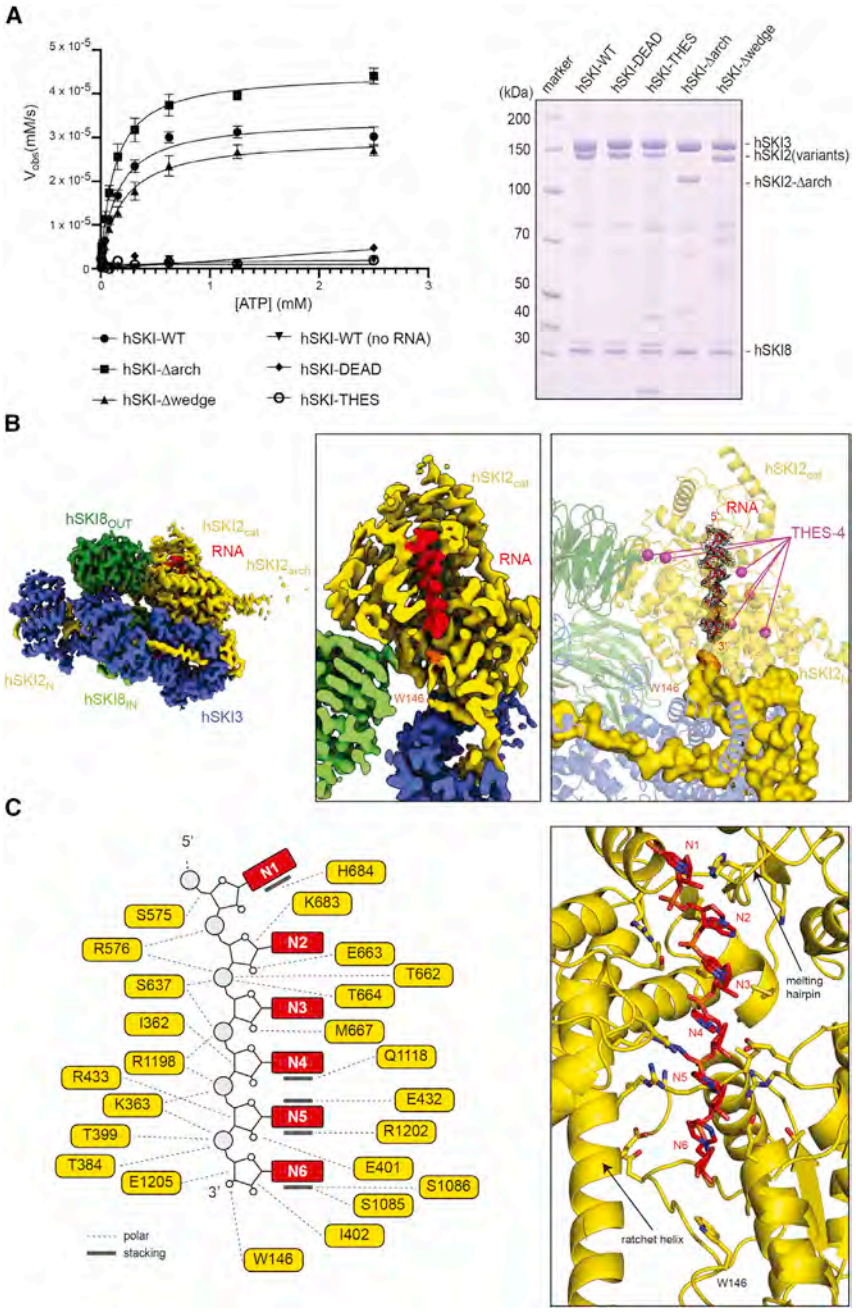

Figure 4. RNA-binding features of hSKI

(A) RNA-dependent ATPase activity of hSKI wild-type and mutants. The mutations Δarch, Δwedge, E424Q (DEAD), and V341G (THES) are in the hSKI2 subunit of the complex. (Left) Enzyme-coupled spectrophotometric assay. Initial ATPase rates are plotted against ATP concentration. Protein and poly(U) RNA concentrations were 50 nM and 10 μg/mL, respectively. Data were fitted according to Michaelis-Menten kinetics (see Table S2 for derived kinetic parameters). Error bar: ±1 standard deviation from three independent experiments. (Right) Coomassie-stained 4%–12% SDS-PAGE of the hSKI samples used in the assay. hSKI2 (variants) refers to all mutants except hSKI2Δarch.

(B) RNA path in the structure of RNA-bound hSKI. The central panel shows a slap view of the 3D reconstruction through the central plane of the RNA channel in $hSKI2_{cat}$. On the right is a zoom-in highlighting the path of the RNA (cartoon representation in red, difference density in black mesh) in hSKI2. The $hSKI2_N$ wedge is indicated in space-fill representation. The position of W146 of the $hSKI2_N$ wedge is indicated in orange. Highlighted as purple spheres are the positions of THES disease mutants in this area of the complex (clustered in the THES-4 group). Note that N1–N6 correspond to uracil nucleotides in the homopolymeric 25U RNA we used in the structural analysis.

(C) Detailed interactions between hSKI2 and the six ordered nucleotides at the RNA 3′ end. (Right) Zoom-in of the structure at the RNA-binding residues. (Left) Corresponding schematic of the interactions (polar and stacking contacts are indicated).

See also Figure S5; Table S1 and S2.

has the characteristic domain organization of DExH helicases: a pair of RecA domains (RecA1 and RecA2) contain the ATPase catalytic site and are juxtaposed to a helical domain, resulting in an overall globular shape with a central channel (Figure S5F) (Ozgur et al., 2015). The 5′ nucleotide (N1) binds at the top surface of $hSKI2_{cat}$, where it engages in base-stacking interactions with the so-called melting hairpin of RecA2 (Figures 4C and S5G). This motif is a conserved structural feature poised to melt RNA duplexes as they enter the DExH core of Ski2-related helicases (Büttner et al., 2007). The ribonucleotide chain then binds along the RNA-binding surface of RecA2 and continues into the helicase channel, threading between the RecA1 domain and the helical domain (at the so-called ratchet helix) (Büttner et al., 2007) (Figure 4C). Several disease-associated mutations in THES patients target the DExH core of hSKI2 in proximity to the ATP-binding site (A332P, V341G, E438K, and R483C substitutions) or adjacent to the RNA-binding surfaces (ΔG1187-Q1193 and ΔS1189-L1195 deletions) and are thus expected to affect the RNA-dependent ATPase properties of the complex (THES-4 hotspot) (Figure 4B, right panel). To test this prediction, we expressed and purified a recombinant hSKI complex mutant with the V341G substitution (hSKI-THES) and indeed found that it is inactive in ATPase assays *in vitro* (Figure 4A; Table S2).

The RNA-binding interactions of the DExH core are evolutionarily conserved not only in hSKI2 orthologs but also in the nuclear helicase Mtr4 (Figure S5F) (Gerlach et al., 2018; Schuller et al., 2018; Weick et al., 2018; Weir et al., 2010). However, the cryo-EM density of hSKI revealed an additional and unexpected feature: the most 3′ end ribonucleotide interacts with the wedge segment of the $hSKI2_N$ domain (Figures 4B and 4C). In particular,

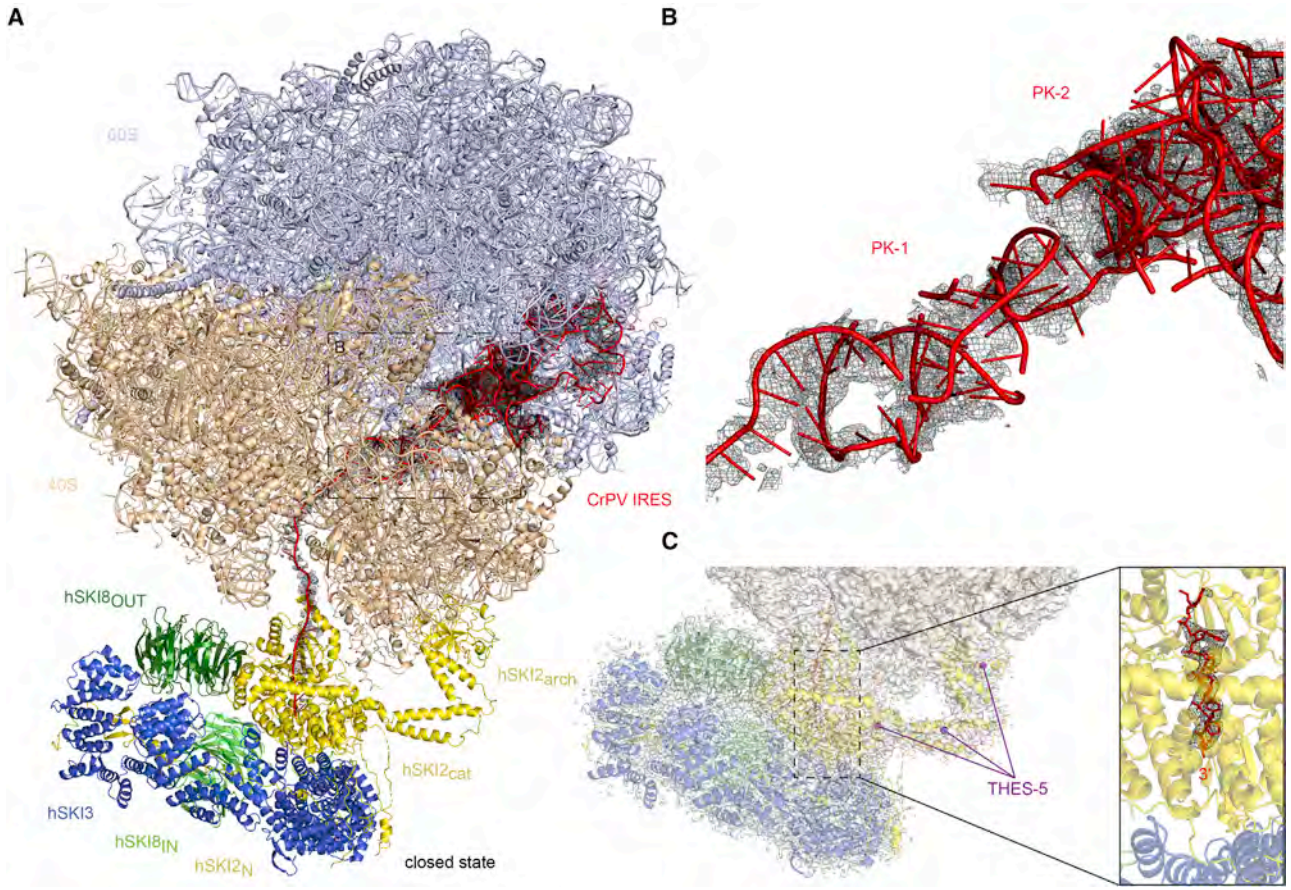

Figure 5. RNA blocked in the hSKI2 helicase in a close-state hSKI-80S complex

(A) Cartoon representation of hSKI bound in a closed state to a human 80S ribosome reconstituted with a CrPV IRES-29 nt RNA. The large and small ribosomal subunits are in light blue and light orange, respectively, and CrPV IRES-29 RNA is in red with corresponding density indicated by black mesh.

(B) Zoom-in view of the 80S-bound RNA at CrPV IRES pseudoknots 1 and 2 (PK-1 and PK-2) with corresponding density.

(C) Zoom-in view of the 80S-bound RNA at the 3′ end. The enlarged photo on the right panel displays the 6 nt that are traceable in hSKI2 in closed-state hSKI. See also Figure S6; Table S1.

a Trp-Gly motif (W146-G147) in the $hSKI2_N$ wedge segment contacts the 3′ hydroxyl group of the N6 ribonucleotide enclosed in the helicase channel. The interactions suggest the presence of a crosstalk between the $hSKI2_N$ wedge loop in the gatekeeping module and the 3′ end of an RNA substrate while in the $hSKI2_{cat}$ core, rationalizing the presence of a single class of particles/states during 3D refinement of the RNA-bound data set as compared with the different subsets of closed and open states in the apo hSKI reconstructions.

80S-bound hSKI is in a closed state in the presence of a prehydrolytic ATP mimic

The observation that the hSKI gatekeeping module obstructs the end of the helicase channel in the closed state raised the hypothesis that in the open state the obstruction in hSKI2 is removed and the exit for the RNA substrate is opened. However, this prediction could not be verified in the context of hSKI complexes in isolation because it was not possible to visualize the detached hSKI2 in open-state hSKI (as the larger gatekeeping module dominates the particle alignment). We proceeded to visualize hSKI bound to a human ribosome (Figure 5).

To reconstitute an appropriate RNA-containing 80S sample, we took advantage of the internal ribosome entry site (IRES) from the cricket-paralysis virus (CrPV) and added a 29-nt sequence at the 3′ end (IRES29 RNA). The CrPV-IRES folds into a stable structure capable of binding directly to the intersubunit space on the ribosomal 40S subunit, which can then join a 60S subunit to form an 80S ribosome (Hellen, 2009). The additional sequence at the 3′ end was included to create a suitable binding platform for hSKI based on previous studies (Schmidt et al., 2016; Zinoviev et al., 2020). In human cells, the SKI complex has been shown to extract 80S-bound mRNAs that contain a 3′ terminal region of at least 19 nt from the P site (Zinoviev et al., 2020).

We incubated the reconstituted 80S-IRES29 with an excess of wild-type hSKI and the nucleotide analog ADP-BeF and purified the assembly by gradient centrifugation for cryo-EM data collection. Data processing yielded a reconstruction with an overall resolution of ~3.1 Å (Figure S6). The density showed significant

flexibility for hSKI, thus requiring an adjustment to the center of mass by subtracting the ribosome signal from the data. The resulting map of 80S-bound hSKI reached a global resolution of 3.6 Å in the core of the helicase complex (Figure S6) and was interpreted by rigid-body fitting the model from the substrate-bound hSKI reconstruction, with no major differences with regard to the position of the four hSKI subunits. The structure of 80S-bound hSKI in the presence of a prehydrolytic ATP mimic thus shows that the hSKI2 helicase module is recruited to the hSKI gatekeeping module in the characteristic closed-state conformation (Figure 5A).

hSKI is flexibly tethered to 80S ribosomes via the hSKI2 helicase module

The hSKI complex binds the 80S ribosome via evolutionarily conserved interactions between hSKI2 and the small ribosomal subunit (Figure 5A). The hSKI2 RecA2 domain binds between the "head" and the "shoulder" of the 40S at ribosomal proteins uS3, uS12, eS10, and rRNA helix 16. The $hSKI2_{arch}$ domain binds the "head" of the 40S at ribosomal protein uS3, uS10, and rRNA helix 41. Several THES-associated disease mutations cluster in positions that would either directly or indirectly affect 40S recognition. For example, the in-frame deletion mutant ΔR888 is in the globular KOW (Kyrpides-Ouzounis-Woese) fold that binds rRNA, while other mutations are within the stalk (the in-frame deletion ΔQ1034) or at the base of the arch (W466G) (THES-5 hotspots; Figure 5C), suggesting the integrity of the arch domain is physiologically important.

Although the positioning of hSKI close to the entry of the ribosome mRNA channel is similar to that of yeast 80S-bound Ski (Schmidt et al., 2016), there are notable differences. First, rRNA helix 16 in the "shoulder" of the 40S is in the classical straight conformation instead of the unusual bent conformation observed in the reconstruction of the yeast complex (Figures S3D and S3E) (Schmidt et al., 2016). Moreover, there is no additional interaction between hSKI and the 40S: the $hSKI8_{OUT}$ subunit is at a distance of 40 Å from the ribosomal proteins uS2, uS5, and eS21 instead of interacting directly with them as was the case for yeast $Ski8_{out}$ (Figure S3E) (Schmidt et al., 2016). Indeed, hSKI is more flexibly tethered to the 40S, rather than packing closely against it as seen in the yeast reconstruction.

In the yeast system, ribosome binding is thought to modulate the conformation of the Ski2 arch domain, thus releasing it from an autoinhibitory state (Schmidt et al., 2016). Although the arch domain of hSKI2 adopts a conformation similar to that observed in the yeast 80S-bound Ski, the same conformation is also observed in the reconstruction of hSKI in isolation (Figure S3D). We therefore conclude that binding to 80S ribosomes does not have a major influence on the hSKI2 arch domain. The differences at the structural level between the two orthologs are consistent with differences at the biochemical level. In yeast, the Ski complex in isolation has only modest ATPase activity that is significantly increased upon removal of the Ski2 arch domain (Halbach et al., 2013). In contrast, removal of the hSKI2 arch domain led only to a minor increase in the ATPase activity of hSKI in isolation (hSKI-Δarch) (Figure 4A; Table S2), suggesting that hSKI is not in a significantly autoinhibited state prior to 80S binding. Whether this reflects physiological differences between the yeast and human complexes is unclear. For example, while hSKI is thought to be exclusively bound to ribosomes (Tuck et al., 2020), yeast Ski is found in mutually exclusive 80S-bound and Ska1-bound complexes (Zhang et al., 2019) and may, accordingly, require additional regulation in this respect.

80S-bound hSKI switches to an open state when in the ATPase active form

The 80S-hSKI (with hSKI in the closed state) shows well-defined density for the ribosome-associated RNA (Figures 5A and 5B). In the structure, the CrPV-IRES RNA has the canonical features expected for the CrPV-IRES alone, with two nested pseudoknots (PK-2 and PK-3) close to the exit of the ribosome mRNA channel and another (PK-1) forming as an independent domain bound in the decoding center of the 40S (Fernández et al., 2014; Schüler et al., 2006). After the A site, the ribonucleotide chain continues until it reaches the surface of the ribosome and then becomes less defined as the RNA reaches solvent. After a distance of about 50 Å from the surface of the 80S, the RNA density becomes well-ordered again as the ribonucleotide chain enters the $hSKI2_{cat}$ core. Here, six nucleotides are bound in the same positions and with the same interactions described for the RNA-bound hSKI structure in isolation, including the interaction of the RNA 3′ end with the wedge segment of the gatekeeping module (Figure 5C). Thus, in the closed state of the 80S-hSKI complex, the RNA 3′ end is trapped in the helicase channel, and the exit site of the RNA substrate is blocked. Consistently, the RNA density also stopped inside the yeast Ski2 helicase core in the reconstruction of the compact RNase-treated yeast 80S-Ski complex (Schmidt et al., 2016).

Previous biochemical experiments have shown that the hSKI complex can extract mRNA from stalled ribosomes (Zinoviev et al., 2020). To recapitulate this scenario in our system, we reconstituted an 80S-CrPV-IRES assembly with wild-type hSKI, incubated with ATP for 15 min and collected cryo-EM data on a Titan Krios microscope (Figure S7). In the corresponding reconstruction, the interaction between 80S and hSKI2 is essentially unchanged with respect to that observed in the presence of a prehydrolytic ATP mimic. Importantly, a fraction of the particles (Figure S7G) showed no ordered density at the base of $hSKI2_{cat}$ for the entire gatekeeping module (Figure 6). Unlike hSKI in isolation, this alignment was dominated by the ribosome-bound hSKI2 in the open state, leaving the separate hSKI gatekeeping module unresolved. Thus, we could now visualize the RNA exiting from the helicase channel of hSKI in the open state (Figure 6C).

The cryo-EM reconstruction of the open state shows that the RNA in the helicase channel extends with well-defined density for three nucleotides more at the 3′ end (N7, N8, and N9) than detected in the closed state (Figure 6C). The base and sugar of ribonucleotide N7 makes polar and stacking interactions with RecA1, resulting in a twist of the ribonucleotide chain of ~180°. The RNA 3′ end exits the helicase core in a bent conformation, with nucleotides N8 and N9 making only minor interactions with the ratchet helix (Figure 6D). Thus, when hSKI is in the open state as observed in the active assembly, the 3′ end of the ribosome-bound RNA traverses the helicase core and occupies the space where the wedge of the gatekeeping module

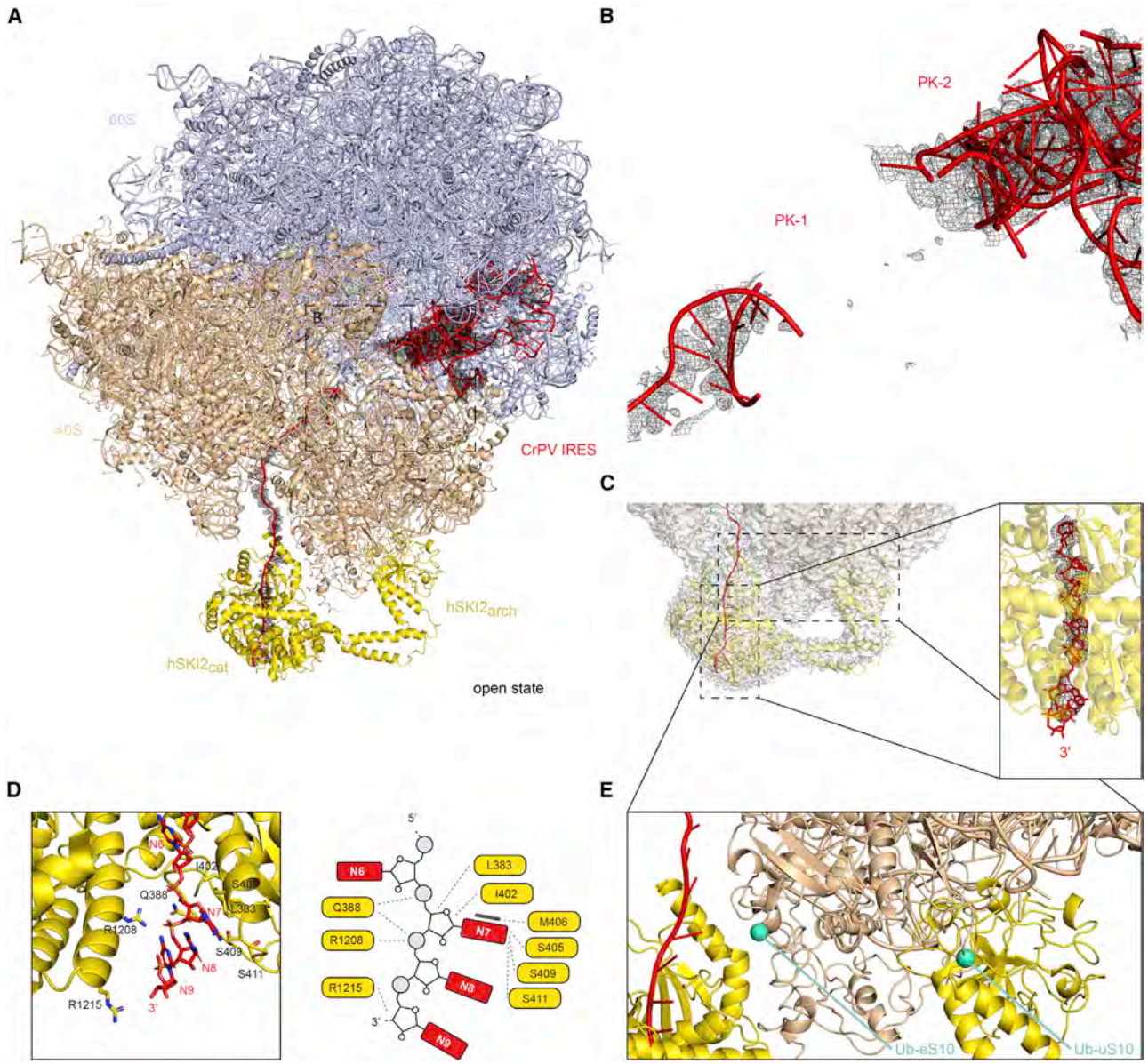

Figure 6. RNA traverses the hSKI2 helicase in an open-state hSKI-80S complex

(A) Cartoon representations of hSKI bound in an open state on a human 80S reconstituted with a CrPV IRES-29 nt RNA. Orientation and coloring as in Figure 5. Note that the gatekeeping module has detached from the helicase module.

(B) Zoom-in view of the 80S-bound RNA at CrPV IRES PK-1 and PK-2. Note that most density for PK-1 has disappeared (compare with Figure 5B), suggesting it has unfolded.

(C) Zoom-in view of the 80S-bound RNA at the 3′ end. The panel on the right shows an enlarged photo of the nine nucleot ides and the RNA 3′ end exiting from hSKI2 in open-state hSKI.

(D) Detailed interactions between hSKI2 and the additional three ordered nucleotides at the RNA 3′ end (downstream of those in Figure 4C). (Right) Zoom-in of the structure at the RNA-binding residues. (Left) Corresponding schematic of the interactions.

(E) N-terminal ubiquitination of eS10 and uS10 ribosomal proteins clashes with binding to the hSKI helicase module. Sites of ubiquitination are indicated as green spheres.

See also Figure S7; Table S1.

was bound in the closed state. Concomitantly, the density for the IRES structure disappears, suggesting that the PKs unfold as the ribosome-bound RNA is extracted and ejected by the hSKI2 helicase (Figure 6B).

The data are consistent with a model whereby the hSKI gatekeeping module detaches when the most 3′ end nucleotide traverses the helicase channel in an ATPase-dependent manner and stays open as the entire ribonucleotide chain is

threaded through, all in an ATPase-dependent manner. The model predicts that the removal of the wedge segment would only impact the initial opening step. Indeed, removal of the wedge segment in the hSKI-Δwedge mutant does not significantly affect the overall ATPase activity of the complex (Figure 4A; Table S2).

Open-state hSKI supports a conserved helicase-exosome RNA channeling mode

The RNA-binding mode observed in the open state of hSKI and, in particular, the bent conformation, with which the ribonucleotide chain traverses the RNA exit channel of hSKI2, are similar in conformation to those observed in the structure of the exosome-bound MTR4 (Weick et al., 2018). These observations suggest that the detached RNA-bound hSKI2 helicase may channel RNA into the cytoplasmic exosome in a manner similar to that observed in the case of MTR4 and the nuclear exosome (Gerlach et al., 2018; Schuller et al., 2018; Weick et al., 2018). To test this prediction, we first biochemically reconstituted the components of the human cytoplasmic exosome (Figure S7A). We purified the inactive 9-subunit core of the human exosome (hEXO9) as previously described for the nuclear complex (Gerlach et al., 2018; Weick et al., 2018). To incorporate the cytoplasmic-specific ribonuclease, we used a human-cell expression system and purified recombinant full-length hDIS3L (with the inactivating D486N mutation). The corresponding 10-subunit cytoplasmic exosome (hEXO10$_c$) binds HBS1L3, a spliced variant of HBS1-like that interacts with hEXO10$_c$ in a similar way as the yeast Ski7 protein interacts with yExo10$_c$ (Kalisiak et al., 2017; Kowalinski et al., 2016). Using size-exclusion chromatography (SEC) experiments, we demonstrated that HBS1L3 also binds hSKI and is required to bridge the interaction between hSKI and hEXO10$_c$ (Figure 7A).

With these purified samples, we performed RNase protection assays (Figure 7B), similar to those we used previously to analyze the RNA-binding properties of exosome complexes (Bonneau et al., 2009; Gerlach et al., 2018). Briefly, a body-labeled, single-stranded RNA was incubated with (catalytically inactive) exosome complexes and treated with benzonase. The footprint (e.g., the size of the RNA fragments that upon protein binding become protected from RNase digestion) was analyzed by denaturing polyacrylamide gel electrophoresis (PAGE) (Figure 7B). The cytoplasmic ribonuclease core complex hEXO10$_c$ gave rise to a characteristic footprint (Figure 7B, lane 1) similar to that previously observed for its nuclear counterpart, hEXO10$_n$ (Gerlach et al., 2018). In the case of the cytoplasmic human exosome, removal of the arch domain was required to observe the increased RNA footprint of the holocomplex with respect to the ribonuclease core (Figure 7B, compare lanes 2 and 4), similarly to its yeast counterpart (Halbach et al., 2013). Remarkably, the difference in footprint between the core and holocomplexes of the cytoplasmic exosome (Figure 7B) is similar to that of the nuclear exosome (Gerlach et al., 2018). Notwithstanding the additional regulatory role of the hSKI2 arch domain, the nuclear and cytoplasmic holoexosomes thus embed a continuous RNA channel of similar length, supporting the notion of a conserved mode of interaction and a conserved channeling mechanism (Figure 7C).

CONCLUSIONS

The hSKI complex undergoes a major remodeling when switching from a closed state to an open state in which the helicase is active and released from the rest of the complex. This large-scale conformational change is underpinned by the structural organization of hSKI into two individual but connected modules: a helicase module and a gatekeeping module. The gatekeeping module can swing open or close toward the helicase module. In the following model, when the hSKI complex is inactive, the gate is closed and binds the helicase module via extensive intermolecular interactions made with the basal surface of the helicase domain. In this closed conformation, the wedge segment in the gate binds and occludes the exit of the helicase channel, enclosing the 3′ end of a bound RNA substrate. Upon activation, that is, in the context of RNA-dependent ATP hydrolysis of 80S-bound hSKI2, the gate opens and detaches from the helicase module, which remains bound to the ribosome. The open state of hSKI is also marked by a movement of the wedge segment, which dissociates from the exit channel of hSKI2, thereby allowing the RNA 3′ end to exit and the ribosome-bound mRNA to be extracted. The efficient interconversion between the large-amplitude conformational changes of the closed and open states is likely due to the covalent tethering of the regulatory and catalytic modules, which can thus remain in proximity even when they are detached from each other.

In contrast to the yeast system, the interaction between hSKI and the 40S ribosomal subunit is exclusively mediated by hSKI2 and is rather flexible in character. The positioning of hSKI2 on the ribosome in the cryo-EM structure explains how it can access a short 3′ overhang of a bound mRNA, a substrate that is expected to arise upon endonucleolytic cleavage after ribosome stalling (Schmidt et al., 2016; Tuck et al., 2020; Zinoviev et al., 2020). The minimal length of the 3′ overhang determined in biochemical assays (Zinoviev et al., 2020) is required to span the distance between the ribosome and the helicase core of hSKI2. However, the SKI complex can also efficiently extract ribosome-bound mRNAs with long overhanging 3′-terminal regions (Zinoviev et al., 2020). The finding that hSKI is flexible when attached to the 80S rationalizes how it can be reached by longer and flexible 3′ overhangs. The position of hSKI in the 80S-bound structure has also interesting repercussions for surveillance mechanisms. The hSKI2 interaction with ribosomal proteins eS10 and uS10 would not be compatible with the ubiquitination of these subunits (Figure 6E), as has been reported to occur on colliding ribosomes (Ikeuchi et al., 2019; Juszkiewicz et al., 2018; Winz et al., 2019).

The gatekeeping mechanism of hSKI does not have a significant inhibitory effect on the ATPase properties of the complex. Once the gate opens, when the most 3′ nucleotide traverses the helicase channel, it stays open until the extraction process is concluded. The arch domain of the helicase also does not have a significant autoinhibitory effect on the ATPase properties of hSKI and, consistently, its conformation is not modulated upon 80S binding, in contrast to what was observed for the yeast ortholog (Schmidt et al., 2016). However, the gatekeeping structure and the arch domain appear to serve an evolutionarily conserved role in regulating RNA channeling to the exosome

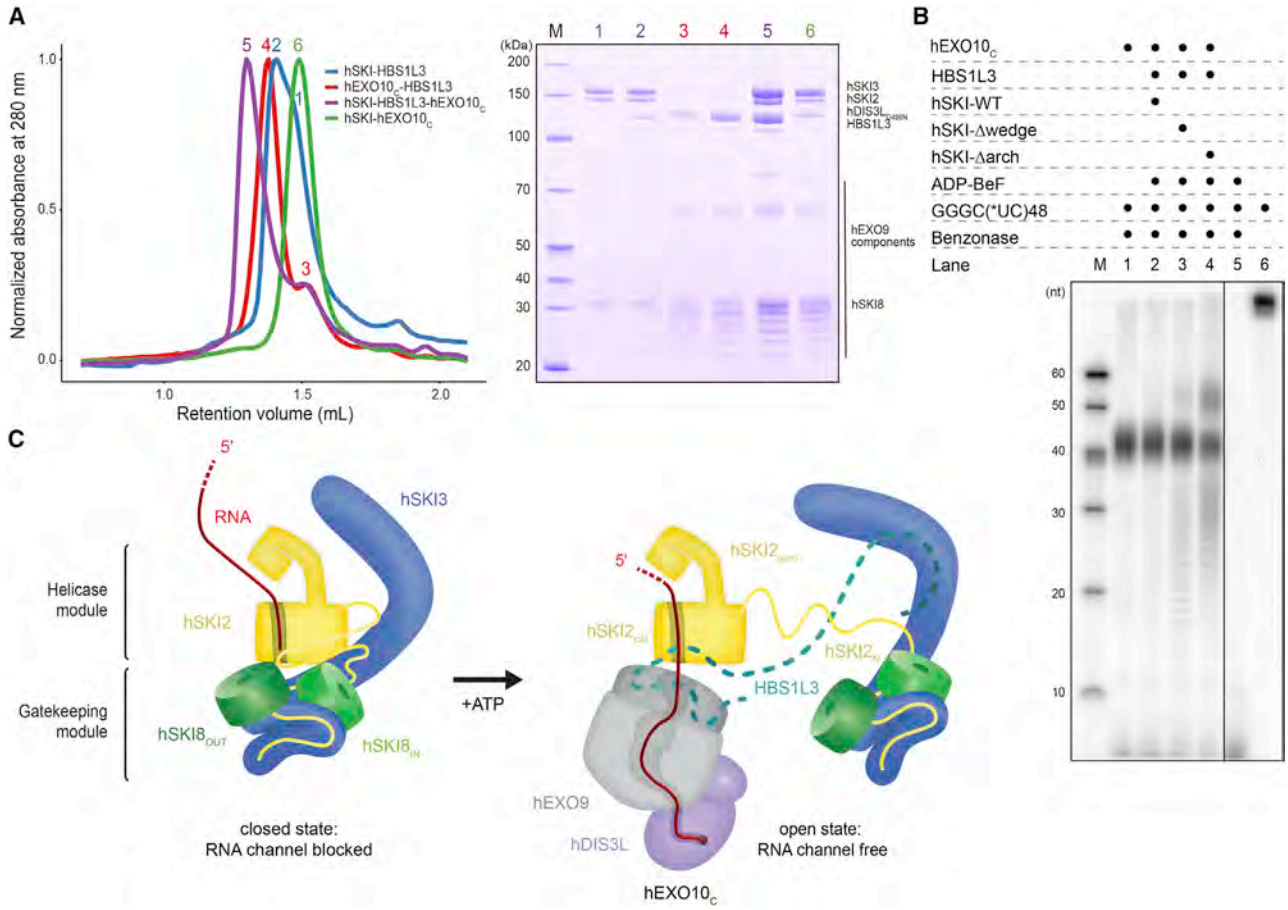

Figure 7. RNA channeling of hSKI to the cytoplasmic exosome

(A) Physical interaction of hSKI and the human cytoplasmic exosome. Size-exclusion chromatography (SEC) assays were carried out with hDIS3L$_{D486N}$ catalytic inactive mutant. The panel on the left is an overlay of the chromatograms, and the panel on the right a Coomassie-stained 4%–12% SDS-PAGE analyzing the peak fractions (as numbered and colored on the left). Note that in the hSKI-HBS1L3 (blue curve) and in the hEXO10$_C$-HBS1L3 (red curve) samples hSKI and hEXO10$_C$ were loaded in excess to control for differences between HBS1L3-bound and -unbound complexes.

(B) RNA path assessed by RNase protection assays of human SKI wild-type and mutants in the context of the human cytoplasmic exosome (human EXO10$_C$ and human HBS1L3). A single-stranded C(*UC)$_{48}$ RNA internally labeled with ^{32}P at the uridine 5′-phosphate was incubated with proteins and nucleotides as indicated and treated with benzonase. The reaction products were analyzed by denaturing urea-PAGE. Note the increase in length of the RNA fragments when the cytoplasmic exosome was incubated with hSKI-Δarch, similar to the increase in length observed in the case of hMTR4 and the nuclear exosome complex (Gerlach et al., 2018). An SDS-PAGE of the proteins and complexes used in this assay is shown in Figure S7A.

(C) Model of the RNA channeling mechanism of the cytoplasmic SKI-exosome holocomplex compatible with the RNA path from (A). In this model, channeling is achieved by hSKI2 in the open-state conformation of hSKI with a similar overall path as observed for the nuclear exosome holocomplex (Gerlach et al., 2018; Schuller et al., 2018; Weick et al., 2018). Note that in context of the wild type, we expect that ATP hydrolysis is required in addition to ATP binding for transition to the hSKI open state and channeling to the exosome.

See also Figure S7.

for degradation (see also Halbach et al., 2013). The current biochemical and structural data suggest that the gatekeeping module dissociates from the hSKI2 helicase module to allow the RNA to progress to the cytoplasmic exosome core with a similar channeling path observed for the nuclear exosome holocomplex. In the context of the nuclear 14-subunit exosome holocomplex, it is likely that a similar gatekeeping mechanism is at play in hMTR4 co-factor complexes. The NEXT (hMTR4-ZCCHC8-RBM7) complex, an assembly that targets noncoding RNAs that are generated upon faulty transcription processes, is a prime candidate for such regulation: the C-terminal domain of hZCCHC8 binds the basal surface of the hMTR4 helicase (Puno and Lima, 2018) and positions Phe673 at the exit of the helicase channel at the equivalent position of hSKI2 W146 (Figure S5H). The similarities suggest parallel evolution of conserved regulatory mechanisms of exosome-associated Ski2-like helicases in different cellular compartments.

Limitations of the study

Conceptual and technical limitations pertain to the ability to further dissect the role of the Trp-containing wedge in a meaningful manner. First, the Trp-RNA interaction is one of the many

RNA-binding interactions in the complex and by itself is unlikely to contribute significant in terms of K_d in biophysical measurements. Second, the wedge segment would only impact the initial opening step and as such it is not possible to measure the impact in bulk ATPase assays. Another limitation is that we cannot assign the exact nucleotides bound in hSKI2 when not using homopolymeric sequences (e.g., in the ribosome-bound structures) nor be sure of the identity of the 3′ end nucleotide. A further limitation is the multiple-days-long time used for the sample preparation in case of the ribosome-bound cryo-EM samples. Over this rather long processing time span, we cannot exclude potential dissociation of hSKI from the ribosome or reversal to the hSKI closed form.

STAR★METHODS

Detailed methods are provided in the online version of this paper and include the following:

- KEY RESOURCES TABLE
- RESOURCE AVAILABILITY
  - Lead contact
  - Materials availability
  - Data and code availability
- EXPERIMENTAL MODEL AND SUBJECT DETAILS
- METHOD DETAILS
  - Cloning, protein expression and purification
  - Ribosome subunit purification
  - *In vitro* transcription of RNA substrates
  - ATPase activity assays
  - Cytoplasmic exosome reconstitution
  - Size exclusion chromatography assays
  - RNase protection assays
  - Cryo-EM sample preparation
  - Cryo-EM data collection and processing
  - Density interpretation and model building
- QUANTIFICATION AND STATISTICAL ANALYSIS

SUPPLEMENTAL INFORMATION

Supplemental information can be found online at https://doi.org/10.1016/j.molcel.2022.01.009.

ACKNOWLEDGMENTS

We are grateful to Daniel Bollschweiler and Tillman Schäfer at the Max Planck Institute of Biochemistry (MPIB) cryo-EM facility for help with EM data collection and the MPIB core facilities for support. We thank Christian Benda and J. Rajan Prabu for maintenance and development of computational infrastructure for EM data processing, Courtney Long for help with the preparation of the manuscript, and members of the lab for discussions. This work was supported by funding from the Max-Planck-Gesellschaft, the European Commission (ERC Advanced Investigator Grant EXORICO), and the Deutsche Forschungsgemeinschaft (DFG SFB1035, GRK1721, SFB/TRR 237) to E.C.

AUTHOR CONTRIBUTIONS

E.C. and A. Kögel initiated the project; A. Kögel, A. Keidel, and F.B. designed and performed experiments; I.B.S. supervised the cryo-EM analyses; E.C., A. Kögel, A. Keidel, and I.B.S. wrote the manuscript.

DECLARATION OF INTERESTS

E.C. is a member of the *Molecular Cell* advisory board.

Received: September 24, 2021
Revised: December 1, 2021
Accepted: January 7, 2022
Published: February 3, 2022

REFERENCES

Afonine, P.V., Klaholz, B.P., Moriarty, N.W., Poon, B.K., Sobolev, O.V., Terwilliger, T.C., Adams, P.D., and Urzhumtsev, A. (2018a). New tools for the analysis and validation of cryo-EM maps and atomic models. Acta Crystallogr. D Struct. Biol. *74*, 814–840. https://doi.org/10.1107/S2059798318009324.

Afonine, P.V., Poon, B.K., Read, R.J., Sobolev, O.V., Terwilliger, T.C., Urzhumtsev, A., and Adams, P.D. (2018b). Real-space refinement in PHENIX for cryo-EM and crystallography. Acta Crystallogr. D Struct. Biol. *74*, 531–544. https://doi.org/10.1107/S2059798318006551.

Anderson, J.S., and Parker, R.P. (1998). The 3′ to 5′ degradation of yeast mRNAs is a general mechanism for mRNA turnover that requires the SKI2 DEVH box protein and 3′ to 5′ exonucleases of the exosome complex. EMBO J *17*, 1497–1506. https://doi.org/10.1093/emboj/17.5.1497.

Araki, Y., Takahashi, S., Kobayashi, T., Kajiho, H., Hoshino, S., and Katada, T. (2001). Ski7p G protein interacts with the exosome and the Ski complex for 3″-to-5″ mRNA decay in yeast. EMBO J *20*, 4684–4693. https://doi.org/10.1093/emboj/20.17.4684.

Bernstein, J., Ballin, J.D., Patterson, D.N., Wilson, G.M., and Toth, E.A. (2010). Unique properties of the Mtr4p-poly(A) complex suggest a role in substrate targeting. Biochemistry *49*, 10357–10370. https://doi.org/10.1021/bi101518x.

Bieniossek, C., Imasaki, T., Takagi, Y., and Berger, I. (2012). MultiBac: expanding the research toolbox for multiprotein complexes. Trends Biochem. Sci. *37*, 49–57. https://doi.org/10.1016/j.tibs.2011.10.005.

Biyani, N., Righetto, R.D., McLeod, R., Caujolle-Bert, D., Castano-Diez, D., Goldie, K.N., and Stahlberg, H. (2017). Focus: the interface between data collection and data processing in cryo-EM. J. Struct. Biol. *198*, 124–133. https://doi.org/10.1016/j.jsb.2017.03.007.

Bonneau, F., Basquin, J., Ebert, J., Lorentzen, E., and Conti, E. (2009). The yeast exosome functions as a macromolecular cage to channel RNA substrates for degradation. Cell *139*, 547–559. https://doi.org/10.1016/j.cell.2009.08.042.

Brown, J.T., Bai, X., and Johnson, A.W. (2000). The yeast antiviral proteins Ski2p, Ski3p, and Ski8p exist as a complex *in vivo*. RNA *6*, 449–457.

Büttner, K., Nehring, S., and Hopfner, K.-P. (2007). Structural basis for DNA duplex separation by a superfamily-2 helicase. Nat. Struct. Mol. Biol. *14*, 647–652. https://doi.org/10.1038/nsmb1246.

Chen, V.B., Arendall, W.B., Headd, J.J., Keedy, D.A., Immormino, R.M., Kapral, G.J., Murray, L.W., Richardson, J.S., and Richardson, D.C. (2010). MolProbity: all-atom structure validation for macromolecular crystallography. Acta Crystallogr. D Biol. Crystallogr. *66*, 12–21. https://doi.org/10.1107/S0907444909042073.

Chlebowski, A., Lubas, M., Jensen, T.H., and Dziembowski, A. (2013). RNA decay machines: the exosome. Biochim. Biophys. Acta *1829*, 552–560. https://doi.org/10.1016/j.bbagrm.2013.01.006.

Dobrev, N., Ahmed, Y.L., Sivadas, A., Soni, K., Fischer, T., and Sinning, I. (2021). The zinc-finger protein Red1 orchestrates MTREC submodules and binds the Mtl1 helicase arch domain. Nat. Commun. *12*, 3456. https://doi.org/10.1038/s41467-021-23565-3.

Dziembowski, A., Lorentzen, E., Conti, E., and Séraphin, B. (2007). A single subunit, Dis3, is essentially responsible for yeast exosome core activity. Nat. Struct. Mol. Biol. *14*, 15–22. https://doi.org/10.1038/nsmb1184.

Eckard, S.C., Rice, G.I., Fabre, A., Badens, C., Gray, E.E., Hartley, J.L., Crow, Y.J., and Stetson, D.B. (2014). The SKIV2L RNA exosome limits activation of

the RIG-I-like receptors. Nat. Immunol. *15*, 839–845. https://doi.org/10.1038/ni.2948.

Emsley, P., Lohkamp, B., Scott, W.G., and Cowtan, K. (2010). Features and development of coot. Acta Crystallogr. D Biol. Crystallogr. *66*, 486–501. https://doi.org/10.1107/S0907444910007493.

Fabre, A., Charroux, B., Martinez-Vinson, C., Roquelaure, B., Odul, E., Sayar, E., Smith, H., Colomb, V., Andre, N., Hugot, J.-P., et al. (2012). SKIV2L mutations cause syndromic diarrhea, or trichohepatoenteric syndrome. Am. J. Hum. Genet. *90*, 689–692. https://doi.org/10.1016/j.ajhg.2012.02.009.

Fabre, A., Martinez-Vinson, C., Roquelaure, B., Missirian, C., Andre, N., Breton, A., Lachaux, A., Odul, E., Colomb, V., Lemale, J., et al. (2011). Novel mutations in TTC37 associated with tricho-hepato-enteric syndrome. Hum. Mutat. *32*, 277–281. https://doi.org/10.1002/humu.21420.

Fabre, A., Martinez-Vinson, C., Goulet, O., and Badens, C. (2013). Syndromic diarrhea/tricho-hepato-enteric syndrome. Orphanet J. Rare Dis. *8*, 5. https://doi.org/10.1186/1750-1172-8-5.

Falk, S., Tants, J.-N., Basquin, J., Thoms, M., Hurt, E., Sattler, M., and Conti, E. (2017). Structural insights into the interaction of the nuclear exosome helicase Mtr4 with the pre-ribosomal protein Nop53. RNA *23*, 1780–1787. https://doi.org/10.1261/rna.062901.117.

Falk, S., Weir, J.R., Hentschel, J., Reichelt, P., Bonneau, F., and Conti, E. (2014). The molecular architecture of the TRAMP complex reveals the organization and interplay of its two catalytic activities. Mol. Cell *55*, 856–867. https://doi.org/10.1016/j.molcel.2014.07.020.

Fernández, I.S., Bai, X.-C., Murshudov, G., Scheres, S.H.W., and Ramakrishnan, V. (2014). Initiation of translation by cricket paralysis virus IRES requires its translocation in the ribosome. Cell *157*, 823–831. https://doi.org/10.1016/j.cell.2014.04.015.

Gerlach, P., Schuller, J.M., Bonneau, F., Basquin, J., Reichelt, P., Falk, S., and Conti, E. (2018). Distinct and evolutionary conserved structural features of the human nuclear exosome complex. Elife *7*, e38686. https://doi.org/10.7554/eLife.38686.

Goddard, T.D., Huang, C.C., Meng, E.C., Pettersen, E.F., Couch, G.S., Morris, J.H., and Ferrin, T.E. (2018). UCSF ChimeraX: meeting modern challenges in visualization and analysis. Protein Sci *27*, 14–25. https://doi.org/10.1002/pro.3235.

Halbach, F., Reichelt, P., Rode, M., and Conti, E. (2013). The yeast ski complex: crystal structure and RNA channeling to the exosome complex. Cell *154*, 814–826. https://doi.org/10.1016/j.cell.2013.07.017.

Halbach, F., Rode, M., and Conti, E. (2012). The crystal structure of *S. cerevisiae* Ski2, a DExH helicase associated with the cytoplasmic functions of the exosome. RNA *18*, 124–134. https://doi.org/10.1261/rna.029553.111.

Hellen, C.U.T. (2009). IRES-induced conformational changes in the ribosome and the mechanism of translation initiation by internal ribosomal entry. Biochim. Biophys. Acta *1789*, 558–570. https://doi.org/10.1016/j.bbagrm.2009.06.001.

Hoh, S.W., Burnley, T., and Cowtan, K. (2020). Current approaches for automated model building into cryo-EM maps using Buccaneer with CCP-EM. Acta Crystallogr. D Struct. Biol. *76*, 531–541. https://doi.org/10.1107/S2059798320005513.

Ikeuchi, K., Tesina, P., Matsuo, Y., Sugiyama, T., Cheng, J., Saeki, Y., Tanaka, K., Becker, T., Beckmann, R., and Inada, T. (2019). Collided ribosomes form a unique structural interface to induce Hel2-driven quality control pathways. EMBO J *38*, e100276. https://doi.org/10.15252/embj.2018100276.

Jackson, R.N., Klauer, A.A., Hintze, B.J., Robinson, H., van Hoof, A., and Johnson, S.J. (2010). The crystal structure of Mtr4 reveals a novel arch domain required for rRNA processing. EMBO J *29*, 2205–2216. https://doi.org/10.1038/emboj.2010.107.

Januszyk, K., and Lima, C.D. (2014). The eukaryotic RNA exosome. Curr. Opin. Struct. Biol. *24*, 132–140. https://doi.org/10.1016/j.sbi.2014.01.011.

Juszkiewicz, S., Chandrasekaran, V., Lin, Z., Kraatz, S., Ramakrishnan, V., and Hegde, R.S. (2018). ZNF598 is a quality control sensor of collided ribosomes. Mol. Cell *72*, 469–481.e7. https://doi.org/10.1016/j.molcel.2018.08.037.

Kalisiak, K., Kuliński, T.M., Tomecki, R., Cysewski, D., Pietras, Z., Chlebowski, A., Kowalska, K., and Dziembowski, A. (2017). A short splicing isoform of HBS1L links the cytoplasmic exosome and SKI complexes in humans. Nucleic Acids Res *45*, 2068–2080. https://doi.org/10.1093/nar/gkw862.

Khatter, H., Myasnikov, A.G., Natchiar, S.K., and Klaholz, B.P. (2015). Structure of the human 80S ribosome. Nature *520*, 640–645. https://doi.org/10.1038/nature14427.

Khemici, V., and Linder, P. (2018). RNA helicases in RNA decay. Biochem. Soc. Trans. *46*, 163–172. https://doi.org/10.1042/BST20170052.

Kowalinski, E., Kögel, A., Ebert, J., Reichelt, P., Stegmann, E., Habermann, B., and Conti, E. (2016). Structure of a cytoplasmic 11-subunit RNA exosome complex. Mol. Cell *63*, 125–134. https://doi.org/10.1016/j.molcel.2016.05.028.

Lee, W.S., Teo, K.M., Ng, R.T., Chong, S.Y., Kee, B.P., and Chua, K.H. (2016). Novel mutations in SKIV2L and TTC37 genes in Malaysian children with tricho-hepatoenteric syndrome. Gene *586*, 1–6. https://doi.org/10.1016/j.gene.2016.03.049.

Li, X., Burnight, E.R., Cooney, A.L., Malani, N., Brady, T., Sander, J.D., Staber, J., Wheelan, S.J., Joung, J.K., McCray, P.B., et al. (2013). piggyBac transposase tools for genome engineering. Proc. Natl. Acad. Sci. USA *110*, E2279–E2287. https://doi.org/10.1073/pnas.1305987110.

Liebschner, D., Afonine, P.V., Baker, M.L., Bunkóczi, G., Chen, V.B., Croll, T.I., Hintze, B., Hung, L.-W., Jain, S., McCoy, A.J., et al. (2019). Macromolecular structure determination using X-rays, neutrons and electrons: recent developments in Phenix. Acta Crystallogr. D Struct. Biol. *75*, 861–877. https://doi.org/10.1107/S2059798319011471.

Lingaraju, M., Johnsen, D., Schlundt, A., Langer, L.M., Basquin, J., Sattler, M., Heick Jensen, T., Falk, S., and Conti, E. (2019a). The MTR4 helicase recruits nuclear adaptors of the human RNA exosome using distinct arch-interacting motifs. Nat. Commun. *10*, 3393. https://doi.org/10.1038/s41467-019-11339-x.

Lingaraju, M., Schuller, J.M., Falk, S., Gerlach, P., Bonneau, F., Basquin, J., Benda, C., and Conti, E. (2019b). To process or to decay: a mechanistic view of the nuclear RNA exosome. Cold Spring Harb. Symp. Quant. Biol. *84*, 155–163. https://doi.org/10.1101/sqb.2019.84.040295.

Liu, Q., Greimann, J.C., and Lima, C.D. (2006). Reconstitution, activities, and structure of the eukaryotic RNA exosome. Cell *127*, 1223–1237. https://doi.org/10.1016/j.cell.2006.10.037.

Mitchell, P., Petfalski, E., Shevchenko, A., Mann, M., and Tollervey, D. (1997). The exosome: a conserved eukaryotic RNA processing complex containing multiple 3′→5′ exoribonucleases. Cell *91*, 457–466.

Olsen, K.J., and Johnson, S.J. (2021). Mtr4 RNA helicase structures and interactions. Biol. Chem. *402*, 605–616. https://doi.org/10.1515/hsz-2020-0329.

Ozgur, S., Buchwald, G., Falk, S., Chakrabarti, S., Prabu, J.R., and Conti, E. (2015). The conformational plasticity of eukaryotic RNA-dependent ATPases. FEBS J *282*, 850–863. https://doi.org/10.1111/febs.13198.

Perez-Riba, A., and Itzhaki, L.S. (2019). The tetratricopeptide-repeat motif is a versatile platform that enables diverse modes of molecular recognition. Curr. Opin. Struct. Biol. *54*, 43–49. https://doi.org/10.1016/j.sbi.2018.12.004.

Petrov, A., Grosely, R., Chen, J., O'Leary, S.E., and Puglisi, J.D. (2016). Multiple parallel pathways of translation initiation on the CrPV IRES. Mol. Cell *62*, 92–103. https://doi.org/10.1016/j.molcel.2016.03.020.

Pettersen, E.F., Goddard, T.D., Huang, C.C., Couch, G.S., Greenblatt, D.M., Meng, E.C., and Ferrin, T.E. (2004). UCSF Chimera—a visualization system for exploratory research and analysis. J. Comput. Chem. *25*, 1605–1612. https://doi.org/10.1002/jcc.20084.

Pisarev, A.V., Unbehaun, A., Hellen, C.U.T., and Pestova, T.V. (2007). Assembly and analysis of eukaryotic translation initiation complexes. Methods Enzymol *430*, 147–177. https://doi.org/10.1016/S0076-6879(07)30007-4.

Puno, M.R., and Lima, C.D. (2018). Structural basis for MTR4-ZCCHC8 interactions that stimulate the MTR4 helicase in the nuclear exosome-targeting

complex. Proc. Natl. Acad. Sci. USA *115*, E5506–E5515. https://doi.org/10.1073/pnas.1803530115.

Rosenthal, P.B., and Henderson, R. (2003). Optimal determination of particle orientation, absolute hand, and contrast loss in single-particle electron cryomicroscopy. J. Mol. Biol. *333*, 721–745. https://doi.org/10.1016/j.jmb.2003.07.013.

Schaeffer, D., and van Hoof, A. (2011). Different nuclease requirements for exosome- mediated degradation of normal and nonstop mRNAs. Proc. Natl. Acad. Sci. USA *108*, 2366–2371. https://doi.org/10.1073/pnas.1013180108.

Schmid, M., and Jensen, T.H. (2019). The nuclear RNA exosome and its cofactors. Adv. Exp. Med. Biol. *1203*, 113–132. https://doi.org/10.1007/978-3-030-31434-7_4.

Schmidt, C., Kowalinski, E., Shanmuganathan, V., Defenouillère, Q., Braunger, K., Heuer, A., Pech, M., Namane, A., Berninghausen, O., Fromont-Racine, M., et al. (2016). The cryo-EM structure of a ribosome-Ski2-Ski3-Ski8 helicase complex. Science *354*, 1431–1433. https://doi.org/10.1126/science.aaf7520.

Schneider, C.A., Rasband, W.S., and Eliceiri, K.W. (2012). NIH Image to ImageJ: 25 years of image analysis. Nat. Methods *9*, 671–675. https://doi.org/10.1038/nmeth.2089.

Schorb, M., Haberbosch, I., Hagen, W.J.H., Schwab, Y., and Mastronarde, D.N. (2019). Software tools for automated transmission electron microscopy. Nat. Methods *16*, 471–477. https://doi.org/10.1038/s41592-019-0396-9.

Schüler, M., Connell, S.R., Lescoute, A., Giesebrecht, J., Dabrowski, M., Schroeer, B., Mielke, T., Penczek, P.A., Westhof, E., and Spahn, C.M.T. (2006). Structure of the ribosome-bound cricket paralysis virus IRES RNA. Nat. Struct. Mol. Biol. *13*, 1092–1096. https://doi.org/10.1038/nsmb1177.

Schuller, J.M., Falk, S., Fromm, L., Hurt, E., and Conti, E. (2018). Structure of the nuclear exosome captured on a maturing preribosome. Science *360*, 219–222. https://doi.org/10.1126/science.aar5428.

Stirnimann, C.U., Petsalaki, E., Russell, R.B., and Müller, C.W. (2010). WD40 proteins propel cellular networks. Trends Biochem. Sci. *35*, 565–574. https://doi.org/10.1016/j.tibs.2010.04.003.

Synowsky, S.A., and Heck, A.J.R. (2008). The yeast Ski complex is a hetero-tetramer. Protein Sci *17*, 119–125. https://doi.org/10.1110/ps.073155908.

Thoms, M., Thomson, E., Baßler, J., Gnädig, M., Griesel, S., and Hurt, E. (2015). The exosome is recruited to RNA substrates through specific adaptor proteins. Cell *162*, 1029–1038. https://doi.org/10.1016/j.cell.2015.07.060.

Toh-E, A., Guerry, P., and Wickner, R.B. (1978). Chromosomal superkiller mutants of *Saccharomyces cerevisiae*. J. Bacteriol. *136*, 1002–1007.

Tomecki, R., Kristiansen, M.S., Lykke-Andersen, S., Chlebowski, A., Larsen, K.M., Szczesny, R.J., Drazkowska, K., Pastula, A., Andersen, J.S., Stepien, P.P., et al. (2010). The human core exosome interacts with differentially localized processive RNaseS: hDIS3 and hDIS3L. EMBO J *29*, 2342–2357. https://doi.org/10.1038/emboj.2010.121.

Tuck, A.C., Rankova, A., Arpat, A.B., Liechti, L.A., Hess, D., Iesmantavicius, V., Castelo-Szekely, V., Gatfield, D., and Bühler, M. (2020). Mammalian RNA decay pathways are highly specialized and widely linked to translation. Mol. Cell *77*, 1222–1236.e13. https://doi.org/10.1016/j.molcel.2020.01.007.

Tunyasuvunakool, K., Adler, J., Wu, Z., Green, T., Zielinski, M., Žídek, A., Bridgland, A., Cowie, A., Meyer, C., Laydon, A., et al. (2021). Highly accurate protein structure prediction for the human proteome. Nature *596*, 590–596. https://doi.org/10.1038/s41586-021-03828-1.

Wang, J., Chen, J., Wu, G., Zhang, H., Du, X., Chen, S., Zhang, L., Wang, K., Fan, J., Gao, S., et al. (2019). NRDE2 negatively regulates exosome functions by inhibiting MTR4 recruitment and exosome interaction. Genes Dev *33*, 536–549. https://doi.org/10.1101/gad.322602.118.

Weick, E.-M., and Lima, C.D. (2021). RNA helicases are hubs that orchestrate exosome-dependent 3′-5′ decay. Curr. Opin. Struct. Biol. *67*, 86–94. https://doi.org/10.1016/j.sbi.2020.09.010.

Weick, E.-M., Puno, M.R., Januszyk, K., Zinder, J.C., DiMattia, M.A., and Lima, C.D. (2018). Helicase-dependent RNA decay illuminated by a cryo-EM structure of a human nuclear RNA exosome-MTR4 complex. Cell *173*, 1663–1677.e21. https://doi.org/10.1016/j.cell.2018.05.041.

Weir, J.R., Bonneau, F., Hentschel, J., and Conti, E. (2010). Structural analysis reveals the characteristic features of Mtr4, a DExH helicase involved in nuclear RNA processing and surveillance. Proc. Natl. Acad. Sci. USA *107*, 12139–12144. https://doi.org/10.1073/pnas.1004953107.

Winz, M.L., Peil, L., Turowski, T.W., Rappsilber, J., and Tollervey, D. (2019). Molecular interactions between Hel2 and RNA supporting ribosome-associated quality control. Nat. Commun. *10*, 563. https://doi.org/10.1038/s41467-019-08382-z.

Zhang, E., Khanna, V., Dacheux, E., Namane, A., Doyen, A., Gomard, M., Turcotte, B., Jacquier, A., and Fromont-Racine, M. (2019). A specialised SKI complex assists the cytoplasmic RNAexosome in the absence of direct association with ribosomes. EMBO J *38*, e100640. https://doi.org/10.15252/embj.2018100640.

Zhang, K. (2016). Gctf: real-time CTF determination and correction. J. Struct. Biol. *193*, 1–12. https://doi.org/10.1016/j.jsb.2015.11.003.

Zheng, S.Q., Palovcak, E., Armache, J.-P., Verba, K.A., Cheng, Y., and Agard, D.A. (2017). MotionCor2: anisotropic correction of beam-induced motion for improved cryo-electron microscopy. Nat. Methods *14*, 331–332. https://doi.org/10.1038/nmeth.4193.

Zinoviev, A., Ayupov, R.K., Abaeva, I.S., Hellen, C.U.T., and Pestova, T.V. (2020). Extraction of mRNA from stalled ribosomes by the ski complex. Mol. Cell *77*, 1340–1349.e6. https://doi.org/10.1016/j.molcel.2020.01.011.

Zivanov, J., Nakane, T., Forsberg, B.O., Kimanius, D., Hagen, W.J., Lindahl, E., and Scheres, S.H. (2018). New tools for automated high-resolution cryo-EM structure determination in RELION-3. Elife *7*, e42166. https://doi.org/10.7554/eLife.42166.

STAR★METHODS

KEY RESOURCES TABLE

REAGENT or RESOURCE	SOURCE	IDENTIFIER
Bacterial and virus strains		
Escherichia coli BL21 (DE3) STAR pRARE	EMBL Heidelberg Core Facility	N/A
Chemicals, peptides, and recombinant proteins		
Sf-900 II SFM medium	Thermo Fisher Scientific	10902096
FreeStyle 293 Expression Medium	Thermo Fisher Scientific	12338018
Polyethylenimine	Polysciences, Inc.	23966
cOmplete protease inhibitor	Roche	5056489001
NuPAGE 4-12% Bis-Tris protein gels	Thermo Fisher Scientific	NP0336BOX
H. sapiens SKI2-SKI3-SKI8 and derivative complexes	This study	N/A
H. sapiens HBS1L3	This study	N/A
H. sapiens hEXO9	Kowalinski et al., 2016	N/A
H. sapiens $DIS3L_{D486N}$	This study	N/A
H. sapiens 40S/60S ribosomal subunits	This study	N/A
T7 RNA Polymerase	MPI Biochemistry Core Facility	N/A
ATP, CTP, GTP, UTP	Jena Bioscience	NU-1010 – 1013
[α^{32}P] UTP	PerkinElmer	NEG007X250UC
DNase I	Roche	4716728001
Benzonase	Merck	71206
ATP	Sigma-Aldrich	A3377
ADP	Sigma-Aldrich	A2754
NADH	Sigma-Aldrich	N4505
Pyruvate kinase/Lactate dehydrogenase	Sigma-Aldrich	P0294
Phosphoenolpyruvate	Sigma-Aldrich	P0564
poly(U) RNA	Sigma-Aldrich	P9528
n-octyl-ß-D-glucoside	Sigma-Aldrich	850511P
BS_3 (bis(sulfosuccinimidyl)suberate)	Thermo Fisher Scientific	A39266
Deposited data		
apo open hSKI cryoEM map and model	This paper	EMD-13925; PDB: 7QDS
apo closed hSKI cryoEM map and model	This paper	EMD-13923; PDB: 7QDR
RNA-bound closed hSKI cryoEM map and model	This paper	EMD-13927; PDB: 7QDY
ribosome-bound closed hSKI complex cryoEM map and model	This paper	EMD-13928; PDB: 7QDZ
ribosome-bound open hSKI complex cryoEM map and model	This paper	EMD-13929; PDB: 7QE0
Raw and analyzed data	This paper	Mendeley doi:10.17632/9w78m35s2v.1
Experimental models: Cell lines		
Spodoptera frugiperda 21 (*Sf21*)	Thermo Fisher Scientific	11497013
Human embryonic kidney 293T (HEK293T)	ATCC	CRL-3216
Oligonucleotides		
$GGGC(*UC)_{48}$_T7_fwd AATTTAATACGACTCACTATA GG	Sigma-Aldrich	N/A
$GGGC(*UC)_{48}$_rev GAGAGAGAGAGAGAGAGAGAGAG AGAGAGAGAGAGAGAGAGAGAGAGAGAGAGAGAGAGA GAGAGAGAGAGAGAGAGAGAGAGAGAGAGA GAGAGCCCTATAGTGAGTCGTATTAAATT	Sigma-Aldrich	N/A

(*Continued on next page*)

Continued

REAGENT or RESOURCE	SOURCE	IDENTIFIER
IRES29_T7_fwd TAATACGACTCACTATAGGGAAAAA TGTGATCTTGCTTGTAAATAC	Sigma-Aldrich	N/A
IRES29_rev GCGTCTTCCATGGTATCTTG	Sigma-Aldrich	N/A
25U RNA	Sigma-Aldrich	N/A
Recombinant DNA		
pACEBac1-hSKI2-10xHIS-3C-hSKI3-hSKI8 and derivative plasmids	This study	N/A
pEC-6HIS-3C-HBS1L3-$(GS)_3$-eGFP-TS	This study	N/A
pPB-TS-3C-hDIS3L_{D486N}	This study	N/A
pUC-CrPV-IRES-luciferase	This study	N/A
Software and algorithms		
SerialEM	Schorb et al., 2019	https://bio3d.colorado.edu/SerialEM/
Focus	Biyani et al., 2017	https://www.focus-em.org
MotionCor2	Zheng et al., 2017	https://msg.ucsf.edu/software/
Gctf	Zhang, 2016	https://www2.mrc-lmb.cam.ac.uk/kzhang/
Gautomatch	N/A	https://www2.mrc-lmb.cam.ac.uk/kzhang/
RELION 3.0/3.1	Zivanov et al., 2018	https://www3.mrc-lmb.cam.ac.uk/relion/
AlphaFold	Tunyasuvunakool et al., 2021	https://alphafold.ebi.ac.uk/
Buccaneer	Hoh et al., 2020	https://phenix-online.org/
Phenix.real_space_refine	Afonine et al., 2018a	https://phenix-online.org/
Phenix.mtriage	Afonine et al., 2018b	https://phenix-online.org/
Coot	Emsley et al., 2010	https://www2.mrc-lmb.cam.ac.uk/personal/pemsley/coot/
PyMOL2	N/A	https://pymol.org/2/
UCSF Chimera	Pettersen et al., 2004	https://www.cgl.ucsf.edu/chimera/
UCSF ChimeraX	Goddard et al., 2018	https://www.cgl.ucsf.edu/chimerax/
ImageJ	Schneider et al., 2012	https://imagej.nih.gov/ij/
Tidyverse	N/A	https://www.tidyverse.org/
Illustrator	Adobe	https://www.adobe.com
Prism9	GraphPad	https://www.graphpad.com
Other		
HisTrap HP 5ml	Cytiva	17524805
Mono Q 5/50 GL	Cytiva	17516601
Superose 6 Increase 10/300 GL	Cytiva	29091596
StrepTrap HP 5 mL	Cytiva	28907548
Mono S 5/50 GL	Cytiva	17516801
Superdex 200 Increase 10/300 GL	Cytiva	28990944
Superose 6 Increase 3.2/300	Cytiva	29091598
Amicon Ultra MWCO100	Merck	UFC9100
Quantifoil R2/1 Cu 200 mesh	Quantifoil	Q210CR1
Quantifoil R2/1 Cu 200 mesh carbon supported	Quantifoil	Q210CR1-2nm

RESOURCE AVAILABILITY

Lead contact

Further information and requests for resources and reagents should be directed to and will be fulfilled by the lead contact, Elena Conti (conti@biochem.mpg.de).

Materials availability

This study did not generate new unique reagents.

Data and code availability

- Cryo-EM density maps have been deposited in the Electron Microscopy Data Bank (EMDB) and the Protein Data Bank (PDB), respectively, under the accession numbers: EMD-13923 (apo human SKI complex in the closed state, PDB: 7QDR), EMD-13925 (apo human SKI complex in the open state, PDB: 7QDS), EMD-13927 (RNA-bound human SKI complex, PDB: 7QDY), EMD-13928 (80S-bound human SKI complex in the closed state, PDB: 7QDZ) and EMD-13929 (80S-bound human SKI complex in the open state, PDB: 7QE0). Data are available at time of publication.
- Unprocessed and uncompressed imaging data is available at Mendeley Data: https://doi.org/10.17632/9w78m35s2v.1.
- This paper does not report original code.
- Any additional information required to reanalyse the data reported in this work/paper is available from the lead contact upon request.

EXPERIMENTAL MODEL AND SUBJECT DETAILS

All bacterial and eukaryotic cell lines in this study were used for protein production for in vitro experiments, rather than being experimental models in the typical sense. They are listed in the key resources table.

Recombinant proteins were either cloned or synthesized as described in the method details. *Spodoptera frugiperda 21* (*Sf21*) cells were maintained in Sf-900 II SFM medium (Thermo Fisher Scientific) at 27°C. *Escherichia coli* expression strains BL21 STAR pRARE (Thermo Fisher Scientific) were grown in TB medium at 37°C under antibiotic selection to an OD_{600nm} = 2 before inducing protein expression by adding 500 μM IPTG for 16 h at 18°C. HEK 293T cells were adapted to grow in suspension and stable transfected using the piggyBac transposon system (Li et al., 2013). Cells were maintained in FreeStyle 293 Expression medium (Thermo Fisher Scientific) at 37°C and 5% CO_2 and protein expression induced by adding 1 μg/mL doxycycline.

METHOD DETAILS

Cloning, protein expression and purification

The complete open reading frames of *SKIV2L*, *TTC37*, and *WDR61* (UniProt: Q6PGP7, Q15477, Q9GZS3) were cloned from a human cDNA library (MegaMan Human Transcriptome Library, Agilent Technologies) into separate expression cassettes on a single pACEBac1 vector (Bieniossek et al., 2012). A 3C protease cleavable 10xHis-tag on the *TTC37* N-terminus for immobilized metal affinity chromatography (IMAC) was added to all human SKI complex constructs (wild-type, E424Q, V341G, Δwedge, Δarch). The vector was integrated into an engineered baculovirus genome (Bieniossek et al., 2012) and cultured in *Sf21* cells for virus production. *Sf21* cells suspended at 10^6 cells/mL were infected with virus and cultured in Sf-900 II SFM medium at 27°C. Cultures were harvested after 72 h by centrifugation at 2000 g. Cell pellets were resuspended in lysis buffer containing 20 mM Hepes pH7.5, 200 mM NaCl, 25 mM Imidazole and 2mM ß-mercaptoethanol (ß-ME), and supplemented with 200 U/mL benzonase (Merck), 500 μM AEBSF protease inhibitor, and cOmplete EDTA-free protease inhibitor cocktail (Roche). The cells were lysed by ultrasonication (Bandelin, Sonopuls basic). The lysate was cleared by centrifugation at 75,000 g and subjected to a HisTrap HP 5ml column (GE Healthcare) for IMAC. The column was washed with 15 column volumes of 20 mM Hepes pH7.5, 1000 mM NaCl, 200 mM KCl, 10 mM $MgCl_2$, 25 mM Imidazole and 2 mM ß-ME, followed by washing with 5 column volumes of lysis buffer. Protein was eluted in lysis buffer supplemented with 350 mM Imidazole. The eluate was treated with 10 μg/mL His-tagged 3C protease (MPI Biochemistry Core Facility) during overnight dialysis against 20 mM Hepes pH7.5, 100 mM NaCl, 25 mM Imidazole and 2mM ß-ME. 3C protease and His-tags were removed by running the eluate over IMAC. The unbound protein fraction was further purified by ion exchange (Mono Q 5/50 GL, GE Healthcare) and size exclusion chromatography (Superose 6 Increase 10/300 GL, GE Healthcare), and eluted in a final buffer containing 20 mM Hepes pH7.5, 100 mM NaCl, 2 mM Dithiothreitol (DTT).

The complete open reading frame of the HBS1L3 (UniProt: Q9Y450) was commercially synthesized (Eurofins Genomics) and cloned with N-terminal 6xHis-thioredoxin and C-terminal eGFP-TwinStrep tags under a IPTG-inducible promotor for expression in *E. coli*. Transformed *E. coli* BL21 STAR pRARE cells were grown in TB medium at 37°C under antibiotic selection to OD_{600nm} = 2. The temperature was reduced to 18°C and protein expression was induced by addition of 500 μM IPTG. Cells were harvested after 16 h by centrifugation at 8,500 g. Cells were ultrasonicated in the same lysis buffer as above, except it contained 300 mM NaCl. The recombinant protein was kept strictly at 4°C and the purification procedure was processed quickly to avoid degradation. The lysate was cleared by centrifugation and loaded on a HisTrap HP 5 mL column (GE Healthcare) for IMAC. Washing was performed as above, and the protein was eluted and equilibrated with lysis buffer supplemented with 350 mM Imidazole into a StrepTrap HP 5 mL column (GE Healthcare) for a second affinity step. The bound protein was washed with 10 column volumes of buffer containing 20 mM Hepes pH7.5, 300 mM NaCl, 2 mM DTT and addition of 5 mM Desthiobiotin (DTB) eluted the protein. The protein was concentrated in 10 % Glycerol (v/v), flash frozen in liquid nitrogen (LN_2), and stored at -80°C.

The complete open reading frame human DIS3L (UniProt: Q8TF46) with the inactivating D486N mutation ($DIS3L_{D486N}$) was tagged with TwinStrep at the N-terminus and expressed in a HEK 293T stable cell line adapted to grow in suspension. Briefly, HEK 293T cells at 10^6 cells/mL were transfected in FreeStyle 293 Expression Medium (Thermo Fisher Scientific) with hDIS3L cloned into the piggyBac vector with a doxycycline-dependant inducible promoter (Li et al., 2013), the piggyBac transactivator and the hyperactive piggyBac transposase using polyethylenimine (PEI). After a 24 h recovery period, cells were positively selected for 21 days using puromycin and geneticin. 400-800 mL of stably transfected cells (10^6 cells/mL) were induced with 1 μg/mL doxycycline for 48 h and harvested by centrifugation at 800 g. Cells were resuspended in buffer containing 20 mM Hepes pH7.5, 300 mM NaCl, and 2 mM DTT and lysed using a dounce homogeniser. After clearing the lysate by centrifugation, it was loaded on a StrepTrap HP 5 mL column (GE Healthcare) and washed with high salt and lysis buffer (similar to hSKI). The protein was eluted in buffer containing 20 mM Hepes pH7.5, 100 mM NaCl, 5 mM DTB, and 2 mM DTT.

Ribosome subunit purification

Ribosomal 40S and 60S subunits were obtained from untransfected HEK 293T cells (using adapted protocols from Fernández et al. (2014) and Pisarev et al. (2007). 600 x 10^6 cells were pelleted and resuspended on ice for 30 min in lysis buffer containing 20 mM Hepes pH7.5, 300 mM NaCl, 6 mM $MgCl_2$, 0.5 % NP40 (v/v), 2 mM DTT, 500 μM AEBSF. The lysate was cleared by centrifugation at 10,000 g for 15 min and loaded on a 30% sucrose cushion in buffer containing 20 mM Hepes pH7.5, 150 mM KCl, 10 mM $MgCl_2$, 2 mM DTT, followed by ultracentrifugation in a TLA-100.3 rotor (Beckman Coulter) at 86,000 RPM for 90 min. The ribosomal pellets were resuspended in buffer containing 20 mM Hepes pH7.5, 75 mM KCl, 5 mM $MgCl_2$, 2 mM DTT, supplemented with 2 mM puromycin and incubated at 37°C for 15 min. The ribosome solution was then adjusted to 500 mM KCl and subjected to gradient centrifugation in a SW-40 Ti rotor (Beckman Coulter). The sucrose gradients (10-30% w/v) used for centrifugation were diluted in buffer containing 20 mM Hepes pH7.5, 500 mM KCl, 4 mM $MgCl_2$, and 2 mM DTT and mixed using a Gradient Station (Biocomp). After 17 h centrifugation at 22,8000 RPM, the gradients were fractionated from the top (Gradient Station, Biocomp). Fractions corresponding to 40S and 60S ribosomal subunits were pooled separately and concentrated in buffer containing 20 mM Hepes pH7.5, 50 mM KCl, 4 mM $MgCl_2$, and 2 mM DTT.

In vitro transcription of RNA substrates

The sequence of the CrPV IRES construct was taken from the intergenic region of the Cricket paralysis virus genome (NCBI GeneBank: 6025-6232 nt, NC_003924.1). The CrPV IRES was transcribed *in vitro* with T7 RNA polymerase by run-off transcription. The genomic sequence of the CrPV IRES was fused to a portion of the firefly luciferase open reading frame (modified from Petrov et al. [2016]). The CrPV-IRES29 construct was amplified by PCR and then gel purified. *In vitro* transcription of 100 nM CrPV IRES DNA template was carried out in 40 mM Tris-HCl pH8.0, 28 mM $MgCl_2$, 0.01% Triton X-100, 1 mM Spermidine, 5 mM DTT in the presence of 25 mM of each ribonucleotide (ATP, CTP, GTP, UTP, Jena Bioscience) and 100 U/μL T7 RNA Polymerase (MPI Biochemistry Core Facility) at 37°C for 4 h. The DNA template was digested with 1 U/μL DNase I (Roche) and purified by $LiCl_2$ precipitation.

The radioactive body-labelled $GGGC(*UC)_{48}$ RNA was transcribed similarly using an annealed duplex of two DNA oligos (5'-AATT TAATACGACTCACTATAGG-3' and 5'-TTAAATTATGCTGAGTGATATCCCGAGAGAGAGAGAGAGAGAGAGAGAGAGA GAGAGA GAGAGAGAGAGAGAGAGAGAGAGAGAGAGAGAGAGAGAGAGAGAGAGAGAGAGAGAGAG-3') as a template. Transcription of 0.1 μM template DNA was carried out in the same buffer containing nucleotides as above but with the addition of 1.5 μM radioactive [α^{32}P] UTP (PerkinElmer). After 4 h at 37°C and DNase I treatment, the reaction was phenol extracted, ethanol precipitated and gel purified from an 8% 7M Urea PAGE. The incorporation rate of [α^{32}P] UTP and final transcript concentration were quantified using a liquid scintillation counter (Hidex 300 SL).

ATPase activity assays

ATPase activity of human SKI complex and derivates were measured using a pyruvate kinase/lactate dehydrogenase enzyme-coupled assay (Bernstein et al., 2010). Reactions were prepared as serial two-fold dilutions of 2.5 mM ATP in buffer containing 50 mM Hepes pH7.5, 50 mM KAc, 5 mM $MgAc_2$, 2 mM DTT and 10 μg/mL poly(U) RNA (Sigma). After 20 min equilibration at 37°C, the reactions were started by adding 50 nM hSKI complex. NADH oxidation was monitored at 1 min intervals over the time course of 20 min by measuring absorbance at 340 nm using an infinite M1000PRO 96-well Plate reader (Tecan). All measurements were done in triplicates. A baseline oxidation level of NADH was established by measuring duplicate reactions without the addition of protein (see below for quantification and statistical analysis).

Cytoplasmic exosome reconstitution

Human cytoplasmic exosome ($hEXO10_c$ with the inactivated $hDIS3L_{D486N}$ nuclease) was reconstituted from equal molecular amounts of pre-assembled hEXO9 (purified as previously described) and freshly purified $hDIS3L_{D486N}$. After incubation for 30 min on ice, the salt concentration was adjusted to 50 mM NaCl. The reconstituted $hEXO10_c$ wild-type and mutant complexes were subjected to ion-exchange chromatography (Mono S 5/50 GL, GE Healthcare) and size exclusion chromatography (Superdex 200 Increase 10/300 GL, GE Healthcare) in a final buffer containing 20 mM Hepes pH7.5, 100 mM NaCl, and 2 mM DTT.

Size exclusion chromatography assays

Size exclusion chromatography studies were carried out sequentially over the course of one day using a Superose 6 Increase 3.2/300 (GE Healthcare) column and a buffer containing 20 mM Hepes pH7.5, 150 mM NaCl, and 2 mM DTT. The samples were prepared by mixing substoichiometric amounts of HBS1L3 with either 100 pmol hSKI (blue chromatogram in Figure 7A), or 100 pmol hEXO10$_c$ (red chromatogram in Figure 7A), or 100 pmol hSKI and 100 pmol hEXO10$_c$ (purple chromatogram in Figure 7A). In order to show that HBS1L3 is required to bridge the interaction between hSKI and hEXO10$_c$ and to from a higher order complex, 100 pmol hSKI with 100 pmol hEXO10$_c$ were mixed in absence of HBS1L3 (green chromatogram in Figure 7A). The samples were adjusted to 35 μl with buffer and incubated at 4°C for 15 min before injecting them onto the column. The absorbance at 280 nm was recorded in the chromatograms. For comparison of the retention volumes of the different complexes, the data was normalised and plotted in R using the tidyverse collection of R packages. Peak fractions of the individual gel filtration runs were TCA precipitated and analysed by SDS-PAGE on a NuPAGE 4-12% Bis-Tris gel (Thermo Fisher Scientific).

RNase protection assays

The cytoplasmic exosome complexes (Figure S7A) were concentrated at 500 nM and incubated with 125 nM radioactive body-labelled GGGC(*UC)$_{48}$ substrate in buffer containing 50 mM Hepes pH7.5, 50 mM NaCl, 5 mM $MgCl_2$, 10% Glycerol, 0.1% NP40, 2 mM DTT, and 1 mM ADP-BeF (premixed 1 mM ADP with 1 mM $BeCl_2$ and 5 mM NaF). After 60 min at 4°C to allow for the formation of the ribonucleoprotein complexes, the samples were RNase treated with 37.5 U/μL nM benzonase (Merck) at 25°C for 20 min. The reaction was stopped by adding 10x excess buffer containing 100 mM Tris-HCl pH7.5, 150 mM NaCl, 300 mM NaAc pH.5.2, 10 mM EDTA, and 1% SDS. The RNase protected RNA fragments were purified by phenol extraction and ethanol precipitation, separated on a denaturing 12% polyacrylamide gel containing 7M Urea, and analysed by phosphorimaging (Typhoon FLA7000, Cytiva).

Cryo-EM sample preparation

The substrate-free human SKI complex sample was prepared by concentrating 600 pmol of purified hSKI in buffer containing 20 mM Hepes pH7.5, 100 mM NaCl, and 2 mM DTT to approximately 30 μl. The sample was then crosslinked with 1.5 mM bissulfosuccinimidyl suberate (BS_3) at RT for 20 min and quenched with 5 mM Tris-HCl pH7.5. After centrifugation at 18,000 RCF for 10 min to pellet larger aggregates, the sample was injected onto a Superose 6 Increase 3.2/300 column (GE Healthcare) for size exclusion chromatography by an Aekta micro (GE Healthcare). A single peak fraction (containing approximately 500 nM) was collected and mixed with 0.04 % (v/v) n-octyl-ß-D-glucoside. 4-5 μl of the sample were applied to holey carbon grids (R2/1, 200 mesh, Quantifoil) and glow discharged with negative polarity at 20 mA for 30 sec using an EMS GloQube (MiTeGen). The sample was plunge frozen in a liquid ethane/propane mix using a Vitrobot Mark IV (Thermo Fisher Scientific) operated at 4°C and 95% humidity. Although we only show data from the samples prepared as above, we also prepared the substrate-free human SKI complex without addition of BS3 crosslinking and found similar distributions of closed and open state particles.

Substrate-bound human SKI was prepared in a similar manner as the substrate-free complex above with a few exceptions. Comparable amounts of purified hSKI were concentrated in buffer containing 20 mM Hepes pH7.5, 100 mM NaCl, 2 mM $MgCl_2$, 2 mM DTT, and supplemented with 1.5x molar excess of a 25-uracil RNA (Sigma) and 2 mM ADP-BeF. After incubation at 37°C for 15 min, the reconstituted complex was subjected to size exclusion chromatography and a single peak fraction was processed further without any BS3 crosslinking as described above.

The samples containing the 80S ribosome bound to human SKI complexes were prepared as follows: 100 pmol of purified human 40S was mixed with 150 pmol CrPV IRES carrying a 29 nt 3' overhang in buffer containing 20 mM Hepes pH7.5, 50 mM KCl, 4 mM $MgCl_2$, and 2 mM DTT. After incubation at 37°C for 5 min, 120 pmol human 60S was added and incubation proceeded for another 10 min. 200 pmol of purified substrate-free human SKI complex was added to the 80S-CrPV-IRES-29nt complex. The total volume was adjusted to 200 μl with the above buffer and incubated at 37°C for another 15 min before the sample was placed at 4°C for further treatment. The samples were either incubated with 2 mM ADP-BeF or 1 mM ATP at 37°C for 15 min. ATP treatment was followed by addition of 2 mM ADP-BeF for another 15 min at 37°C to block the ATPase activity of hSKI. The samples were subjected to gradient centrifugation in a SW-40 Ti rotor (Beckman Coulter) at 4°C. 15-40% sucrose gradients (w/v) in buffer containing 20 mM Hepes pH7.5, 50 mM KCl, 4 mM $MgCl_2$, and 2 mM DTT were mixed using the Gradient Master (Biocomb). After 17 h centrifugation at 22,800 RPM, the gradients were fractionated using a Piston Gradient Fractionator (Biocomb). Fractions corresponding to the 80S-CrPV-IRES-SKI complex were concentrated in buffer containing 20 mM Hepes pH7.5, 50 mM KCl, 4 mM $MgCl_2$, and 2 mM DTT by centrifugation at 3,000 RCF using an Amicon Ultra MWCO100 centricon (Millipore). The concentrated samples at an OD_{260} of approximately 8 was supplemented with 0.04 % (v/v) n-octyl-ß-D-glucoside and subsequently used for plunge freezing. The sample was incubated twice for 2 min on carbon supported grids (R2/1, 200 mesh, Quantifoil), previously glow discharged with negative polarity at 20 mA for 20 sec using an EMS GloQube (MiTeGen). Plunge freezing was otherwise carried out as for the substrate-free sample above.

Cryo-EM data collection and processing

The cryo-EM data from substrate-free human SKI were collected on a FEI Titan Krios microscope (Thermo Fisher Scientific) at 300 kV equipped with a Gatan K3 direct electron detector operating in electron counting mode. The microscope is equipped with a post column energy filter set to slit-width of 20 eV. Images were collected by under-focused acquisition (target range

of -0.6 and -2.4 μm) at a nominal magnification of 81,000x set up in SerialEM (Schorb et al., 2019) utilising a beam-tilt based multi-shot acquisition scheme for faster imaging. This resulted in 11,079 micrograph movies (40 movie frames each) acquired at a pixel size of 1.094 Å/pixel with a total exposure of 47.44 e/Å^2 over 4 sec. The collected data were processed in RELION 3.0 and 3.1 (Zivanov et al., 2018). To correct for beam-induced motions and minimize effects of radiation damage, the raw movie frames were aligned using MotionCor2 (Zheng et al., 2017). The aligned micrographs were used to estimate per-micrograph contrast transfer function (CTF) parameters with GCTF (Zhang, 2016). Initial particles (4,400,241) were selected using Gautomatch (http://www.mrc-lmb.cam.ac.uk/kzhang/). Four times down-sampled particles were extracted from the aligned, exposure-weighted micrographs. Reference-free 2D classification and classification in 3D using a 40 Å low-pass filtered starting model based on the crystal structure of the yeast SKI complex (PDB: 4BUJ) resulted in an intermediate subset of 350,147 well-aligning hSKI particles. 3D classification of this particle subset, extracted at the original pixel size, into six classes gave three reconstructions of human SKI complex in the closed state (global resolutions ranging from 8.4 to 10.6 Å), one reconstruction in the open state (9.2 Å), and two at lower resolution. A 40 Å low-pass filtered reconstruction of the closed state complex served as a starting model for the classification. Accuracy and resolution of the reconstructions could be improved by extending to 40 iterations of classification. However, it proved difficult to quantify an equilibrium between open and closed state particles from this classification, in part because a large portion of the particles, e.g. the gatekeeping module, adopts a very similar conformation in the two states. Therefore, we deliberately biased the classification of a particle subset after an initial round of 2D classification using 30 Å low-pass filtered open and closed state starting models (Figure S1). These classifications suggest a particle distribution of roughly 40% in closed and 60% in open state. The classification procedures resulted in two homogenous subsets of particles for open and closed state human SKI complex. Their reconstructions reached a global nominal resolution of 3.7 Å and 3.8 Å after masked 3D auto-refinement and automatic b-factor sharpening (-88.1 and -145.3) in the RELION post-processing routine (Zivanov et al., 2018) according to the Fourier shell correlation (FSC) cut-off criterion for the independent half maps of 0.143 (Rosenthal and Henderson, 2003). Peripheral regions of the reconstructions, particularly for the closed state, could be improved by focused refinements with local searches. Masks were applied to TPRs 34-40 of hSKI3$_C$, hSKI2$_{cat}$, hSKI2$_{arch}$ and the hSKI2$_N$ outer segments to improve local resolutions and volume connectivity.

Substrate-bound human SKI data were collected similar to the substrate-free complex above, but at 105,000x nominal magnification. A total of 11,413 micrograph movies were acquired at a pixel size 0.8512 Å/pixel with a total exposure of 68.31 e/Å^2 over 3 sec and spread over 30 movie frames. Beam-induced motion correction, CTF estimation, particle picking, and processing were done in a similar way as for the substrate-free data. 6,036,405 down-scaled particles were initially extracted from the aligned, exposure-weighted micrographs and particles that appeared to be non-hSKI discarded by 2D and 3D classification. A resulting subset of 534,613 human SKI particles were found and extracted at the original pixel size of 0.8512 Å/pixel. Further 3D classification into 6 classes, using a starting model based on these data, lead to the selection of a final subset of 144,441 particles. Initial 3D refinement estimated an overall nominal resolution of 3.5 Å. The quality of the reconstruction and the level of resolved detail was further improved by Bayesian polishing to correct for per-particle motion and by stepwise refinement of the per-particle CTF (taking into account the beam-tilted data acquisition scheme). This resulted in a final reconstruction with an overall global resolution estimated as 3.1 Å according to the gold-standard Fourier shell correlation (0.143) criterion. Masking and map sharpening using an automatically determined global b-factor of -52.3 was carried out in the RELION post-processing routine (Zivanov et al., 2018).

ADP-BeF-treated hSKI-ribosome data were measured on a FEI Titan Krios microscope at 105,000x nominal magnification. The K3 detector was used in correlated-double sampling mode (CDS) and the energy filter set to slit width of 10 eV. 15,073 micrographs movies were acquired with a total exposure of 55.8 e/Å ^{2} equally spread over 35 frames during 5 sec. On-the-fly micrograph movie processing was assisted by Focus (Biyani et al., 2017), which ran Motioncor2 (Zheng et al., 2017), GCTF (Zhang, 2016), and Gautomatch (https://www2.mrc-lmb.cam.ac.uk/research/locally-developed-software/zhang-software/#gauto) on individual images while the data were being collected. Subsequent particle processing was carried out in RELION 3.1 (Zivanov et al., 2018). Down-scaled particles were extracted from the aligned, exposure-weighted micrographs and classified in 2D and 3D to discard non-ribosomal and low-resolution particles from the data. The cleaned ribosomal particles (1,601,273) were extracted at the original pixel size of 0.8512 Å/pixel and aligned in a 3D auto-refinement with a spherical mask using a 40 Å down-filtered starting model based on PDB: 4UG0 (Khatter et al., 2015). The refined particles were then used to subtract a large portion of the 80S ribosome signal from the corresponding particle images. To improve alignment precision and the quality of the reconstructions in the subsequent steps, the particle images were then recentred on the remaining hSKI signal and re-extracted in a smaller box in RELION 3.1 (Zivanov et al., 2018). The subtracted particle images were 3D classified with local search into 7 classes using a wide mask. The final subset of consisted of 51,048 particles. The ribosome-signal-subtracted particles were aligned by 3D auto-refinement, which resulted in a reconstruction of hSKI in the closed state at an overall nominal resolution of 3.6 Å according to the FSC cut-off criterion of 0.143. For masking and map sharpening in the RELION 3.1 post-processing procedure (Zivanov et al., 2018), an ad-hoc b-factor of -20 was applied. The automatically determined b-factor of -122.6 resulted in an over-sharpened map with loss of connectivity. This discrepancy might be due to successive subtraction of a large portion of the total signal in the particle stacks. Next, the signal subtraction was reverted and the corresponding 80S-IRES-hSKI particles refined to 3.1 Å global resolution according to the FSC cut-off criterion of 0.143. A b-factor of -70.7 was automatically estimated in the RELION post-processing routine (Zivanov et al., 2018). The quality of the map in areas of the

CrPV IRES and hSKI complex, however, was not satisfactory. Therefore, we subtracted the signal of the 60S ribosomal subunit from the reconstruction and aligned the remaining 40S-IRES-hSKI particles by 3D auto-refinement, which yielded a reconstruction at 3.1 Å global resolution according to the FSC cut-off criterion of 0.143. Masking and map sharpening in RELION post-processing (Zivanov et al., 2018) was performed using an ad-hoc b-factor of -10 (automatically determined b-factor -73.6). While the map quality for hSKI in this reconstruction improved only marginally, the resolution and volume connectivity for the CrPV IRES in the intersubunit space improved significantly.

ATP-treated hSKI-ribosome data were collected on a FEI Titan Krios microscope at 105,000x nominal magnification. 21,212 micrograph movies were acquired with a total dose of 67.6 e/Å^2 equally spread over 40 movie frames during 6 sec exposure time. On-the-fly data processing was assisted by Focus (Biyani et al., 2017) as described above and continued in RELION 3.1 (Zivanov et al., 2018). 2D and 3D classification resulted in 1,089,263 clean ribosomal particles, which were aligned in 3D auto-refinement for subsequent subtraction of a large portion of the 80S ribosome signal. The subtracted particle images of the ATP-treated hSKI-ribosome data were 3D classified with local searches into 6 classes using a wide mask. The classification resulted in one class that shows well-aligning density for the hSKI complex. In a second round of 3D classification using a 30 Å low-pass filtered starting model of the open state, separation of open and closed particles was possible and resulted in selection of a final subset of 76,838 open state particles. 3D auto-refinement of the subset was exclusively possible with local searches and resulted in a reconstruction at 6.5 Å global resolution according to the FSC cut-off criterion of 0.143. A b-factor of -210.6 was estimated automatically using a tight mask in the RELION post-processing procedure (Zivanov et al., 2018). For the corresponding ribosome-bound reconstructions, signal reversion and subtraction procedures similar to the ADP-BeF-treated hSKI-ribosome data above were applied. This led to an open 80S-IRES-hSKI reconstruction at 3.0 Å global resolution using a -76.3 b-factor and an open 40S-IRES-hSKI reconstruction at 3.0 Å global resolution using an ad-hoc b-factor of -10 (automatically determined b-factor -79.2).

Data processing on both hSKI-ribosome data sets required signal subtraction of the ribosome to yield reconstructions of comparable interpretability and quality as those described in the manuscript. Classical focused classification and refinement procedures did not yield results of comparable quality and interpretability.

Density interpretation and model building

Resolution and quality of the substrate-free hSKI reconstruction in closed state enabled us to build its structure de novo. Structure building was guided by a Buccaneer initial model within the CCP-EM suite (Hoh et al., 2020) based on published high-resolution yeast Ski structures (Halbach et al., 2012, 2013). The structure was then further completed and refined in Coot (Emsley et al., 2010) and iteratively finalised using real-space refinement in the Phenix suite (Liebschner et al., 2019). Rigid-body fitting using UCSF Chimera (Pettersen et al., 2004) into focussed refined maps enabled us to build peripheral regions of the complex: TPRs 34-40 in the C-terminus of hSKI3$_C$; TPRs 10-14 in the N-terminal region of hSKI3$_C$ (α-helices without sequence); parts of the solvent exposed areas of hSKI2$_N$ (with register defined by AlphaFold prediction); the globular part of hSKI2$_{arch}$ (which was interpreted with an AlphaFold prediction) (Figure S2H**)**. The reconstruction of substrate-free hSKI in open state was interpreted by rigid-body fitting (UCSF Chimera) a hSKI2$_{cat/arch}$ depleted version of substrate-free hSKI structure in closed state followed by modulating and refinement of the open state hSKI structure in Coot (Emsley et al., 2010) and real-space refinement (Phenix). Both closed and open state substrate-free human SKI reconstructions were validated using MolProbity (Chen et al., 2010) within the cryo-EM validation tool in the phenix suite (Liebschner et al., 2019).

The substrate-bound hSKI reconstruction was interpreted by rigid-body fitting (UCSF Chimera) of the substrate-free hSKI structure in the closed state described above. The six ribonucleotides of the 25-uracil RNA substrate were built into the structure of substrate-bound hSKI using Coot, and then refined and finalised by real-space refinement (Phenix). The final substrate-bound human SKI complex reconstruction was validated using MolProbity (within the cryo-EM validation tool in the phenix suite).

The reconstruction of closed state hSKI bound to ribosome was interpreted by rigid-body fitting (UCSF Chimera) the structure of substrate-bound hSKI. Small variations in hSKI2$_{cat}$ and the six ribonucleotides within hSKI2$_{cat}$ were adjusted and refined using Coot and real-space refinement (Phenix). This model along with the structure of the 40S ribosomal subunit taken from PDB: 4UG0 (Khatter et al., 2015) and the structure of the CrPV IRES mimicking a pre-translocated ribosomal state (PDB: 4V92 [Fernández et al., 2014]) were all used to interpret the corresponding 40S-IRES-hSKI reconstruction in closed state by rigid-body fitting (UCSF Chimera). The corresponding 80S-IRES-hSKI reconstruction in closed state was subsequently interpreted by rigid-body fitting the above mentioned 40S-IRES-hSKI structure in closed state together with the structure of the 60S ribosomal subunit from the structure of the human 80S ribosome (PDB: 4UG0).

The reconstruction of open state hSKI bound to ribosome was interpreted by rigid-body fitting (UCSF Chimera) the structure of the helicase module from the structure of substrate-bound hSKI detailed above. The structure was further completed in Coot by building additional downstream ribonucleotides traversing hSKI2$_{cat}$. Small variations with respect to hSKI2$_{cat}$ and the ribonucleotides inside hSKI2$_{cat}$ were adjusted and refined in Coot and real-space refinement. The corresponding 40S-IRES-hSKI reconstruction in open state was interpreted similar to the closed state above by rigid-body fitting the ribosome-bound structure of hSKI in open state and the structures of human 40S ribosomal subunit (PDB: 4UG0) and CrPV IRES (PDB: 4V92). The PK-1 nucleotides of the CrPV IRES in the intersubunit space of the ribosome were omitted from the structure where there was no apparent density. The corresponding full 80S-IRES-hSKI reconstruction in open state was interpreted similarly as the one in the closed state above by rigid-body

fitting the 40S-IRES-hSKI structure in the open state together with the structure of the 60S ribosomal subunit (PDB: 4UG0). In the closed and open state 40S-IRES-hSKI reconstructions the same volume level was applied to compare the PK-1 CrPV IRES densities in the intersubunit space without bias.

QUANTIFICATION AND STATISTICAL ANALYSIS

The kinetic parameters of ATP hydrolysis by human SKI were calculated according to Michaelis-Menten theory at various ATP substrate concentrations under steady-state conditions. The baseline corrected initial velocities (v_0) as a function of substrate concentration were used to approximate the Michaelis-Menten equation ($v_0 = (v_{max} \cdot [S]) / (K_m + [S])$). The kinetic parameters v_{max}, K_m and k_{cat} were derived from the approximation using a total enzyme concentration $[E_{tot}] = 0.05\ \mu M$. The approximation of the Michaelis-Menten equation was done using a non-linear regression model in the Prism9 (GraphPad) software.

Molecular Cell, Volume *82*

Supplemental information

The human SKI complex regulates channeling of ribosome-bound RNA to the exosome via an intrinsic gatekeeping mechanism

Alexander Kögel, Achim Keidel, Fabien Bonneau, Ingmar B. Schäfer, and Elena Conti

Supplementary Figure S1. Cryo-EM data analysis of recombinant apo hSKI (related to Figures 1, 2 and 3)

Characteristics of the apo hSKI single particle cryo-EM sample and data. **(A) On the left,** analytical size exclusion chromatography profile on a S6 increase column (Cytiva) of a representative hSKI preparation, and on the right is a 4-12 % Coomassie stained SDS-PAGE of a peak fraction of the SEC run (labelled with *, M is Marker). In **(B)** a representative cryo-EM micrograph of the apo hSKI sample (A) is shown. This image was recorded at 300 kV with a pixel size of 1.024 Å/pix using a post-GIF K3 direct detector. **(C)** 2D class averages of the apo hSKI sample in the closed (left hand panel, red frame) and open (right hand panel, blue frame) state conformations. **(D)** Processing scheme of the single particle cryo-EM dataset of the apo hSKI sample resulting in 3D reconstructions for the closed (red frame) and open (blue frame) states.

Supplementary Figure S2. Cryo-EM reconstruction analysis of apo hSKI (related to Figures 1, 2 and 3)

Quality indicators of the apo hSKI closed and open 3D reconstructions. Local resolution estimates and Fourier Shell Correlations (FSC) of the closed **((A)** and **(B))** and the open **((D)** and **(E))** reconstructions of the apo hSKI cryo-EM SPA data. The FSC of the masked independent half maps were calculated in the RELION 3.1 postprocessing routine and the map vs model FSC using phenix.mtriage. The FSC cut-off criteria of 0.5 and 0.143 are indicated by dotted lines. Angular sampling distributions of the closed **(C)** and open **(F)** reconstructions of the apo hSKI data. Sampling angle data were plotted in 3º by 3º bins and sampling bins coloured according to particle number with red indicating more and blue fewer particles. **(G)** Selected model and map regions of the closed state reconstructions showing the quality of the structural data. **(H)** Local resolution estimate of a focused 3D reconstruction of the $hSKI2_{arch}$ (panel on the left) used for rigid fitting of a homology model of this domain (panel on the right) and completion of the closed state model.

Supplementary Figure S3. Structural conservation between human SKI and yeast Ski (related to Figures 2, 3, 5 and 6)

Comparisons of the hSKI apo and the *S. cerevisiae* Ski structures. In **(A)** the model of hSKI closed apo state is juxtaposed to the yeast Ski model. SKI2 is coloured in yellow,

SKI3 in blue, $SKI8_{IN}$ in green and $SKI8_{OUT}$ in dark green. The SKI3 C-terminal module is absent in the yeast structure (box (B)). **(B)** Detailed view of the C-terminal module of hSKI3 in complex with the N-terminus of the hSKI2. **(C)** The hSKI2 N-terminal outer a-helix is sandwiched between hSKI3 TPR13 and TPR14. Note that the residue numbering of the $Ski2_N$ a-helix (see also Figure 2C) is based on prediction from AlphaFold (Tunyasuvunakool et al., 2021). A focused 3D reconstruction on the first superhelical turn of hSKI3 in the hSKI apo closed state is coloured according to local resolution on the left and displayed together with the respective part of the model on the right. **(D)** hSKI2 helicase modules of the apo hSKI closed state, the RNA-bound hSKI closed state and the *S.c.* Ski structure in comparison. Note the similar orientation and conformation of the $SKI2_{arch}$ with respect to the $SKI2_{cat}$ in all three structures. **(E)** Comparison of the human and the yeast 80S bound by human and yeast SKI complex respectively (*S. cerevisiae* 80S-Ski complex from PDB:5MC6). SKI2 is coloured in yellow, SKI3 in blue, $SKI8_{IN}$ in green, $SKI8_{OUT}$ in dark green, the CrPV IRES in the human case and the mRNA and tRNA in the yeast case in red, the 60S ribosomal subunit is in light blue and the 40S ribosomal subunit in light orange. The yeast and human SKI complexes sit in different orientations on the respective 80S and the RNAs appear differently bound to the helicase modules. In the yeast case this leaves 2-3 nucleotide positions to ySki2 R149 unoccupied (ySki2 R149 is structurally in the equivalent position as hSKI2 W146).

Supplementary Figure S4. SKI2 elements impacting the open/closed state (related to Figure 2, 3 and 4)

Details of selected elements in the $hSKI2_N$. In **(A)** a multiple sequence alignment (MSA) of eukaryotic SKI2 homologs focussed on the N-terminal wedge and a schematic representation of this region in the hSKI2 construct used for the hSKI-Δwedge complex is plotted. Degrees of conservation are indicated by shades of yellow in the MSA with darker shades highlighting stronger conservation. The organisation of the different motives of interest in proximity to the hSKI2 wedge is indicated in the cartoon atop the MSA by thicker yellow lines. A Coomassie stained SDS-PAGE of this sample is shown in Fig. 7B. These samples were vitrified on holey-carbon Cu grids and imaged at 200kV using a K2 direct detector in counting model at a pixel size of 1.885 Å/pix. In the top panel in **(B)** reference-free 2D class averages of these cryo-EM SPA data of the

hSKIΔwedge complex are displayed. These 2D class averages are overall similar to those of the apo open hSKI particles in Fig. S1C. The apo open hSKI complex was fitted into the low-resolution 3D reconstruction of the hSKIΔwedge complex in the panel at the bottom. The unmodelled density on the right with corkscrew-like appearance corresponds to the unmodelled hSKI3 N-terminal TPRs. Note the absence of any interpretable density for the hSKI2 helicase module. hSKI2 is coloured in yellow, hSKI3 in blue, $hSKI8_{IN}$ in green and $hSKI8_{OUT}$ in dark green. In single particle cryo-EM, a *S. cerevisiae* Ski-Δarch complex adopts an open and closed conformation. **(C)** Coomassie stained 4-12 % SDS-PAGE of the yeast SkiΔarch complex. These samples were vitrified on holey-carbon Cu grids and imaged at 200kV using a K2 direct detector operated as above. Reference-free 2D class averages and the final 3D reconstruction of the closed state of the yeast Ski-Δarch complex are in **(D)**. **(E)** shows reference-free 2D class averages and the final 3D reconstruction of the open state of the yeast Ski-Δarch complex. Ski2 is coloured in yellow, Ski3 in blue, $Ski8_{IN}$ in green and $Ski8_{OUT}$ in dark green. **(F)** Fourier shell correlation of the masked independent half-maps for the 3D reconstructions of hSKIΔwedge (shown in **(B)**, forest green) as well as the closed and open states of the yeast Ski-Δarch complex (shown in **(D)** and **(E),** coloured in salmon and olive, respectively)**.**

Supplementary Figure S5. Characteristics of the RNA-bound closed hSKI single particle cryo-EM data (related to Figure 4)

(A) shows a representative cryo-EM micrograph and reference-free 2D class averages of the RNA-bound closed hSKI sample recorded at 300 kV with a pixel size of 0.8512 Å/pix using a Gatan K3 camera. In **(B)** the processing scheme of the single particle cryo-EM dataset of the hSKI sample is outlined. This resulted in the final 3D reconstruction with a global resolution estimate of 3.1 Å for the closed RNA-bound state (red frame). The local resolution estimates are plotted on the final reconstruction in **(C)**, the FSC of the masked independent half-maps of the final reconstruction and the model vs map FSC in **(D)**. Here the FSC cut-off criteria of 0.5 and 0.143 are indicated by dotted lines. The angular sampling distribution for the final reconstruction is in **(E).** Angular sampling data were plotted in 3º by 3º bins in this panel. Note the absence of any noticeable fraction of open state particles in these SPA data (see 3D classification in **(B)**). Comparisons of the closed RNA-bound hSKI2 helicase with

hMTR4. In **(F)** RNA-bound human MTR4 in grey is superposed onto the closed RNA-bound hSKI2 helicase in yellow (human MTR4 from PDB:6D6Q). The RNA is coloured in red. Note the very similar path of the RNA in both structures. **(G)** Details of the RNA channel in the helicase module of the RNA-bound hSKI apo closed state similar to Fig. 4C. Residues interacting with the RNA are shown in stick representation. Colour scheme as in **(F)**. **(H)** Superposition of the RNA bound hSKI2 with human MTR4 bound to ZCCHC8$_{CTD}$. Residues W146 of the hSKI2$_{wedge}$ and F673 of the ZCCHC8$_{CTD}$ occupy very similar positions at one end of the RNA channel in the two structures (MTR4: ZCCHC8$_{CTD}$ from PDB:6C90). In the RNA-bound closed hSKI structures this residue closes off the RNA channel of the hSKI2 helicase at the 3' end prohibiting the RNA from further threading through.

Supplementary Figure S6. Characteristics of the closed ribosome-bound hSKI single particle cryo-EM sample and data (related to Figure 6)

(A) Typical 15-40 % (w/v) Sucrose gradient profile used for reconstitution of the closed state ADP-BeF-treated human 80S-IRES-hSKI complex on the left (80S-IRES-hSKI black curve; 80S-IRES grey curve). Peak fractions (indicated by *) were run out on a 4-12 % SDS-PAGE and the Coomassie stained gel is in the right panel. hSKI8 is not clearly identifiable on the gel most likely due to the prevalence of human 80S ribosomal proteins between 30 and 40 kDa. These peak fractions were vitrified and imaged at 300 kV using a post-GIF K3 camera with a pixel size of 0.8512 Å/pix **(B)**. Reference-free 2D class averages of the closed state 80S-IRES-hSKI sample are shown in **(C)**. Density for the hSKI complex is discernible atop the 40S ribosomal subunit in most of these 2D class averages. **(D)** displays the processing workflow for the closed ribosome-bound hSKI single particle cryo-EM data resulting, after subtraction of the 80S density, in a reconstruction of the hSKI complex at 3.6 Å resolution. The red masks indicate the regions of the map not subtracted from the data. The angular sampling distribution, the FSC of the independent masked half-maps and the map vs model FSC as well as the local resolution estimates plotted on the final closed ribosome-bound hSKI structure are shown in **(E)**, **(F)** and **(G)** respectively. In **(F)** dotted lines indicate the FSC cut-off criteria of 0.5 and 0.143.

Supplementary Figure S7. Characteristics of the open ribosome-bound hSKI single particle cryo-EM data (related to Figure 7)

(A) The purified protein samples used in the RNase protection assays in Figure 7B are shown on a Coomassie-stained 4-12 % SDS-PAGE. The samples are peak fractions from size-exclusion chromatography purifications. In **(B)** a representative micrograph (at a pixel size of 0.8512 Å/pix) and in **(C)** reference-free 2D class averages of the ATP-treated 80S-IRES-hSKI complex in open state are shown. In most 2D class averages density for the hSKI2 helicase at the top of the 40S ribosomal subunit is identifiable. Note the distinct structure of the $hSKI2_{arch}$ in these 2D class averages. **(D)** shows the local resolution estimates for the open ribosome bound hSKI structure from which the density of the 80S has been subtracted. In **(E)** angular sampling distribution for the reconstruction in **(D)** is plotted and in **(F)** the FSC for the masked independent half-maps and the model vs map for said reconstruction with dotted lines indicate the FSC cut-off criteria of 0.5 and 0.143. **(G)** shows the processing scheme with the red masks indicating the region of the map not subtracted from the data. After subtraction both 3D classifications with either apo closed hSKI or open ribosome-bound hSKI as reference model identify sub-populations of both the open and the closed hSKI state in these data. Of the ~110 000 particles identified initially as hSKI-bound, approximately 65% appear clearly in the open state in the second round of focused 3D classification using the open state as start model. The hSKI2 helicase is well ordered in these data since the 80S serves as an anchor for its substrate engagement. This is in contrast and somewhat paradoxical to the apo open hSKI state, where the helicase domain appears flexible in relation to the rest of the complex.

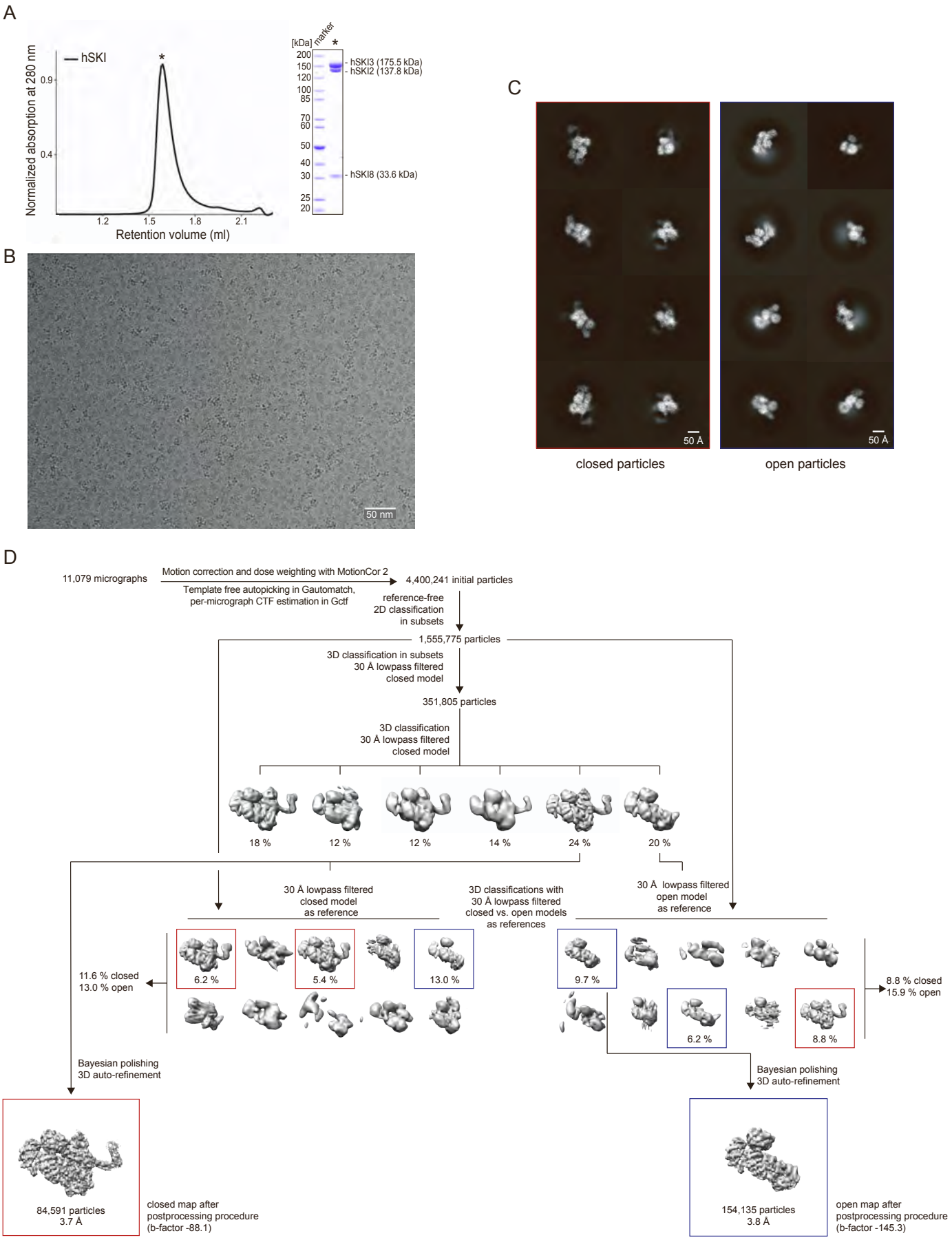
A
hSKI
Normalized absorption at 280 nm
0.9
0.4
1.2
1.5
1.8
2.1
Retention volume (ml)
[kDa]
marker
200
150
120
100
85
70
60
50
40
30
25
20
hSKI3 (175.5 kDa)
hSKI2 (137.8 kDa)
hSKI8 (33.6 kDa)
B
50 nm
C
50 Å
50 Å
closed particles
open particles
D
11,079 micrographs
Motion correction and dose weighting with MotionCor 2
Template free autopicking in Gautomatch,
per-micrograph CTF estimation in Gctf
4,400,241 initial particles
reference-free
2D classification
in subsets
1,555,775 particles
3D classification in subsets
30 Å lowpass filtered
closed model
351,805 particles
3D classification
30 Å lowpass filtered
closed model
18 %
12 %
12 %
14 %
24 %
20 %
30 Å lowpass filtered
closed model
as reference
3D classifications with
30 Å lowpass filtered
closed vs. open models
as references
30 Å lowpass filtered
open model
as reference
11.6 % closed
13.0 % open
6.2 %
5.4 %
13.0 %
9.7 %
6.2 %
8.8 %
8.8 % closed
15.9 % open
Bayesian polishing
3D auto-refinement
Bayesian polishing
3D auto-refinement
84,591 particles
3.7 Å
closed map after
postprocessing procedure
(b-factor -88.1)
154,135 particles
3.8 Å
open map after
postprocessing procedure
(b-factor -145.3)

Figure S1

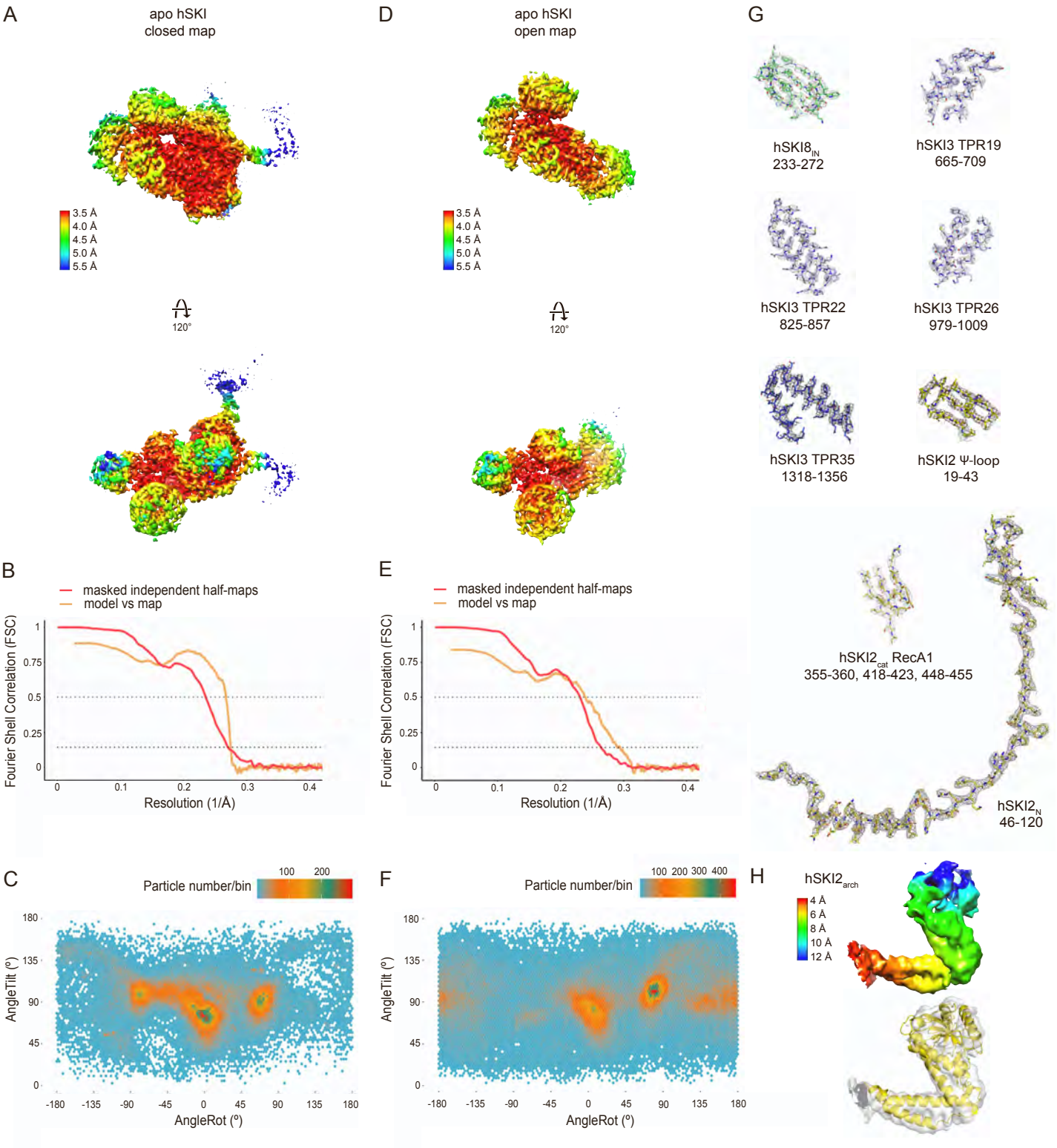
A
apo hSKI
closed map
3.5 Å
4.0 Å
4.5 Å
5.0 Å
5.5 Å
120°
D
apo hSKI
open map
3.5 Å
4.0 Å
4.5 Å
5.0 Å
5.5 Å
120°
G
hSKI8IN
233-272
hSKI3 TPR19
665-709
hSKI3 TPR22
825-857
hSKI3 TPR26
979-1009
hSKI3 TPR35
1318-1356
hSKI2 Ψ-loop
19-43
hSKI2cat RecA1
355-360, 418-423, 448-455
hSKI2N
46-120
B
masked independent half-maps
model vs map
Fourier Shell Correlation (FSC)
Resolution (1/Å)
E
masked independent half-maps
model vs map
Fourier Shell Correlation (FSC)
Resolution (1/Å)
C
Particle number/bin
100 200
AngleTilt (°)
AngleRot (°)
F
Particle number/bin
100 200 300 400
AngleTilt (°)
AngleRot (°)
H
hSKI2arch
4 Å
6 Å
8 Å
10 Å
12 Å

Figure S2

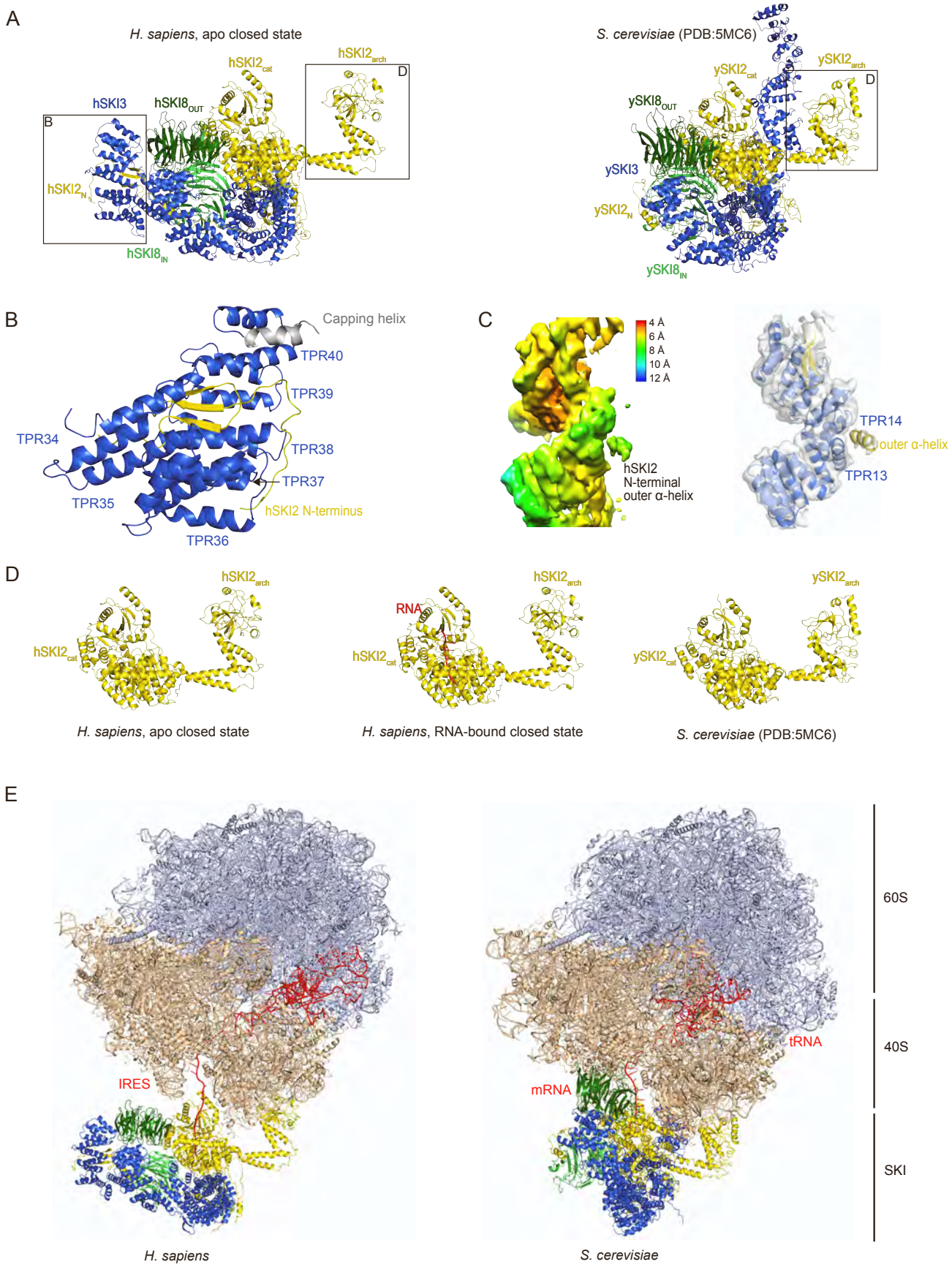
A
H. sapiens, apo closed state
hSKI2cat
hSKI2arch
D
hSKI3
hSKI8OUT
B
hSKI2N
hSKI8IN
S. cerevisiae (PDB:5MC6)
ySKI2cat
ySKI2arch
D
ySKI8OUT
ySKI3
ySKI2N
ySKI8IN
B
Capping helix
TPR40
TPR39
TPR34
TPR38
TPR37
TPR35
hSKI2 N-terminus
TPR36
C
4 Å
6 Å
8 Å
10 Å
12 Å
hSKI2
N-terminal
outer α-helix
TPR14
outer α-helix
TPR13
D
hSKI2arch
hSKI2cat
H. sapiens, apo closed state
RNA
hSKI2arch
hSKI2cat
H. sapiens, RNA-bound closed state
ySKI2arch
ySKI2cat
S. cerevisiae (PDB:5MC6)
E
IRES
H. sapiens
tRNA
mRNA
S. cerevisiae
60S
40S
SKI

Figure S3

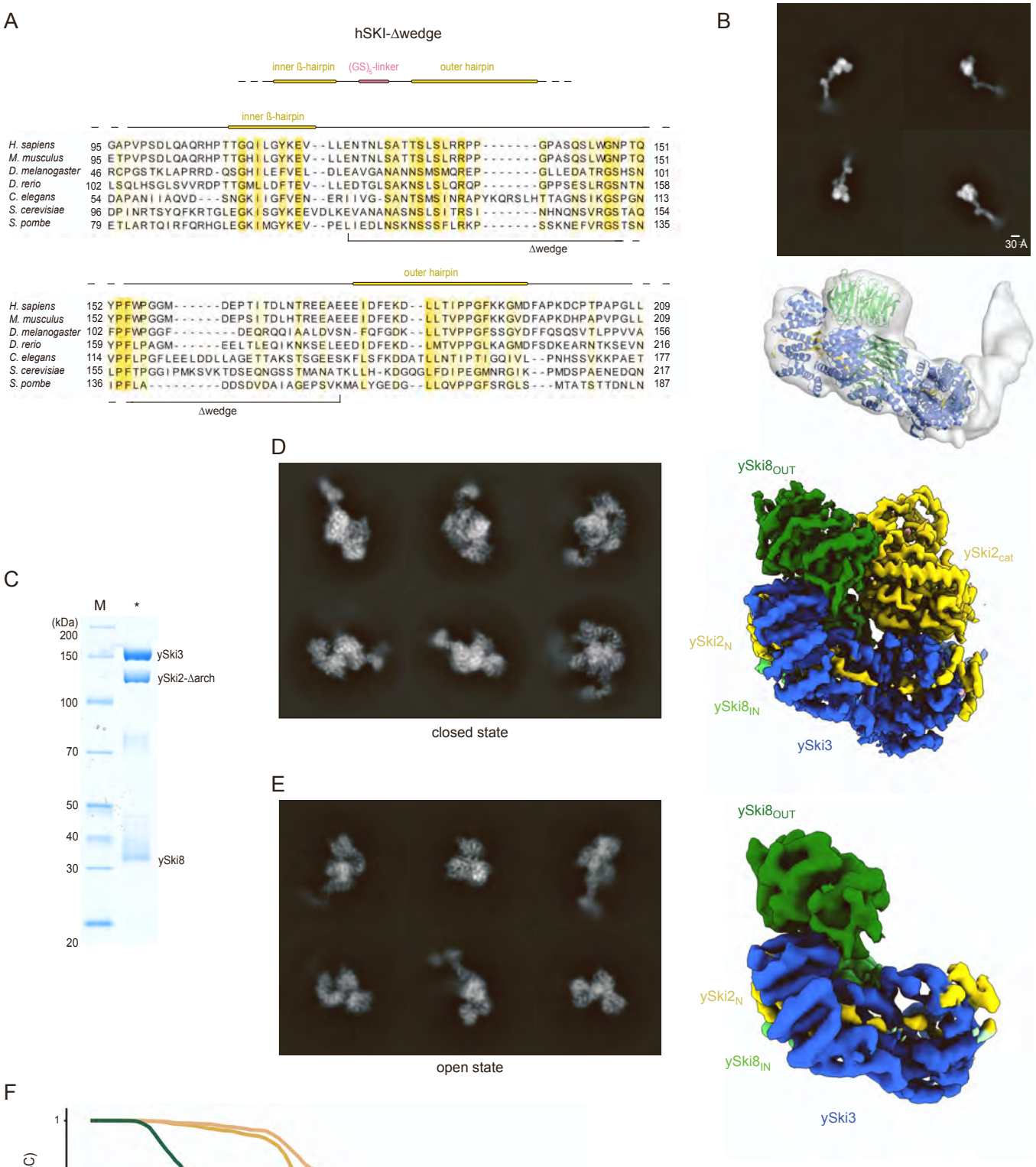
A
hSKI-Δwedge
inner ß-hairpin
(GS)5-linker
outer hairpin
H. sapiens 95 GAPVPSDLQAQRHPTTGQILGYKEV--LLENTNLSATTSLSLRRPP-------GPASQSLWGNPTQ 151
M. musculus 95 ETPVPSDLQAQRHPTTGHILGYKEV--LLENTNLSATTSLSLRRPP-------GPASQSLWGNPTQ 151
D. melanogaster 46 RCPGSTKLAPRRD-QSGHILEFVEL--DLEAVGANANNSMSMQREP-------GLLEDATRGSHSN 101
D. rerio 102 LSQLHSGLSVVRDPTTGMLLDFTEV--LLEDTGLSAKNSLSLQRQP-------GPPSESLRGSNTN 158
C. elegans 54 DAPANIIAQVD---SNGKIIGFVEN--ERIIVG-SANTSMSINRAPYKQRSLHTTAGNSIKGSPGN 113
S. cerevisiae 96 DPINRTSYQFKRTGLEGKISGYKEEVDLKEVANANASNSLSITRSI-------NHNQNSVRGSTAQ 154
S. pombe 79 ETLARTQIRFQRHGLEGKIMGYKEV--PELIEDLNSKNSSSFLRKP-------SSKNEFVRGSTSN 135
Δwedge
outer hairpin
H. sapiens 152 YPFWPGGM------DEPTITDLNTREEAEEEIDFEKD--LLTIPPGFKKGMDFAPKDCPTPAPGLL 209
M. musculus 152 YPFWPGGM------DEPSITDLHTREEAEEEIDFEKD--LLTVPPGFKKGVDFAPKDHPAPVPGLL 209
D. melanogaster 102 FPFWPGGF--------DEQRQQIAALDVSN-FQFGDK--LLTVPPGFSSGYDFFQSQSVTLPPVVA 156
D. rerio 159 YPFLPAGM------EELTLEQIKNKSELEEDIDFEKD--LMTVPPGLKAGMDFSDKEARNTKSEVN 216
C. elegans 114 VPFLPGFLEELDDLLAGETTAKSTSGEESKFLSFKDDATLLNTIPTIGQIVL--PNHSSVKKPAET 177
S. cerevisiae 155 LPFTPGGIPMKSVKTDSEQNGSSTMANATKLLH-KDGQGLFDIPEGMNRGIK--PMDSPAENEDQN 217
S. pombe 136 IPFLA---------DDSDVDAIAGEPSVKMALYGEDG--LLQVPPGFSRGLS---MTATSTTDNLN 187
Δwedge
B
30 Å
C
M
*
(kDa)
200
150
100
70
50
40
30
20
ySki3
ySki2-Δarch
ySki8
D
closed state
E
open state
ySki8OUT
ySki2cat
ySki2N
ySki8IN
ySki3
F
Fourier Shell Correlation (FSC)
1
0.75
0.5
0.25
0
0
0.1
0.2
Resolution (1/Å)
masked independent half-maps of:
ySki-Δarch open state
ySki-Δarch closed state
hSKI-Δwedge

Figure S4

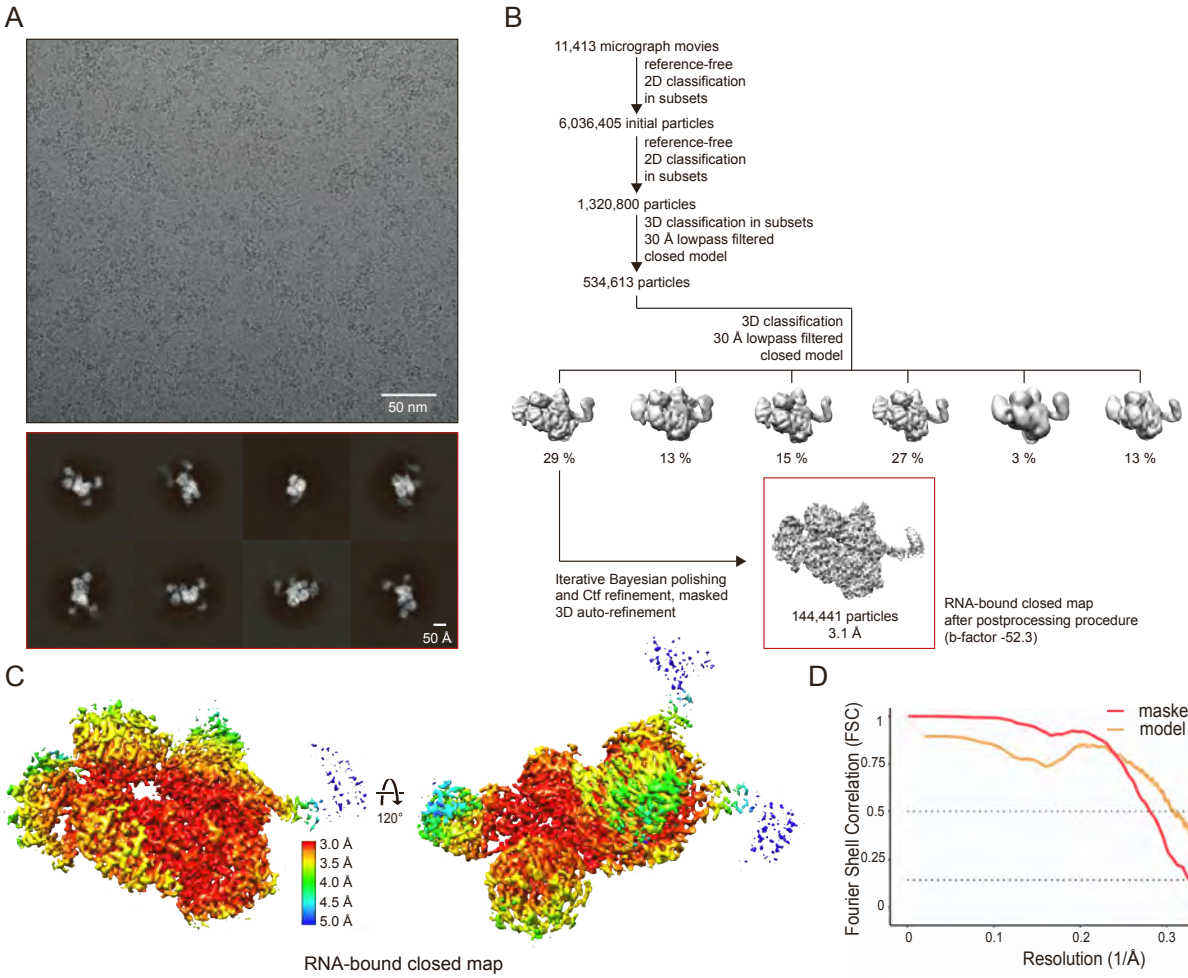
A
50 nm
50 Å
B
11,413 micrograph movies
reference-free
2D classification
in subsets
6,036,405 initial particles
reference-free
2D classification
in subsets
1,320,800 particles
3D classification in subsets
30 Å lowpass filtered
closed model
534,613 particles
3D classification
30 Å lowpass filtered
closed model
29 %
13 %
15 %
27 %
3 %
13 %
Iterative Bayesian polishing
and Ctf refinement, masked
3D auto-refinement
144,441 particles
3.1 Å
RNA-bound closed map
after postprocessing procedure
(b-factor -52.3)
C
120°
3.0 Å
3.5 Å
4.0 Å
4.5 Å
5.0 Å
RNA-bound closed map
D
masked independent half-maps
model vs map
Fourier Shell Correlation (FSC)
Resolution (1/Å)
E
Particle number/bin
100 200 300 400 500
AngleTilt (°)
AngleRot (°)
F
helical bundle
SKI2
MTR4
RNA
5'
3'
RecA1
RecA2
H.s. MTR4 (PDB:6D6Q)
G
5'
N1
H684
S575
melting
hairpin
R576
K683
N2
T662
S637
T664
N3
M667
Q1118
N4
E432
R1198
I362
N5
R433
R1202
K363
T399
E1205
N6
E401
D386
3'
W146
ratchet helix
H
SKI2cat
W146
MTR4
SKI2wedge
RNA 5'
ZCCHC8CTD
F673
90°
90°
SKI2cat
RNA
5'
MTR4
W146
F673
ZCCHC8CTD
SKI2wedge
H.s. MTR4-ZCCHC8-CTD (PDB:6C90)

Figure S5

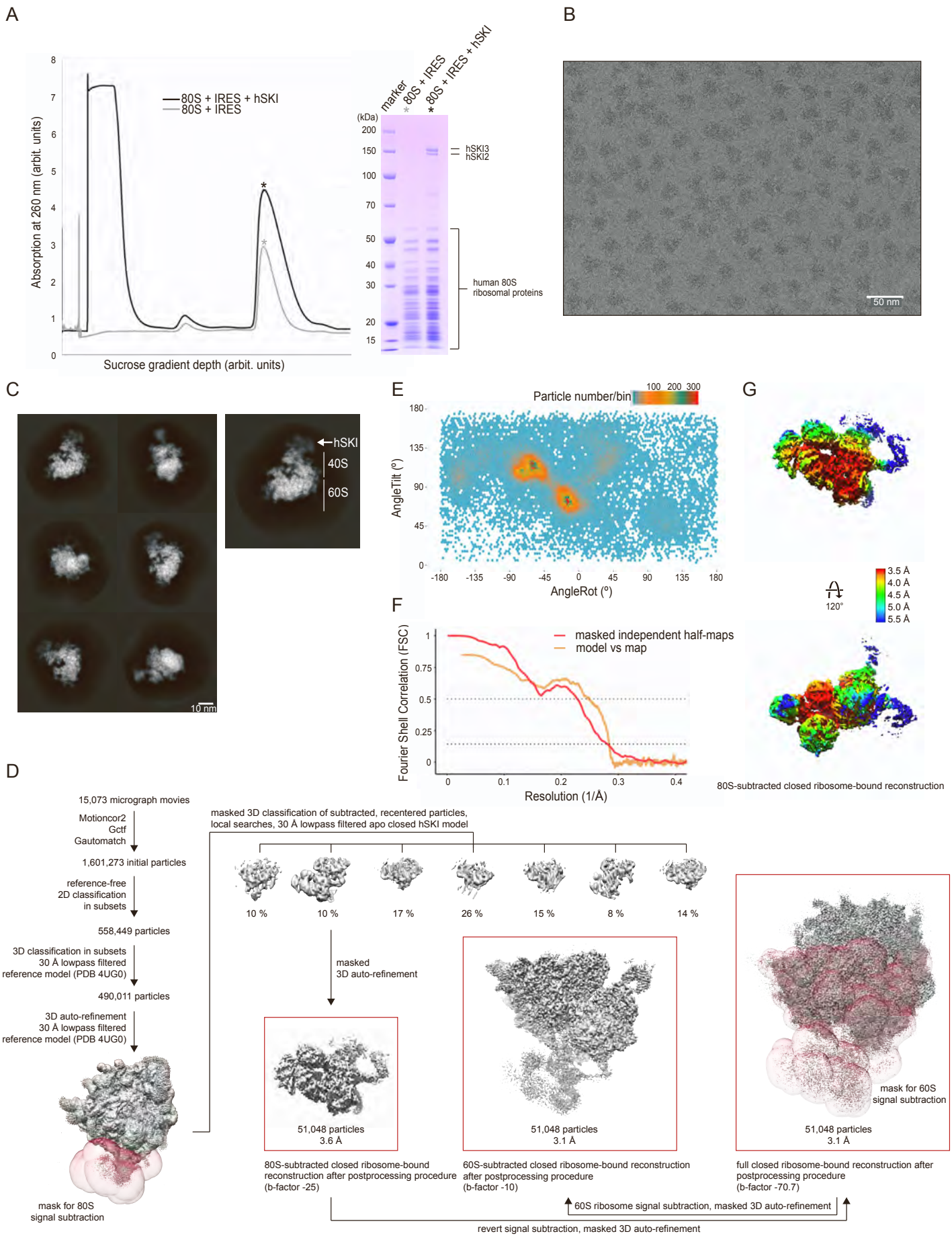
A
80S + IRES + hSKI
80S + IRES
Absorption at 260 nm (arbit. units)
Sucrose gradient depth (arbit. units)
marker
80S + IRES
80S + IRES + hSKI
(kDa)
hSKI3
hSKI2
human 80S ribosomal proteins
B
50 nm
C
hSKI
40S
60S
10 nm
E
Particle number/bin
AngleTilt (°)
AngleRot (°)
F
masked independent half-maps
model vs map
Fourier Shell Correlation (FSC)
Resolution (1/Å)
G
120°
3.5 Å
4.0 Å
4.5 Å
5.0 Å
5.5 Å
80S-subtracted closed ribosome-bound reconstruction
D
15,073 micrograph movies
Motioncor2
Gctf
Gautomatch
1,601,273 initial particles
reference-free 2D classification in subsets
558,449 particles
3D classification in subsets 30 Å lowpass filtered reference model (PDB 4UG0)
490,011 particles
3D auto-refinement 30 Å lowpass filtered reference model (PDB 4UG0)
mask for 80S signal subtraction
masked 3D classification of subtracted, recentered particles, local searches, 30 Å lowpass filtered apo closed hSKI model
10 %
10 %
17 %
26 %
15 %
8 %
14 %
masked 3D auto-refinement
51,048 particles 3.6 Å
80S-subtracted closed ribosome-bound reconstruction after postprocessing procedure (b-factor -25)
51,048 particles 3.1 Å
60S-subtracted closed ribosome-bound reconstruction after postprocessing procedure (b-factor -10)
mask for 60S signal subtraction
51,048 particles 3.1 Å
full closed ribosome-bound reconstruction after postprocessing procedure (b-factor -70.7)
60S ribosome signal subtraction, masked 3D auto-refinement
revert signal subtraction, masked 3D auto-refinement

Figure S6

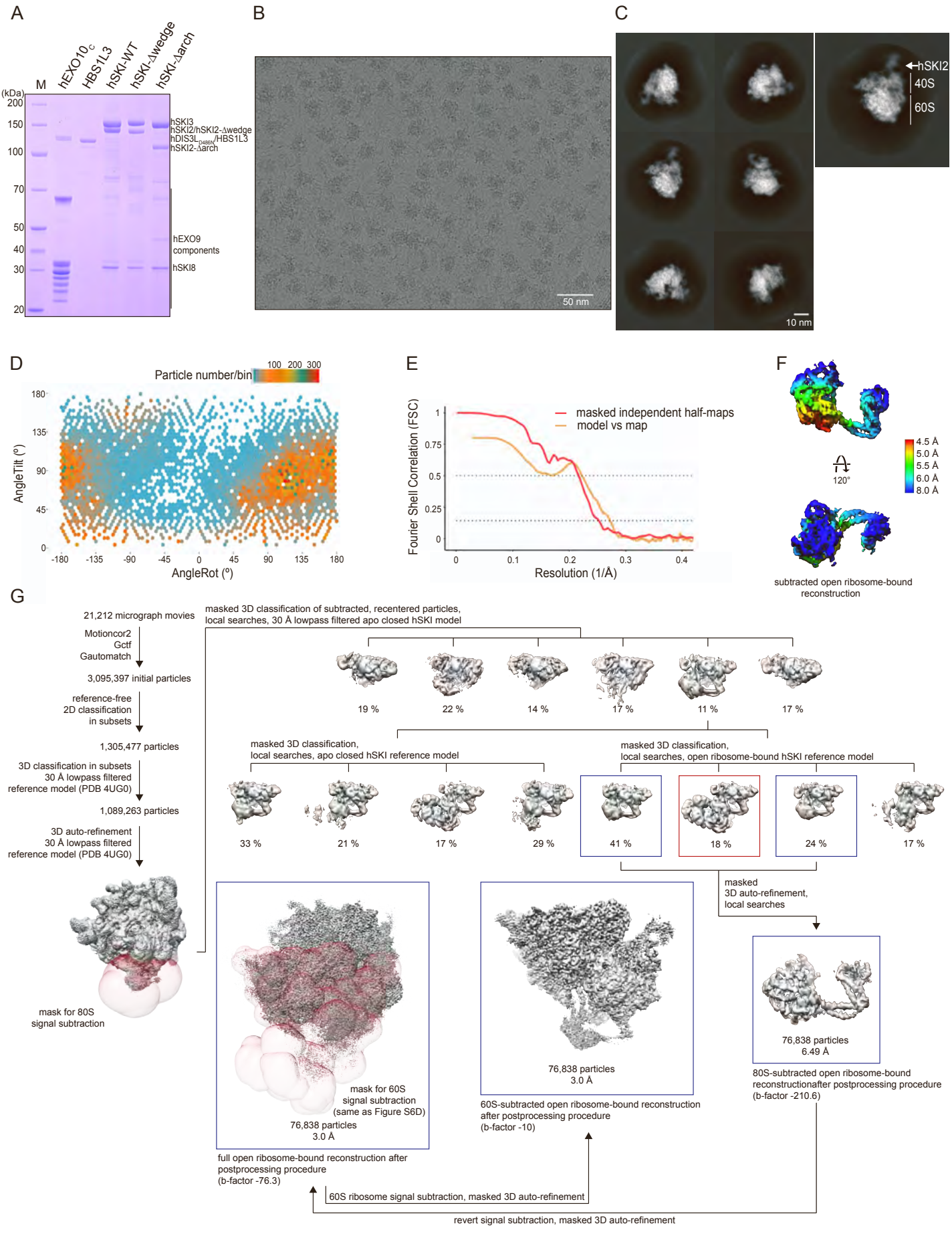
A
M
hEXO10c
HBS1L3
hSKI-WT
hSKI-Δwedge
hSKI-Δarch
(kDa)
200
150
100
70
50
40
30
20
hSKI3
hSKI2/hSKI2-Δwedge
hDIS3L D486N/HBS1L3
hSKI2-Δarch
hEXO9 components
hSKI8
B
50 nm
C
hSKI2
40S
60S
10 nm
D
Particle number/bin
100 200 300
AngleTilt (°)
AngleRot (°)
E
masked independent half-maps
model vs map
Fourier Shell Correlation (FSC)
Resolution (1/Å)
F
120°
4.5 Å
5.0 Å
5.5 Å
6.0 Å
8.0 Å
subtracted open ribosome-bound reconstruction
G
21,212 micrograph movies
Motioncor2
Gctf
Gautomatch
3,095,397 initial particles
reference-free 2D classification in subsets
1,305,477 particles
3D classification in subsets 30 Å lowpass filtered reference model (PDB 4UG0)
1,089,263 particles
3D auto-refinement 30 Å lowpass filtered reference model (PDB 4UG0)
mask for 80S signal subtraction
masked 3D classification of subtracted, recentered particles, local searches, 30 Å lowpass filtered apo closed hSKI model
19 %
22 %
14 %
17 %
11 %
17 %
masked 3D classification, local searches, apo closed hSKI reference model
masked 3D classification, local searches, open ribosome-bound hSKI reference model
33 %
21 %
17 %
29 %
41 %
18 %
24 %
17 %
masked 3D auto-refinement, local searches
mask for 60S signal subtraction (same as Figure S6D)
76,838 particles
3.0 Å
full open ribosome-bound reconstruction after postprocessing procedure (b-factor -76.3)
76,838 particles
3.0 Å
60S-subtracted open ribosome-bound reconstruction after postprocessing procedure (b-factor -10)
76,838 particles
6.49 Å
80S-subtracted open ribosome-bound reconstructionafter postprocessing procedure (b-factor -210.6)
60S ribosome signal subtraction, masked 3D auto-refinement
revert signal subtraction, masked 3D auto-refinement

Figure S7

Table S1. Cryo electron microscopy data collection summary, processing statistics and model quality indicators (related to Figures 1, 4, 5 and 6)

Cryo electron microscopy data collection					
Microscope	FEI Titan Krios GII				
Voltage (kV)	300				
Camera	Gatan K3-Summit				
Energy Filter	Gatan Quantum-LS (GIF)				
Pixel size (Å/pix)	1.094		0.851		
Preset target global defocus range (µm)	0.6 - 2.4				
3D reconstruction	**apo closed *H.s.* SKI**	**apo open *H.s.* SKI**	**RNA bound closed *H.s.* SKI**	**ribosome bound closed *H.s.* SKI**	**ribosome bound open *H.s.* SKI**
Number of movies	11,079		11,413	15,073	21,212
Exposure per sec (e^-/Å^2/s) /total exposure (e^-/Å^2)	11.86/47.44		22.77/68.31	11.16/55.8	11.27/67.62
Number of frames/movie	40		30	35	40
Initially selected particle candidates	4,400,241		6,036,405	1,601,273	3,095,397
Final number of particles	84,591	154,135	144,441	51,048	76,838
Resolution $_{\text{FSC independent halfmaps}}$ (Å)[a]	3.7	3.8	3.1	3.6	6.5
Local resolution range (Å)	3.3-15.8	3.4-13.1	2.8-12.6	3.1-15.6	4.6-10.7
Sharpening B-factor determined/applied (Å^2)	-88.1/-88.1	-145.3/-145.3	-52.3/-52.3	-73.6/-25	-210.6/-210.6
EMDB accession number	EMD-13923	EMD-13925	EMD-13927	EMD-13928	EMD-13929

Table S1 - continued.

Refinement	**apo closed *H.s.* SKI**	**apo open *H.s.* SKI**	**RNA bound closed *H.s.* SKI**	**ribosome bound closed *H.s.* SKI**	**ribosome bound open *H.s.* SKI**
PDB code	7QDR	7QDS	7QDY	7QDZ	7QE0
No atoms	22,827	13,798	22,933	22,598	7,619
Residues (protein)	2,991	1,771	2,991	2,924	949
Residues (RNA)	-	-	6	6	9
CC_{box}, CC_{mask}, CC_{volume}[b]	0.81, 0.86, 0.85	0.80, 0.82, 0.81	0.77, 0.80, 0.77	0.86, 0.81, 0.79	0.87, 0.74, 0.73
Resolution $_{\text{FSC map vs. model@0.143}}$ (Å)[b]	3.6	3.3	2.7	3.0	4.0
r.m.s. deviations					
Bond lengths (Å)	0.006	0.005	0.009	0.007	0.004
Bond angles (°)	0.819	0.852	1.101	0.969	0.998
Ramachandran favored (%)	94.25	94.32	94.39	95.05	96.19
Ramachandran allowed (%)	5.75	5.68	5.61	4.95	3.81
Ramachandran disallowed (%)	0.00	0.00	0.00	0.00	0.00
MolProbity score	1.99	2.04	1.96	2.09	2.07
Clash score	12.26	14.02	11.49	17.6	20.94

[a]according to the Fourier Shell Correlation (FSC) cut-off criterion of 0.143 defined in (Rosenthal and Henderson, 2003)
[b]according to the map-vs.-model Correlation Coefficient definitions in (Afonine et al., 2018)

Table S2. Kinetic parameters of hSKI ATP hydrolysis derived according to Michaelis-Menten (related to Figure 4A)

	hSKI-WT	hSKI-Δarch	hSKI-Δwedge	hSKI-WT (no RNA)	hSKI-DEAD*	hSKI-THES
V_{max} (μM/s)	0.03427	0.04478	0.02990	0.002387	N/A	0.0009766
K_m (μM)	149.4	121.5	190.5	582.2	N/A	-2.574
k_{cat} (s^{-1})	0.6853	0.8957	0.5981	0.04775	N/A	0.01953
R^2	0.9817	0.9871	0.9822	0.2016	N/A	0.1477

*The hSKI-DEAD data could not be reconciled with the Michaelis-Menten equation. No kinetic parameters were derived (N/A, not applicable).

3.2 Paper 2

Kowalinski E., Kögel A., Ebert J., Reichelt P., Stegmann E., Habermann B. and Conti E. (2016). Structure of a Cytoplasmic 11-Subunit RNA Exosome Complex. Molecular Cell, 63(1), 125-134.

Article

Molecular Cell

Structure of a Cytoplasmic 11-Subunit RNA Exosome Complex

Graphical Abstract

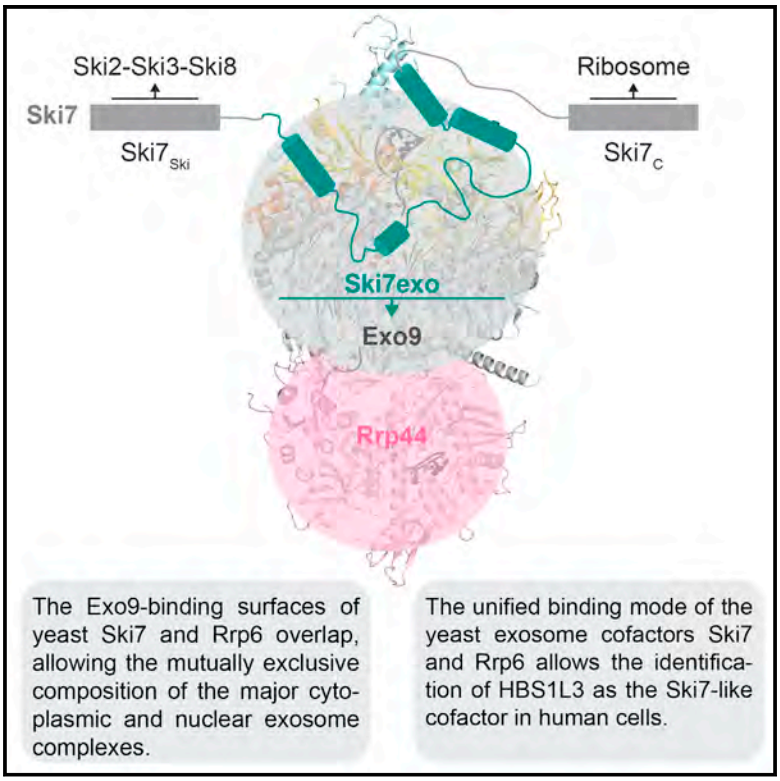

Highlights

- The yeast exosome binds Ski7 with low nanomolar affinity and extensive interactions
- The Ski7 exosome-binding domain folds upon recognizing Csl4, Mtr3, and Rrp43 subunits
- Ski7 and Rrp6 lack sequence homology but form a similar interface with the exosome
- The exosome interface residues of yeast Ski7 are conserved in human Hbs1L isoform 3

Authors

Eva Kowalinski, Alexander Kögel, Judith Ebert, Peter Reichelt, Elisabeth Stegmann, Bianca Habermann, Elena Conti

Correspondence

conti@biochem.mpg.de

In Brief

Kowalinski et al. (2016) show that the yeast exosome core complex recognizes the cytoplasmic cofactor Ski7 and the nuclear cofactor Rrp6 similarly. Through structural analyses, they identify a splice variant of HSB1-Like as the long-sought Ski7-like exosome binding cofactor in humans.

Accession Numbers

5JEA

Kowalinski et al., 2016, Molecular Cell *63*, 125–134
July 7, 2016
http://dx.doi.org/10.1016/j.molcel.2016.05.028

Molecular Cell
Article

Structure of a Cytoplasmic 11-Subunit RNA Exosome Complex

Eva Kowalinski,[1] Alexander Kögel,[1] Judith Ebert,[1] Peter Reichelt,[1] Elisabeth Stegmann,[1] Bianca Habermann,[2] and Elena Conti[1,*]
[1]Department of Structural Cell Biology
[2]Computational Biology
Max Planck Institute of Biochemistry, Am Klopferspitz 18, 82152 Martinsried, Germany
*Correspondence: conti@biochem.mpg.de
http://dx.doi.org/10.1016/j.molcel.2016.05.028

SUMMARY

The RNA exosome complex associates with nuclear and cytoplasmic cofactors to mediate the decay, surveillance, or processing of a wide variety of transcripts. In the cytoplasm, the conserved core of the exosome (Exo_{10}) functions together with the conserved Ski complex. The interaction of *S. cerevisiae* Exo_{10} and Ski is not direct but requires a bridging cofactor, Ski7. Here, we report the 2.65 Å resolution structure of *S. cerevisiae* Exo_{10} bound to the interacting domain of Ski7. Extensive hydrophobic interactions rationalize the high affinity and stability of this complex, pointing to Ski7 as a constitutive component of the cytosolic exosome. Despite the absence of sequence homology, cytoplasmic Ski7 and nuclear Rrp6 bind Exo_{10} using similar surfaces and recognition motifs. Knowledge of the interacting residues in the yeast complexes allowed us to identify a splice variant of human HBS1-Like as a Ski7-like exosome-binding protein, revealing the evolutionary conservation of this cytoplasmic cofactor.

INTRODUCTION

The eukaryotic RNA exosome is a conserved ribonuclease complex that controls the quantity and quality of a large number of RNAs. Exosome-mediated RNA degradation leads to the elimination of nuclear and cytoplasmic transcripts in turnover and quality control pathways or to partial trimming of RNA precursors in processing pathways (reviewed in Chlebowski et al., 2013; Houseley et al., 2006; Lebreton and Séraphin, 2008; Lebreton et al., 2008; Lykke-Andersen et al., 2009; Schaeffer et al., 2011). The core complex of the RNA exosome was originally discovered from genetic and biochemical analyses in budding yeast (Mitchell et al., 1997) and has since been characterized at the molecular and structural level (reviewed in Januszyk and Lima, 2014; Makino et al., 2013). Orthologs have also been identified in other eukaryotes and have been linked to Mendelian diseases in the human population (Allmang et al., 1999; Fabre and Badens, 2014).

The yeast exosome core complex is formed by ten different proteins. Only a single subunit (Rrp44, also known as Dis3) is catalytically active (Dziembowski et al., 2007; Liu et al., 2006). The other nine core subunits (Exo_9) form a cylindrical structure that threads RNA substrates to the Rrp44 exoribonuclease site (Bonneau et al., 2009; Liu et al., 2006; Makino et al., 2013; Wasmuth et al., 2014). Yeast Exo_{10} is present in the nucleus as well as in the cytoplasm but binds compartment-specific cofactors. In the nucleus, the exosome associates with an additional ribonuclease complex (Rrp6-Rrp47), an RNA helicase (Mtr4), and a small protein (Mpp6) to form a 14-subunit assembly (Butler and Mitchell, 2010; Schuch et al., 2014). In the cytoplasm, the exosome functions together with the Ski2-Ski3-Ski8-Ski8 (Ski) complex, a tetrameric assembly centered at an Mtr4-like RNA helicase (Ski2) (Anderson and Parker, 1998; Brown et al., 2000; Halbach et al., 2013). Orthologs of these exosome cofactors are well conserved in eukaryotes (Schilders et al., 2007; Butler and Mitchell, 2010; Schaeffer et al., 2011), and several are mutated in human diseases (reviewed in Fabre and Badens, 2014; Staals and Pruijn, 2010).

An additional cofactor, Ski7, bridges the interaction between the exosome and Ski complexes in *S. cerevisiae* (Araki et al., 2001; Halbach et al., 2013; van Hoof et al., 2000; Wang et al., 2005). The N-terminal exosome-binding and Ski-binding domains of Ski7 are required for all known exosome functions in the cytoplasm, including mRNA turnover and quality-control pathways (Araki et al., 2001; Schaeffer et al., 2011; van Hoof et al., 2002. The C-terminal GTPase-like domain of Ski7 has instead a specific role in nonstop decay (NSD) (van Hoof et al., 2002). NSD is one of the quality-control pathways that monitors the process of mRNA translation: it eliminates defective transcripts where the absence of in-frame termination codons causes ribosomes to stall upon translating the 3′ poly(A) tail (reviewed in Inada, 2013; Klauer and van Hoof, 2012; Lykke-Andersen and Bennett, 2014; Shoemaker and Green, 2012). *S. cerevisiae* Ski7 is a paralogue of the ribosome recycling factor Hbs1. Hbs1 functions in no-go decay (NGD), another translational quality-control pathway that targets and degrades transcripts with ribosomes stalled in the coding region or in the 3′ untranslated region (Doma and Parker, 2006; Guydosh and Green, 2014; and reviewed in Inada, 2013; Lykke-Andersen and Bennett, 2014; Shoemaker and Green, 2012). Yeast Hbs1 and Dom34 have also been recently implicated in NSD (Tsuboi et al., 2012).

Molecular Cell *63*, 125–134, July 7, 2016

The *SKI7* and *HBS1* paralogous genes originated from an ancestral genome duplication event in budding yeast (Marshall et al., 2013). The Ski7 and Hbs1 proteins comprise a similar translational GTPase-like domain (Kowalinski et al., 2015) and are expected to share similarities in recognizing stalled ribosomes (van Hoof et al., 2002). However, they diverge in their activities (GTP binding versus GTP hydrolysis), mRNA targets (nonstop versus no-go mRNAs), and interacting proteins (exosome-Ski versus Dom34). Another conspicuous difference is that Hbs1 is conserved across eukaryotes while Ski7 orthologs have only been identified in a subset of fungal species (Marshall et al., 2013). Although Ski7 is currently assumed to be a specialized protein in yeasts, several observations argue against such evolutionary restriction. First, given that the exosome and Ski complexes are conserved from yeast to human, it is reasonable to expect that a Ski7-like cofactor would bridge their interaction also in higher eukaryotes. Second, NSD is not limited to yeast but also exists in mammalian cells, where it depends on HBS1-DOM34 as well as exosome and SKI proteins (Saito et al., 2013). In this work, we set out to visualize how the yeast exosome interacts with Ski7, and based on the structural information, we identified isoform 3 of HBS1L as the human counterpart of Ski7.

RESULTS AND DISCUSSION

Identification and Structure Determination of a Minimal Exosome-Ski7 Complex

Ski7 mediates the interaction between the RNA degrading exosome and the Ski complex in vivo (Araki et al., 2001) and in vitro (see Figure S1A available online). Coimmunoprecipitation studies from yeast strains expressing different tagged versions of Ski7 have identified two separate domains in the N-terminal region as responsible for binding the Ski and exosome complexes (Araki et al., 2001). We recapitulated the interactions in vitro with purified recombinant proteins and more precisely defined the domain boundaries within Ski7. Using a combination of secondary structure prediction, limited proteolysis, and pull-down assays (Figure S1B), we mapped the Ski2-Ski3-Ski8-interacting domain of Ski7 at residues 1–105 and the Exo_9-interacting domain at residues 116–235 (Figure 1A). Both domains are predicted to contain sparse secondary structure elements.

We proceeded to crystallize a yeast exosome core bound to the interacting domain of Ski7. To this end, we used a catalytically inactive 10-subunit exosome complex where the Rrp44 subunit had been mutated to impair the exonuclease and endonuclease active sites (D551N, D171N substitutions), hereafter referred to as Exo_{10} (Bonneau et al., 2009; Liu et al., 2006; Makino et al., 2013). Based on the approach we have previously used for crystallizing an exosome core bound to the nuclear cofactor Rrp6 (Makino et al., 2013), we added an RNA substrate featuring a tetra-loop at the 5′ end and a single-stranded extension of 28 ribonucleotides at the 3′ end ($U_{loop-28}$). The Exo_{10}-$U_{loop-28}$ complex bound to Ski7 residues 116–235 yielded crystals, but the hair-like needles were unsuitable for diffraction studies. To promote additional crystal packing interactions, we followed a protein engineering strategy (Chun et al., 2012) and fused T4 lysozyme (T4L) to the C terminus of the construct. $Ski7_{116-235}$-T4L yielded thicker needles of the complex that diffracted to 4.2 Å resolution. Structure determination by molecular replacement and model building suggested that truncating the C terminus of Ski7 and thus shortening the linker to T4L could improve crystal quality (Figure S1C). Indeed, the corresponding exosome complex with a truncated Ski7 domain (residues 116–225, $Ski7_{exo}$) fused to T4L showed improved diffraction properties (Figure 1A). The crystal structure of *S. cerevisiae* Exo_{10}-$Ski7_{exo}$T4L-$U_{loop-28}$ (hereafter referred to as Exo_{10}-Ski7-RNA) was determined and refined to 2.65 Å resolution with R_{free} of 25.9% R_{factor} of 21.5% and good stereochemistry (Figure 1B and Table 1).

Exo_{10}–Ski7–RNA Complex: The Exosome Core

The 10-subunit exosome core in the Ski7-bound complex is overall similar to that observed in Rrp6-bound complexes (Makino et al., 2013; 2015; Wasmuth et al., 2014) (Figures 1B and S2A). In particular, the ring formed by the six RNase PH-like proteins (Rrp41, Rrp45, Rrp46, Rrp43, Mtr3, and Rrp42) superposes well with that observed in other exosome structures (root-mean-square deviation [rmsd] of less than 1.22 Å over all α-carbon atoms) (Makino et al., 2015; 2013; Wasmuth et al., 2014). At the top of the RNase PH-like subunits, the three so-called cap proteins (Rrp4, Rrp40, and Csl4) form an upper ring that closes around part of the RNA 5′ tetra-loop (Makino et al., 2013). Near the bottom of the RNase PH-like subunits, the Rrp44 nuclease is in a closed conformation reminiscent of that found in an exosome complex crystallized before in the presence of a long RNA in the central channel (Makino et al., 2013) (Figure S2A).

Despite the overall similarity with previous structures, there are several differences. Starting from the top of the complex, a loop of Csl4 (residues 158–200) undergoes a large conformational change when compared to Rrp6-bound structures (Makino et al., 2013, 2015; Wasmuth et al., 2014): instead of protruding from the outer surface of the exosome, it lines the inner cavity of the complex, where it approaches the RNA in the central channel (Figures 1C and S2B). The outward facing conformation of this loop observed in Rrp6-bound complexes would not be compatible with the Ski7-bound complex because of steric clashes with the N terminus of Rrp43 (Figure S2C). However, whether this loop influences the specific activity of the nuclear and cytoplasmic exosomes in *S. cerevisiae* is currently unclear, as we could not detect obvious changes with the assays and substrates we have tested.

Another significant difference in comparison to earlier structures is that one of the three OB-fold domains of Rrp44 (CSD1) is shifted away from the RNase PH-like ring by about 10 Å. In turn, the opposite loops from Rrp42 and Rrp43 are disordered (residues 159–169 and 250–270, respectively). The alternative conformation of CSD1 changes the shape of the internal RNA-binding channel in this part of the complex, and in parallel the ribonucleotide chain also deviates in its path (Figures 1D and S2D). Although the movement of CSD1 appears to be due to crystal packing rather than to Ski7 binding, it highlights the conformational plasticity of the Rrp44 subunit and of how RNA substrates can thread through it. Interestingly, such a movement

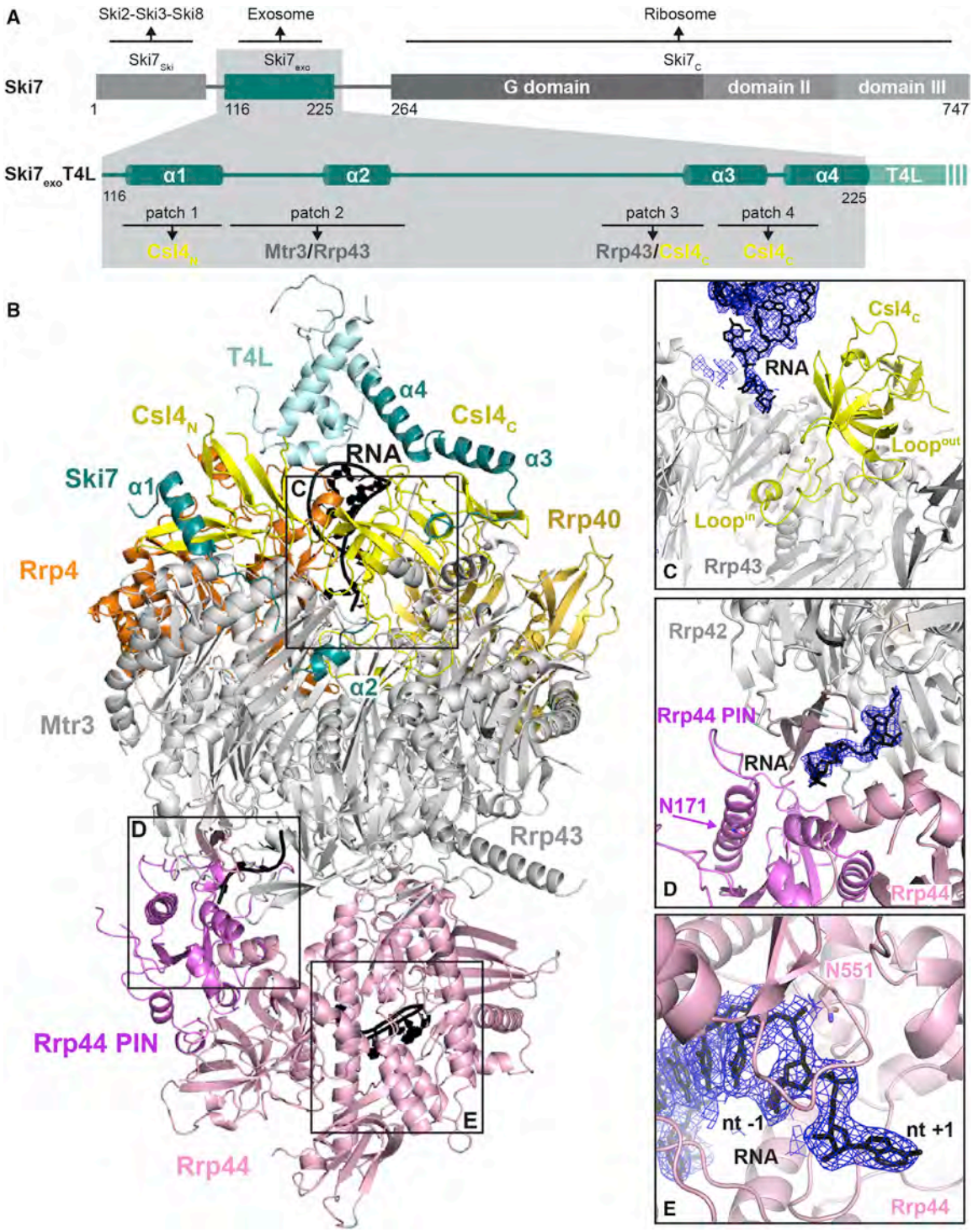

Figure 1. The Atomic Structure of a *S. cerevisiae* Exo_{10}–$Ski7_{exo}$–RNA Complex

(A) The overall domain structure of Ski7 is shown on top, together with its binding partners. The region of the molecule in the present structure ($Ski7_{exo}$) is shown in teal. At the bottom is a zoom-in view with the secondary structure elements of $Ski7_{exo}$ followed by the C-terminal T4 lysozyme (T4L). The main exosome-binding patches of $Ski7_{exo}$ are annotated together with the Exo_9 subunits they bind to.

(B) Overview of the structure of Exo_{10}–$Ski7_{exo}$–RNA. Cartoon representation of the exosome with Rrp44 in light pink (Rrp44 PIN domain in violet), Csl4, Rrp4, and Rrp40 in yellow, orange, and champagne, respectively; the RNase PH ring in gray; and RNA in black. $Ski7_{exo}$T4L is shown with $Ski7_{exo}$ in teal and T4L in light teal.

(C–E) Zoom-in views of three portions of the structure that are indicated in boxes in (B). Representation and colors are as in Figure 1B. RNA is in stick representation. Electron density $2F_o$–F_c map is shown in blue mesh around the RNA (contoured at 0.9 σ). See also Figure S2.

Table 1. X-Ray Data Collection and Refinement Statistics

Dataset	Exo_{10}-Ski7-RNA
Wavelength (Å)	0.97852
Resolution range (Å)	66.69–2.65 (2.75–2.65)
Space group	$P\ 2_12_12_1$
a, b, c (Å)	106.08, 182.53, 250.55
α, β, γ (°)	90, 90, 90
Total reflections	2,802,181 (233,628)
Unique reflections	272,923 (28,614)
Multiplicity	10.26 (8.16)
Completeness (%)	100.0 (99.9)
Mean I/sigma (I)	7.33 (1.14)
R_{merge} (%)	21.1 (176.2)
CC(1/2)	99.0 (36.2)
Refinement	
R work (%)	21.52 (33.39)
R free (%)	25.86 (36.24)
Protein residues	3,446
RNA residues	27
Ligands	7 × MPD, 1 × Zn^{2+}, 4 × Na^{+}
Water	134
Stereochemistry	
Rms (bonds)	0.004
Rms (angles)	0.77
Ramachandran favored (%)	97
Ramachandran outliers (%)	0.27

Values for the highest-resolution shell are given in parentheses. MPD, 2-Methyl-2,4-pentanediol. See also Figure S1.

might also open an alternative RNA path from the central channel to the endonuclease site of the PIN domain (Figures 1D and S2D). This potential RNA path would be consistent with previous biochemical data supporting the presence of a channel-dependent path to the exosome endonuclease site (Drazkowska et al., 2013; Wasmuth and Lima, 2012).

Finally, a difference with previous structures is observed at the RNA 3′ end, where density for one additional ribonucleotide is present (Figures 1E and S2E). It appears that the RNA substrate continues with one nucleotide beyond the inactive exonuclease site (D551N), toward the solvent. This position likely reflects the exit route taken by the cleaved 3′ end nucleotide that would be produced and expelled by a wild-type active complex.

Exo_{10}–Ski7–RNA Complex: The Cytoplasmic Cofactor Ski7

The N-terminal region of Ski7 is natively unfolded in solution (Figure S3A) but adopts well-defined secondary structure elements when bound to Exo_{10} (Figure 1B). $Ski7_{exo}$ folds into four helices (α1–α4) connected by extended linkers. Most of the polypeptide chain has well-ordered electron density (Figure S3B), with the exception of residues 142–147 and residues 159–179 in the linkers connecting $Ski7_{exo}$ helices α1-α2 and α2-α3, respectively. $Ski7_{exo}$ binds at the upper half of the exosome core, where it interacts with the cap protein Csl4 and with the RNase PH-like proteins Mtr3 and Rrp43 (Figure 2A). In the structure, $Ski7_{exo}$ helix α4 directly continues into the T4L molecule that was artificially fused to it for crystallization purposes. T4L is partially ordered at the top of the exosome and interacts with the cap protein Rrp4. With hindsight, the T4L engineering strategy not only contributed an additional crystal contact but also likely stabilized the cap proteins via a contact to Rrp4 (Figure S1C). The position of T4L in the structure is far from Ski7-exosome interaction sites (Figures 1B and 2A), and as such it will not be discussed further.

Ski7 Wraps around Csl4, Rrp43, and Mtr3 with Extensive Interactions

$Ski7_{exo}$ wraps around the exosome covering about 3,150 $Å^2$ of its accessible surface area (1,625 $Å^2$ of Csl4, 870 $Å^2$ of Rrp43, and 660 $Å^2$ of Mtr3), as calculated with the PISA server (Krissinel and Henrick, 2007). Starting from the N terminus, the α1 helix of $Ski7_{exo}$ docks into a conserved hydrophobic pocket present on the side of the Csl4 N-terminal domain (patch 1) (Figure 2B). Here, hydrophobic side chains of Ski7 ($Leu121^{Ski7}$, $Trp125^{Ski7}$, $Ile128^{Ski7}$, $Met131^{Ski7}$) engage in van der Waals interactions with Csl4 (Figure 2B). Following the first helix, an extended segment with hydrophobic residues (e.g., $Tyr134^{Ski7}$) stretches over the surface of Mtr3, connecting to the second helix (Figure 2B). The short α2 helix of $Ski7_{exo}$ wedges into a hydrophobic cleft formed at the junction between Mtr3 and Rrp43 (patch 2) (Figure 2C). Here, the interaction is mediated by a cluster of apolar side chains (including $Phe149^{Ski7}$, $Phe151^{Ski7}$, $Phe154^{Ski7}$, $Ile155^{Ski7}$, $Ile156^{Ski7}$) (Figure 2C). After a disordered segment, the linker connecting to the third helix coils around Rrp43 and projects hydrophobic residues ($Leu186^{Ski7}$, $Leu187^{Ski7}$, $Ile189^{Ski7}$, $Phe190^{Ski7}$, $Pro192^{Ski7}$) into a cleft formed at the junction with the Csl4 C-terminal domain (patch 3) (Figure 2D). Finally, $Ski7_{exo}$ helix α3 and the tip of helix α4 bind onto a conserved hydrophobic surface at the side of the Csl4 C-terminal domain (via $Leu195^{Ski7}$, $Ala203^{Ski7}$, $Phe207^{Ski7}$, $Pro212^{Ski7}$) (patch 4) (Figure 2E).

The interaction between Ski7 and the exosome is overall dominated by hydrophobic contacts, but there are additional polar interactions (e.g., $Asn132^{Ski7}$ at patch 1, $Thr152^{Ski7}$ at patch 2, $Glu185^{Ski7}$ at patch 3 and $Asp213^{Ski7}$, $Asp214^{Ski7}$, $Gln217^{Ski7}$ at patch 4). With hindsight, the recently reported crosslinking-mass spectrometry data on the Ski7-exosome interaction support well-ordered parts of the complex structure (crosslinks between $Lys180^{Ski7}$ and $Lys45^{Rrp43}$, and $Lys181^{Ski7}$ and $Lys45^{Rrp43}$) (Figure S3C) (Shi et al., 2015). Multiple crosslinks observed beyond the boundaries of our crystallization construct might have been caused by the collapse of flexible regions of Ski7 upon crosslinking treatment, but are consistent with the overall directionality of the Ski7 polypeptide on the exosome.

Effect of Specific Structure-Based Mutations In Vitro and In Vivo

Based on the structural analysis, we engineered a series of substitutions at the largest interaction hotspots of $Ski7_{exo}$ and tested the ability of the mutants to bind the exosome in pull-down assays with purified proteins. Mutations of Ski7 residues at patch 1 (Trp125Asp, Ile128Asp, or $Ski7_{exomut-1}$), patch 2

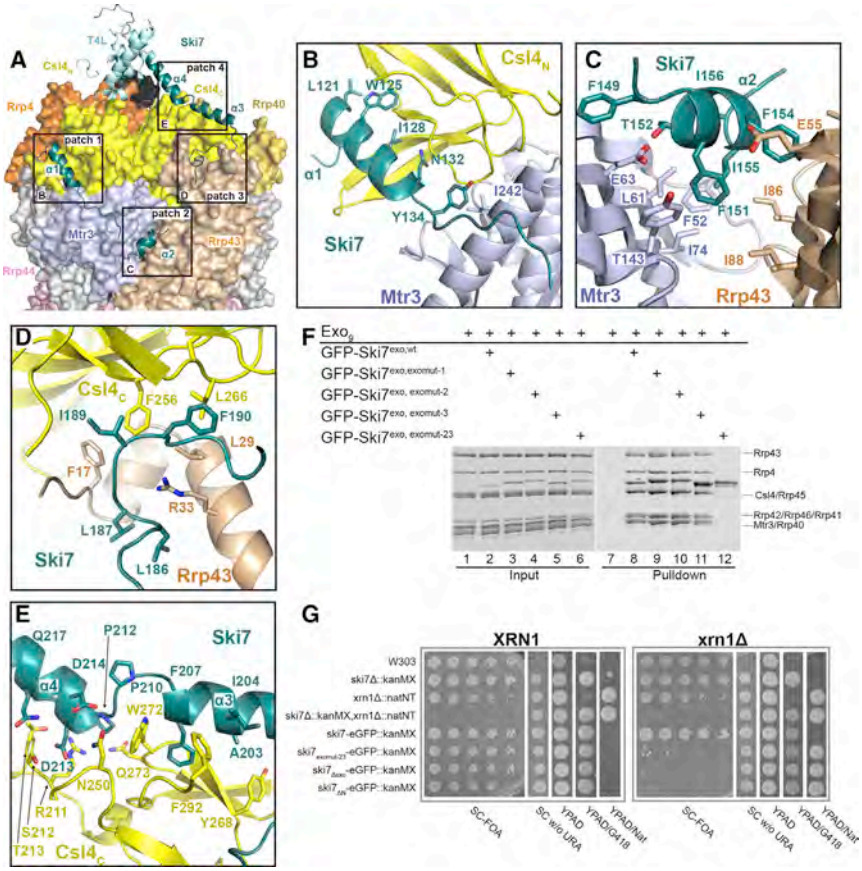

Figure 2. Ski7 Binds the Exosome with an Extensive Interaction Network

(A) The exosome is shown in a surface representation and Ski7$_{exo}$T4L in cartoon representation. Colors are as in Figure 1B, except for Mtr3 (pale blue) and Rrp43 (pale orange).

(B–D). Zoom-in views of the interaction patches 1–4 in cartoon representation, with colors as in Figure 2A. Interacting residues are in stick representation as indicated.

(F) Protein coprecipitations in GFP pull-down assays. The exosome coprecipitates with double or triple mutants of GFP-Ski7 in a single binding patch (lanes 8–11). Only when combining mutants of two patches (Ski7$^{exo,exomut-23}$, lane 12) the interaction lost. See also Figure S3D.

(G) Growth assay of wild-type and mutant yeast strains. Endogenous *SKI7* was replaced by wild-type or mutant *SKI7-EGFP* fusions in a strain where endogenous *XRN1* was present (left panel) or deleted (right panel). All strains (except wild-type) also carried an YCplac33[*XRN1,URA3*] rescue vector. For the growth assay, cells were grown to early exponential phase and spotted in serial dilutions onto 5-fluoroorotic acid (5-FOA) medium or control plates. Medium containing 5-FOA selects for cells that have lost the YCplac33[*XRN1,URA3*] rescue vector. Deletions of either Ski7$_{exo}$ (row 7) or Ski7$_N$ (row 8) as well as the Ski7$^{exo,exomut-23}$ mutant (row 6) had a lethal effect. Controls: SC w/o URA, presence of rescue shuffle vector carrying *wt XRN1*; YPAD, general growth control on nonselective/permissive media; YPAD/G418, maker associated with Ski7 genomic integration; YPAD/Nat marker associated with *XRN1* knockout. For expression controls and yeast strains, see Figure S3E and Table S1. SC, synthetic complete medium; URA, uracil. See also Figures S3 and S4.

(Phe149Asp, Phe151Asp, Phe154Asp, or Ski7$_{exomut-2}$), or patch 3 (Ile189Asp, Phe190Asp or Ski7$_{exomut-3}$) were not sufficient to individually impair the interaction with Exo$_9$ (Figure 2F, lanes 8–11). Exo$_9$ binding was disrupted in vitro only when impairing two interaction hotspots simultaneously (Ski7$_{exomut-23}$, with 5 combined mutations at patches 2 and 3) (Figure 2F, lane 12). Similarly mutating a binding surface in patch 4 on Csl4 (Trp272Glu, Phe292Glu, Asn250Ala or Csl4$_{exomut-4}$) did only disrupt interaction in combination with one of the Ski7 mutations (Figure S3D). Albeit qualitative, these assays suggested the presence of a high-affinity interaction between Ski7 and the exosome. Indeed, quantitative measurements by microscale thermophoresis (MST) revealed a dissociation constant in the low nanomolar range (K_d ~5 nM, Figure S4A). When impairing a single patch in Ski7$_{exomut-1}$, the binding affinity decreased 10-fold but remained relatively high (K_d 50 nM, Figure S4A).

Next, we tested the effect of Ski7 mutants in complementation assays in yeast. We integrated wild-type *SKI7*, *ski7*$_{ΔN}$, *ski7*$_{Δexo}$ (lacking the entire exosome-binding domain), or *ski7*$_{mut-23}$ (with the five substitutions at patches 2 and 3) as C-terminal eGFP fusions at the endogenous locus in a W303 diploid yeast strain in which one of the chromosomal copies of *SKI7* had been deleted. To assess growth defects in the absence of *XRN1*, we used an *XRN1/xrn1Δ* diploid strain that we had previously generated (Halbach et al., 2013). After sporulation and tetrad dissection, haploids were mated accordingly to generate *ski7Δ/xrn1Δ*, *ski7*$_{Δexo}$*-eGFP/xrn1Δ*, *ski7ΔN/xrn1Δ*, *ski7exo*$_{mut-23}$*-eGFP*/xrn1Δ, and *SKI7-eGFP/xrn1Δ* strains (Figure 2G; Table S1). Consistent with previous reports, disruption of *SKI7* and *XRN1* was synthetically lethal (*ski7Δ/xrn1Δ*, Figure 2G) (van Hoof et al., 2000). In the *ski7*$_{Δexo}$*-eGFP/xrn1Δ*, *ski7ΔN/xrn1Δ* and *ski7*$_{mut-23}$*-eGFP/xrn1*Δ strain, the mutant proteins were expressed at levels comparable to wild-type Ski7-eGFP as judged by western blot (Figure S4B), but cells showed synthetic growth defects (Figure 2G). These data are consistent with the notion that the high-affinity interactions between yeast Ski7 and the exosome are important for function in vivo.

Ski7 and Rrp6 Share a Common Interaction Surface on the Exosome Core

We analyzed the Ski7-bound and Rrp6-bound structures to compare how the cytoplasmic and nuclear cofactors recognize the core complex. Ski7$_{exo}$ and the C-terminal exosome-binding domain of Rrp6 (Rrp6$_C$ or Rrp6$_{exo}$) do not share apparent similarity at the sequence level (Figure 3A). However, they adopt a similar topology of secondary structure elements and engage analogous surfaces of Csl4, Mtr3, and Rrp43 (Figure 3A). In particular, Ski7$_{exo}$ and Rrp6$_{exo}$ bind at the patch 1 and patch 2

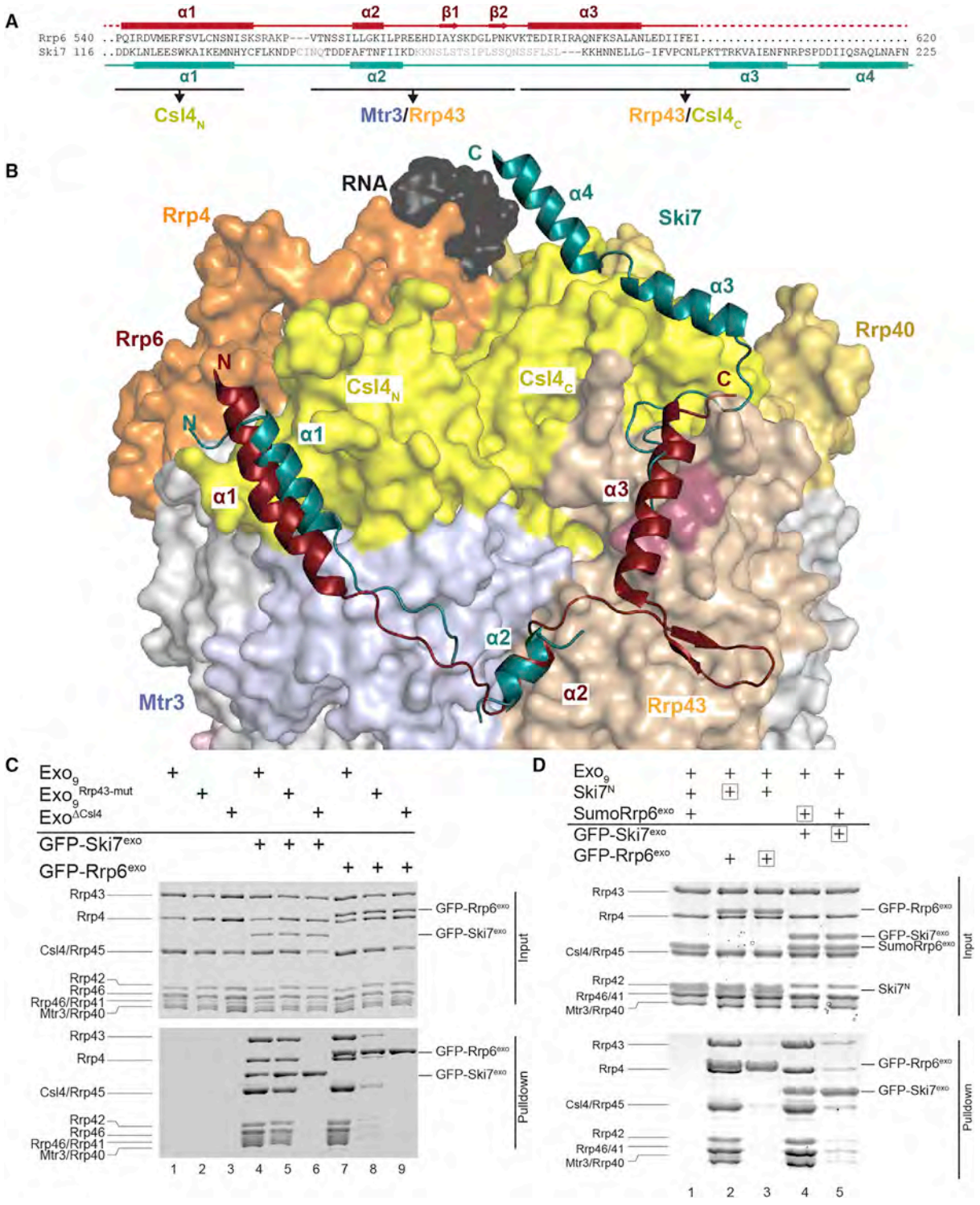

Figure 3. Ski7 and Rrp6 Share Similar Exosome-Binding Surfaces

(A) Topology-based sequence alignment of $Rrp6_{exo}$ and $Ski7_{exo}$. Structural elements of Rrp6 are in red and of Ski7 in teal. Residues not visible in the Ski7 structure are in gray. The corresponding exosome-interacting proteins are annotated.

(B) Comparison of Ski7 and Rrp6 binding to the exosome. Top view on the superposition of the nuclear (PDB: 5c0w) and cytosolic exosome (superposition based on Mtr3, yielding an optimal fit for $Ski7_{exo}$ and $Rrp6_{exo}$). The cytosolic exosome is shown in surface representation with colors as in Figure 2A. The Rrp43 surface residues mutated in $Exo9_{,Rrp43\text{-}mut}$ are in pale red. Ski7 and Rrp6 are displayed in cartoon representation. Rrp6 is in red. See also Figure S5.

(legend continued on next page)

surfaces of the exosome with remarkably similar interactions (Figure 3B). For example, Phe549^{Rrp6} and Trp125^{Ski7} occupy the equivalent position at patch 1, and Leu572^{Rrp6} and Phe151^{Ski7} occupy the same position at patch 2 (Figures S5A and S5B). After patch 2, the mode of interaction diverges. In the case of Rrp6$_{exo}$, the polypeptide chain folds into a β-hairpin that extends toward the outer surface of Rrp43, as it does not have structural elements equivalent to Ski7$_{exo}$ helices α3 and α4 (Figure 3A).

We evaluated the similarities and differences of Ski7 and Rrp6 binding on the exosome surface. Csl4 provides an important anchoring point for both cofactors (Figure 3B). Indeed, in vitro pull-down assays with GFP-tagged Ski7$_{exo}$ or GFP-tagged Rrp6$_{exo}$ showed that neither the cytoplasmic nor the nuclear cofactor coprecipitated with an exosome complex lacking Csl4 (Exo$_{\Delta Csl4}$) (Figure 3C, lanes 6 and 9, respectively). The C-terminal domain of Csl4 is involved more specifically in the interaction with Ski7 (Figure 3B). Consistently, in the *ski4-1* allele, a single-point mutation (Gly253Glu) in the C-terminal domain of Csl4 has been shown to severely reduce the association with Ski7 in vivo (van Hoof et al., 2002) and to affect mRNA turnover (van Hoof et al., 2000). Conversely, the structural analysis indicates that a surface of Rrp43 is involved in the interaction with Rrp6, but not with Ski7 (Figures 3B and S5C). We engineered an Rrp43 mutant with three substitutions at this surface (Leu37Asp^{Rrp43}, Ile39Asp^{Rrp43}, Leu43Asp^{Rrp43}, or Rrp43$_{mut}$ mutant) (Figures 3B and S5C), reconstituted the corresponding exosome complex (Exo$_{9,Rrp43\text{-}mut}$), and tested it in pull-down assays with GFP-tagged Rrp6$_{exo}$ or GFP-tagged Ski7$_{exo}$. In these assays, the interaction of the mutant exosome with the nuclear cofactor was strongly reduced, while the cytoplasmic cofactor was not significantly affected (Figure 3C, lanes 5 and 8, respectively).

Given the overlapping binding sites of Ski7 and Rrp6, we assessed their competition for exosome binding. In devising the pull-down assays, we took into account the high affinity with which Exo$_9$ binds not only Ski7$_{exo}$ (K_d ~5 nM, Figure S4) but also Rrp6$_{exo}$ (K_d ~10 nM, Figure S4). We preincubated Exo$_9$ with either Ski7$_{exo}$ or Rrp6$_{exo}$ and then added the corresponding GFP-tagged competitor (GFP-Rrp6$_{exo}$ or GFP-Ski7$_{exo}$, respectively). In the GFP pull-down assays, GFP-Rrp6$_{exo}$ was not able to displace bound Ski7$_{exo}$ from the complex (Figure 3D, lane 3), while GFP-Ski7$_{exo}$ could partially displace Rrp6$_{exo}$ (Figure 3D, lane 5), in line with the slightly higher exosome-binding affinity of Ski7$_{exo}$ than Rrp6$_{exo}$ (Figure S4A). We then reversed the order of events by incubating Exo$_9$ with the GFP-tagged component first, before adding the untagged competitor. In the GFP pull-down assays, none of the untagged components could displace the tagged competitor (Figure 3D, lanes 2 and 4). We concluded that Ski7$_{exo}$ and Rrp6$_{exo}$ have similar and mutually exclusive binding surfaces on the exosome and that detailed differences in these interfaces can be exploited to selectively dissociate the cofactors from the complex.

HBS1-like Isoform 3 Is a Human Ski7-like Protein

The identification of the exosome-binding residues in Ski7 prompted us to search for the long sought-after ortholog in human cells. In *L. kluyveri* and other fungi that split off from the *S. cerevisiae* branch before genome duplication, a single gene (*HBS1*/*SKI7*) gives rise to separate Hbs1-like and Ski7-like proteins by alternative splicing (Marshall et al., 2013). Interestingly, human HBS1 has been shown to coimmunoprecipitate with human DIS3L and SKI2W in HeLa cells (Saito et al., 2013), but the caveat from these experiments is that the interactions could be indirect.

From the analysis of the NCBI RefSeq sequences, three splice variants are generated from a single *HBS1* gene in human cells (Figure 4A). All three HBS1-Like (HBS1L) isoforms share a similar N-terminal region, encoded by exons 1, 2, and 4. While isoforms 1 and 3 also share the region encoded by exon 3 (residues 37–78), this exon is skipped in isoform 2. The major difference, however, lies in the C-terminal domain. In isoforms 1 and 2 the C-terminal domain is a GTPase-like fold that binds the protein DOM34 (Saito et al., 2013) and that is encoded by skipping exon 5 and starting from exon 6 (to 19). In contrast, isoform 3 contains an unrelated C-terminal domain that is encoded by exon 5 (residues 144–632). Bioinformatic analyses revealed a similarity between the yeast Ski7$_{exo}$ domain and a C-terminal segment of HBS1-like isoform 3 (HBS1L3) (residues 540–632) (Figure 4B). In particular, several residues that mediate the interaction of Ski7 with the patch 1, patch 2, and patch 4 surfaces of the exosome appeared to be conserved in HBS1L3. This analysis suggested the HBS1L3 might bind the human exosome analogously to how Ski7 binds the yeast exosome. We tested this hypothesis using in vitro pull-down assays with purified proteins. We reconstituted human Exo$_9$ and found that indeed it coprecipitated with the GFP-tagged C-terminal segment of human HBS1L3 (HBS1L3$_{exo}$) (Figure 4C, lane 4) and not with GFP-tagged Mtr4$^{\Delta N80\Delta SK}$ (Falk et al., 2014), which was used as negative control. We concluded that HBS1L3 is a human Ski7-like protein in human that is capable of interacting with the human exosome.

Conclusions

The "Superkiller" *SKI* genes were all originally identified from mutations resulting in the overexpression of a killer toxin in virus-infected yeast strains (Toh-E et al., 1978). Two decades later, it has become clear that Ski2, Ski3, and Ski8 form an obligate protein complex in vivo and that Ski7 is not stably associated with it (Brown et al., 2000). However, Ski7 consistently

(C) Pull-down of mutant exosomes on GFP-Ski7 or GFP-Rrp6, respectively. SDS PAGE of a GFP-binder pull-down experiment. Mutation of a hydrophobic patch on Rrp43 does not alter the interaction with Ski7 but weakens binding of Rrp6 (lanes 5 and 8, respectively). Neither Ski7 nor Rrp6 coprecipitates with an exosome lacking Csl4 (Exo$_{\Delta Csl4}$) (lanes 6 and 9).

(D) Competition of Ski7 and Rrp6 binding to the exosome. SDS PAGE of a GFP-binder pull-down experiment. Tagged (1×) and nontagged (4× molar ratio) Ski7 (GFP-Ski7$_{exo}$ and Ski7$_N$) and Rrp6$_{exo}$ (GFP-Sumo-Rrp6$_C$ and Sumo-Rrp6$_C$) constructs were incubated with 1.2× molar excess of exosome complex. Reaction components that are annotated with a box were added 20 min after nonboxed components and before incubation with GFP-binder resin. Rrp6 does not displace bound Ski7 (lane 3), while Ski7 can partially displace Rrp6 (lane 5).

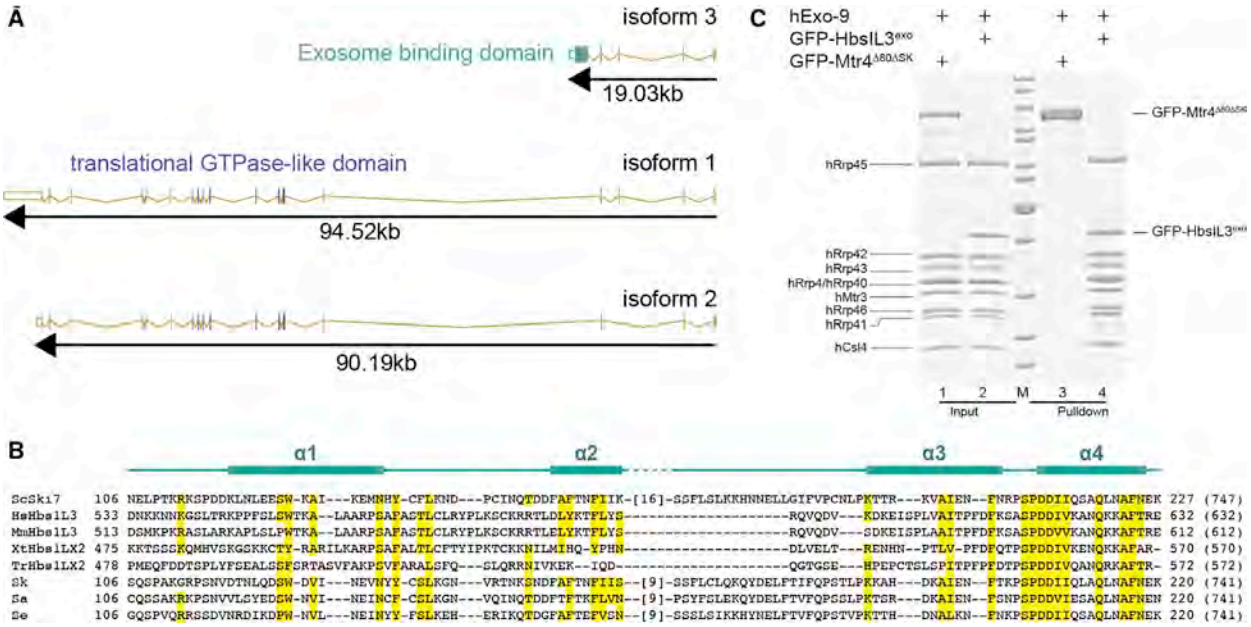

Figure 4. HBS1-Like Isoform 3 Is a Human Ski7-like Protein

(A) Exon-intron structure of human HBS1L. The three verified isoforms are shown. The exosome-binding region (exon 5) and the translational GTPase-like domain (exons 7–13) are indicated in teal and blue, respectively.

(B) Multiple sequence alignment of the exosome-binding region of Ski7 from *S. cerevisiae* and the exosome-binding isoform HBS1L3 from different vertebrates. Structural elements of *Sc*. Ski7 are indicated in teal; conserved residues between Ski7 and HBS1L family members are highlighted in yellow. Abbreviations and accession numbers are as follows: Hs, *Homo sapiens*, NP_001138679; Mm, *Mus musculus*, NP_001138681; Xt, *Xenopus tropicalis*, XP_012818244; Tr, *Takifugu rubripes*, XP_011610307; Sc, *Saccharomyces cerevisiae*, NP_014719; Sk, *Saccharomyces kudriavzevii*, EJT42305; Sa, *Saccharomyces arboricola*, EJS41691; and Se, *Saccharomyces eubayanus*, KOG96583.

(B) Pull-down assay of human exosome with GFP-tagged C terminus of HBS1L3. SDS PAGE of a GFP-binder pull-down experiment. GFP-tagged Mtr4$^{\Delta N80\Delta SK}$ (Falk et al., 2014) was used as negative control.

coimmunoprecipitates and copurifies with endogenous exosome subunits (Dziembowski et al., 2007; van Hoof et al., 2002). Indeed, the interaction of Ski7 with exosome subunits is even more salt resistant than that of Rrp44, an intrinsic subunit of the *S. cerevisiae* core complex (Dziembowski et al., 2007). Our data support the notion that Ski7 is a constitutively bound component of the cytoplasmic yeast exosome: its N-terminal domain binds with low nanomolar affinity in vitro and engages the outer surfaces of the exosome rings with strong interactions. Indeed, impairing a single interaction hotspot is not sufficient to abrogate binding: the concomitant mutation of two interaction hotspots is required to impair binding in vitro and in vivo. Interestingly, the nature of the interactions of the cytoplasmic exosome-Ski7 complex is very similar to that of the nuclear exosome-Rrp6 complex. The similarities in the structures were unexpected, as Ski7 and Rrp6 do not share noticeable homology at the sequence level. Thus, Ski7 and Rrp6 appear to have evolved to exploit the same surface features of the exosome core. We speculate that the mutually exclusive interaction of Ski7 and Rrp6 with the exosome physically separates the binding to the two cofactors and potentially prevents Ski7 from being transported into to the nucleus with Rrp6-bound exosome complexes.

The N-terminal domain of yeast Ski7 does not share noticeable sequence homology with human proteins. Yet, the interacting surfaces on the yeast exosome are conserved in higher eukaryotes. Combining structural information with bioinformatic analysis, we identified the C-terminal domain of human HBS1L3 as a Ski7-like exosome-binding region. HBS1L3 also appears to contain regions with sparse sequence similarity to the Ski-complex-binding domain of yeast Ski7, but future structural studies will be required to understand the molecular mechanisms with which Ski7-like cofactors recognize and recruit the Ski complex. In contrast to the general importance of the exosome-binding and Ski-binding regions of Ski7, the C-terminal translational GTPase-like domain is required solely for the yeast NSD pathway (Araki et al., 2001; van Hoof et al., 2002). HBS1L3 clearly lacks an analogous GTPase-like domain. This domain is instead present in human HBS1L1 and HBS1L2 as well as in yeast Hbs1, whereby it functions in the release of stalled ribosomes in the NGD pathway (Becker et al., 2011; Guydosh and Green, 2014; Matsuda et al., 2014; reviewed in Shoemaker et al., 2010). Our results thus raise a set of questions on whether the different human HBS1L isoforms might have acquired specific roles in mRNA turnover and surveillance. Understanding their detailed functions in the decay of different mRNAs in human cells is an important quest for future studies, not least because of the involvement of cytoplasmic exosome cofactors in human diseases and in the modulation of the immune system (reviewed in Fabre and Badens, 2014; Rigby and Rehwinkel, 2015).

EXPERIMENTAL PROCEDURES

Expression and Purification

S. cerevisiae Exo_9 subunits, Rrp44 (1–1,001, D171N, D551N) and $Rrp6_{exo}$ (518–693) were expressed in *E. coli* and purified with similar protocols as described before (Bonneau et al., 2009; Makino et al., 2013). All Ski7 constructs were expressed in *E. coli* as a fusion protein with an N-terminal His tag and either a thioredoxin polypeptide cleavable with prescission protease (for structural studies) or GFP (for biochemical studies). Ski7 was purified by affinity chromatography followed by ion exchange (heparin column) and size-exclusion chromatography (SEC). The *S. cerevisiae* Exo10 complex was reconstituted as described before (Bonneau et al., 2009; Makino et al., 2013), and after addition of 1.2× molar excess of Ski7 another size-exclusion chromatography was performed on a Superose 6 column (GE Healthcare). *H. sapiens* Exo_9 proteins were expressed and purified similarly to the protocols previously described (Greimann and Lima, 2008). C-terminally GFP-tagged human $HBS1L3_{exo}$ (comprising residues 540–632) was purified via Ni-affinity and after prescission protease aided cleavage of a his-thioredoxin tag, reversely passed through an Ni-affinity column, and subjected to SEC. Detailed protocols are in the Supplemental Information.

Crystallization and Structure Determination

Exo_{10}–Ski7 crystallized at a concentration of 12.5 mg/ml upon the addition of 1.3× molar excess of a stem-loop RNA with sequence CCCCCGAGAGGGG-$G(U)_{27}A$ ($U_{loop\text{-}28}$). The complex (in 20 mM HEPES [pH 7.5], 100 mM NaCl, 2 mM $MgCl_2$, and 5 mM TCEP) crystallized in 27% 2-Methyl-2,4-pentanediol (MPD), 0.1 M 2-(*N*-morpholino)ethanesulfonic acid (MES) (pH 6), and 10 mM $CaCl_2$. Crystals grew typically within 10 days and were cryo-protected (in 32% MPD, 0.1 M MES [pH 6]) and flash-cooled in liquid nitrogen before X-ray exposure. All X-ray diffraction data were collected at 100 K at the Swiss Light Source (SLS) synchrotron in Villigen (Switzerland). The data were processed and scaled with XDS (Kabsch, 2010). The crystals belong to the space group $P2_12_12_1$ and contain one complex in the asymmetric unit. The data processing statistics are summarized in Table 1. The atomic model of Exo_9 (4ifd) was used as a molecular replacement model in PHASER (McCoy et al., 2007). The single domains of Rrp44 and the visible T4L moiety were placed partly manually (as rigid bodies) and partly automatically (by PHASER runs with the fixed refined model). Manual model building with COOT (Emsley and Cowtan, 2004) was aided by models resulting from automated model building with BUCCANEER (Cowtan, 2006). The refinement was performed with Phenix Refine (Afonine et al., 2012), and the stereochemistry was assessed by MolProbity (Davis et al., 2007). Interface area calculations were done with the PISA server (Krissinel and Henrick, 2007). PyMOL was used for producing the figures (Schrödinger, 2011).

Pull-Down Experiments

A total of 5 μg of tagged bait was incubated with 1.2× molar excess of untagged prey to pull down in a volume of 50 μl of pull-down buffer (20 mM Tris [pH 7.5], 100 mM NaCl, 0.01% NP40, 2 mM DTT). After incubation with GSH Sepharose (GE Healthcare) or GFP-binder resin, respectively, and three washing steps with pull-down buffer the resin was dried and taken up in SDS buffer. Input and pull-down fractions were analyzed on denaturing 12% SDS-PAGE.

Microscale Thermophoresis

For affinity measurements, Exo_9 (no Rrp44 subunit) was buffered in 20 mM HEPES (pH 7.5), 100 mM NaCl, 2.5 mM $MgCl_2$. GFP-tagged protein constructs were diluted in MST (microscale thermophoresis) buffer (20 mM HEPES [pH 7.5], 100 mM NaCl, 2.5 mM $MgCl_2$, 0.2% Tween 20, 1 mg/ml BSA). A dilution series of Exo_9 was produced and supplemented with even amounts of GFP-tagged protein (4–5 nM for WT Ski7 and Rrp6 constructs, 25 nM for the mutant Ski7). Different constructs were chosen due to difficult behavior of the highly hydrophobic Ski7 peptide. Thermophoresis was measured at 87%–90% LED power for Rrp6 and Ski7 WT and 20% LED power for the Ski7 mutant with standard parameters in a NanoTemper Monolith NT.115 machine. The data were analyzed with the MO software (NanoTemper Technologies), choosing a cold region between −1 and 0 and a hot region including the time range of 5 to 7 s as indicated in Figure S3.

Yeast Experiments

See Supplemental Information.

ACCESSION NUMBERS

The coordinates and structure factors of Exo_{10}-Ski7-RNA have been deposited in the Protein Data Bank with the accession code 5JEA.

SUPPLEMENTAL INFORMATION

Supplemental Information includes five figures and Supplemental Experimental Procedures and can be found with this article at http://dx.doi.org/10.1016/j.molcel.2016.05.028.

AUTHOR CONTRIBUTIONS

E.K. and E.C. started the project and wrote the paper. Exosome subunits were purified by E.S. and J.E. The complex was crystallized by J.E. and E.K. The structure was determined by E.K.; A.K. assembled and tested human exosome and HBS1L. P.R. performed in vivo experiments in yeast. B.H. did the bioinformatical analysis.

ACKNOWLEDGMENTS

We thank the Max Planck Institute of Biochemistry (MPIB) Crystallization and Core Facilities; the beam line scientists at PXII and PXIII at SLS for assistance with data collection and members of our lab for useful discussions and critical reading of the manuscript. We are grateful to Ajla Hrle (NanoTemper Technologies) for advice with the MST data and to Marc Baumgärtner and Max Fastner for assistance in protein purification. This study was supported by the Max Planck Gesellschaft, the European Research Council (ERC Advanced Investigator Grant 294371), and the Deutsche Forschungsgemeinschaft (DFG SFB1035, GRK1721 and CIPSM) to E.C.; and by an EMBO long-term fellowship, Marie Curie Actions Intra-European Fellowship (IEF) and a Daimler-Benz Postdoctoral stipend to E.K.

Received: February 8, 2016
Revised: April 26, 2016
Accepted: May 18, 2016
Published: June 23, 2016

REFERENCES

Afonine, P.V., Grosse-Kunstleve, R.W., Echols, N., Headd, J.J., Moriarty, N.W., Mustyakimov, M., Terwilliger, T.C., Urzhumtsev, A., Zwart, P.H., and Adams, P.D. (2012). Towards automated crystallographic structure refinement with phenix.refine. Acta Crystallogr. D Biol. Crystallogr. *68*, 352–367.

Allmang, C., Kufel, J., Chanfreau, G., Mitchell, P., Petfalski, E., and Tollervey, D. (1999). Functions of the exosome in rRNA, snoRNA and snRNA synthesis. EMBO J. *18*, 5399–5410.

Anderson, J.S., and Parker, R.P. (1998). The 3′ to 5′ degradation of yeast mRNAs is a general mechanism for mRNA turnover that requires the SKI2 DEVH box protein and 3′ to 5′ exonucleases of the exosome complex. EMBO J. *17*, 1497–1506.

Araki, Y., Takahashi, S., Kobayashi, T., Kajiho, H., Hoshino, S., and Katada, T. (2001). Ski7p G protein interacts with the exosome and the Ski complex for 3′-to-5′ mRNA decay in yeast. EMBO J. *20*, 4684–4693.

Becker, T., Armache, J.-P., Jarasch, A., Anger, A.M., Villa, E., Sieber, H., Motaal, B.A., Mielke, T., Berninghausen, O., and Beckmann, R. (2011). Structure of the no-go mRNA decay complex Dom34-Hbs1 bound to a stalled 80S ribosome. Nat. Struct. Mol. Biol. *18*, 715–720.

Bonneau, F., Basquin, J., Ebert, J., Lorentzen, E., and Conti, E. (2009). The yeast exosome functions as a macromolecular cage to channel RNA substrates for degradation. Cell *139*, 547–559.

Brown, J.T., Bai, X., and Johnson, A.W. (2000). The yeast antiviral proteins Ski2p, Ski3p, and Ski8p exist as a complex in vivo. RNA *6*, 449–457.

Butler, J.S., and Mitchell, P. (2010). Rrp6, Rrp47 and cofactors of the nuclear exosome. Adv. Exp. Med. Biol. *702*, 91–104.

Chlebowski, A., Lubas, M., Jensen, T.H., and Dziembowski, A. (2013). RNA decay machines: the exosome. Biochim. Biophys. Acta *1829*, 552–560.

Chun, E., Thompson, A.A., Liu, W., Roth, C.B., Griffith, M.T., Katritch, V., Kunken, J., Xu, F., Cherezov, V., Hanson, M.A., and Stevens, R.C. (2012). Fusion partner toolchest for the stabilization and crystallization of G protein-coupled receptors. Structure *20*, 967–976.

Cowtan, K. (2006). The Buccaneer software for automated model building. 1. Tracing protein chains. Acta Crystallogr. D Biol. Crystallogr. *62*, 1002–1011.

Davis, I.W., Leaver-Fay, A., Chen, V.B., Block, J.N., Kapral, G.J., Wang, X., Murray, L.W., Arendall, W.B., 3rd, Snoeyink, J., Richardson, J.S., and Richardson, D.C. (2007). MolProbity: all-atom contacts and structure validation for proteins and nucleic acids. Nucleic Acids Res. *35*, W375–W383.

Doma, M.K., and Parker, R. (2006). Endonucleolytic cleavage of eukaryotic mRNAs with stalls in translation elongation. Nature *440*, 561–564.

Drazkowska, K., Tomecki, R., Stoduś, K., Kowalska, K., Czarnocki-Cieciura, M., and Dziembowski, A. (2013). The RNA exosome complex central channel controls both exonuclease and endonuclease Dis3 activities in vivo and in vitro. Nucleic Acids Res. *41*, 3845–3858.

Dziembowski, A., Lorentzen, E., Conti, E., and Séraphin, B. (2007). A single subunit, Dis3, is essentially responsible for yeast exosome core activity. Nat. Struct. Mol. Biol. *14*, 15–22.

Emsley, P., and Cowtan, K. (2004). Coot: model-building tools for molecular graphics. Acta Crystallogr. D Biol. Crystallogr. *60*, 2126–2132.

Fabre, A., and Badens, C. (2014). Human Mendelian diseases related to abnormalities of the RNA exosome or its cofactors. Intractable Rare Dis. Res. *3*, 8–11.

Falk, S., Weir, J.R., Hentschel, J., Reichelt, P., Bonneau, F., and Conti, E. (2014). The molecular architecture of the TRAMP complex reveals the organization and interplay of its two catalytic activities. Mol. Cell *55*, 856–867.

Greimann, J.C., and Lima, C.D. (2008). Reconstitution of RNA exosomes from human and Saccharomyces cerevisiae cloning, expression, purification, and activity assays. Methods Enzymol. *448*, 185–210.

Guydosh, N.R., and Green, R. (2014). Dom34 rescues ribosomes in 3′ untranslated regions. Cell *156*, 950–962.

Halbach, F., Reichelt, P., Rode, M., and Conti, E. (2013). The yeast ski complex: crystal structure and RNA channeling to the exosome complex. Cell *154*, 814–826.

Houseley, J., LaCava, J., and Tollervey, D. (2006). RNA-quality control by the exosome. Nat. Rev. Mol. Cell Biol. *7*, 529–539.

Inada, T. (2013). Quality control systems for aberrant mRNAs induced by aberrant translation elongation and termination. Biochim. Biophys. Acta *1829*, 634–642.

Januszyk, K., and Lima, C.D. (2014). The eukaryotic RNA exosome. Curr. Opin. Struct. Biol. *24*, 132–140.

Kabsch, W. (2010). XDS. Acta Crystallogr. D Biol. Crystallogr. *66*, 125–132.

Klauer, A.A., and van Hoof, A. (2012). Degradation of mRNAs that lack a stop codon: a decade of nonstop progress. Wiley Interdiscip. Rev. RNA *3*, 649–660.

Kowalinski, E., Schuller, A., Green, R., and Conti, E. (2015). Saccharomyces cerevisiae Ski7 is a GTP-binding protein adopting the characteristic conformation of active translational GTPases. Structure *23*, 1336–1343.

Krissinel, E., and Henrick, K. (2007). Inference of macromolecular assemblies from crystalline state. J. Mol. Biol. *372*, 774–797.

Lebreton, A., and Séraphin, B. (2008). Exosome-mediated quality control: substrate recruitment and molecular activity. Biochim. Biophys. Acta *1779*, 558–565.

Lebreton, A., Tomecki, R., Dziembowski, A., and Séraphin, B. (2008). Endonucleolytic RNA cleavage by a eukaryotic exosome. Nature *456*, 993–996.

Liu, Q., Greimann, J.C., and Lima, C.D. (2006). Reconstitution, activities, and structure of the eukaryotic RNA exosome. Cell *127*, 1223–1237.

Lykke-Andersen, J., and Bennett, E.J. (2014). Protecting the proteome: Eukaryotic cotranslational quality control pathways. J. Cell Biol. *204*, 467–476.

Lykke-Andersen, S., Brodersen, D.E., and Jensen, T.H. (2009). Origins and activities of the eukaryotic exosome. J. Cell Sci. *122*, 1487–1494.

Makino, D.L., Baumgärtner, M., and Conti, E. (2013). Crystal structure of an RNA-bound 11-subunit eukaryotic exosome complex. Nature *495*, 70–75.

Makino, D.L., Schuch, B., Stegmann, E., Baumgärtner, M., Basquin, C., and Conti, E. (2015). RNA degradation paths in a 12-subunit nuclear exosome complex. Nature *524*, 54–58.

Marshall, A.N., Montealegre, M.C., Jiménez-López, C., Lorenz, M.C., and van Hoof, A. (2013). Alternative splicing and subfunctionalization generates functional diversity in fungal proteomes. PLoS Genet. *9*, e1003376.

Matsuda, R., Ikeuchi, K., Nomura, S., and Inada, T. (2014). Protein quality control systems associated with no-go and nonstop mRNA surveillance in yeast. Genes Cells *19*, 1–12.

McCoy, A.J., Grosse-Kunstleve, R.W., Adams, P.D., Winn, M.D., Storoni, L.C., and Read, R.J. (2007). Phaser crystallographic software. J. Appl. Cryst. *40*, 658–674.

Mitchell, P., Petfalski, E., Shevchenko, A., Mann, M., and Tollervey, D. (1997). The exosome: a conserved eukaryotic RNA processing complex containing multiple 3′–>5′ exoribonucleases. Cell *91*, 457–466.

Rigby, R.E., and Rehwinkel, J. (2015). RNA degradation in antiviral immunity and autoimmunity. Trends Immunol. *36*, 179–188.

Saito, S., Hosoda, N., and Hoshino, S. (2013). The Hbs1-Dom34 protein complex functions in non-stop mRNA decay in mammalian cells. J. Biol. Chem. *288*, 17832–17843.

Schaeffer, D., Clark, A., Klauer, A.A., Tsanova, B., and van Hoof, A. (2011). Functions of the cytoplasmic exosome. Adv. Exp. Med. Biol. *702*, 79–90.

Schilders, G., van Dijk, E., and Pruijn, G.J.M. (2007). C1D and hMtr4p associate with the human exosome subunit PM/Scl-100 and are involved in pre-rRNA processing. Nucleic Acids Res. *35*, 2564–2572.

Schrödinger, L. (2011). The PyMOL Graphics System. Version. v1.5.0.4.

Schuch, B., Feigenbutz, M., Makino, D.L., Falk, S., Basquin, C., Mitchell, P., and Conti, E. (2014). The exosome-binding factors Rrp6 and Rrp47 form a composite surface for recruiting the Mtr4 helicase. EMBO J. *33*, 2829–2846.

Shi, Y., Pellarin, R., Fridy, P.C., Fernandez-Martinez, J., Thompson, M.K., Li, Y., Wang, Q.J., Sali, A., Rout, M.P., and Chait, B.T. (2015). A strategy for dissecting the architectures of native macromolecular assemblies. Nat. Methods *12*, 1135–1138.

Shoemaker, C.J., and Green, R. (2012). Translation drives mRNA quality control. Nat. Struct. Mol. Biol. *19*, 594–601.

Shoemaker, C.J., Eyler, D.E., and Green, R. (2010). Dom34:Hbs1 promotes subunit dissociation and peptidyl-tRNA drop-off to initiate no-go decay. Science *330*, 369–372.

Staals, R.H.J., and Pruijn, G.J.M. (2010). The human exosome and disease. Adv. Exp. Med. Biol. *702*, 132–142.

Toh-E, A., Guerry, P., and Wickner, R.B. (1978). Chromosomal superkiller mutants of Saccharomyces cerevisiae. J. Bacteriol. *136*, 1002–1007.

Tsuboi, T., Kuroha, K., Kudo, K., Makino, S., Inoue, E., Kashima, I., and Inada, T. (2012). Dom34:hbs1 plays a general role in quality-control systems by dissociation of a stalled ribosome at the 3′ end of aberrant mRNA. Mol. Cell *46*, 518–529.

van Hoof, A., Staples, R.R., Baker, R.E., and Parker, R. (2000). Function of the ski4p (Csl4p) and Ski7p proteins in 3′-to-5′ degradation of mRNA. Mol. Cell. Biol. *20*, 8230–8243.

van Hoof, A., Frischmeyer, P.A., Dietz, H.C., and Parker, R. (2002). Exosome-mediated recognition and degradation of mRNAs lacking a termination codon. Science *295*, 2262–2264.

Wang, L., Lewis, M.S., and Johnson, A.W. (2005). Domain interactions within the Ski2/3/8 complex and between the Ski complex and Ski7p. RNA *11*, 1291–1302.

Wasmuth, E.V., and Lima, C.D. (2012). Exo- and endoribonucleolytic activities of yeast cytoplasmic and nuclear RNA exosomes are dependent on the non-catalytic core and central channel. Mol. Cell *48*, 133–144.

Wasmuth, E.V., Januszyk, K., and Lima, C.D. (2014). Structure of an Rrp6-RNA exosome complex bound to poly(A) RNA. Nature *511*, 435–439.

Molecular Cell, Volume *63*

Supplemental Information

Structure of a Cytoplasmic 11-Subunit RNA Exosome Complex

Eva Kowalinski, Alexander Kögel, Judith Ebert, Peter Reichelt, Elisabeth Stegmann, Bianca Habermann, and Elena Conti

SUPPLEMENTAL MATERIAL

Supplemental Figure 1, related to Table 1

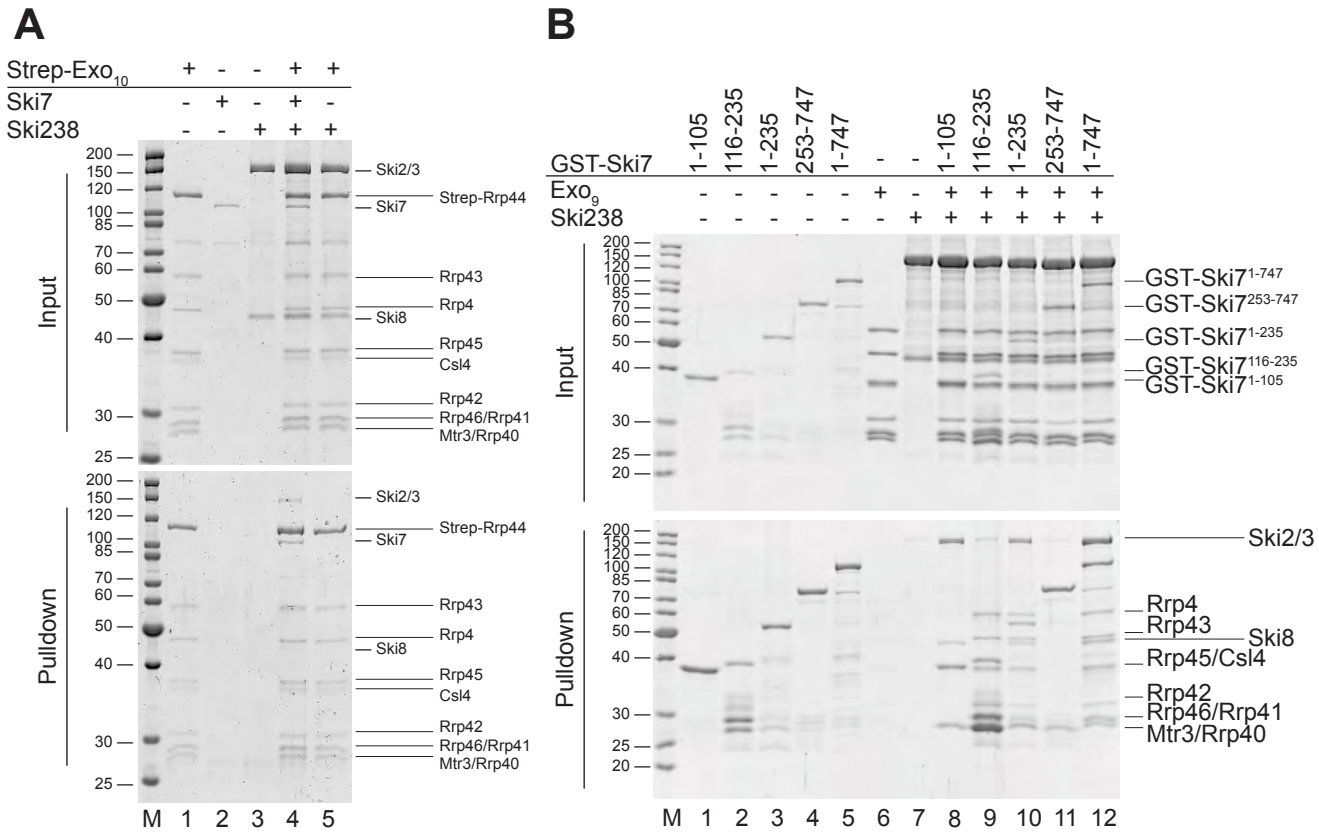

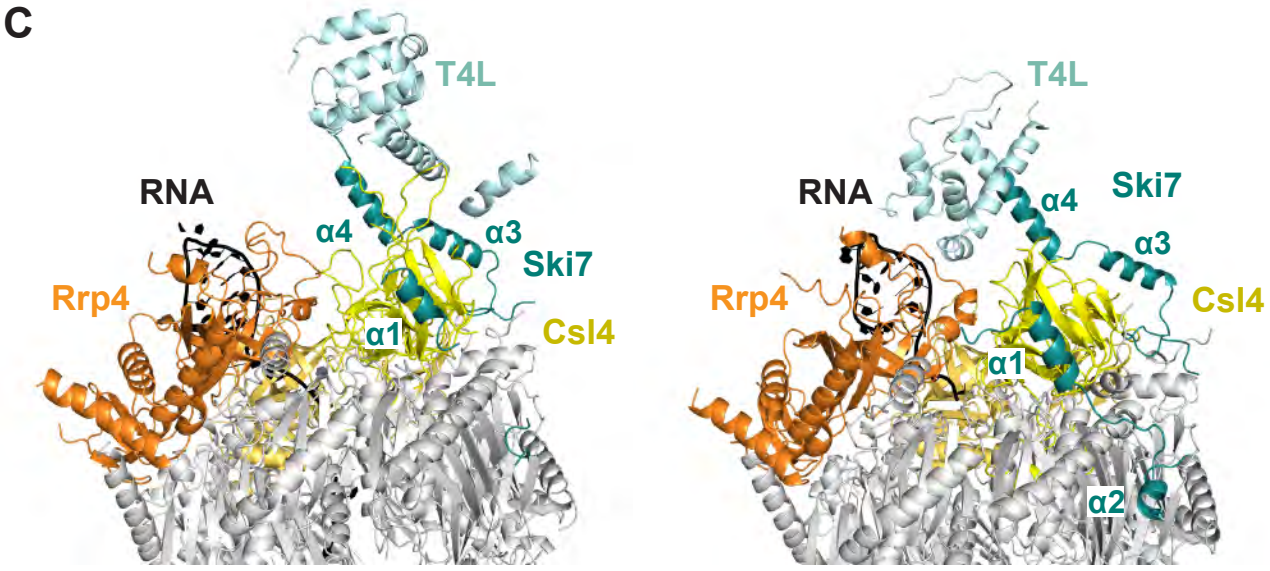

Supplemental Figure 2, related to Figure 1

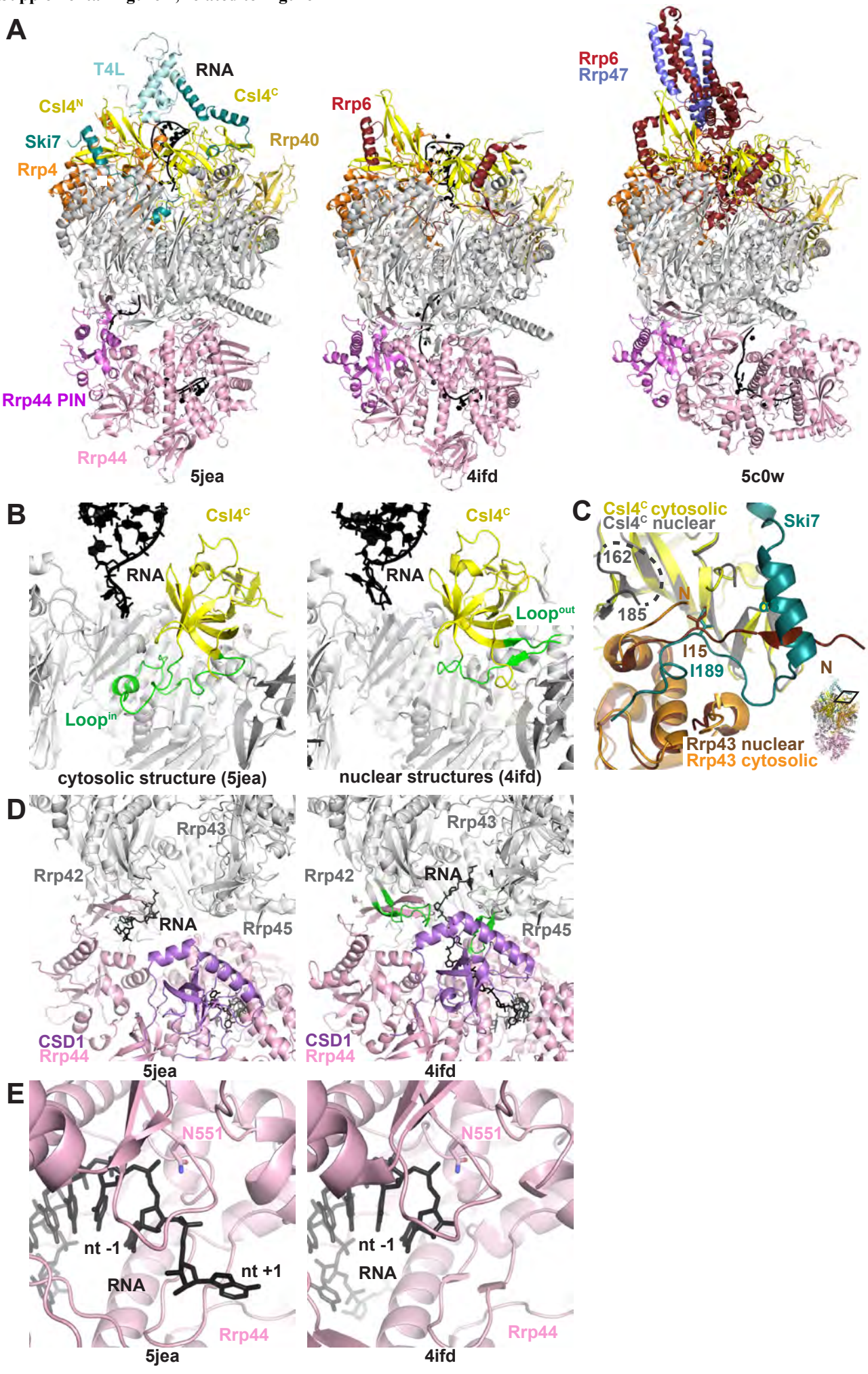

Supplemental Figure 3, related to Figure 2

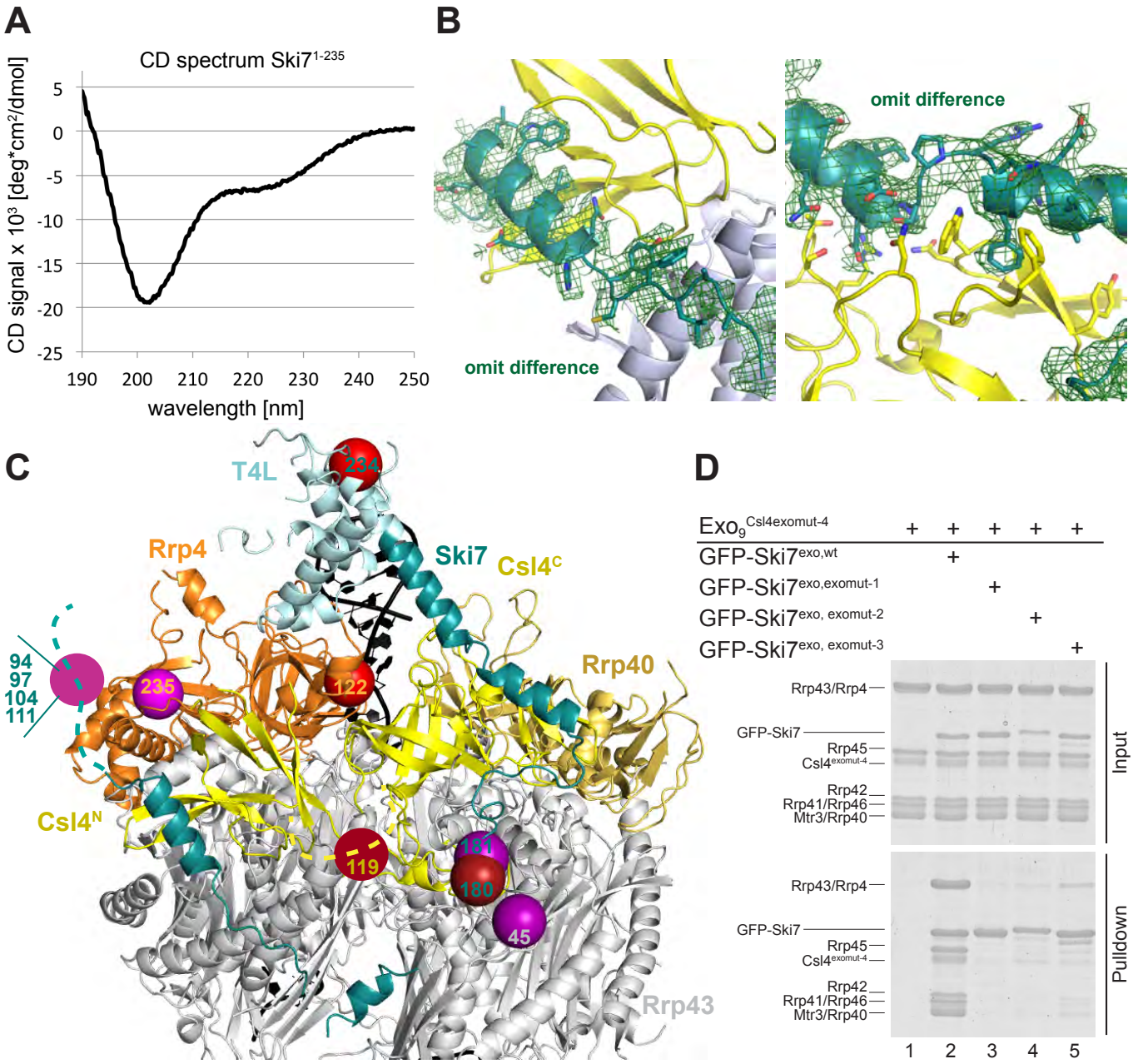

Supplemental Figure 4, related to Figure 2

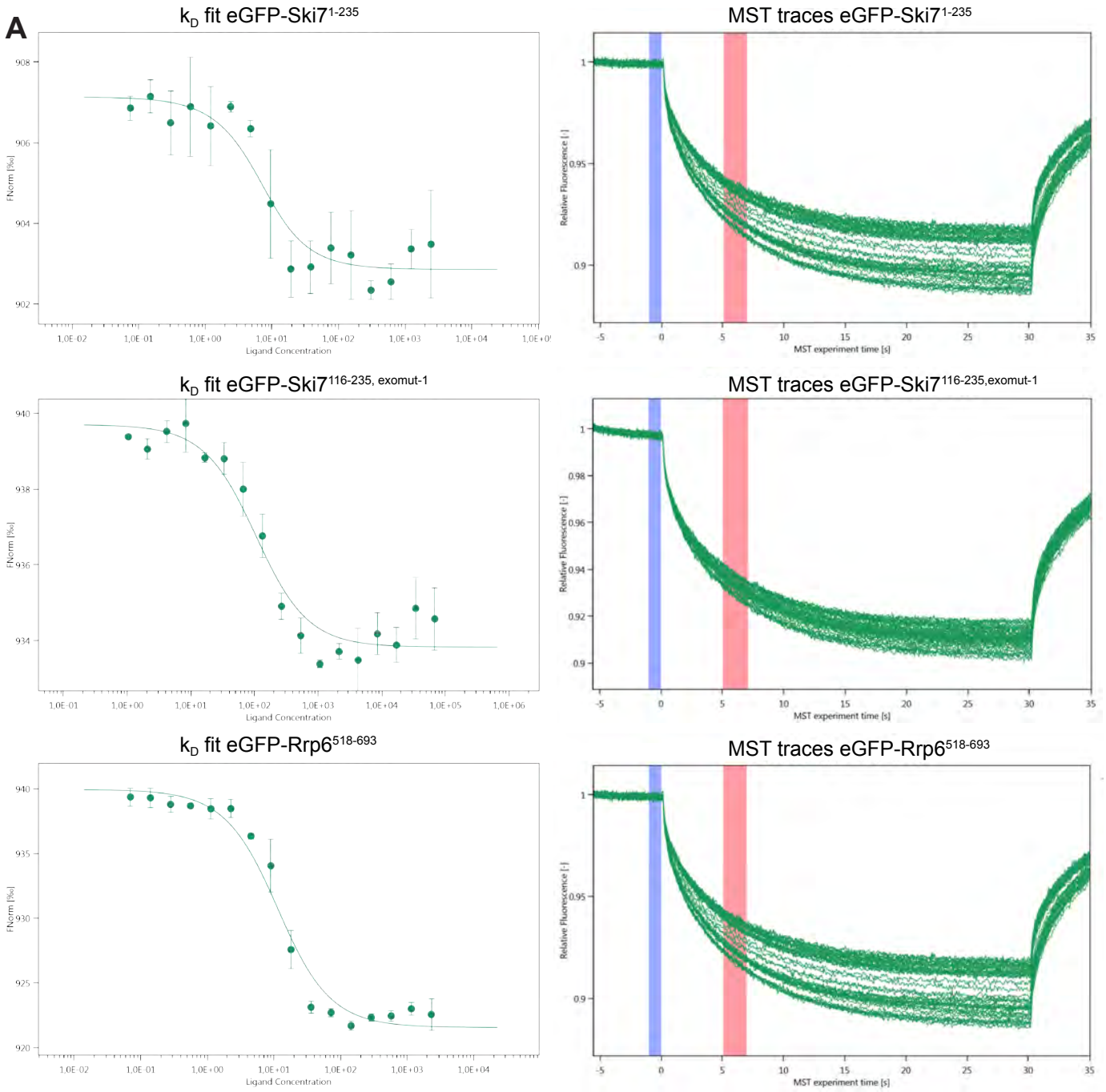

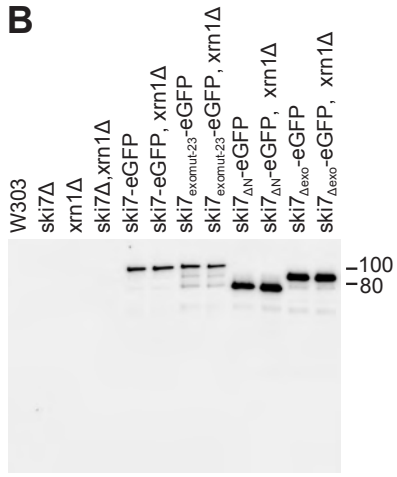

Supplemental Figure 5, related to Figure 3

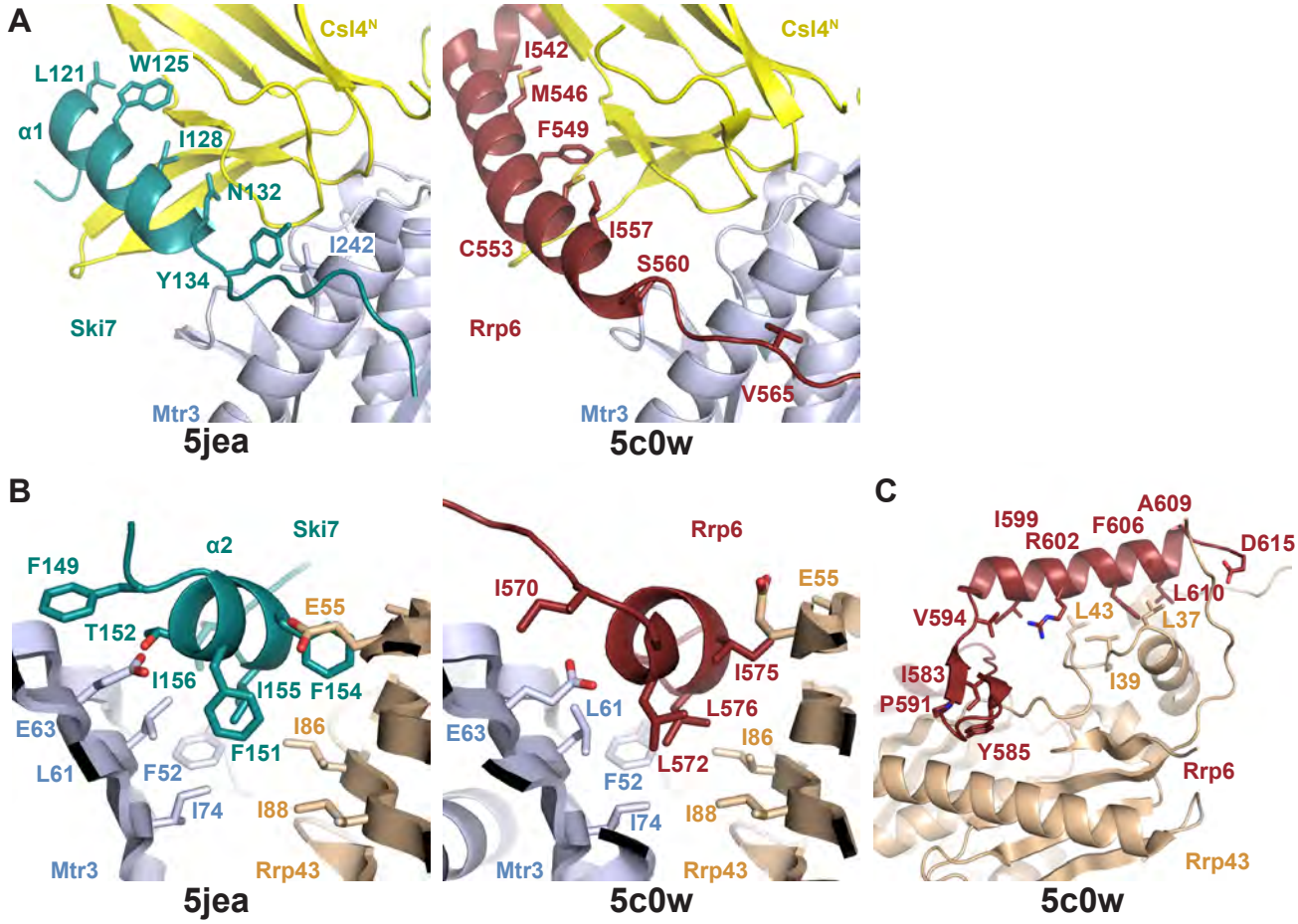

Supplemental Table 1, related to Figure 2

Yeast strains based on W303 *MATa/MATα {leu2-3,112 trp1-1 can1-100 ura3-1 ade2-1 his3-11,15, RAD5}*

Label	ID	Relevant genotype
ski7Δ/SKI7	scCLPR625	W303 *MAT**a**/MATα, ski7Δ::klURA3/SKI7*
W303	scCLPR272	W303 *MATα , SKI7*
ski7Δ	scCLPR673	W303 *MATα, ski7Δ::kanMX4, YCplac33 [XRN1, URA3]*
SKI7-EGFP	scCLPR676	W303 *MAT**a**, ski7-EGFP::kanMX4, YCplac33 [XRN1, URA3]*
ski7$_{exomut-2-3}$ -EGFP	scCLPR678	W303 *MAT**a**, ski7$_{exomut-2-3}$-EGFP::kanMX4, YCplac33 [XRN1, URA3]*
ski7$_{\Delta exo}$-EGFP	scCLPR680	W303 *MATα, Δ116-235-ski7-EGFP::kanMX4, YCplac33 [XRN1, URA3]*
ski7$_{\Delta N}$-EGFP	scCLPR682	W303 *MATα, Δ1-235-ski7-EGFP::kanMX4, YCplac33 [XRN1, URA3]*
xrn1Δ	scCLPR674	W303 *MAT**a**, xrn1Δ::natNT2, YCplac33 [XRN1, URA3]*
ski7Δ/ xrn1Δ	scCLPR675	W303 *MAT**a**, ski7Δ::kanMX4, xrn1Δ::natNT2, YCplac33 [XRN1, URA3]*
SKI7-EGFP, xrn1Δ	scCLPR677	W303 *MAT**a**, ski7-EGFP::kanMX4 xrn1Δ::natNT2, YCplac33 [XRN1, URA3]*
ski7 $_{exomut-2-3}$ -EGFP, xrn1Δ	scCLPR679	W303 *MAT**a**, ski7$_{exomut-2-3}$-EGFP::kanMX4 xrn1Δ::natNT2, YCplac33 [XRN1, URA3]*
ski7$_{\Delta exo}$-EGFP, xrn1Δ	scCLPR681	W303 *MATα, Δ116-235-ski7-EGFP::kanMX4 xrn1Δ::natNT2, YCplac33 [XRN1, URA3]*
ski7$_{\Delta N}$-EGFP, xrn1Δ	scCLPR683	W303 *MAT**a**, Δ1-235-ski7-EGFP::kanMX4 xrn1Δ::natNT2, YCplac33 [XRN1, URA3]*
mating strain		
xrn1Δ	scCLPR476	W303 *MAT**a**, xrn1Δ::natNT2, YCplac33 [XRN1, URA3]*

SUPPLEMENTAL FIGURE LEGENDS

FIGURE S1 (referring to Table 1)
***In vitro* dissection of Ski7 interaction with the Ski-complex and the exosome.**
(A) Ski7 is necessary and sufficient for interaction of the exosome and the Ski complex. An SDS-PAGE of a pull down experiment of Exo_{10} with Strep-tagged Rrp44 on Strep-tactin resin is shown. The Ski-exosome complex is only precipitated in the presence of Ski7 (lane 4) and not when Ski7 is absent (lane 5).
(B) Establishing minimal binding regions. In a GST pull down different GST-tagged Ski7 constructs were incubated with Exo_9 and GSH resin. $Ski7_{1\text{-}105}$ precipitates Ski-complex (lane 8), $Ski7_{116\text{-}235}$ precipitates Exo_9 (lane 9) and $Ski7_{1\text{-}235}$ and $Ski7_{1\text{-}747}$ precipitate both complexes (lanes 10 and 12). $Ski7_{235\text{-}747}$ (GTP binding domain) does not interact with either complex (lane 11).
(C) Optimization of the crystallization construct. The preliminary Exo_{10} - $Ski7_{116\text{-}235}$T4L that yielded crystals diffracting to 4.2 Å on the left and the final Exo_{10} - $Ski7_{116\text{-}225}$T4L that yielded crystals diffracting to 2.65 Å on the right.

FIGURE S2 (referring to Figure 1)
Comparison of exosome structures.
(A) Comparison of exosome complex structures. The Exo_{10}-Ski7 complex (5jea), Exo_{10}-Rrp6 complex (4ifd) and the Exo_{10}-Rrp6-Rrp47 (5c0w) complex are shown. Colours as in Figure 1B with Rrp6 in Red and Rrp47 in blue.
(B) Comparison of the Csl4 conformation in the cytosolic versus the nuclear exosome. 5jea and 4ifd are shown side by side. Representation and colors like Figure 1B, residues 158 to 200 of the described loop of Csl4 are shown in green.
(C) Ski7 is triggering the alternative Csl4 loop conformation. Superposition of the nuclear (4ifd) and the cytosolic exosome based on the C-terminal domain of Csl4. Nuclear Csl4 in grey, the outside position of the displaced loop is shown as dotted line, nuclear Rrp43 in chocolate. Colours of the cytosolic exosome like in Figure 1B. The nuclear conformation of the Rrp43 N-terminus is not compatible with the binding of Ski7, as both dock on the same surface of the exosome (with $Ile189^{Ski7}$ occupying the same position of $Ile15^{Rrp43}$). It is thus possible that the alternative conformation of the Rrp43 N-terminus upon Ski7 binding indirectly impinges on the position of the Csl4 loop and provokes a RNA-binding conformation inside the central channel instead of the solvent-exposed conformation as observed in the nuclear exosome.
(D) Mobility of the CSD1 domain of Rrp44. 5jea and 4ifd are shown side by side. Representation and colors like Figure 1C with the CSD1 domain of Rrp44 highlighted in purple. Loops of Rrp42 (residues 159-169) and Rrp43 (residues 250-270), that are disordered in 5jea are highlighted in green in the nuclear structure.
(E) The leaving position of the cleaved nucleotide in Rrp44. 5jea and 4ifd are shown side by side. Representation and colors like Figure 1E. The nuclear (4ifd) and the cytosolic exosome (5jea) were superposed based on the position of the RNB domain of Rrp44.

FIGURE S3 (referring to Figure 2)
Additional biochemical data
(A) Experimental data from a circular dichroism (CD) experiment. 10 µM $Ski7_{1\text{-}235}$ buffered in 20 mM NaPO4 pH 7.4, 50 mM NaF and subjected to a JASCO 810 Spectropolarimeter at 20 °C in a 1-mm path-length cuvette. The scan was taken from 250 to 190 nm in 0.1-nm increments and corrected by subtraction of the buffer spectrum. $Ski7_{1\text{-}235}$ is rather unstructured in solution.
(B) Example Fc-Fo map omitting Ski7 in the last step of refinement. Isomesh is shown in green at $\sigma = 1.5$ in a radius of 1.8 Å from the Ski7 chain. Views as in Figures 2B and 2E.
(C) Mapping mass-spec cross-linking data in the structure (Shi et al., 2015). Cross-linked residues are numbered and shown as spheres of the same color. Cross-linked residues in close-by loops (dotted lines) or beyond the boundaries of the crystallization constructs are shown as well, as colored circles or mapped in the corresponding residue in T4L, respectively. Cross-linked lysine residues: 87^{Ski7}, 94^{Ski7}, 104^{Ski7}, 111^{Ski7} with 235^{Rrp4}; 180^{Ski7} with 119^{Csl4} and 45^{Rrp43}; 181^{Ski7} with 45^{Rrp43}, 234^{Ski7} with 122^{Rrp4}.
(D) Mutating a binding surface in patch 4 on Csl4 (Trp272Glu, Phe292Glu, Asn250Ala or $Csl4_{exomut\text{-}4}$) on the exosome only impairs the interaction with Ski7 in combination with one of the other binding patches mutated (lanes 3, 4 and 5). Protein co-precipitation in a GFP pull down assay is shown.

FIGURE S4 (referring to Figure 2)
Additional biochemical data
(A) Microscale thermophoresis traces (right) and k_D fit curves (left) of constructs as annotated. Exo_9 was titrated. Cold (blue) and hot (red) regions that were used for analysis are marked in the traces. Experiments were conducted in triplicates and averaged before the curve fit as indicated by error bars.
(B) eGFP-tagged proteins were enriched by immunoprecipitation from soluble lysate of the yeast strains shown in Figure 2G and analyzed by SDS-PAGE and anti-GFP western blotting.

FIGURE S5 (referring to Figure 3)
Comparison of Ski7 and Rrp6 binding to the exosome
(A) Comparison of Ski7 and Rrp6 binding in patch 1. 5jea and 5c0w are shown side by side. Representation and colors like Figure 3C and Rrp6 in red.
(B) Comparison of Ski7 and Rrp6 binding in patch 2. 5jea and 5c0w are shown side by side. Representation and colors like Figure 3D and Rrp6 in red.
(C) Rrp6 interaction with Rrp43. Representation and colors like Supplemental figure S4B. The Rrp43 residues that were mutated for the pull down in Figure 3D are represented as sticks.

SUPPLEMENTAL EXPERIMENTAL PROCEDURES

Purification of yeast exosome subunits

S. cerevisiae Exo_9, Rrp44 (1-1001, D171N, D551N) and $Rrp6_{exo}$ (518-693) were expressed in *E. coli* and purified with similar protocols as described before (Bonneau et al., 2009; Makino et al., 2013), with the main difference that we used an N-terminally truncated Rrp4 (residues 51-359) and a C-terminally truncated Rrp46 (residues 1-223) to remove regions that were disordered in previous structures. For some of the pull-downs full length Rrp4 was used with the same experimental outcome. Furthermore, it was crucial to employ a lysis buffer containing 1M KCl for high yields of nucleotide-free full length Rrp44. In all expression vectors (except the Rrp43/Rrp46 plasmid) we replaced TEV (tobacco etch virus) cleavage sites with a Prescission protease cleavage site.

Purification of human exosome subunits and $HBS1L3_{exo}$

H. sapiens Exo_9 proteins were expressed and purified similarly to the protocols previously described (Greimann and Lima, 2008) with the following exceptions: Rrp42, Mtr3 and Rrp43 were co-expressed and the ternary complex was purified via Ni-affinity chromatography, ion exchange and size exclusion chromatography. For all subunits a high salt wash with 1M NaCl, 50mM KCl, 10mM $MgCl_2$ and 2mM ATP was included in the first Ni-affinity step to remove chaperones and nucleic acids from the sample. Prescission Protease was used to remove His_{10}- and SUMO-tags after the initial Ni-affinity step. $HBS1L3_{exo}$ (540-632) was expressed in *E. coli* with N-terminal His_6-thioredoxin-tag and C-terminal GFP-tag. The protein was purified on a Ni-affinity column, a reverse Ni-affinity step after cleavage of the thioredoxin-tag with Prescission Protease, followed by size exclusion chromatography.

Yeast strain generation

Starting from a haploid *ski7Δ* strain, PCR generated mutated *ski7-EGFP::kanMX4* constructs were integrated at the genomic locus by gene replacement. The haploid strains bearing the *ski7* mutations were mated with a *Δxrn1* strain carrying the YCplac33-XRN1 rescue plasmid. The resulting diploid strains were sporulated and tetrads were analyzed to select haploid cells for the desired combination of *Δxrn1* or *XRN1* and *ski7* constructs. Detailed descriptions of the genotypes are listed in Table S1.

Spotting assays

Cells were grown to an OD_{600nm} of 0.5 in 20 ml of Yeast extract-peptone-dextrose medium supplemented with adenine (YPAD), starting from a saturated overnight culture in SC w/o URA. Except the W303 wildtype strain that was grown in YPAD. 1 OD_{600nm} of cells was harvested and suspended in 200 µl H_2O. The cell suspension was serially diluted 1:5 in 96 well plates and then spotted onto the following media plates: YPAD, YPAD-G418 (200 mg/l), YPAD-Nat (100 mg/l), SC w/o URA, SC-FOA (uracil 50 mg/l ; 5-FOA 1gr/l). Cells were grown for 3 days at 30°C. SC: synthetic complete medium; URA: uracil; 5-FOA: 5-fluoroorotic acid.

Western blot analysis

Cells were grown in 200 ml YPAD to an OD_{600nm} of 3. 200 OD_{600nm} of cells were harvested and suspended in 750 µl of lysis buffer (20 mM Hepes, 150 mM NaCl, 0.5 mM EDTA pH 7.4 supplemented with 1mM PMSF and Roche EDTA free protease inhibitor according to instructions). 0.5 mm glass beads were added to 1/3 of the total volume. Cells were lysed in a Precellys Evolution bead beater at 7500 rpm, 5 cycles of 20 s and 45 s pause. The temperature was kept within -2 °C and 2 °C with the Precellys Cryolys cooling device. Lysates were cleared at 13000 rpm for 15 min at 4 °C in a tabletop centrifuge. 200 µl of the supernatant/lysate was incubated with 25 µl GFP-trap_A slurry (Chromotek) for 2 h at 4 °C on a rotating platform. The agarose beads were spun down at 2000 rpm in a tabletop centrifuge for 5 minutes at 4 °C. The supernatant was removed and the beads were washed twice with lysis/binding buffer. The last wash was transferred to fresh tubes, spun again at 2000 rpm at 4 °C for minutes. The supernatant was removed as much as possible and the agarose beads were immediately resuspended in 2 x SDS loading buffer and boiled for 10 min at 95 °C. 10 µl sample were loaded on a 8-16 % mini-Protean TGX stain free gradient gel (Biorad). The gel was developed and imaged with a Bio-Rad EZ-Imager. Proteins were transferred to a nitrocellulose membrane in 1 x Towbin buffer at 400 mA for 1 h at 4 °C. Immunodetection was done with a Life Technologies iBind device. The primary antibody was an anti-GFP (B-2) monoclonal antibody (Santa Cruz sc-9996) at a concentration of 1:1000 and the secondary antibody was a goat anti mouse HRP conjugated monoclonal antibody (Biorad 172-1011) at a concentration of 1:20000. Detection was done with a GE Healthcare LAS4000 imager.

4 DISCUSSION

4.1 The molecular mechanisms of the human SKI complex

The mechanistic study of the human SKI complex in presence or absence of different substrates and in different activity states provides important insights into the molecular mechanisms of the helicase complex, and furthermore forms the basis for a continuative understanding of the coordinated hSKI-exosome function.

4.1.1 hSKI adopts closed and open states marked by the detachment of the helicase core

The apo human SKI complex exists in an equilibrium of two fundamentally different conformational states: a closed state, that is similar to published structures of the orthologous yeast complex and an open state that has not been described to date.

The overall structure of the apo human SKI complex in the closed state resembles its yeast homologue (Paper 1, Figure 2) (Halbach et al. 2013; Schmidt et al. 2016). It consists of four proteins: the DExH helicase hSKI2 at the center of the complex, surrounded by the tetratricopeptide repeat (TPR) containing protein hSKI3 and the two copies of the ß-propeller $hSKI8_{IN/OUT}$. The hSKI3 protein consists of 40 TPRs which arrange in a large solenoid structure with four superhelical turns. The overall function of the hSKI3 C-terminal arm ($hSKI3_C$, superhelical turns 3 and 4) as an interaction hub seems to be well conserved between the human and yeast complexes. It binds the $hSKI8_{IN/OUT}$ proteins at TRPs 32/33 and 30/31 at inside and outside locations within the complex, respectively. Furthermore, $hSKI3_C$ maintains an intricate network of interactions with the hSKI2 helicase core ($hSKI2_{cat}$) and its naturally unstructured N-terminus ($hSKI2_N$). In comparison, the hSKI3 N-terminal arm ($hSKI3_N$, superhelical turns 1 and 2) engages only in sparse interactions with $hSKI2_N$ and appears to be flexible, as observed in the yeast homologue (Halbach et al. 2013). The structured helicase core of the hSKI2 protein has the typical domain architecture of a DExH-box helicase from the SF2 family (Ozgur et al. 2015) with two RecA, a winged helix (WH) and a helical bundle (HB) domain, similar to yeast Ski2 and other representatives of the family, like Hel308, Prp43 (Halbach et al. 2012; Büttner et al. 2007; Tauchert et al. 2017). Inserted into the WH domain, is an arch domain which is specific to the exosome helicases and consequently present in Mtr4 (Lingaraju et al. 2019; Falk et al. 2014;

Weir et al. 2010). The elongated, unstructured N-terminus of hSKI2 ($hSKI2_N$) assumes a well-defined position in the hSKI closed state complex with extensive interactions to the concave and convex surfaces of the hSKI3 solenoid, which tightly tether the structured hSKI2 helicase core ($hSKI2_{cat}$) to it (Paper 1, Figure 2). Its presence is important for the regulation of the complex, and it is therefore not surprising that crucial $hSKI2_N$ elements, like the inner ß-hairpin, the wedge, the outer hairpin and the outer α-helix, as well as their corresponding hSKI3 and $hSKI2_{cat}$ interaction sites, are conserved in the yeast complex, where it is thought to maintain a similar function (Halbach et al. 2013).

In the open state of apo human SKI, the hSKI2 helicase is detached from the rest of the complex. The transition between detached and attached helicase conformations appears to be related to the wedge segment in the $hSKI2_N$. For simplicity and based on the structural analysis of the hSKI closed and open states, $hSKI2_N$, hSKI3 and $hSKI8_{IN/OUT}$ are referred to as the gatekeeping module, whereas $hSKI2_{cat}$ and $hSKI2_{arch}$ as the helicase module. In the open state structure (Paper 1, Figure 3), the hSKI3 solenoid winds around the $hSKI2_N$ as in the closed state hSKI structure, and the two $hSKI8_{IN/OUT}$ bind to the same hSKI3 locations. The inner and outer hairpin elements of $hSKI2_N$ also remain bound to hSKI3 at the same positions. The wedge segment in between the two hairpin elements tethers $hSKI2_{cat}$ to the complex in the closed state. In the open state, the wedge segment together with the outer α-helix and the entire hSKI2 helicase core is flexible and no longer visible. The participation of the wedge in transitioning between the two states is further supported by an analysis of a hSKI-Δwedge complex, in which the wedge segment is replaced with a short linker (Paper 1, Figure S4). It shows the complex in a constitutive open state that can no longer tether the helicase to the complex. It becomes clear that the wedge segment tethers the helicase module to the complex in closed state and that it is capable of detaching it from the gatekeeping module in a wedge-dependent manner.

The yeast Ski complex shows a similar propensity to adopt closed and open conformational states as its conservation would suggest (Paper 1, Figure S4). Cryo-EM analysis of an apo ySki-Δarch complex shows it in an equilibrium of closed and open states, similar to the wildtype apo hSKI complex and confirms that the helicase detachment is a conserved mechanism common to both yeast and human SKI complexes. Cryo-EM analysis of a human SKI-Δarch complex (Figure 10), in comparison, shows the complex in a constitutive open state, similar to the Δwedge

complex above. It is unclear how the removal of the arch domain supports a detachment of the hSKI2 helicase from the complex, but the different behavior of the human and yeast Δarch complexes with respect to their conformational plasticity points towards a possible species-specific regulation by the arch domain.

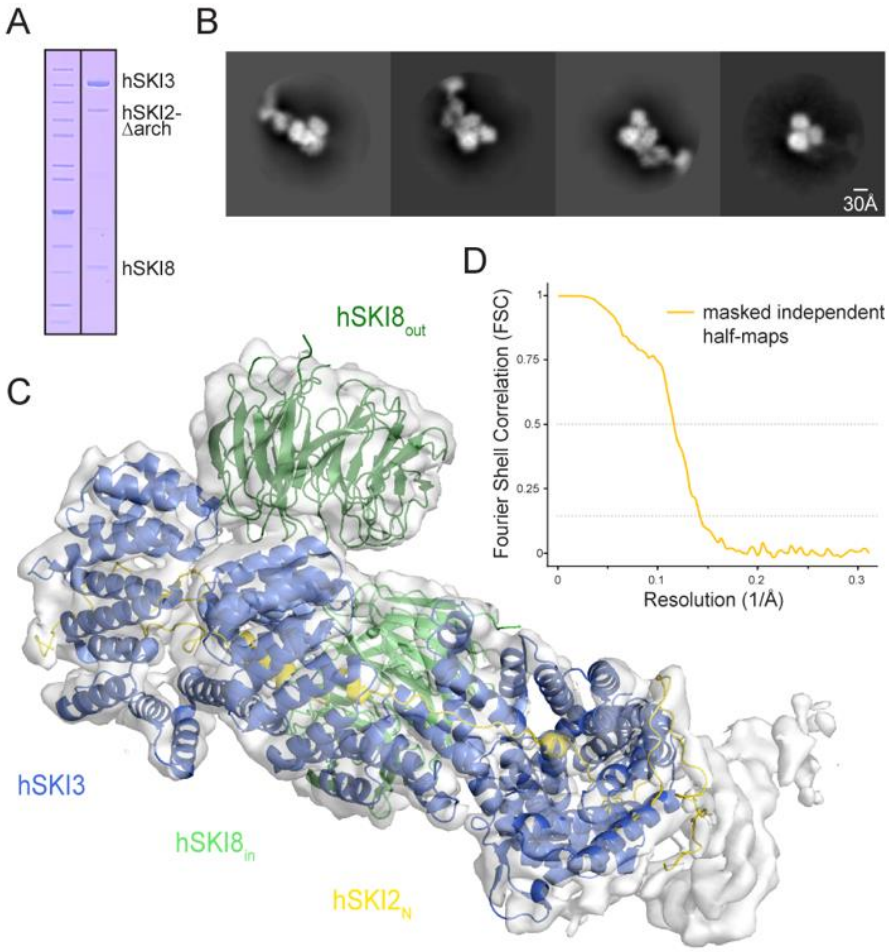

Figure 10. Cryo-EM analysis of the hSKI-Δarch complex. **(A)** shows a coomassie stained 4-12% SDS-PAGE of the hSKI-Δarch complex after gel filtration. The sample was vitrified on holey-carbon Cu grids and imaged at 200 kV using a K2 detector in counting mode at a pixel size of 1.885 Å/pix. Reference-free 2D class averages **(B)** and the final 3D reconstruction at 7 Å global resolution **(C)** of the cryo-EM SPA data show the complex in a constitutively open state. The low-resolution 3D reconstruction was interpreted by fitting the structure of apo human SKI in the open state. $hSKI2_N$ is colored in yellow, hSKI3 in blue and the two $hSKI8_{IN/OUT}$ in green and dark green. Note that the N-terminus of hSKI3 is flexible as observed in 3D reconstructions of the open states of apo hSKI and hSKI-Δwedge, and is therefore left unmodelled. **(D)** Fourier shell correlation of the masked independent half-maps of the 3D reconstruction of hSKI-Δarch shown in (C).

4.1.2 hSKI accommodates RNA in the closed state prior to activation

The closed state conformation is also the conformation in which hSKI binds RNA prior to activation. The structure of RNA-bound hSKI in the closed state shows binding of six ribonucleotides in the attached hSKI2 helicase core (Paper 1, Figure 4). Most of the interactions with the RNA are established with residues of the RecA1, RecA2 and helical bundle domains of $hSKI2_{cat}$, and are similar to published substrate-bound structures of related DExH-box helicases like Mtr4, Hel308 and Prp43 (Weir et al. 2010; Büttner et al. 2007; Tauchert et al. 2017). The interaction of the RNA 3' end with Trp146 in the $hSKI2_N$, however, is unusual, as it is part of the wedge segment that tethers the helicase core to the complex.

Similar hSKI-RNA interactions are observed when the complex is analyzed bound to the ribosome in presence of the non-hydrolysable nucleotide analogue ADP-BeF. In the structure, the hSKI complex binds the mRNA entry site at the 40S ribosomal subunit between the head and shoulder (Paper 1, Figure 5). It maintains interactions with several ribosomal proteins (eS10, uS10, uS3) and RNA (18S rRNA h16, h41), which are exclusively mediated by $hSKI2_{cat}$ and the arch domain of hSKI2. An interaction of $hSKI8_{OUT}$ with uS2, uS5 and eS21, as observed in the yeast Ski-ribosome structure (Figure 9; Schmidt et al. 2016), could not be observed, which is likely to be the reason why hSKI binds the ribosome with more flexibility. When bound to the ribosome, hSKI recognizes a short 3' overhang of the CrPV IRES at the mRNA entry site. Interactions with the RNA 3' overhang are essentially the same as observed in the RNA-bound structure described above. In the structure, six nucleotides are coordinated by the same residues of the hSKI2 RecA1, RecA2 and helical bundle domains, and the unusual Trp146 of the wedge segment, which recognizes the 3' end of the RNA.

In comparison to the cryo-EM analysis of the apo human SKI complex, the RNA-bound complexes in presence of ADP-BeF show the complex only in closed conformation (Paper 1, Figure S4), both in isolation and bound to the 80S ribosome (Paper 1, Figure S5). It appears that RNA-binding in presence of ADP-BeF favors the recruitment of the hSKI2 helicase core to the complex, which can be explained by the stabilization of the wedge segment between the helicase and gatekeeping modules due to the interaction of Trp146 with the RNA 3' end. Several DExH helicases that were crystallized in RNA-binding mode (in presence of a RNA substrate and a non-hydrolysable ATP analogue)

show the potential 3'-most nucleotide at the same position as in the RNA-bound hSKI (Weir et al. 2010; Tauchert et al. 2017). In these structures however, the RNA 3' ends are exposed to solvent and potentially accessible to other, unwanted enzymes. Thus, in the RNA-binding mode prior to activation of the helicase activity described here, the gatekeeping module blocks the exit site of the helicase core to prevent access to the RNA 3' end.

4.1.3 Active human SKI unwinds RNA in the open state

Activation of the SKI complex, in presence of ATP, initiates the unwinding of the RNA 3' end, which is accompanied by a detachment of the helicase core from the complex. This process could only be structurally analyzed in context of the ribosome. The complex binds in proximity of the mRNA entry site of the ribosome, where it maintains interactions with the same ribosomal proteins and RNA segments via $hSKI2_{cat}$ and the arch domain as observed in the ribosome-bound structure in presence of ADP-BeF. In presence of ATP, however, the hSKI complex assumes an open conformation, characterized by the detachment of the helicase core from the complex (Paper 1, Figure 6). Bound to the ribosome, it was possible to visualize the detached hSKI2 helicase core, which was too small to capture in the previous analysis of the apo complex in open state. At the ribosome, the activated hSKI2 helicase interacts with the CrPV IRES RNA at the mRNA entry site. Contacts are made with the six nucleotides by residues of the RecA1, RecA2 and helical bundle domains, as seen in the RNA-bound structures - except for Trp146. At the position where Trp146 recognizes the RNA 3' end in the RNA-bound structures, the backbone of the RNA undergoes an approximately 180° twist before an additional three nucleotides traverse the helicase core in a bent conformation, making additional contacts with residues of the RecA1 and HB domains. Coincidentally, with the RNA translocation through the helicase core, the electron density of one of the pseudoknots of the CrPV IRES in the intersubunit space of the ribosome disappears.

Based on these findings, we propose a model for the molecular mechanisms of the human SKI complex, in which substrate binding recruits the gatekeeping module to the complex to trap the RNA inside the helicase core and protect the 3' end. The activation of the complex in presence of ATP triggers the extraction of the mRNA from the ribosome. As the RNA is being translocated through the helicase core, the gatekeeping

module detaches to free the RNA exit site. Ongoing ATP hydrolysis continues to thread the RNA while keeping the complex in an open state until the extraction process is complete.

An analysis of a hSKI-RNA sample in presence of ATP and absence of the ribosome has not been tried but would be an interesting addition to the experiments described above. The prediction would be that all hydrolyzing hSKI particles are in an open helicase-detached state. Such an outcome would further support the proposed molecular mechanisms, but insight beyond that would be limited because it is unlikely that the detached helicase can be visualized in context of the complex in isolation.

4.2 Interaction and RNA channeling of the human SKI-exosome complex

The identification of HBS1L as a Ski7-like protein that bridges the interaction between hSKI and the cytoplasmic exosome in humans paves the road for biochemical characterization of the two complexes in combination (Paper 2, Figure 4; Paper 1, Figure 7). The analysis of their interactions and RNA-channeling properties, particularly considering the above-described molecular mechanisms of hSKI, has interesting repercussions for their combined function, and sets the foundation for structural and biochemical studies of the coordinated hSKI-exosome function in the future.

4.2.1 HBS1L bridges the interaction between hSKI and the cytoplasmic exosome

The SKI and exosome complexes are conserved in humans, but a protein similar to Ski7 in yeast that interacts between them to coordinate their functions had not been identified. In size-exclusion chromatography assays, the human SKI and exosome complexes do not interact, supporting the requirement of a Ski7-like protein to bridge their interaction in humans (Paper 1, Figure 7). Structural analysis of Ski7 in complex with the yeast exosome gave insight into the function of Ski7 in mediating the interaction between the Ski and exosome complexes and helped identifying a potential Ski7-like protein in a splicing variant of the HBS1L protein in humans.

The crystal structure of the *S. cerevisiae* Exo10-Ski7 complex shows how four α-helices of the Ski7 N-terminus (residues 116-225) interact with the exosome (Paper 2,

Figure 1; Figure 11A). The four helices bind to four conserved patches at Csl4, Mtr3 and Rrp43, covering parts of the S1/KH cap and RNase PH ring on the side of the exosome. This substantial interaction interface is in agreement with the high-affinity binding with a K_D in the nanomolar range in microscale thermophoresis measurements and suggests that Ski7 is a constitutive component of the exosome in the cytoplasm (Paper 2, Figure 2, Figure S3). The nuclear exosome adapter, Rrp6, uses the same four patches to interact with the exosome in the nucleus via similar secondary structure elements (Makino et al. 2013), revealing a conserved and mutually exclusive binding mode between the cytosolic Ski7 and nuclear Rrp6 adaptor proteins and the exosome in different cellular compartments (Paper 2, Figure 3).

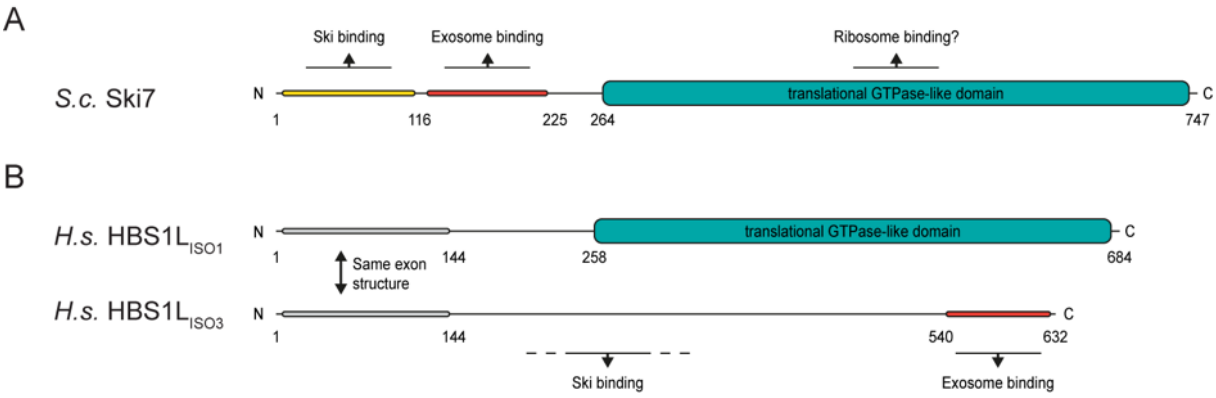

Figure 11. Domain organization of *S. cerevisiae* Ski7 **(A)** and two *H. sapiens* HBS1L splicing variants **(B)**. $HBS1L_{ISO1}$ represents the canonical translational GTPase that functions with PELO in ribosome recycling; $HBS1L_{ISO3}$ (HBS1L3) the hSKI-exosome bridging protein. The numbers below indicate the register of the protein sequence.

Computational analyses of the interacting residues in the amino acid sequence of Ski7 and its related eRF3-like GTPases identified an exosome-binding region in a splicing variant of the HBS1-like (HBS1L) protein in humans (Paper 2, Figure 4). The variant, from here onwards called HBS1L3, shows a similar exon-intron structure in the N-terminal region (residues 1-144) as the other HBS1L isoforms. The proceeding exons, which make up the GTPase-like domain, are skipped and replaced with a single and comparatively lengthy exon, containing the hEXO-binding site. Pull-down assays with recombinant proteins confirm that the C-terminal region of HBS1L3 (HBS1L3-CTD, residues 540-632, Figure 11B) interacts with the cytosolic human exosome. In a homology model of the region in complex with the hEXO9 proteins, obtained using the

AlphaFold2 algorithm for multiprotein complexes (Tunyasuvunakool et al. 2021), the HBS1L3-CTD is predicted to form a similar set of secondary structure elements, which interact with the human exosome at similar locations as Ski7 and Rrp6 do with the yeast exosomes (Figure 12). This finding supports a conservation of the binding interface in humans.

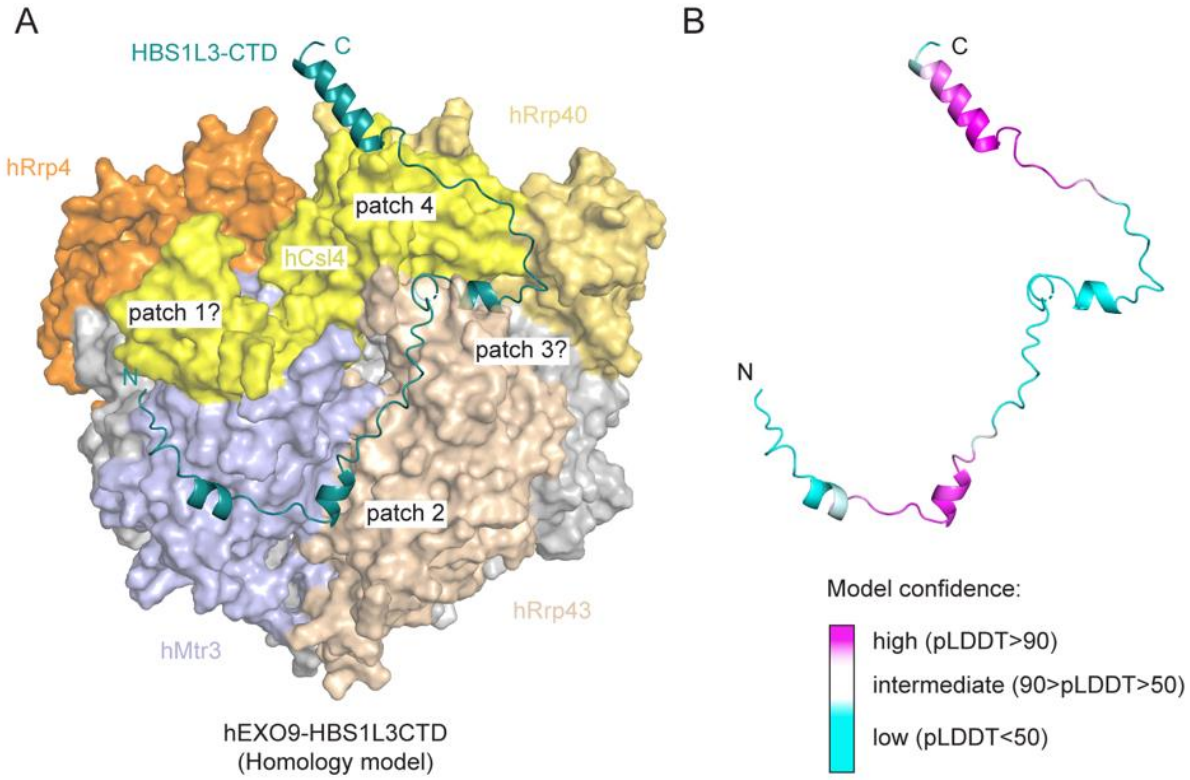

Figure 12. Homology model of the *H. sapiens* EXO9-HBS1L3 complex. In the model **(A)** the C-terminal domain (CTD) of HBS1L3 (residues 540-632) binds the human exosome similar to Ski7 the yeast exosome. The interactions at patches 2 and 4 with Mtr3/Rrp43 of the RNase PH ring and Csl4 of the S1/KH cap, respectively, are with high confidence and appear to be conserved. **(B)** The isolated HBS1L3-CTD prediction is colored according to model confidence as indicated.

HBS1L3 also interacts with the hSKI complex in size-exclusion chromatography assays, satisfying a second criterium of a Ski7-like protein (Paper 1, Figure 7A). Moreover, the protein is able to bind hSKI and the exosome at the same time to form a hSKI-exosome holo-complex. Simultaneous binding of the two complexes to HBS1L3 suggests that the hSKI interacting region is likely to localize to the N-terminal part of the protein (residues 1-539) (Figure 11B). While this is still a very large region, and not all of it may be involved in the hSKI interaction, the order of the respective

hSKI and hEXO binding sites in the protein sequence is conserved between the HBS1L3 and Ski7 proteins. Future studies of the HBS1L3 N-terminal region will show whether the corresponding hSKI interacting region is as compact as in yeast Ski7 (residues 1-105) or whether it is more spread to adapt to the potential different regulation of the human SKI complex. Nevertheless, based on this data, it seems likely that HBS1L3 is the sought-after Ski7-like protein that coordinates the function of SKI and exosome complexes in humans.

4.2.2 Open state hSKI channels RNA to the exosome via a conserved helicase-exosome mechanism

The discovery of the HBS1L3 protein opens the possibility to further characterize hSKI in the context of the exosome. In RNase protection experiments, the human SKI complex in presence of HBS1L3 is able to extend the continuous RNA channel of the cytoplasmic exosome (Paper 1, Figure 7). The length of the RNase-protected fragments is similar to the nuclear hMTR4-exosome complex (Gerlach et al. 2018), with approximately 50 nucleotides. In the structure of the nuclear hMTR4-exosome complex, the hMTR4 helicase binds directly to the S1/KH cap of the exosome, where it channels RNA from the exit site of the helicase core directly into the exosome (Figure 6) (Gerlach et al. 2018; Weick et al. 2018; Schuller et al. 2018). The conformation of the RNA as it exits the hMTR4 helicase core is similar to the conformation observed in the open state, ribosome-bound hSKI structure described above (Paper 1, Figure 6). Considering the similar length of the RNA channel, this comparison leads to the conclusion that the detached hSKI2 helicase binds in close proximity to the entry of the RNA channel of the exosome to thread RNA directly into the cytoplasmic exosome, similar to the nuclear Mtr4-exosome complex.

It is worth mentioning that both the human and yeast SKI-exosome complexes (in presence of HBS1L3 or Ski7) are only able to partially extend the exosome RNA channel. A possible explanation is the labile binding or the flexibility between the complexes, which is not surprising considering that SKI assumes closed and open conformational states. The human and yeast MTR4-exosome complexes (in presence of RRP6 and RRP47) also show only a partial extension of the RNA exosome channel and it requires the presence of MPP6 for a complete extension of continuous RNA channel with the exosome (Falk et al. 2017; Gerlach et al. 2018). Therefore, it cannot

be excluded that additional interactions or factors are needed to strengthen the SKI-exosome interaction to potentially form a more uniform continuous RNA channel.

4.3 Structural and functional differences between human and yeast Ski complexes

The comparison of the structural and biochemical data further explains common mechanistic principles of the human and yeast Ski complexes, but also uncovers discrepancies, which point towards different, species-specific mechanisms of regulation.

4.3.1 The arch domain and other structural differences

Even though all is pointing to an overall similar mechanism of the human and yeast Ski complexes, there are several structural differences. In the functional states of hSKI analyzed so far, the hSKI2 arch domain assumes the same straight conformation, pointing away from the helicase core in a perpendicular fashion (Paper 1, Figure S3). The yeast arch domain, in comparison, is more dynamic. Despite the absence of ySki3 and ySki8, the crystal structure of yeast Ski2-ΔN shows the yeast arch domain bent towards the helicase core (Section 1.5, Figure 9) (Halbach et al. 2012). Bound to the ribosome, it adopts a straight conformation as in hSKI, but is also subject to some flexibility that has not been further described (Schmidt et al. 2016, supplementary data). The human and yeast arch domains have about 20% sequence identity (as compared to 40% for the entire proteins). This suggests that it has undergone evolutionary change when compared to the rest of the protein. The purpose of the different dynamics of the otherwise structurally similar arch domains remains currently unclear.

The human and yeast Ski3 proteins also show several, notable structural differences. Besides seven additional TPRs at the hSKI3 C-terminus, which potentially extend the interaction platform of the protein (Paper 1, Figure S3) (Zeytuni & Zarivach 2012), hSKI3 shows two TPR-connecting regions that have diversified significantly from the yeast protein (described in detail in Figure 13) (Halbach et al. 2013). The relevance of these structural differences for the regulation of the human and yeast Ski complexes has not yet been explored, but they may be the object of future studies.

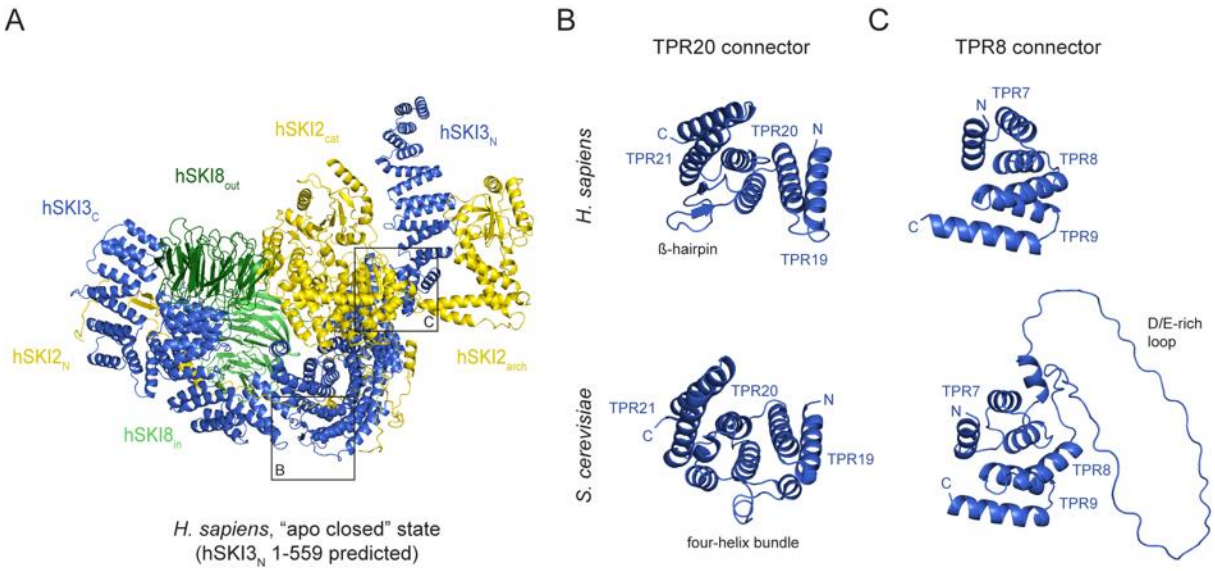

Figure 13. Diversification of human and yeast Ski3 TPR-connectors. The structure in **(A)** shows the human SKI complex in the apo closed state. Its naturally flexible hSKI3 N-terminus ($hSKI3_N$) could not be modeled in cryo-EM 3D reconstructions and was interpreted with a high confidence prediction of $hSKI3_N$ (residues 1-559), for the purpose of this human-yeast comparison. With a few exceptions, the two antiparallel α-helices of the Ski3 TRPs are connected by a short 5-10 residue long linker. The close-up view in **(B)** shows the unusual insertion of a ß-hairpin motif into the TPR20 connecting region of hSKI3. The corresponding connection of yeast TPR20, in comparison, has evolved into a bundle of four short α-helices (Halbach et al. 2013). The TPR8-connector in **(C)** is inconspicuous in humans but exhibits a long loop structure in yeast that is rich in glutamates and aspartates and results in an overall negative charge (Halbach et al. 2013). Please note that the comparison of the TPR8-connector in (C) is based on prediction models of human and yeast $Ski3_N$.

4.3.2 The effects of the human arch domain go beyond the auto-inhibition described in yeast

The yeast Ski complex is reported to possess an intrinsic auto-inhibitory mechanism in which a presumed interaction between the ySki2 arch domain and the ySki3 N-terminal arm regulates access of the RNA to the Ski2 helicase core (Halbach et al. 2013).

In ATPase and strand displacement assays, a yeast Ski complex lacking either of the domains shows greatly increased activity (Table 1) (Halbach et al. 2013). Such a behavior could not be observed for the human SKI complex. The deletion of the hSKI2 arch domain does not significantly impact ATPase activity in comparison to the wildtype complex, and neither does the deletion of the hSKI2 wedge (Paper 1, Figure

4). This suggests that the wildtype human SKI complex is not in an inhibited ground state as the yeast complex. Consequently, its less dynamic hSKI2 arch domain is not consistent with an interaction with the hSKI3 N-terminal arm.

Cryo-EM analyses of these mutant complexes show that the apo ySki-Δarch complex assumes both closed and open conformations and that they exist in an equilibrium (Table 1; Paper 1, Figure S4), as was seen for the apo wildtype hSKI. In contrast to the yeast complex, the deletion of the arch domain (hSKI-Δarch, Figure 10) or the wedge (hSKI-Δwedge, Paper 1, Figure S4) in the human complex shows all particles in the open conformation, as can be seen in cryo-EM data sets acquired under similar apo conditions. While it is evident that the removal of the wedge, which tethers the helicase to the complex, constitutively detaches the helicase, it remains unclear why the removal of the arch domain has the same effect. Nonetheless, these findings confirm that the gatekeeping mechanism is a conserved functional element in both species, and it appears that the hSKI2 helicase more 'readily' detaches from the human complex.

In RNase protection experiments, wildtype ySKI, in presence of Ski7, is able to partly extend the RNA channel of the exosome (Table 1) (Halbach et al. 2013). This effect is enhanced upon the deletion of the arch domain. RNase protection experiments with the human complex show that wildtype hSKI, in presence of HBS1L3, does not extend the RNA channel of the exosome (Paper 1, Figure 7). It requires the deletion of either the wedge or the arch domain to see a fainter or stronger protection of an extended exosome RNA channel of similar length, respectively.

Taken together, the cryo-EM data of the yeast Ski-Δarch complex provides a sound addition to published experiments (Table 1) (Halbach et al. 2013). It links the detachment of the helicase in a subset of particles to an evasion of the auto-inhibition, as described above. The underlying mechanism, that involves the arch domain regulating helicase detachment and a potential interaction between the arch domain and the N-terminal arm of ySki3, needs to be investigated in future studies.

The picture is less clear for the human complex (Table 1). hSKI is not inherently auto-inhibited and shows a more 'readily' detaching helicase, yet the wildtype complex does not extend the RNA channel of the exosome in RNase protection experiments, for which the removal of the arch domain is required. These findings suggest that the human complex is also subject to an arch-dependent regulation. In cryo-EM analyses,

hSKI-Δarch and hSKI-Δwedge adopt nearly identical constitutively open conformations and it would seem that either could well extend the RNA channel of exosome; however, that is not what is observed. Therefore, it is possible that the arch dependent regulation in humans goes beyond the mere detachment of the helicase and should be explored in subsequent research.

Analyzed behavior	*S. cerevisiae*			*H. sapiens*		
	ySki-WT	ySki-3ΔN	ySki-Δarch	hSKI-WT	hSKI-Δwedge	hSKI-Δarch
ATP hydrolysis	Moderate	High	High	Moderate	Moderate	Moderate
Strand dis-placement	Moderate	High	High	N/A	N/A	N/A
Conforma-tional states	N/A	N/A	Closed & open	Closed & open	Open only	Open only
Channel formation	Partly extended, weak	N/A	Partly extended, strong	Not extended	Partly extended, weak	Partly extended, strong

Table 1. Overview of the different yeast and human Ski complexes and their properties. The different mutant versions of the yeast and human complexes are compared in ATPase activity and strand displacement experiments, in cryo-EM with respect to their appearance in different conformational states and in RNase protection experiments, comparing their ability to extend the continuous RNA channel of the exosome. The colored cells in the table highlight a significant 'activating' effect of the mutant complexes in comparison to wildtype. N/A marks experimental data that is not available.

5 FUTURE DIRECTIONS

The findings of this dissertation have provided interesting insights into the molecular mechanisms of the human SKI complex, the function of hSKI in the context of the cytoplasmic exosome, the role of HBS1L3 as a potential mediator of the hSKI-exosome interaction as well as the differences and similarities between the human and yeast Ski complexes. There remain, however, several open questions regarding the interplay of the hSKI and exosome complexes and their recognition of mRNA substrates that could be investigated in future research.

One of the main outstanding questions is how the respective unwinding and nuclease activities of the Ski and exosome complexes are coordinated in a Ski-exosome holocomplex at the molecular level. Answering this question would entail an advanced biochemical and structural characterization of Ski7 and Hbs1L3. While the interaction of Ski7 with the S1/KH cap of the exosome is understood at the molecular level, and it appears to be conserved in the human HBS1L3 protein, their interactions with the Ski complex have not yet been explored in either species. In particular, it would be fundamental to gain a detailed understanding of how Ski7 and HBS1L3 interact with the complex to coordinate the Ski2 helicase detachment, so as to obtain a more complete picture of the open and closed conformational states of the Ski complex described in this dissertation. Except for the exosome-binding site, the Ski7 and HBS1L3 proteins do not share significant sequence homology; therefore, their action on the conformational states of the Ski complex may be different between yeast and humans.

Another interesting avenue for future research is the association of the yeast Ski complex with the adaptor protein Ska1 (Zhang et al. 2019). It is thought to recruit the exosome to untranslated mRNAs devoid of ribosomes. Structural analyses of the Ski-Ska1 complex may explain the preference of the complex for translationally inactive over active mRNAs and the reported mutually exclusive behavior.

Furthermore, the human SKI complex was reported to recruit the exosome mainly to aberrant mRNAs in surveillance pathways (Tuck et al. 2020). Understanding the function of the hSKI-exosome complex in these pathways would require a detailed investigation of the upstream processes. The principle of ribosome collisions as a sensor of aberrant transcripts in mRNA surveillance could generate novel questions concerning the precise substrate of hSKI-exosome. Answering these questions will

ultimately necessitate the knowledge of where and when the putative endonuclease strikes.

In the same study that analyzed mammalian mRNA decay pathways (Tuck et al. 2020), two proteins that had remained inconspicuous so far, Aven and Focad, were found to interact with the human SKI complex. The association of hSKI in a complex with the Aven and Focad proteins to counteract ribosome stalling during mRNA surveillance is another interesting potential area for research. The known function of the hSKI complex in the recruitment of the exosome to terminally degrade defective mRNAs is seemingly in opposition to the resolution of ribosome stalls in a complex with the two proteins. Solving this paradox would require more information about the two proteins and may be addressed in future studies.

6 REFERENCES

Allmang, C., Petfalski, E., Podtelejnikov, A., Mann, M., Tollervey, D., & Mitchell, P. (1999). The yeast exosome and human PM-Scl are related complexes of 3' --> 5' exonucleases. *Genes & Development*, *13*(16), 2148–2158. http://doi.org/10.1101/gad.13.16.2148

Anderson, J. S. J., & Parker, R. (1998). The 3′ to 5′ degradation of yeast mRNAs is a general mechanism for mRNA turnover that requires the SKI2 DEVH box protein and 3′ to 5′ exonucleases of the exosome complex. *The EMBO Journal*, *17*(5), 1497–1506. http://doi.org/10.1093/emboj/17.5.1497

Anderson, J. T., & Wang, X. (2009). Nuclear RNA surveillance: no sign of substrates tailing off. *Critical Reviews in Biochemistry and Molecular Biology*, *44*(1), 16–24. http://doi.org/10.1080/10409230802640218

Araki, Y., Takahashi, S., Kobayashi, T., Kajiho, H., Hoshino, S. I., & Katada, T. (2001). Ski7p G protein interacts with the exosome and the Ski complex for 3′-to-5′ mRNA decay in yeast. *The EMBO Journal*, *20*(17), 4684–4693. http://doi.org/10.1093/emboj/20.17.4684

Basquin, J., Roudko, V. V., Rode, M., Basquin, C., Séraphin, B., & Conti, E. (2012). Architecture of the nuclease module of the yeast Ccr4-not complex: the Not1-Caf1-Ccr4 interaction. *Molecular Cell*, *48*(2), 207–218. http://doi.org/10.1016/j.molcel.2012.08.014

Becker, T., Armache, J.-P., Jarasch, A., Anger, A. M., Villa, E., Sieber, H., et al. (2011). Structure of the no-go mRNA decay complex Dom34–Hbs1 bound to a stalled 80S ribosome. *Nature Structural & Molecular Biology*, *18*(6), 715–720. http://doi.org/10.1038/nsmb.2057

Benard, L., Carroll, K., Valle, R. C., & Wickner, R. B. (1998). Ski6p is a homolog of RNA-processing enzymes that affects translation of non-poly(A) mRNAs and 60S ribosomal subunit biogenesis. *Molecular and Cellular …*, *18*(5), 2688–2696. http://doi.org/10.1128/MCB.18.5.2688

Bernstein, P., Peltz, S. W., & Ross, J. (1989). The poly(A)-poly(A)-binding protein complex is a major determinant of mRNA stability in vitro. *Molecular and Cellular …*, *9*(2), 659–670. http://doi.org/10.1128/mcb.9.2.659-670.1989

Bonneau, F., Basquin, J., Ebert, J., Lorentzen, E., & Conti, E. (2009). The Yeast Exosome Functions as a Macromolecular Cage to Channel RNA Substrates for Degradation. *Cell*, *139*(3), 547–559. http://doi.org/10.1016/j.cell.2009.08.042

Bourgeois, P., Esteve, C., Chaix, C., Béroud, C., Levy, N., The THES clinical consortium, et al. (2018). Tricho-Hepato-Enteric Syndrome mutation update: Mutations spectrum of TTC37and SKIV2L, clinical analysis and future prospects. *Human Mutation*, *39*(6), 774–789. http://doi.org/10.1002/humu.23418

Bouveret, E., Rigaut, G., Shevchenko, A., Wilm, M., & SERAPHIN, B. (2000). A Sm-like protein complex that participates in mRNA degradation. *The EMBO Journal*, *19*(7), 1661–1671. http://doi.org/10.1093/emboj/19.7.1661

Briggs, M. W., Burkard, K. T. D., & Butler, J. S. (1998). Rrp6p, the Yeast Homologue of the Human PM-Scl 100-kDa Autoantigen, Is Essential for Efficient 5.8 S rRNA 3′ End Formation. *Journal of Biological Chemistry*, *273*(21), 13255–13263. http://doi.org/10.1074/jbc.273.21.13255

Brown, A., Shao, S., Murray, J., Hegde, R. S., & Ramakrishnan, V. (2015). Structural basis for stop codon recognition in eukaryotes. *Nature*, *524*(7566), 493–496. http://doi.org/10.1038/nature14896

Brown, C. E., & Sachs, A. B. (1998). Poly(A) tail length control in Saccharomyces cerevisiae occurs by message-specific deadenylation. *Molecular and Cellular …*, *18*(11), 6548–6559. http://doi.org/10.1128/MCB.18.11.6548

Brown, J. T., Bai, X., & Johnson, A. W. (2000). The yeast antiviral proteins Ski2p, Ski3p, and Ski8p exist as a complex in vivo. *RNA (New York, N.Y.)*, *6*(3), 449–457.

Büttner, K., Nehring, S., & Hopfner, K.-P. (2007). Structural basis for DNA duplex separation by a superfamily-2 helicase. *Nature Structural & Molecular Biology*, *14*(7), 647–652. http://doi.org/10.1038/nsmb1246

Büttner, K., Wenig, K., & Hopfner, K.-P. (2005). Structural framework for the mechanism of archaeal exosomes in RNA processing. *Molecular Cell*, *20*(3), 461–471. http://doi.org/10.1016/j.molcel.2005.10.018

Chandrasekaran, V., Juszkiewicz, S., Choi, J., Puglisi, J. D., Brown, A., Shao, S., et al. (2019). Mechanism of ribosome stalling during translation of a poly(A) tail. *Nature Structural & Molecular Biology*, *26*(12), 1132–1140. http://doi.org/10.1038/s41594-019-0331-x

Chen, C. Y., Gherzi, R., Ong, S. E., Chan, E. L., Raijmakers, R., Pruijn, G. J., et al. (2001). AU binding proteins recruit the exosome to degrade ARE-containing mRNAs. *Cell*, *107*(4), 451–464. http://doi.org/10.1016/s0092-8674(01)00578-5

Chowdhury, A., Mukhopadhyay, J., & Tharun, S. (2007). The decapping activator Lsm1p-7p-Pat1p complex has the intrinsic ability to distinguish between oligoadenylated and polyadenylated RNAs. *RNA (New York, N.Y.)*, *13*(7), 998–1016. http://doi.org/10.1261/rna.502507

Das, M., Zattas, D., Zinder, J. C., Wasmuth, E. V., Henri, J., & Lima, C. D. (2021). Substrate discrimination and quality control require each catalytic activity of TRAMP and the nuclear RNA exosome. *Proceedings of the National Academy of Sciences of the United States of America*, *118*(14). http://doi.org/10.1073/pnas.2024846118

Decker, C. J., & Parker, R. (1993). A turnover pathway for both stable and unstable mRNAs in yeast: evidence for a requirement for deadenylation. *Genes & Development*, *7*(8), 1632–1643. http://doi.org/10.1101/gad.7.8.1632

Decker, C. J., & Parker, R. (2012). P-bodies and stress granules: possible roles in the control of translation and mRNA degradation. *Cold Spring Harbor Perspectives in Biology*, *4*(9), a012286. http://doi.org/10.1101/cshperspect.a012286

Doma, M. K., & Parker, R. (2006). Endonucleolytic cleavage of eukaryotic mRNAs with stalls in translation elongation. *Nature*, *440*(7083), 561–564. http://doi.org/10.1038/nature04530

Dunckley, T., Tucker, M., & Parker, R. (2001). Two related proteins, Edc1p and Edc2p, stimulate mRNA decapping in Saccharomyces cerevisiae. *Genetics*, *157*(1), 27–37. http://doi.org/10.1093/genetics/157.1.27

Dziembowski, A., Lorentzen, E., Conti, E., & Séraphin, B. (2007). A single subunit, Dis3, is essentially responsible for yeast exosome core activity. *Nature Structural & Molecular Biology*, *14*(1), 15–22. http://doi.org/10.1038/nsmb1184

D'Orazio, K. N., Wu, C. C.-C., Sinha, N., Loll-Krippleber, R., Brown, G. W., & Green, R. (2019). The endonuclease Cue2 cleaves mRNAs at stalled ribosomes during No Go Decay. *eLife*, *8*. http://doi.org/10.7554/eLife.49117

Eberle, A. B., Lykke-Andersen, S., Mühlemann, O., & Jensen, T. H. (2009). SMG6 promotes endonucleolytic cleavage of nonsense mRNA in human cells. *Nature Structural & Molecular Biology*, *16*(1), 49–55. http://doi.org/10.1038/nsmb.1530

Fabre, A., Breton, A., Coste, M.-E., Colomb, V., Dubern, B., Lachaux, A., et al. (2014). Syndromic (phenotypic) diarrhoea of infancy/tricho-hepato-enteric syndrome. *Archives of Disease in Childhood*, *99*(1), 35–38. http://doi.org/10.1136/archdischild-2013-304016

Fabre, A., Charroux, B., Martinez-Vinson, C., Roquelaure, B., Odul, E., Sayar, E., et al. (2012). SKIV2L Mutations Cause Syndromic Diarrhea, or Trichohepatoenteric Syndrome. *The American Journal of Human Genetics*, *90*(4), 689–692. http://doi.org/10.1016/j.ajhg.2012.02.009

Fairman-Williams, M. E., Guenther, U.-P., & Jankowsky, E. (2010). SF1 and SF2 helicases: family matters. *Current Opinion in Structural Biology*, *20*(3), 313–324. http://doi.org/10.1016/j.sbi.2010.03.011

Falk, S., Bonneau, F., Ebert, J., Kögel, A., & Conti, E. (2017). Mpp6 Incorporation in the Nuclear Exosome Contributes to RNA Channeling through the Mtr4 Helicase. *CellReports*, *20*(10), 2279–2286. http://doi.org/10.1016/j.celrep.2017.08.033

Falk, S., Finogenova, K., Melko, M., Benda, C., Lykke-Andersen, S., Jensen, T. H., & Conti, E. (2016). Structure of the RBM7-ZCCHC8 core of the NEXT complex reveals connections to splicing factors. *Nature Communications*, *7*(1), 13573–10. http://doi.org/10.1038/ncomms13573

Falk, S., Weir, J. R., Hentschel, J., Reichelt, P., Bonneau, F., & Conti, E. (2014). The Molecular Architecture of the TRAMP Complex Reveals the Organization and Interplay of Its Two Catalytic Activities. *Molecular Cell*, *55*(6), 856–867. http://doi.org/10.1016/j.molcel.2014.07.020

Frazão, C., McVey, C. E., Amblar, M., Barbas, A., Vonrhein, C., Arraiano, C. M., & Carrondo, M. A. (2006). Unravelling the dynamics of RNA degradation by ribonuclease II and its RNA-bound complex. *Nature*, *443*(7107), 110–114. http://doi.org/10.1038/nature05080

Frischmeyer, P. A., van Hoof, A., O'Donnell, K., Guerrerio, A. L., Parker, R., & Dietz, H. C. (2002). An mRNA surveillance mechanism that eliminates transcripts lacking termination codons. *Science*, *295*(5563), 2258–2261. http://doi.org/10.1126/science.1067338

Garzia, A., Jafarnejad, S. M., Meyer, C., Chapat, C., Gogakos, T., Morozov, P., et al. (2017). The E3 ubiquitin ligase and RNA-binding protein ZNF598 orchestrates ribosome quality control of premature polyadenylated mRNAs. *Nature Communications*, *8*, 16056. http://doi.org/10.1038/ncomms16056

Gerlach, P., Schuller, J. M., Bonneau, F., Basquin, J., Reichelt, P., Falk, S., & Conti, E. (2018). Distinct and evolutionary conserved structural features of the human nuclear exosome complex. *eLife*, *7*, e38686–22. http://doi.org/10.7554/eLife.38686

Girault, D., Goulet, O., Le Deist, F., Brousse, N., Colomb, V., Césarini, J. P., et al. (1994). Intractable infant diarrhea associated with phenotypic abnormalities and immunodeficiency. *The Journal of Pediatrics*, *125*(1), 36–42. http://doi.org/10.1016/s0022-3476(94)70118-0

Glover, M. L., Burroughs, A. M., Monem, P. C., Egelhofer, T. A., Pule, M. N., Aravind, L., & Arribere, J. A. (2020). NONU-1 Encodes a Conserved Endonuclease Required for mRNA Translation Surveillance. *CellReports*, *30*(13), 4321–4331.e4. http://doi.org/10.1016/j.celrep.2020.03.023

Grishin, N. V. (2001). KH domain: one motif, two folds. *Nucleic Acids Research*, *29*(3), 638–643. http://doi.org/10.1093/nar/29.3.638

Halbach, F., Reichelt, P., Rode, M., & Conti, E. (2013). The Yeast Ski Complex: Crystal Structure and RNA Channeling to the Exosome Complex. *Cell*, *154*(4), 814–826. http://doi.org/10.1016/j.cell.2013.07.017

Halbach, F., Rode, M., & Conti, E. (2012). The crystal structure of S. cerevisiae Ski2, a DExH helicase associated with the cytoplasmic functions of the exosome. *RNA (New York, N.Y.)*, *18*(1), 124–134. http://doi.org/10.1261/rna.029553.111

He, F., Li, X., Spatrick, P., Casillo, R., Dong, S., & Jacobson, A. (2003). Genome-wide analysis of mRNAs regulated by the nonsense-mediated and 5“ to 3” mRNA decay pathways in yeast. *Molecular Cell*, *12*(6), 1439–1452. http://doi.org/10.1016/s1097-2765(03)00446-5

Hernández, H., Dziembowski, A., Taverner, T., Séraphin, B., & Robinson, C. V. (2006). Subunit architecture of multimeric complexes isolated directly from cells. *EMBO Reports*, *7*(6), 605–610. http://doi.org/10.1038/sj.embor.7400702

Herrick, D., Parker, R., & Jacobson, A. (1990). Identification and comparison of stable and unstable mRNAs in Saccharomyces cerevisiae. *Molecular and Cellular …*, *10*(5), 2269–2284. http://doi.org/10.1128/mcb.10.5.2269-2284.1990

Hillman, R. T., Green, R. E., & Brenner, S. E. (2004). An unappreciated role for RNA surveillance. *Genome Biology*, *5*(2), R8–16. http://doi.org/10.1186/gb-2004-5-2-r8

Ikeuchi, K., Tesina, P., Matsuo, Y., Sugiyama, T., Cheng, J., Saeki, Y., et al. (2019). Collided ribosomes form a unique structural interface to induce Hel2-driven quality control pathways. *The EMBO Journal*, *38*(5), e100276. http://doi.org/10.15252/embj.2018100276

Ishii, R., Nureki, O., & Yokoyama, S. (2003). Crystal Structure of the tRNA Processing Enzyme RNase PH from Aquifex aeolicus *. *Journal of Biological Chemistry*, *278*(34), 32397–32404. http://doi.org/10.1074/jbc.M300639200

Januszyk, K., Liu, Q., & Lima, C. D. (2011). Activities of human RRP6 and structure of the human RRP6 catalytic domain. *RNA (New York, N.Y.)*, *17*(8), 1566–1577. http://doi.org/10.1261/rna.2763111

Jia, H., Wang, X., Liu, F., Guenther, U.-P., Srinivasan, S., Anderson, J. T., & Jankowsky, E. (2011). The RNA helicase Mtr4p modulates polyadenylation in the TRAMP complex. *Cell*, *145*(6), 890–901. http://doi.org/10.1016/j.cell.2011.05.010

Jinek, M., Coyle, S. M., & Doudna, J. A. (2011). Coupled 5' nucleotide recognition and processivity in Xrn1-mediated mRNA decay. *Molecular Cell*, *41*(5), 600–608. http://doi.org/10.1016/j.molcel.2011.02.004

Johnson, A. W., & Kolodner, R. D. (1995). Synthetic lethality of sep1 (xrn1) ski2 and sep1 (xrn1) ski3 mutants of Saccharomyces cerevisiae is independent of killer virus and suggests a general role for these genes in translation control. *Molecular and Cellular …*, *15*(5), 2719–2727. http://doi.org/10.1128/MCB.15.5.2719

Johnson, S. J., & Jackson, R. N. (2013). Ski2-like RNA helicase structures: common themes and complex assemblies. *RNA Biology*, *10*(1), 33–43. http://doi.org/10.4161/rna.22101

Juszkiewicz, S., & Hegde, R. S. (2017). Initiation of Quality Control during Poly(A) Translation Requires Site-Specific Ribosome Ubiquitination. *Molecular Cell*, *65*(4), 743–750.e4. http://doi.org/10.1016/j.molcel.2016.11.039

Juszkiewicz, S., Chandrasekaran, V., Lin, Z., Kraatz, S., Ramakrishnan, V., & Hegde, R. S. (2018). ZNF598 Is a Quality Control Sensor of Collided Ribosomes. *Molecular Cell*, *72*(3), 469–481.e7. http://doi.org/10.1016/j.molcel.2018.08.037

Karousis, E. D., & Mühlemann, O. (2019). Nonsense-Mediated mRNA Decay Begins Where Translation Ends. *Cold Spring Harbor Perspectives in Biology*, *11*(2). http://doi.org/10.1101/cshperspect.a032862

Kilchert, C., Wittmann, S., & Vasiljeva, L. (2016). The regulation and functions of the nuclear RNA exosome complex. *Nature Reviews. Molecular Cell Biology*, *17*(4), 227–239. http://doi.org/10.1038/nrm.2015.15

Klauer, A. A., & van Hoof, A. (2012). Degradation of mRNAs that lack a stop codon: a decade of nonstop progress. *Wiley Interdisciplinary Reviews: RNA*, *3*(5), 649–660. http://doi.org/10.1002/wrna.1124

Kowalinski, E., Schuller, A., Green, R., & Conti, E. (2015). Saccharomyces cerevisiae Ski7 Is a GTP-Binding Protein Adopting the Characteristic Conformation of Active

Translational GTPases. *Structure*, *23*(7), 1336–1343. http://doi.org/10.1016/j.str.2015.04.018

Kshirsagar, M., & Parker, R. (2004). Identification of Edc3p as an enhancer of mRNA decapping in Saccharomyces cerevisiae. *Genetics*, *166*(2), 729–739. http://doi.org/10.1534/genetics.166.2.729

Kuroha, K., Akamatsu, M., Dimitrova, L., Ito, T., Kato, Y., Shirahige, K., & Inada, T. (2010). Receptor for activated C kinase 1 stimulates nascent polypeptide-dependent translation arrest. *EMBO Reports*, *11*(12), 956–961. http://doi.org/10.1038/embor.2010.169

Kurosaki, T., Popp, M. W., & Maquat, L. E. (2019). Quality and quantity control of gene expression by nonsense-mediated mRNA decay. *Nature Reviews. Molecular Cell Biology*, 1–15. http://doi.org/10.1038/s41580-019-0126-2

Kühn, U., & Wahle, E. (2004). Structure and function of poly(A) binding proteins. *Biochimica Et Biophysica Acta*, *1678*(2-3), 67–84. http://doi.org/10.1016/j.bbaexp.2004.03.008

LaCava, J., Houseley, J., Saveanu, C., Petfalski, E., Thompson, E., Jacquier, A., & Tollervey, D. (2005). RNA degradation by the exosome is promoted by a nuclear polyadenylation complex. *Cell*, *121*(5), 713–724. http://doi.org/10.1016/j.cell.2005.04.029

Lebreton, A., Tomecki, R., Dziembowski, A., & Séraphin, B. (2008). Endonucleolytic RNA cleavage by a eukaryotic exosome. *Nature*, *456*(7224), 993–996. http://doi.org/10.1038/nature07480

Lee, S. G., Lee, I., Park, S. H., Kang, C., & Song, K. (1995). Identification and characterization of a human cDNA homologous to yeast SKI2. *Genomics*, *25*(3), 660–666. http://doi.org/10.1016/0888-7543(95)80008-a

Letzring, D. P., Dean, K. M., & Grayhack, E. J. (2010). Control of translation efficiency in yeast by codon-anticodon interactions. *RNA (New York, N.Y.)*, *16*(12), 2516–2528. http://doi.org/10.1261/rna.2411710

Lingaraju, M., Johnsen, D., Schlundt, A., Langer, L. M., Basquin, J., Sattler, M., et al. (2019). The MTR4 helicase recruits nuclear adaptors of the human RNA exosome using distinct arch-interacting motifs. *Nature Communications*, *10*(1), 3393–11. http://doi.org/10.1038/s41467-019-11339-x

Liu, Q., Greimann, J. C., & Lima, C. D. (2006). Reconstitution, activities, and structure of the eukaryotic RNA exosome. *Cell*, *127*(6), 1223–1237. http://doi.org/10.1016/j.cell.2006.10.037

Lorentzen, E., Basquin, J., Tomecki, R., Dziembowski, A., & Conti, E. (2008). Structure of the active subunit of the yeast exosome core, Rrp44: diverse modes of substrate recruitment in the RNase II nuclease family. *Molecular Cell*, *29*(6), 717–728. http://doi.org/10.1016/j.molcel.2008.02.018

Lorentzen, E., Walter, P., Fribourg, S., Evguenieva-Hackenberg, E., Klug, G., & Conti, E. (2005). The archaeal exosome core is a hexameric ring structure with

three catalytic subunits. *Nature Structural & Molecular Biology*, *12*(7), 575–581. http://doi.org/10.1038/nsmb952

Lowell, J. E., Rudner, D. Z., & Sachs, A. B. (1992). 3'-UTR-dependent deadenylation by the yeast poly(A) nuclease. *Genes & Development*, *6*(11), 2088–2099. http://doi.org/10.1101/gad.6.11.2088

Lubas, M., Andersen, P. R., Schein, A., Dziembowski, A., Kudla, G., & Jensen, T. H. (2015). The human nuclear exosome targeting complex is loaded onto newly synthesized RNA to direct early ribonucleolysis. *CellReports*, *10*(2), 178–192. http://doi.org/10.1016/j.celrep.2014.12.026

Lubas, M., Christensen, M. S., Kristiansen, M. S., Domanski, M., Falkenby, L. G., Lykke-Andersen, S., et al. (2011). Interaction profiling identifies the human nuclear exosome targeting complex. *Molecular Cell*, *43*(4), 624–637. http://doi.org/10.1016/j.molcel.2011.06.028

Lykke-Andersen, J., & Wagner, E. (2005). Recruitment and activation of mRNA decay enzymes by two ARE-mediated decay activation domains in the proteins TTP and BRF-1. *Genes & Development*, *19*(3), 351–361. http://doi.org/10.1101/gad.1282305

Lykke-Andersen, S., Brodersen, D. E., & Jensen, T. H. (2009). Origins and activities of the eukaryotic exosome. *Journal of Cell Science*, *122*(Pt 10), 1487–1494. http://doi.org/10.1242/jcs.047399

Makino, D. L., Baumgärtner, M., & Conti, E. (2013). Crystal structure of an RNA-bound 11-subunit eukaryotic exosome complex. *Nature*, *495*(7439), 70–75. http://doi.org/10.1038/nature11870

Makino, D. L., Schuch, B., Stegmann, E., Baumgärtner, M., Basquin, C., & Conti, E. (2015). RNA degradation paths in a 12-subunit nuclear exosome complex. *Nature*, *524*(7563), 54–58. http://doi.org/10.1038/nature14865

Marshall, A. N., Han, J., Kim, M., & van Hoof, A. (2018). Conservation of mRNA quality control factor Ski7 and its diversification through changes in alternative splicing and gene duplication. *Proceedings of the National Academy of Sciences*, *115*(29), E6808–E6816. http://doi.org/10.1073/pnas.1801997115

Marshall, A. N., Montealegre, M. C., Jiménez-López, C., Lorenz, M. C., & van Hoof, A. (2013). Alternative splicing and subfunctionalization generates functional diversity in fungal proteomes. *PLoS Genetics*, *9*(3), e1003376. http://doi.org/10.1371/journal.pgen.1003376

Matsuo, Y., Ikeuchi, K., Saeki, Y., Iwasaki, S., Schmidt, C., Udagawa, T., et al. (2017). Ubiquitination of stalled ribosome triggers ribosome-associated quality control. *Nature Communications*, *8*(1), 159–14. http://doi.org/10.1038/s41467-017-00188-1

Meola, N., Domanski, M., Karadoulama, E., Chen, Y., Gentil, C., Pultz, D., et al. (2016). Identification of a Nuclear Exosome Decay Pathway for Processed Transcripts. *Molecular Cell*, *64*(3), 520–533. http://doi.org/10.1016/j.molcel.2016.09.025

Mitchell, P., Petfalski, E., & Tollervey, D. (1996). The 3' end of yeast 5.8S rRNA is generated by an exonuclease processing mechanism. *Genes & Development*, *10*(4), 502–513. http://doi.org/10.1101/gad.10.4.502

Mitchell, P., Petfalski, E., Shevchenko, A., Mann, M., & Tollervey, D. (1997). The Exosome: A Conserved Eukaryotic RNA Processing Complex Containing Multiple 3′→5′ Exoribonucleases. *Cell*, *91*(4), 457–466. http://doi.org/10.1016/S0092-8674(00)80432-8

Munchel, S. E., Shultzaberger, R. K., Takizawa, N., & Weis, K. (2011). Dynamic profiling of mRNA turnover reveals gene-specific and system-wide regulation of mRNA decay. *Molecular Biology of the Cell*, *22*(15), 2787–2795. http://doi.org/10.1091/mbc.E11-01-0028

Nissan, T., Rajyaguru, P., She, M., Song, H., & Parker, R. (2010). Decapping activators in Saccharomyces cerevisiae act by multiple mechanisms. *Molecular Cell*, *39*(5), 773–783. http://doi.org/10.1016/j.molcel.2010.08.025

Ozgur, S., Buchwald, G., Falk, S., Chakrabarti, S., Prabu, J. R., & Conti, E. (2015). The conformational plasticity of eukaryotic RNA-dependent ATPases. *The FEBS Journal*, *282*(5), 850–863. http://doi.org/10.1111/febs.13198

Parker, R. (2012). RNA Degradation in Saccharomyces cerevisae. *Genetics*, *191*(3), 671–702. http://doi.org/10.1534/genetics.111.137265

Parker, R., & Song, H. (2004). The enzymes and control of eukaryotic mRNA turnover. *Nature Structural & Molecular Biology*, *11*(2), 121–127. http://doi.org/10.1038/nsmb724

Pellegrini, O., Mathy, N., Condon, C., & Benard, L. (2008). In vitro assays of 5“ to 3-”exoribonuclease activity. *Methods in Enzymology*, *448*, 167–183. http://doi.org/10.1016/S0076-6879(08)02609-8

Pisareva, V. P., Skabkin, M. A., Hellen, C. U. T., Pestova, T. V., & Pisarev, A. V. (2011). Dissociation by Pelota, Hbs1 and ABCE1 of mammalian vacant 80S ribosomes and stalled elongation complexes. *The EMBO Journal*, *30*(9), 1804–1817. http://doi.org/10.1038/emboj.2011.93

Puno, M. R., & Lima, C. D. (2018). Structural basis for MTR4-ZCCHC8 interactions that stimulate the MTR4 helicase in the nuclear exosome-targeting complex. *Proceedings of the National Academy of Sciences of the United States of America*, *115*(24), E5506–E5515. http://doi.org/10.1073/pnas.1803530115

Qu, X., Yang, Z., Zhang, S., Shen, L., Dangel, A. W., Hughes, J. H., et al. (1998). The human DEVH-box protein Ski2w from the HLA is localized in nucleoli and ribosomes. *Nucleic Acids Research*, *26*(17), 4068–4077. http://doi.org/10.1093/nar/26.17.4068

Raisch, T., Chang, C.-T., Levdansky, Y., Muthukumar, S., Raunser, S., & Valkov, E. (2019). Reconstitution of recombinant human CCR4-NOT reveals molecular insights into regulated deadenylation. *Nature Communications*, *10*(1), 3173–14. http://doi.org/10.1038/s41467-019-11094-z

Ridley, S. P., Sommer, S. S., & Wickner, R. B. (1984). Superkiller mutations in Saccharomyces cerevisiae suppress exclusion of M2 double-stranded RNA by L-A-HN and confer cold sensitivity in the presence of M and L-A-HN. *Molecular and Cellular …*, *4*(4), 761–770. http://doi.org/10.1128/MCB.4.4.761

Saito, K., Horikawa, W., & Ito, K. (2015). Inhibiting K63 polyubiquitination abolishes no-go type stalled translation surveillance in Saccharomyces cerevisiae. *PLoS Genetics*, *11*(4), e1005197. http://doi.org/10.1371/journal.pgen.1005197

Schaeffer, D., Tsanova, B., Barbas, A., Reis, F. P., Dastidar, E. G., Sanchez-Rotunno, M., et al. (2009). The exosome contains domains with specific endoribonuclease, exoribonuclease and cytoplasmic mRNA decay activities. *Nature Structural & Molecular Biology*, *16*(1), 56–62. http://doi.org/10.1038/nsmb.1528

Schäfer, I. B., Rode, M., Bonneau, F., Schüssler, S., & Conti, E. (2014). The structure of the Pan2-Pan3 core complex reveals cross-talk between deadenylase and pseudokinase. *Nature Structural & Molecular Biology*, *21*(7), 591–598. http://doi.org/10.1038/nsmb.2834

Schäfer, I. B., Yamashita, M., Schuller, J. M., Schüssler, S., Reichelt, P., Strauss, M., & Conti, E. (2019). Molecular Basis for poly(A) RNP Architecture and Recognition by the Pan2-Pan3 Deadenylase. *Cell*, *177*(6), 1619–1631.e21. http://doi.org/10.1016/j.cell.2019.04.013

Schmidt, C., Kowalinski, E., Shanmuganathan, V., Defenouillère, Q., Braunger, K., Heuer, A., et al. (2016). The cryo-EM structure of a ribosome–Ski2-Ski3-Ski8 helicase complex. *Science*, *354*(6318), 1431–1433. http://doi.org/10.1126/science.aaf7520

Schneider, C., Leung, E., Brown, J., & Tollervey, D. (2009). The N-terminal PIN domain of the exosome subunit Rrp44 harbors endonuclease activity and tethers Rrp44 to the yeast core exosome. *Nucleic Acids Research*, *37*(4), 1127–1140. http://doi.org/10.1093/nar/gkn1020

Schuch, B., Feigenbutz, M., Makino, D. L., Falk, S., Basquin, C., Mitchell, P., & Conti, E. (2014). The exosome-binding factors Rrp6 and Rrp47 form a composite surface for recruiting the Mtr4 helicase. *The EMBO Journal*, *33*(23), 2829–2846. http://doi.org/10.15252/embj.201488757

Schuller, J. M., Falk, S., Fromm, L., Hurt, E., & Conti, E. (2018). Structure of the nuclear exosome captured on a maturing preribosome. *Science*, *360*(6385), 219–222. http://doi.org/10.1126/science.aar5428

Shao, S., Murray, J., Brown, A., Taunton, J., Ramakrishnan, V., & Hegde, R. S. (2016). Decoding Mammalian Ribosome-mRNA States by Translational GTPase Complexes. *Cell*, *167*(5), 1229–1240.e15. http://doi.org/10.1016/j.cell.2016.10.046

Shoemaker, C. J., Eyler, D. E., & Green, R. (2010). Dom34:Hbs1 promotes subunit dissociation and peptidyl-tRNA drop-off to initiate no-go decay. *Science*, *330*(6002), 369–372. http://doi.org/10.1126/science.1192430

Sikorska, N., Zuber, H., Gobert, A., Lange, H., & Gagliardi, D. (2017). RNA degradation by the plant RNA exosome involves both phosphorolytic and hydrolytic activities. *Nature Communications*, 1–15. http://doi.org/10.1038/s41467-017-02066-2

Simms, C. L., Thomas, E. N., & Zaher, H. S. (2017). Ribosome-based quality control of mRNA and nascent peptides. *Wiley Interdisciplinary Reviews: RNA*, *8*(1), e1366. http://doi.org/10.1002/wrna.1366

Staals, R. H. J., Bronkhorst, A. W., Schilders, G., Slomovic, S., Schuster, G., Heck, A. J. R., et al. (2010). Dis3-like 1: a novel exoribonuclease associated with the human exosome. *The EMBO Journal*, *29*(14), 2358–2367. http://doi.org/10.1038/emboj.2010.122

Steiger, M., Carr-Schmid, A., Schwartz, D. C., Kiledjian, M., & Parker, R. (2003). Analysis of recombinant yeast decapping enzyme. *RNA (New York, N.Y.)*, *9*(2), 231–238. http://doi.org/10.1261/rna.2151403

Stowell, J. A. W., Webster, M. W., Kögel, A., Wolf, J., Shelley, K. L., & Passmore, L. A. (2016). Reconstitution of Targeted Deadenylation by the Ccr4-Not Complex and the YTH Domain Protein Mmi1. *CellReports*, *17*(8), 1978–1989. http://doi.org/10.1016/j.celrep.2016.10.066

Subtelny, A. O., Eichhorn, S. W., Chen, G. R., Sive, H., & Bartel, D. P. (2014). Poly(A)-tail profiling reveals an embryonic switch in translational control. *Nature*, *508*(7494), 66–71. http://doi.org/10.1038/nature13007

Suryanarayana, T., & Subramanian, A. R. (1984). Function of the repeating homologous sequences in nucleic acid binding domain of ribosomal protein S1. *Biochemistry*, *23*(6), 1047–1051. http://doi.org/10.1021/bi00301a002

Synowsky, S. A., & Heck, A. J. R. (2008). The yeast Ski complex is a hetero-tetramer. *Protein Science*, *17*(1), 119–125. http://doi.org/10.1110/ps.073155908

Tauchert, M. J., Fourmann, J.-B., Lührmann, R., & Ficner, R. (2017). Structural insights into the mechanism of the DEAH-box RNA helicase Prp43. *eLife*, *6*. http://doi.org/10.7554/eLife.21510

Tesina, P., Heckel, E., Cheng, J., Fromont-Racine, M., Buschauer, R., Kater, L., et al. (2019). Structure of the 80S ribosome-Xrn1 nuclease complex. *Nature Structural & Molecular Biology*, *26*(4), 275–280. http://doi.org/10.1038/s41594-019-0202-5

Tharun, S., & Parker, R. (2001). Targeting an mRNA for decapping: displacement of translation factors and association of the Lsm1p-7p complex on deadenylated yeast mRNAs. *Molecular Cell*, *8*(5), 1075–1083. http://doi.org/10.1016/s1097-2765(01)00395-1

Toh-E, A., & Wickner, R. B. (1979). A mutant killer plasmid whose replication depends on a chromosomal “superkiller” mutation. *Genetics*, *91*(4), 673–682.

Tomecki, R., Kristiansen, M. S., Lykke-Andersen, S., Chlebowski, A., Larsen, K. M., Szczesny, R. J., et al. (2010). The human core exosome interacts with

differentially localized processive RNases: hDIS3 and hDIS3L. *The EMBO Journal*, *29*(14), 2342–2357. http://doi.org/10.1038/emboj.2010.121

Tsuboi, T., Kuroha, K., Kudo, K., Makino, S., Inoue, E., Kashima, I., & Inada, T. (2012). Dom34:hbs1 plays a general role in quality-control systems by dissociation of a stalled ribosome at the 3' end of aberrant mRNA. *Molecular Cell*, *46*(4), 518–529. http://doi.org/10.1016/j.molcel.2012.03.013

Tuck, A. C., Rankova, A., Arpat, A. B., Liechti, L. A., Hess, D., Iesmantavicius, V., et al. (2020). Mammalian RNA Decay Pathways Are Highly Specialized and Widely Linked to Translation. *Molecular Cell*, *77*(6), 1222–1236.e13. http://doi.org/10.1016/j.molcel.2020.01.007

Tucker, M., Valencia-Sanchez, M. A., Staples, R. R., Chen, J., Denis, C. L., & Parker, R. (2001). The transcription factor associated Ccr4 and Caf1 proteins are components of the major cytoplasmic mRNA deadenylase in Saccharomyces cerevisiae. *Cell*, *104*(3), 377–386. http://doi.org/10.1016/s0092-8674(01)00225-2

Tunyasuvunakool, K., Adler, J., Wu, Z., Green, T., Zielinski, M., Žídek, A., et al. (2021). Highly accurate protein structure prediction for the human proteome. *Nature*, *596*(7873), 590–596. http://doi.org/10.1038/s41586-021-03828-1

van Dijk, E., Cougot, N., Meyer, S., Babajko, S., Wahle, E., & Séraphin, B. (2002). Human Dcp2: a catalytically active mRNA decapping enzyme located in specific cytoplasmic structures. *The EMBO Journal*, *21*(24), 6915–6924. http://doi.org/10.1093/emboj/cdf678

van Hoof, A. (2005). Conserved functions of yeast genes support the duplication, degeneration and complementation model for gene duplication. *Genetics*, *171*(4), 1455–1461. http://doi.org/10.1534/genetics.105.044057

van Hoof, A., Frischmeyer, P. A., Dietz, H. C., & Parker, R. (2002). Exosome-mediated recognition and degradation of mRNAs lacking a termination codon. *Science*, *295*(5563), 2262–2264. http://doi.org/10.1126/science.1067272

van Hoof, A., Staples, R. R., Baker, R. E., & Parker, R. (2000). Function of the ski4p (Csl4p) and Ski7p proteins in 3“-to-5” degradation of mRNA. *Molecular and Cellular …*, *20*(21), 8230–8243. http://doi.org/10.1128/MCB.20.21.8230-8243.2000

Verloes, A., Lombet, J., Lambert, Y., Hubert, A. F., Deprez, M., Fridman, V., et al. (1997). Tricho-hepato-enteric syndrome: Further delineation of a distinct syndrome with neonatal hemochromatosis phenotype, intractable diarrhea, and hair anomalies. *American Journal of Medical Genetics*, *68*(4), 391–395. http://doi.org/10.1002/(SICI)1096-8628(19970211)68:4<391::AID-AJMG3>3.0.CO;2-P

Vuković, L., Chipot, C., Makino, D. L., Conti, E., & Schulten, K. (2016). Molecular Mechanism of Processive 3“ to 5” RNA Translocation in the Active Subunit of the RNA Exosome Complex. *Journal of the American Chemical Society*, *138*(12), 4069–4078. http://doi.org/10.1021/jacs.5b12065

Wahle, E., & Winkler, G. S. (2013). RNA decay machines: deadenylation by the Ccr4-not and Pan2-Pan3 complexes. *Biochimica Et Biophysica Acta*, *1829*(6-7), 561–570. http://doi.org/10.1016/j.bbagrm.2013.01.003

Webster, M. W., Chen, Y.-H., Stowell, J. A. W., Alhusaini, N., Sweet, T., Graveley, B. R., et al. (2018). mRNA Deadenylation Is Coupled to Translation Rates by the Differential Activities of Ccr4-Not Nucleases. *Molecular Cell*, *70*(6), 1089–1100.e8. http://doi.org/10.1016/j.molcel.2018.05.033

Webster, M. W., Stowell, J. A., & Passmore, L. A. (2019). RNA-binding proteins distinguish between similar sequence motifs to promote targeted deadenylation by Ccr4-Not. *eLife*, *8*. http://doi.org/10.7554/eLife.40670

Weick, E.-M., Puno, M. R., Januszyk, K., Zinder, J. C., DiMattia, M. A., & Lima, C. D. (2018). Helicase-Dependent RNA Decay Illuminated by a Cryo-EM Structure of a Human Nuclear RNA Exosome-MTR4 Complex. *Cell*, *173*(7), 1663–1677.e21. http://doi.org/10.1016/j.cell.2018.05.041

Weir, J. R., Bonneau, F., Hentschel, J., & Conti, E. (2010). Structural analysis reveals the characteristic features of Mtr4, a DExH helicase involved in nuclear RNA processing and surveillance. *Proceedings of the National Academy of Sciences of the United States of America*, *107*(27), 12139–12144. http://doi.org/10.1073/pnas.1004953107

Wells, S. E., Hillner, P. E., Vale, R. D., & Sachs, A. B. (1998). Circularization of mRNA by eukaryotic translation initiation factors. *Molecular Cell*, *2*(1), 135–140. http://doi.org/10.1016/s1097-2765(00)80122-7

Wu, G., Schmid, M., Rib, L., Polak, P., Meola, N., Sandelin, A., & Jensen, T. H. (2020). A Two-Layered Targeting Mechanism Underlies Nuclear RNA Sorting by the Human Exosome. *CellReports*, *30*(7), 2387–2401.e5. http://doi.org/10.1016/j.celrep.2020.01.068

Yi, H., Park, J., Ha, M., Lim, J., Chang, H., & Kim, V. N. (2018). PABP Cooperates with the CCR4-NOT Complex to Promote mRNA Deadenylation and Block Precocious Decay. *Molecular Cell*, *70*(6), 1081–1088.e5. http://doi.org/10.1016/j.molcel.2018.05.009

Zeytuni, N., & Zarivach, R. (2012). Structural and functional discussion of the tetra-trico-peptide repeat, a protein interaction module. *Structure*, *20*(3), 397–405. http://doi.org/10.1016/j.str.2012.01.006

Zhang, E., Khanna, V., Dacheux, E., Namane, A., Doyen, A., Gomard, M., et al. (2019). A specialised SKI complex assists the cytoplasmic RNA exosome in the absence of direct association with ribosomes. *The EMBO Journal*, *38*(14), e100640. http://doi.org/10.15252/embj.2018100640

Zinoviev, A., Ayupov, R. K., Abaeva, I. S., Hellen, C. U. T., & Pestova, T. V. (2020). Extraction of mRNA from Stalled Ribosomes by the Ski Complex. *Molecular Cell*, *77*(6), 1340–1349.e6. http://doi.org/10.1016/j.molcel.2020.01.011

Zuo, Y., Vincent, H. A., Zhang, J., Wang, Y., Deutscher, M. P., & Malhotra, A. (2006). Structural basis for processivity and single-strand specificity of RNase II. *Molecular Cell*, *24*(1), 149–156. http://doi.org/10.1016/j.molcel.2006.09.004

7 ACKNOWLEDGEMENTS

First, I would like to express my gratitude to my supervisor, Prof. Dr. Elena Conti, for entrusting me with the possibility to work on this exciting project in the encouraging scientific environment of her lab. Her supervision included a well-balanced combination of guidance and the freedom to follow my own scientific ideas, which was invaluable for me to grow as a scientist. I am grateful to her for all the patience and support during this journey.

Second, I would like to thank the people from whose teaching I benefitted the most. Ingmar for initially teaching and supervising the cryo-EM work, but also for valuable scientific advice throughout the years. Fabien for sharing his critical way of thinking when it comes to the interpretation of scientific experiments and for all kinds of technical suggestions. Eva for introducing me to the project and for the initial guidance which lead to a great start after joining the lab. Rajan for his computational support, but moreover for introducing me to this exciting area of research during an earlier internship in the lab.

Third, I would like to thank the scientists behind the ‘Electron Microscopy Facility’, the ‘Crystallization Facility, the ‘Biophysics Facility’ and the ‘Biochemistry Core Facility’ at the Max Planck Institute of Biochemistry. Your scientific input was invaluable for the success of the project.

Fourth, I would like to thank all past and present members of the lab for countless scientific discussions and technical support and in particular Achim for the discussion of project-specific matters. Your combined efforts enabled me to successfully complete this project. Besides creating a fruitful and encouraging scientific environment, I am grateful for the friendly atmosphere in the lab during and also past working hours. You made this time truly memorable.

Finally, I would like thank Carla, my sister and my parents for their unlimited support and patience throughout the entire time of this undertaking.